Assessment of Factors Affecting Accuracy of Standardised Uptake Values in Positron Emission Tomography

PETRUS DANIEL DU TOIT

Submitted in fulfilment of the requirements in respect of the Philosophiae Doctor (Ph.D.) degree qualification in the Department of Medical Physics in the Faculty of Health Sciences at the University of the Free State.

31 January 2015

Promotor: Dr H. du Raan

Co-promotors: Prof. W.I.D. Rae

Dr D. Visvikis (Brest, France)

1. I, Petrus Daniel du Toit, declare that the doctoral research thesis that I herewith submit at the University of the Free State, is my independent work and that I have not previously submitted it for a qualification at another institution of higher education.

2. I, Petrus Daniel du Toit, hereby declare that I am aware that the copyright is vested in the University of the Free State.

3. I, Petrus Daniel du Toit, hereby declare that all royalties as regards intellectual property that was developed during the course of and/or in connection with the study at the University of the Free State will accrue to the University.

4. I, Petrus Daniel du Toit, hereby declare that I am aware that the research may only be published with the dean's approval.

Signed at BLOEMFONTEIN on this THIRTY-FIRST day of JANUARY 2015

PD du Toit

Acknowledgements

I would like to acknowledge Professor Tys Lötter and Professor Andries van Aswegen for their contributions and advice at the onset of this project.

I would like to thank Dr Frederic Lamare for his assistance with the installation and use of the GATE and reconstruction software as well as for answering many of my questions during the course of this study.

I thank Dr Paul Segars for his assistance in providing me with the XCAT phantom and its use, as well as Dr Assen Kirov and Dr Ross Schmidtlein for their help with the GATE version of the GE Discovery ST PET scanner.

Albert van Eck at the High Performance Computing Cluster at the University deserves a special mention for hours of installing software, problem-solving and ensuring that my simulations did eventually complete.

I thank my colleagues at the Free State PET/CT Centre for letting me use the scanner and obtaining the FDG for the phantom scans.

The Dean, Professor Gert van Zyl, deserves a thank you for his encouragement and believing that I would finish this study.

My promotors, Dr Hanlie du Raan, Prof William Rae and Dr Dimitris Visvikis, deserve the credit for their dedication, for their guidance and for their patience during this project. Thank you for your availability and for leading me to the end.

I wish to thank my parents, family and special friends for their support and encouragement throughout the duration of this research. Without those I would not have succeeded.

I thank Him in whom all Knowledge is vested for His grace and for the abilities I was given to be who I am.

“In physical science the first essential step in the direction of learning any subject is to find principles of numerical reckoning and practicable methods for measuring some quality connected with it. I often say that when you can measure what you are speaking about, and express it in numbers, you know something about it; but when you cannot measure it, when you cannot express it in numbers, your knowledge is of a meagre and unsatisfactory kind; it may be the beginning of knowledge, but you have scarcely in your thoughts advanced to the state of ***Science****, whatever the matter may be.”*

[William Thomson, 1st Baron Kelvin (1824-1907)]

Assessment of Factors Affecting Accuracy of Standardised Uptake Values in Positron Emission Tomography

Table of Contents

I. List of Abbreviations

1D: one-dimensional

2D: Two-dimensional

3D: Three-dimensional

4D: Four-dimensional, including the temporal dimension

ACD: Annihilation coincidence detection

AMIDE: A Medical Image Data Examiner

ASCII: American Standard Code for Information Interchange

BGO: Bismuth Germinate

Bq: becquerel

cm: centimeter

CT: Computed Tomography

EORTC: European Organisation for Research and Treatment of Cancer

FBP: Filtered backprojection

FDG: 2-[^{18}F]fluoro-2deoxy-D-glucose

FORE: Fourier Rebinning algorithm

FoV: Field-of-view

FWHM: Full width at half maximum

g: gram

GATE: Geant 4 Application for Tomographic Emission

GE: General Electric

GTV: Gross Tumour Volume

H_0: Null hypothesis

IEC: International Electrotechnical Commission

kBq: kilobecquerel

keV: kilo electron volt

kV: kilovolt

LBR: Lesion to Background ratio

LL1: apical lesion in left lung

LL2: mid lesion in left lung

LL3: basal lesion in left lung

LoR: Line of Response

LSO: Lutetium oxyorthosilicate

MHz: megahertz

ML-EM: Maximum-likelihood expectation maximisation

MBq: megabecquerel

ml: millilitre

mm: millimeter

MRI: Magnetic Resonance Imaging

NEMA: National Electrical Manufacturers Association

NURBS: Non-Uniform Rational B-Splines

OPL-EM: One-Pass List-Mode Expectation Maximisation

OSEM: Ordered Subset Expectation Maximisation

PET/CT: Combined Positron Emission Tomography and Computed Tomography

PET: Positron Emission Tomography

PMMA: Poly(methyl methacrylate)

PMT: Photomultiplier tube

PSF: Point Spread Function

PVC: Partial Volume Correction

PVE: Partial Volume Effect

QC: Quality Control

RAM: Random Access Memory

RoI: Region of Interest

RL1: apical lesion in right lung

RL2: mid lesion in right lung

RL3: basal lesion in right lung

SNR: Signal to Noise Ratio

SPECT: Single Photon Emission Computed Tomography

SSRB: Single Slice Rebinning Algorithm

SUV: Standardised Uptake Value

SUV_{max}: The SUV derived from the maximum value of a region or volume

SUV_{mean}: The SUV derived from the mean value of a region or volume

UFS: University of the Free State

VoI: Volume of Interest

XCAT phantom: 4D Extended NURBS-Based Cardiac-Torso Phantom

Chapter I

Introduction

Table of Contents

1.1 Overview of the use of Positron Emission Tomography

Positron emission tomography (PET) is a non-invasive functional imaging technique that uses specific tracers labelled with positron emitting isotopes for the monitoring and evaluation of *in vivo* molecular processes. Typically a labelled compound is injected into the body and is distributed throughout the body in a way that is determined by its biochemical characteristics. The use of a wide range of biologically significant elements (such as ^{13}N, ^{11}C, ^{15}O and ^{18}F) provides a strong basis for molecular imaging using PET. The most widely used PET radioisotope to date is an ^{18}F labelled glucose analogue known as 2-[^{18}F]fluoro-2deoxy-D-glucose (FDG).

PET has been used routinely in clinical practice since the mid 1980s. PET technology development over the past decades has gone through a number of significant changes, driven mainly by the request for whole body acquisitions, which dominate diagnostic oncology investigations. The combination of PET and FDG has already demonstrated its advantages over conventional imaging modalities in tumour diagnosis and staging for a large number of oncology applications. These include particular tumours such as lymphoma, melanoma, lung and colorectal cancer where evidence-based studies in a number of European Union countries have indicated the need for a PET scanner for every 1–1.5 million inhabitants. (Visvikis *et al.*, 2004)

FDG PET has been proven to be of value in characterising the nature of a lesion by measuring its metabolic activity. Transport of glucose into the cell across the plasma membrane is made possible by the glucose plasma proteins. Inside the cell, the glucose is phosphorylated into glucose-6-phosphate and [^{18}F]-FDG is phosphorylated into [^{18}F]-FDG-6-phosphate by the enzyme hexokinase. The glucose-6-phosphate is further metabolised, but the [^{18}F]-FDG-6-phosphate is not and it then remains in the cell in that form. This happens since [^{18}F]-FDG-6-phosphate is a poor substrate for the enzymes that are responsible for de-phosphorylation and also because it and its metabolites do not enter the glycolytic pathway. Imaging can thus be performed without change or washout of the ^{18}F in the cells (Alazraki *et al.*, 2007; Hallet, 2004). Malignant cells actively

metabolise glucose and, consequently, appear more active on FDG images. The FDG-PET scans can be interpreted qualitatively or semi-quantitatively and both approaches have been employed to determine the degree of metabolic activity in the lesion.

The combined use of PET and computed tomography (CT) allows the clinician to localise lesions precisely within the anatomical structure of interest provided by the CT scan through image fusion with the PET scan. In addition, attenuation correction is performed concurrently by using the CT transmission beam. (Von Schulthess *et al.*, 2006)

Qualitative evaluation of lung lesions on images that were corrected for attenuation is based upon comparison of the intensity of uptake in the lesion with normal mediastinal activity; if the intensity of uptake is higher than that in the mediastinum, malignancy is suspected. Semi-quantitative determination of FDG activity of the lesion is accomplished by calculating the standardised uptake value (SUV). The SUV is a simple index of the glucose metabolism on FDG-PET images and represents the amount of uptake in a given region-of-interest (RoI) in relation to the average uptake throughout the body, normalised for body weight, lean body mass or body surface area. Visual interpretation of FDG-PET imaging has been reported to have a slightly higher sensitivity but lower specificity when compared to the semi-quantitative SUV measurement. Quantitative evaluation of the lesion provides a more objective and precise description of the uptake of the tracer in the lesion (Weber *et al.*, 2000; Graham *et al.*, 2000; Basu and Nair, 2006; Marsden, 2004). Percentage changes in SUV in the tumours or SUV thresholds can be defined and used to differentiate malignancy from benign changes in lung lesions e.g. 2.5, above which the lesion is considered to be malignant (Boellaard, 2011; Boellaard *et al.*, 2014; Hickeson *et al.*, 2002; Eschmann *et al.*, 2007; Paulino and Johnstone., 2004). SUV may also be used to characterise or predict the morphological changes within an uptake region (Bagci *et al.*, 2013).

The SUV is however influenced by biological factors such as plasma glucose levels, time of uptake, patient movement and breathing as well as by the normal uptake that is present in the brain, heart, kidneys and bladder as well as abnormal uptake that may be seen in

inflammatory tissue or infections. Physical phenomena such as imaging resolution and imaging contrast also affect the SUV. The spatial resolution of PET systems can be typically between 4 and 10 mm FWHM. This is significantly worse than the best possible spatial resolution, measured under ideal conditions and which is used by manufacturers as a reproducible baseline measurement. The loss of spatial resolution as a result of changes in sampling and filtering, scattered and random events, and respiratory motion may cause SUVs that increase with an increase in lesion size and noise in the image. The contrast between tumour and normal lung that decreases as the size of the lesion becomes smaller and which may eventually disappear may result in false negative results using SUVs for small lesions since the partial volume effect introduces averaging effects due to the limited resolution of the system. (Boellaard *et al.*, 2004; Boellaard, 2011; Hickeson *et al.*, 2002).

The use of the SUV to monitor the response to therapy and to determine the prognosis of the cancer patient becomes increasingly important (Borst *et al.*, 2005; Bryant *et al.*, 2006; Okereke *et al.*, 2009). For response evaluations, scans are performed before and after treatment to determine the amount of tracer uptake, and it is important to limit changes to the minimum to ensure that comparisons are relevant and appropriate. It should be noted that changes in SUV in small lesions or lesions with low activity uptake cannot be determined with enough certainty and precision to be used for decision making and it is therefore necessary to investigate the factors affecting the SUV or to use other comparative methods to aid in deciding whether a lesion did respond adequately to therapy or not (Boellaard, 2011; Boellaard *et al.*, 2014). This becomes even more significant when PET imaging and the SUV thresholds are used for therapy planning to delineate tumours (Grégoire *et al.*, 2007; Schaefer A, 2008; Van Baardwijk *et al.*, 2007; Black *et al.*, 2004; Nestle *et al*, 2005; Nehmeh *et al.*, 2009)

As mentioned before, many factors exist that influence the calculation of the SUV (Berghmans *et al.*, 2008; Huang, 2000). The relevant aspects of these factors that affect the accuracy of these SUVs are discussed in more detail in the next chapter in order to place the elements of this project in context.

1.2 Aim

The aim of this study was to assess the relative importance of the physical factors that affect the accuracy of a single SUV measurement using Monte Carlo modelling.

1.3 References

Alazraki NP, Shumate MJ, Kooby DA. 2007. A Clinician's Guide to Nuclear Oncology: Practical Molecular Imaging and Radionuclide Therapies. 1st ed., SNM, Reston, VA, USA :1-2.

Bagci U, Yao J, Miller-Jaster K, Chen X, Mollura DJ. 2013. Predicting Future Morphological Changes of Lesions from Radiotracer Uptake in 18F_FDG_PET Images. *Plos ONE* 8(2):e57105.

Basu S and Nair N. 2006. Is it time to incorporate quantitative functional imaging data, FDG PET in particular, into responsive evaluation criteria in solid tumours? *Nucl Med Commun* 27:413-416.

Berghmans T, Dusart M, Paesmans M, Hossein-Foucher C, Buvat I, Castaigne C, Scherpereel A, Mascaux C, Moreau M, Roelandts M, Alard S, Meert AP, Patz EF, Lafitte JJ, Sculier JP. 2008. Primary Tumor Standardized Uptake Value (SUV_{max}) Measured on Fluorodeoxyglucose Positron Emission Tomography (FDG-PET) is of Prognostic Value for Survival in Non-small Cell Lung Cancer (NSCLC). *J Thorac Oncol* 3:6-12.

Black QC, Grills IS, Kestin LL, Wong C-YO, Wong JW, Martinez A, Yan D. 2004. Defining a Radiotherapy Target with Positron Emission Tomography. *Int J Radiation Oncology Biol Phys* 60:1272-1282.

Boellaard R, Krak NC, Hoekstra OS, Lammertsma AA. 2004. Effects of Noise, Image Resolution, and ROI Definition on the Accuracy of Standard Uptake Values: A Simulation Study. *J Nucl Med* 45:1519-1527.

Boellaard R. 2011. Need for Standardization of 18F-FDG PET/CT for Treatment Response Assessments. *J Nucl Med* 52:93S-100S.

Boellaard R, Delgado-Bolton R, Oyen WJG, Giammarile F, Tatsch K, Eschner W, Verzijlbergen FJ, Barrington SF, Pike LC, Weber WA, Stroobants S, Delbeke D, Donohoe KJ, Holbrook S, Graham MM, Testanera G, Hoekstra OS, Zijlstra J, Visser E, Hoekstra CJ, Pruim J, Willemsen A, Arends B, Kotzerke J, Bockisch A, Beyer T, Chiti A, Krause BJ. 2014. FDG PET/CT: EANM procedure guidelines for tumour imaging: version 2.0. *Eur J Nucl Med Mol Imaging* :.

Borst GR, Belderbos JSA, Boellaard R, Comans EFI, de Jaeger K, Lammertsma AA, Lebesque JV. 2005. Standardised FDG uptake: A prognostic factor for inoperable non-small cell lung cancer. *Eur J Cancer* 41:1533-1541.

Bryant AS, Cerfolio RJ, Klemm KM, Ojha B. 2006. Maximum Standard Uptake Value of Mediastinal Lymph Nodes on Integrated FDG-PET-CT Predicts Pathology in Patients with Non-Small Cell Lung Cancer. *Ann Thorac Surg* 82:417-423.

Eschmann SM, Friedel G, Paulsen F, Reimold M, Hehr T, Budach W, Langen H-J, Bares R. 2007. ^{18}F-FDG PET for assessment of therapy response and preoperative re-evaluation after neoadjuvant radio-chemotherapy in stage III non-small cell lung cancer. *Eur J Nucl Med Mol Imaging* 34:463-471.

Graham MM, Peterson LM, Hayward RM. 2000. Comparison of Simplified Quantitative Analyses of FDG Uptake. *Nucl Med Biol* 27:647-655.

Grégoire V, Haustermans K, Geets X, Roels S, Lonneux M. 2007. PET-based Treatment Planning in Radiotherapy: A New Standard? *J Nucl Med* 48:68S-77S.

Hallet WA. 2004. Quantitation in clinical fluorodeoxyglucose positron emission tomography. *Nucl Med Commun* 25:647-650.

Hickeson M, Yun M, Matthies, Zhuang H, Adam L-E, Lacorte L, Alavi A. 2002. Use of a corrected standardized uptake value based on the lesion size on CT permits

accurate characterization of lung nodules on FDG-PET. *Eur J Nucl Med* 29:1639-1647.

Huang S-C. 2000. Anatomy of SUV. *Nucl Med Biol.* 27:643-646.

Marsden PK. 2004. Quantitation in PET: What is it? Can we do it? Do we need it? *Nucl Med Commun* 25:635-636.

Nehmeh SA, El-Zeftawy H, Schwartz J, Erdi YE, Kirov AS, Schmidtlein CR, Gyau AB, Larson SM, Humm JL. 2009. An iterative technique to segment PET lesions using a Monte Carlo based mathematical model. *Med Phys* 36:4803-4809.

Nestle U, Kremp S, Schaefer-Schuler A, Sebastian-Welsch C, Hellwig D, Rübe C, Kirsch C-M. 2005. Comparison of Different Methods for Delineation of 18F-FDG PET-Positive Tissue for Target Volume Delineation in Radiotherapy of Patients with Non-Small Cell Lung Cancer. *J Nucl Med* 46:1342-1348.

Okereke IC, Gangadharan SP, Kent MS, Nicotera SP, Shen C, deCamp MM. 2009. Standard Uptake Value Predicts Survival in Non-Small Cell Lung Cancer. *Ann Thorac Surg* 88:911-916.

Paulino AC and Johnstone PAS. 2004. FDG-PET in Radiotherapy Treatment Planning: Pandora's Box*? Int J Radiation Onocology Biol Phys* 59:4-5.

Schaefer A, Kremp S, Hellwig D, Rübe C, Kirsch C-M, Nestle U. 2008. A contrast-oriented algorithm for FDG-PET-based delineation of tumour volumes for the radiotherapy of lung cancer: derivation from phantom measurements and validation in patient data. *Eur J Nucl Med Mol Imaging* 35:1989-1999.

Van Baardwijk A, Bosmans G, Boersma L, Buijsen J, Wanders S, Hochstenbag M, Van Suylen R-J, Dekker A, Dehing-Oberije C, Houben R, Bentzen S, Van Kroonenburgh M, Lambin P, De Ruysscher D. 2007. PET-CT-based Auto-contouring in Non-Small-Cell Lung Cancer Correlates with Pathology and Reduces Interobserver Variability in the Delineation of the Primary Tumor and Involved Nodal Volumes. *Int J Radiation Oncology Biol Phys* 68:771-778.

Visvikis D, Cheze-Le Rest C, Jarritt P. 2004. PET technology: current trends and future developments. *Br J Radiol* 77:906-910.

Von Schulthess GK, Steinert HC, Hany TF. 2006. Integrated PET/CT: Current Applications and Future Directions. *Radiology* 238:405-422.

Weber WA, Schwaiger M, Avril N. 2000. Quantitative Assessment of Tumor Metabolism Using FDG-PET Imaging. *Nucl Med Biol* 27:683-687.

Chapter II

Literature Overview

Table of Contents

2.1 PET Quantification

As mentioned in the previous chapter PET quantification plays an important role in Nuclear Medicine for diagnosis as well as follow-up on cancer patients. The principles of SUV calculation as well as the influence of various factors on quantification accuracy will be discussed in this chapter.

2.1.1 Principles of Positron Emission Tomography

When a patient is injected with the radiopharmaceutical FDG, the radionuclide ^{18}F will decay to ^{18}O through positron decay (Saha, 2005).

$$^{18}_{9}F_{9} \rightarrow ^{18}_{8}O_{10} + \beta^{+} + \nu$$

..... Equation 2-1

Positron Emission Tomography (PET) is based on the principle of coincidence detection of the two photons that may arise from the annihilation of the abovementioned positron and an electron. The positron has its origin from the nucleus of the injected radiopharmaceutical as shown in Equation 2-1 and when it collides with any electron, their rest masses are converted fully into two photons that are emitted simultaneously at ~180° with respect to each other, each with energy of 511 keV. Detector arrays surrounding the patient detect the emerging annihilation photons. (Visvikis *et al*., 2004b)

The inorganic scintillator crystals that are most frequently used in PET scanners are bismuth germinate $Bi_4Ge_3O_{12}$ (BGO), lutetium oxyorthosilicate $Lu_2SiO_5:Ce^{3+}$ (LSO), lutetium yttrium orthosilicate $Lu_xY_{2-x}SiO_5$:Ce (LYSO) and gadolinium oxyorthosilicate Gd_2SiO_5:Ce (GSO) (Melcher, 2000). The most important properties of scintillation detectors are high density and high effective atomic number, high light output and short decay time. A high mass number and high effective atomic number will maximise the crystal's stopping power and therefore detecting more photons. The amount of photoelectric interactions versus Compton interactions is also increased with a high effective atomic number scintillator resulting in improved energy discrimination of scattered photons. An increased light output will reduce the statistical uncertainty or

noise in the scintillation event and thus in the related electronic signal. This will result in an improvement of the energy resolution and therefore the amount of scatter events that will be discarded is increased. A crystal with a short scintillation decay-time makes the use of a narrow coincidence timing window possible which in turn reduces the random coincidences count rate. (Zanzonico, 2004)

Using Annihilation Coincidence Detection (ACD), a *single* constitutes each of the two annihilation photons. The total count rate, in counts per second (cps), for the individual annihilation photons is in turn called the *singles count rate*. Each single is time-stamped and a *true* coincidence event is defined as a pair of singles counted by the coincidence detectors within a time interval called the coincidence timing window (see Figure 1). When signals from the two coincidence detectors trigger the coincidence circuit within a specific timing period, a *true* is generated by this circuit. Each annihilation occurence does not produce a counted event however, since both singles must strike the coincident detectors for an event to be recorded. As a result, the *singles count rate* in PET is naturally much higher than the *trues count rate*. Typically the timing resolution for e.g. BGO crystals is in the order of 6 ns full width at half the maximum (FWHM) and for LSO scintillators approximately 3 ns FWHM. (Zanzonico, 2004)

A line can be drawn between the two opposite locations of detection and the origin of annihilation therefore lies on that line. This line or the volume that lies between the opposing coincidence detectors is referred to as the line-of-response (LoR). Coincidences are collected for each LoR and stored in a 2D array, or sinogram. In each sinogram, there is one row containing the LoRs for a particular azimuthal angle; each such row corresponds to a one-dimensional (1D) parallel projection of the tracer distribution at a different coordinate along the scanner axis. An event is registered if both crystals detect an annihilation photon within a coincidence time window in the order of 10 ns, depending on the timing properties of the scintillator. Coincidence detection therefore uses a technique called electronic collimation since only two photons on the straight line that arrive almost simultaneously at opposing detectors are recorded and the need for physical collimation falls away. This in turn results in the sensitivity (measured

count rate per unit activity) of PET being much higher than that of single photon nuclear medicine imaging by orders of magnitude. An image can be reconstructed from the large amount of different coincidences that are recorded at different angles and radial offsets covering the field-of-view (FoV) in a full-ring system. Absolute measurements of tracer concentration in the tissues can be made by using corrections for the self-absorption of photons within the patient. Although the physics of positron annihilation limits the spatial resolution to, at best, 2–3 mm, the accuracy is related to the sensitivity of the detection system. (Zanzonico, 2004, Zaidi, 1999)

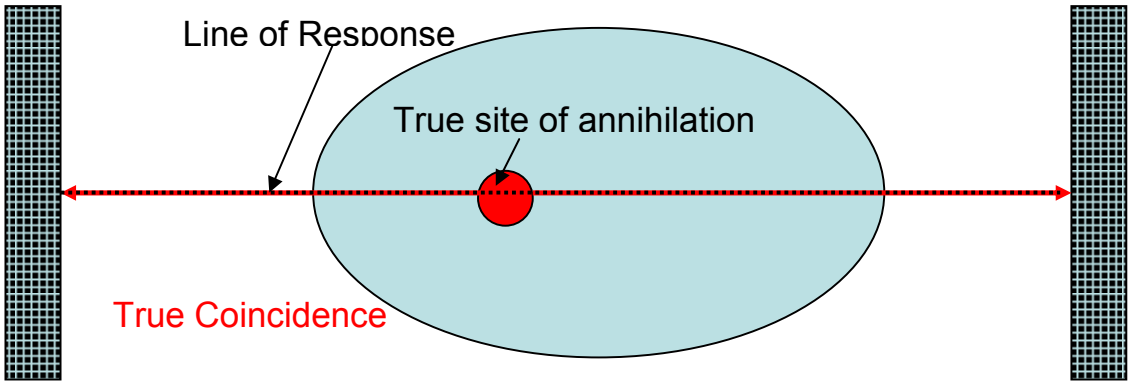

Figure 1: Example of a True Coincidence

False coincidence events (scatter and random coincidences) are also detected in PET. These events degrade quantitative accuracy as well as image quality. A *scatter coincidence* is recorded when two annihilation photons are emitted from the same site, but one photon undergoes Compton scatter before being detected within the specified time-window as is shown in Figure 2. The LoR between the two detectors do not pass through the original point of annihilation and therefore also not through the target object (organ) of interest. (Budinger *et al.*, 1996; Visvikis *et al*., 2004b; Zanzonico, 2004)

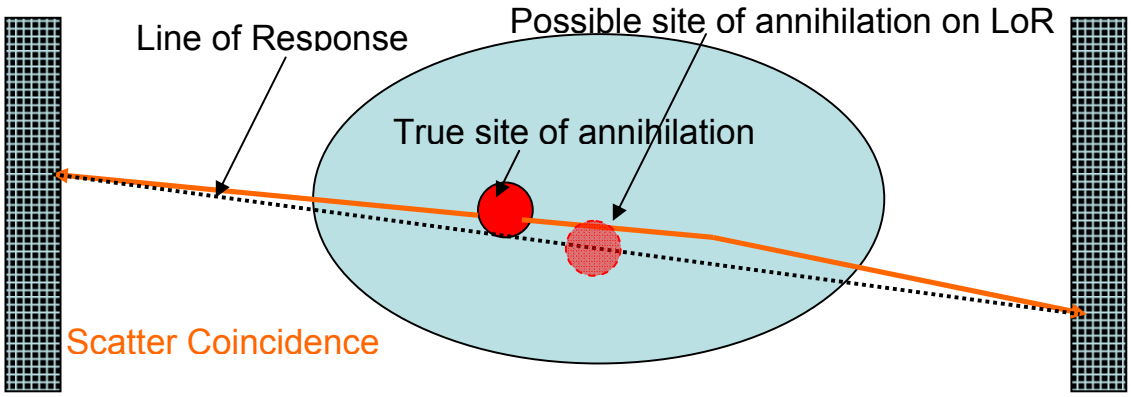

Figure 2: Example of a Scatter Coincidence

A *random coincidence* is registered when two annihilation photons from any location arrive at two detectors within the specified coincidence timing window. The LoR drawn between the two detectors do not cross the point of annihilation and therefore also not to the object that is being imaged as is presented in Figure 3. Random coincidences will therefore increase the detected coincidence count rate by contributing false coincidence events. The random coincidence rate increases linearly with the width of the time window and quadratically with the rate of single photons interacting in the detectors and because the total activity-containing volume is typically much greater than the LoR, the random coincidences are common and therefore *randoms* count rate exceeds the *trues* count rate. (Budinger *et al.*, 1996; Visvikis *et al.*, 2004b; Zanzonico, 2004)

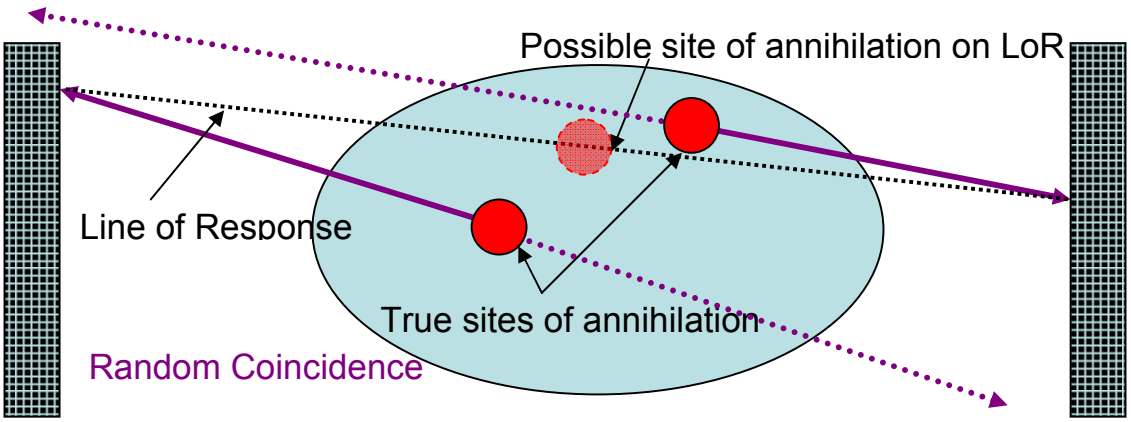

Figure 3: Example of a Random Coincidence

The detection of random and scatter coincidences increases background counts and this decreases the accuracy of quantification of the reconstructed images. The amount of scatter and random coincidences has to be minimised in order to improve the accuracy of PET quantification and the quality of PET images. This can be achieved by utilising hardware or software in PET scanner systems. Hardware reduction of these unwanted false coincidences is achieved by using septa in the imaging FoV. The solid angle of acceptance is hereby reduced and as a result the scatter and random coincidences from neighbouring rings are minimised. True coincidences are however also minimised. This is referred to as two-dimensional (2D) imaging. Three-dimensional (3D) imaging is achieved when no septa are used. With 3D-imaging the sensitivity of the scanning is higher compared to 2D-imaging since the detectability of coincidences is increased between six- and eight-fold, but so are the scatter and random coincidences. Software reduction of scatter and random coincidences is achieved by using a delayed time-window to correct for randoms or by calculation of the fractions of scatter-to-true events and random-to-true events and using these as corrections. (Budinger *et al.*, 1996; Visvikis *et al*., 2004b; Basu *et al.*, 2011; Cherry *et al.*, 2012). The effect of scatter and random coincidence detection on PET imaging will be discussed in more detail in section 2.1.4.2. The available correction techniques for these false coincidences will also be discussed.

When 2D-PET is employed, the emission data are the one-dimensional (1D) projections (sets of parallel line-integrals) of the direct planes at the azimuthal angles ϕ relative to the axis of the scanner. Thus, each 2D transverse section of the tracer distribution is reconstructed independently of adjacent sections. The full set of 2D projection data is then represented as a two-dimensional matrix in polar coordinates with a distance x_r and the azimuthal angle ϕ which is known as a *sinogram* (or *histogram*). Each row represents the projected intensity across a single direct plane and each column represents the projected intensity at the same distance x_r across the projection at successive azimuthal angles ϕ, as is demonstrated in Figure 4.

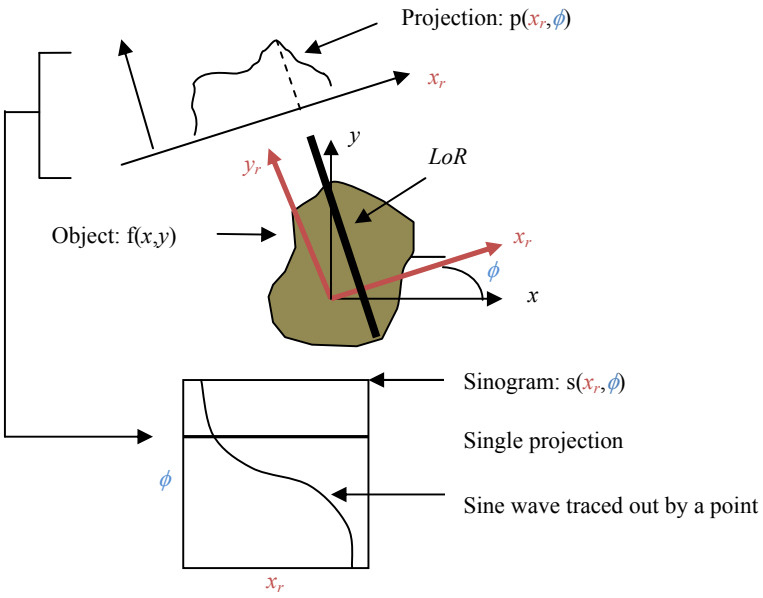

Figure 4: Schematic diagram of image reconstruction in 2D PET (Zanzonico, 2004)

In 3D- PET, the data are sorted into sets of LoRs, where each set is parallel to an individual direction, and is therefore a 2D parallel projection of the 3D tracer distribution. Therefore, as demonstrated in Figure 5, in 3D-PET, the projections are two-dimensional (x_r,y_r) parallel line-integrals with azimuthal angle ϕ and oblique angle θ. The full set of 3D projection data is then represented as a set of sinograms. Each row in the sinogram represents the projected intensity across a single oblique plane at angle θ and each column is the projected intensity at the same position across the projection at successive azimuthal angles ϕ (Zanzonico, 2004; Zaidi, 1999).

For the creation of quantitative PET images an emission data file needs to be reconstructed, a normalisation file is needed to correct the emission data for system response and an attenuation map for attenuation correction (Zanzonico, 2004; Cherry *et al.*, 2012). The normalisation file is acquired as part of routine quality control (QC). The attenuation map can be obtained from computed tomography (CT) or transmission point- or rod source data with a corresponding blank (or "air") image file (Costa *et al.*, 2003). When using the CT, attenuation correction factors for each tissue type are determined from the lower energy X-ray photons (typically with mean energy of 70 keV) and scaled

to be used for the 511 keV photons. The same technique is employed when using another radionuclide such as ^{137}Cs for which the attenuation correction factors must be scaled from those obtained using e.g. 662 keV to 511 keV photons.

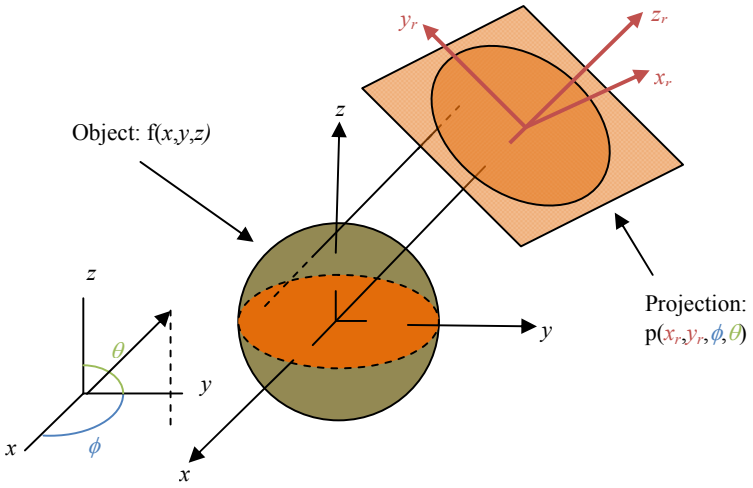

Figure 5: Schematic diagram of image reconstruction in 3D PET (Zanzonico, 2004)

Normalisation is needed to correct for the variation in detector response that can be found in a PET scanner. There are thousands of detectors arranged in blocks that are coupled to hundreds of photomultiplier tubes (PMTs). Since the gain to each PMT may vary, each detector may vary physically from another, detectors are arranged differently in each block and the sensitivity of each detector-pair may vary from others, a large amount of non-uniformity in the raw data may result. By exposing all detectors to a uniform source such as a ^{68}Ge source, the response of the detectors are normalised. This is done separately for 2D and 3D modes (Saha, 2005). The normalisation corrects for the variation of the solid angle for the different LoRs as a function of the distance from the axis of the scanner,

2.1.2 Principles of Reconstruction in PET

As was mentioned before the projection data that are acquired in 2D or 3D modes are stored as sinograms consisting of rows and columns that respectively represent the

intensities across the plane and across the projection at various azimuthal angles. The data is usually compressed along the depth of the object and is recovered by way of reconstruction. 3D data in addition used to be re-binned into 2D format before reconstruction in older scanners but nowadays can be reconstructed directly. In PET two kinds of reconstruction are usually performed viz. by filtered backprojection and by using iterative methods. The aim of reconstruction is to provide accurate cross-sectional images of the distribution of the PET radionuclide throughout the body.

With 2D acquisition the activity represented in the sinogram is the sum of all activity that was detected along the LoR through the body. Using backprojection the image is then reconstructed from all LoRs by adding the counts from the preceding backprojected data to the subsequent LoRs. Simple backprojection may create star pattern artefacts that are caused by counts that lie outside the true location of the objects and causes blurring of the original image. By increasing the amount of projections, the star pattern is suppressed but the final image still remains to be blurred. The blurring effect can be minimised by employing a ramp filter to the acquired data and the filtered projection data are then backprojected. This is called filtered backprojection (FBP) and is widely used in nuclear medicine (Hounsfield, 1973; Cormack, 1963 & 1964; Brooks and Di Chiro, 1976). With attenuation correction the other major limitations of FBP are aliasing at sharp boundaries and the Gibbs phenomenon or ringing (Brooks and Di Chiro, 1976).

Most iterative reconstruction methods are based on statistical principles and can account for the statistical nature associated with SPECT and PET. With iterative algorithms non-uniform attenuation correction is also possible. The most generally used iterative methods that are used in PET are the maximum-likelihood expectation maximisation (ML-EM) algorithm (Shepp and Vardi, 1982) and the ordered subset expectation maximisation (OSEM) method (Hudson and Larkin, 1994). It was reported by Defrise *et al.* (2005) that the differences of using ML-EM or OSEM compared to FBP were a reduction in streak artefacts; that the signal-to-noise ratio (SNR) was better in regions where there was a low tracer uptake which resulted specifically in the body contours becoming more visible; that to some extent non-uniformity or non-isotropy of the spatial

resolution were found in the chest area where the range in attenuation coefficient values is large; and that there was a faster convergence for regions with high tracer uptake than for those with a low uptake of radiotracer.

When 3D PET data is to be reconstructed the 3D data can be reconstructed using a 3D FBP method. Since the LoRs are much more than when using 2D mode the reconstruction process will take much longer. To speed up the process the 3D data needs to be rebinned into 2D data sets and sorted into sinograms per slice as if the data was acquired in 2D mode. When the rebinning is completed a 2D FBP algorithm can be applied to each slice individually. The rebinning of 3D data and subsequent reconstruction is a timely process and methods have been described to speed up the process such as the Single Slice Rebinning Algorithm (SSRB) (Daube-Witherspoon and Muehllehner, 1987) and the Fourier rebinning algorithm (FORE) that was developed by Defrise *et al.* (1997). The FORE algorithm speeds up the reconstruction time for 3D PET data without significant loss in SNR and is regarded as more accurate than the SSRB method. Taking into account the advantages that have been proven using iterative methods compared to FBP, iterative methods have been combined with algorithms such as FORE.

The ML-EM algorithm can be described by the following formula

$$n_j^{k+1} = \frac{n_j^k}{\sum_{i=1}^{I} a_{ij}} \sum_{i=1}^{I} a_{ij} \frac{m_i}{q_i^k}$$

with **.....Equation 2-2**

$$q_i^k = \sum_{j=1}^{J} a_{ij} n_j^k$$

and q_i^k is the expected count in LoR$_i$ if the intensity was n_j^k (at the k^{th} iteration), a_{ij} is the probability of an emission from voxel j being detected along LoR i, m_i is the number of events recorded along LoR i, I is the number of all possible LoRs and J is the number of voxels in the image (Shepp and Vardi, 1982).

Reader *et al.* (1998) proposed a List-Mode ML-EM formula be described by

$$n_j^{k+1} = \frac{n_j^k}{\sum_{i=1}^{I} a_{ij}} \sum_{i=1}^{M} a_{ij} \frac{1}{q_i^k}$$

.....Equation 2-3

where the list-mode data consisting of a list of M line definitions are now 1 for each LoR that is acquired. This is however a slow algorithm that requires that the list-mode data must be passed through every time for each image update. By using subsets, the process may be sped up considerably. Reader *et al.* (2002) modified their original proposal to accommodate subsets and that requires the list-mode data to be passed through only once. The modified algorithm which is called the One-Pass List-Mode Expectation Maximisation (OPL-EM) algorithm may then be represented by

$$n_j^{k+1} = \frac{n_j^k}{\sum_{i=1}^{I} a_{ij}} \sum_{i \in T^k}^{M} a_{ij} \frac{1}{q_i^k}, \quad \text{for } k = 1, \ldots, K$$

.....Equation 2-4

OPL-EM generates a sequence of image estimates n_j^k, where k indicates both the k^{th} iteration as well as the k^{th} subset of the list-mode data that was used to update the image from n_j^{k-1} to n_j^k . Image n_j^K will then represent the final reconstructed image.

Although PET images need to be interpreted clinically without an overemphasis on quantification as was advocated by Di Chiro and Brooks (1988), there is also a need to describe the uptake in lesions mathematically for clinical referencing and quantitative analysis. The mathematical quantifier that is applied most is the standardised uptake value (SUV).

2.1.3 Standardised Uptake Value (SUV) in clinical Practice

The most utilised index for the assessment of tumour uptake of FDG is a semi-quantitative measure known as the standardised uptake value (SUV) (Zasadny KR and Wahl RL, 1993).

The activity concentration in the lesion is normally expressed as:

$$SUV = \frac{Activity\ concentration\ in\ a\ voxel\ (\text{MBq/ml})}{Injected\ Dose\ (\text{MBq}) / Body\ mass\ (\text{g})} e^{\lambda(t_{scan}-t_{inj})} \quad \textbf{.....Equation 2-5}$$

Where: λ = decay-constant for ^{18}F (= 0.382), t_{scan} and t_{inj} are the time of the start of the scan and the time of injection respectively and thus the term $e^{\lambda(t_{scan}-t_{inj})}$ represents the decay factor of the radionuclide (Hickeson *et al.*, 2002; Saha, 2005; Zanzonico, 2004; Adams *et al.*, 2010).

SUV is mostly reported as the mean SUV (SUV_{mean}) or maximum SUV (SUV_{max},) depending on whether the mean activity concentration or the maximum activity concentration of all voxels within the RoI was used. SUV_{mean} incorporates information from multiple voxels, making it less susceptible to image noise. The measured SUV_{mean} is dependent on the voxels that are included in the average, so it is sensitive to RoI definition and therefore also dependent on the observer. SUV_{max} reflects the highest voxel value within the RoI, and is thus independent of RoI definition, but it is more noise dependent. SUV_{max} is most conveniently measured by surrounding the target lesion with a 3D RoI or Volume of Interest (VoI), taking care to avoid the inclusion of regions of high activity outside the RoI. The use of SUV_{max} is less observer dependent and more reproducible (Adams *et al.*, 2010). Other representations of SUVs have been made that were designed to estimate tumour volumes more accurately (Tylski *et al.*, 2010) or to correct for lean body mass or body surface area (Sugawara *et al.*, 1999).

Boellaard *et al*. (2004) observed that SUVs that are obtained under specific conditions for diagnosis may not be compared directly with those that were obtained, reconstructed or analysed under different conditions. Keyes (1995) has also warned against the overt use of SUV without taking many factors into account that could influence the SUV.

Consistency in data acquisition and analysis protocols is therefore required. SUV threshold values used in one centre are applicable to that centre only and threshold values from literature should not be used without proper validation.

SUVs often determine what tumour volume should be used during radiation treatment planning. SUV thresholds must be determined on what is regarded as the tumour volume and no validated standardised method exists for setting this threshold. Various methods have been used and these include using the absolute SUV of e.g. more than 2.5 to set the gross tumour volume (GTV) (Biel *et al.*, 2006), using percentages of the SUV_{max} e.g. that the GTV equals the volume encompassed by more than 40% of SUV_{max} (Biehl *et al.*, 2006), using the anatomic biologic halo method, or ignoring the threshold setting and simply contouring the CT volume corresponding to the visually identified lesion (Biehl *et al.*, 2006; Ashamalla *et al.*, 2005). Although other thresholds have been used as percentage of SUV_{max} that ranged from 15% to 50% (Biehl *et al.*, 2006), Fernando *et al.* (2005) recommended specifically a 20% of SUV_{max} threshold to determine the tumour volume.

Treatment response of a tumour may be measured using SUV if consistent data acquisition and processing protocols are used. The European Organisation for Research and Treatment of Cancer (EORTC) Guidelines 1999 recommends that an SUV increase of less than 25% or a decrease of less than 15% indicates stable metabolic disease. Reduction of SUV after a single cycle of chemotherapy and a reduction of more than 25% after more than one cycle of treatment is considered to demonstrate a partial metabolic response. If the SUV in a lesion cannot be distinguished from the background it is considered to indicate a complete metabolic response (Lucignani *et al*, 2004).

SUV is widely used to assess tumour uptake and to quantify tumour response to therapy and to determine patient survival (Al-Sarraf *et al.*, 2008). Overestimation of the SUVs is found when normalising to the actual patient weight. Normalising to ideal body weight, lean body mass or body surface area can reduce this effect. Other factors that have significant effects on image quantification include plasma glucose level, the time of

imaging after injection and the size of the lesion. These factors interfere with tumour glucose metabolism quantification, but by using reproducible protocols, the influence of these factors can be minimised or controlled (Boucher *et al.*, 2004).

The most important factor that affects the accuracy of quantitative studies with PET is the accuracy of the detected data. Corrections can be applied for the existence of random coincidences, scatter coincidences, attenuation effects, effects of the efficiency differences of detectors, and effects due to detection geometry and dead-time (Visvikis *et al.*, 2004c; Brasse *et al.*, 2005; Pan T *et al.*, 2005; Ay and Sarkar, 2005, Chi *et al.*, 2007; Visvikis *et al.*, 2003). Most of these corrections are effective in improving the accuracy of the acquired data and are widely utilised.

The factors that are difficult to control will be discussed in the following section. These include patient respiratory motion, scatter and random coincidences, and partial volume effects.

2.1.4 Factors impeding image quality and quantification

2.1.4.1 Respiratory motion

Respiratory motion results in reduction of qualitative and quantitative accuracy in PET imaging as it takes a few minutes to acquire the images at each bed position. Movement in the respiratory area causes blurring of the images and thus a loss of sensitivity in lesion detection (Visvikis *et al.*, 2004a). Erdi *et al.* (2004) reported that SUV changes due to breathing have never been observed with PET scanners using rod transmission sources to acquire attenuation correction maps. The reason being that rod transmission scans acquire data averaged over many breathing cycles. During CT acquisition, movement usually does not affect the resolution during image acquisition since the time to acquire an image is in the order of seconds. The patient is usually requested to hold breath at inspiration during the imaging process.

Patient breathing can also affect measured SUVs, particularly in lesions in the lung bases or upper abdomen (Liu *et al.*, 2009). If the diaphragm position in CT does not match the average position during PET, the attenuation correction may inaccurately adjust for the radioactivity concentration, which in turn would change the measured SUV.

Respiratory motion influences the qualitative aspects of imaging the heart, muscles of the diaphragm, liver, spleen, pancreas and imaging of the lung area. Motion also interferes with attempts to use fused PET/CT images. With the advent of combined PET/CT imaging, the impact of respiratory motion during PET/CT imaging gained even larger importance as it interferes with the co-registration of anatomic images (obtained from CT) and the metabolic PET data (Boucher *et al.*, 2004).

Compensating for respiratory movement includes respiratory gating which results in multiple image frames that correspond to different periods of the respiratory cycle and there exist many techniques to implement respiratory gating or to perform breath-hold acquisitions to improve image quality and quantification (Nehmeh *et al.*, 2002; Bruyant *et al.*, 2007; Nehmeh *et al.,* 2007; Kawano *et al.*, 2008; Dawood *et al.*, 2007). The challenge still remains to accurately co-register the gated PET images that are obtained over a longer time-period to the breath-hold or gated CT-images that are obtained over a shorter time period (Erdi *et al.*, 2004; Meirelles *et al.*, 2007; Werner *et al.*, 2009; Daouk *et al.*, 2009). Images in gated frames have a loss of resolution since only a fraction of the available counts are acquired during normal respiration. This is more significant in imaging of the thorax and abdomen where physiological motion that is associated with respiration, cardiac movement and movement in the gastro-intestinal area is present. The data that are obtained through respiratory gating are satisfactorily free of inaccuracies that are associated with breathing (Chi *et al.*, 2008). Quantitative information can be recovered by accounting for scatter, random coincidences and attenuation of photons. Compensating for these factors will result in an increase in background noise due to the propagation of inherent noise associated with scatters and randoms recovery as well as correcting for attenuation. This will reduce image quality and the quantitative accuracy of results obtained from the PET images (Visvikis, *et al.*, 2004a).

The effective lung attenuation effect obtained during the PET scan will be different from the exact attenuation coefficient determined from the CT scan, as it will be an average during the PET phase while during CT it will be an exact measurement. Therefore the attenuation measured during CT produces an inaccurate correction of the PET data, which can significantly affect the SUV calculation. Adams *et al.* (2010) found that if the patient is taught quiet breathing during PET, the CT images are most accurately co-registered when single breath-hold CT is obtained at quiet end-expiration. When following lesions at the lung base or in the upper abdomen, it is important for the CT scans to be consistently obtained in this phase. Notwithstanding the attenuation correction issues, a moving lesion will be quantified inaccurately because of the effects of blurring. It can be assumed that the effects of blurring between the baseline and follow-up scans will be similar, but even this may not be true if breathing patterns are different during the two PET scans. (Adams *et al.*, 2010; Erdi *et al.*, 2004).

2.1.4.2 Scatter and Random Coincidences

As with any imaging technique, not all acquired events represent a reflection of the true image. Contributions to the background noise include photons that scatter prior to detection and random coincidence detection. Both of these background processes introduce a bias into the reconstructed images, a bias that can be reduced or eliminated by modelling each process, although at the expense of increasing image noise.

For scatter events, one or both photons interact with the tissue before reaching the detectors and as a consequence the event is assigned incorrectly to the line joining the two detectors (as explained in section 2.1.1 and Figure 2). The amount of scatter, which is primarily due to the Compton process at this energy, is characterised by the scatter fraction, the ratio of scattered events to total events. Scatter photons can be identified and rejected by applying a simple energy threshold. However, the energy resolution of current PET detectors, e.g. 12% for BGO, 9.1% for LSO (Zaidi and Alavi, 2007), is unable to accurately distinguish scattered from non-scattered photons above a certain threshold that may be as low as 350 keV. In addition to a lower energy threshold, sophisticated scatter correction models have been developed to remove the residual scatter bias (Cherry *et al.*, 2012). The scatter background cannot be measured directly

and should be estimated from the emission data. In a typical clinical imaging situation, the fraction of scattered events remaining even after applying an energy threshold can be greater than 40% of the total events in the image. (Townsend, 2004)

Scatter from outside the FoV in 3D-PET is a challenging issue especially in large axial FoV scanners. The effect of energy window setting combined with the contribution of scatter from activity that lay outside the FoV was extensively studied (Zaidi, 2000).

Random coincidences are a consequence of two unrelated annihilation photons arriving within the time window used to define a coincidence. As mentioned before, the random coincidence rate is proportional to the square of the singles count rate that is incident on the detectors. This radiation arises not only from the radioactivity in the FoV of the scanner, but also from radioactivity outside the FoV when one of the two photons from a given positron annihilation enters the scanner FoV and reaches the detectors. It is observed that radioactivity that localises in regions not within the FoV of the scanner will increase the overall randoms rate to more than 50% of the total acquisition rate. The randoms rate can be estimated from the singles rate (and the coincidence time window), or it can be determined using a direct measurement of events that fall into a delayed window. The advantage of using the delayed window technique is that it can account for any spatial variations in the distribution. Subtraction of the number of randoms recorded in the delayed window from the total number of events acquired will however increase the statistical noise (Townsend, 2004).

As was previously mentioned, two modes of scanning are available in PET, viz. 2D-PET, where septa are present during the scan process, and 3D-PET, where the septa are retracted. In 2D-PET only the coincidences between crystals in the same or adjacent rings are allowed. In 3D-PET coincidences from all ring combinations are possible. It therefore increases the measured LoRs through a related increase in the solid angle of the system. This in turn will increase the sensitivity of the system in 3D mode which should also lead to a higher signal-to-noise ratio and increased quantitative accuracy. However, without septa and in comparison with 2D-PET, the amount of scatter coincidences is also

increased by more than a factor three and for the amount of random coincidences a factor of five is reported. All of these false coincidences lead to an increase in background noise and in turn diminishes the quantitative results that are obtained from higher sensitivity 3D-PET (Visvikis, 2004c).

2.1.4.3 Partial Volume Effect

The partial volume effect (PVE) is one the most important factors that limits accurate quantification in PET and is mostly related to scanner resolution. Physiological and patient movement during acquisition also contribute to degrading spatial resolution and therefore also the PVE. The phenomenon is not only applicable in PET, but can be found in other imaging modalities such as SPECT when objects are imaged with less than two to three times the spatial resolution of the scanner as is defined by the FWHM of a PSF (Erlandsson, 2012). Theoretically, the best resolution that can be attained is 2.36 mm in clinical PET scanners (Moses, 2011). This is based *inter alia* on the size of the detector, the range the positron travels before being annihilated as well as the depth the photon travels into the detector, asymmetric blurring and sampling errors. The resolution observed clinically is usually less and factors such as scatter and distance of the object to the detector also have an influence on the deterioration of resolution. The limited spatial resolution does not make it possible to obtain accurate measurements of the true concentration of the radiotracer in structures and lesions of less than two to three times the spatial resolution of the PET scanner. Spatial resolution determines how far the signal spreads around its actual location. High spatial resolution introduces little spread, whereas poor spatial resolution introduces a large amount of spread. Therefore, a given lesion will vary in size, intensity and SUV depending on the spatial resolution of the imaging system. Spatial resolution is partly determined by scanner features as mentioned before but it also depends on reconstruction parameters viz. the number of iterations, number of subsets in ordered subset-type algorithms, filter in filtered back-projection algorithms, and post-filtering.

PVE results in a decreased contrast between the lesion and the surrounding background with lesion size reduction. The visibility of the lesion may even be reduced to such an

extent that beyond a certain point the lesion may disappear totally (Basu *et al.*, 2007; Marsden, 2004).

PVE involves three particular effects for which the intensity values in images may appear different from what they are.

a) The first effect is 3D image blurring resulting from the finite spatial resolution of the acquisition system. The spatial resolution in PET images is limited by the detector design and by the reconstruction process. Consequently, 3D blurring results in a spill-over between regions. In quantitative studies, PVE introduces distortions that depend on the distribution of the tracer in the targeted region as well as in the adjacent tissue. For example, a small lesion with a relative higher amount of activity versus its background may seem larger than it actually is but with less intensity because of the spill-out effect (see Figure 6). PVE strongly depends on the size of the tumour. The smaller the tumour, the greater the underestimation of the uptake value will be. If a tumour shrinks in size as a result of the therapy, then it will mistakenly appear to have a mean lower activity concentration when it is small than when it was larger. On the contrary, if a tumour is small to begin with, but it increases in size over the course of therapy, then mean uptake will incorrectly seem to increase, even if the true metabolic rate has decreased or remained constant. The net change in uptake will therefore depend on the respective changes in tumour volume and the changes in tumour uptake. Thus PVE incorporate both aspects of poor spatial resolution, viz. partial volume and the spill-over effect i.e. contamination of activity from neighbouring tissues.

b) Image sampling is the second effect causing PVE. When large pixels are used (or a smaller matrix) an object will have a greater chance of containing a combination of tissues than when using a larger matrix resulting in smaller pixels. This is because the radiotracer distribution is sampled on a grid of voxels but the limits of the voxels and the actual contours of the distribution being sampled do not match, thereby increasing the probability of including tumour tissue with necrotic or healthy tissues and consequently underestimating the actual metabolic activity of the tumour. Ideally, compensation for PVE should account for both the finite resolution effect and the tissue fraction effect.

c) Another effect causing PVE is motion, especially respiratory motion as the blurring effect decreases the resolution that results in additional PVE.
(Hoffman *et al.*, 1979; Soret *et al.*, 2007; Rousset *et al.*, 1998, Frey *et al.*, 2012)

PVE affects images both qualitatively and quantitatively. For any lesion with increased uptake of radiotracer (a ***hot*** lesion) and of a small size that is surrounded by a background with a lower amount of the tracer present (a ***cold*** area), PVE spreads out the signal. This effect is always present and is most noticeable when the size of the lesion is less than three times the FWHM of the reconstructed image resolution. The maximum intensity in the tumour then will be lower than the actual maximum value. A small tumour will appear larger, but will seem metabolically less active than it actually is. Correction for PVE is complicated because not only does activity from inside the tumour spill out into the surrounding background tissue, but also activity from outside the tumour e.g. originating from a nearby organ filled with a high concentration of activity, spills into the tumour, compensating partially for the spill-out. The spill-out depends on the uptake inside the lesion. Since it is not always balanced by the spill-in, it is difficult to predict the overall effect of PVE. When lesions are imaged that contain whole or partial necrotic centres, a spill-in of activity will cause an assumption that more viable tumour tissue within the tumour centre is present than there is in reality. Simultaneously, the more active part of the lesion will appear metabolically less active than it really is. Changes in the noticed lesion uptake therefore should be interpreted only after changes in the nearby background tissue have been taken into account as well. A change in apparent lesion uptake may reflect only a change in spill-in, without any change in the metabolic activity of the tumour. (Soret *et al.*, 2007)

PVE also affects the visible size of the lesion. When PET is used in conjunction with radiotherapy treatment planning the phenomenon becomes a problem. The contours of the lesion as seen on the PET image may include more than the real metabolically active part of the tumour because of the limited spatial resolution in PET images. In PET/CT, when the PET images and the CT images are fused, it often clearly shows this disagreement between the tumour contours as displayed on the CT image and on the PET

image. However, the contours seen on the CT image often do not coincide with the metabolically active part of the tumour, since CT does not show metabolically active tissue but more of the structure of the tissue and tumour. Only high-resolution functional imaging provides an accurate delineation of the metabolically active part of the tumour. When there is no background activity present, PVE should not have an influence on the total activity in the lesion. If the selected volume around the lesion is large enough then the total activity in the lesion could be recovered. Thus, PVE will not cause any loss of the signal but will merely displace the signal in the image (Soret *et al.*, 2007).

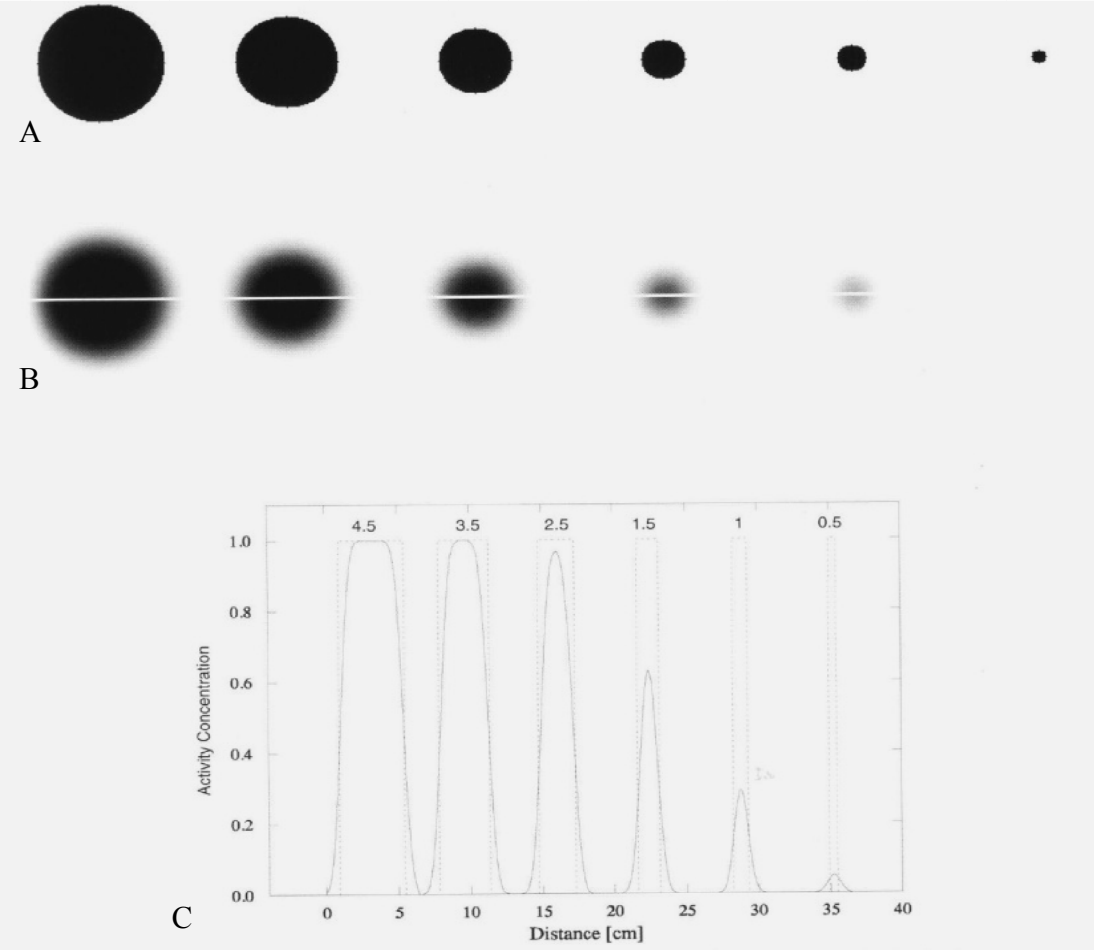

Figure 6: Simulated data showing the partial volume effect on a set of spheres (Cherry and Dahlbom, 2004).

In Figure 6, a set of reconstructed images of spheres with equal activity concentration was obtained from simulated data (A). The diameters ranged from 0.5 cm to 4.5 cm. Profiles through the centres of the spheres (B) demonstrated that the activity concentration (C) appears less due to PVE. (The diameters of the spheres are indicated at the top of the respective profiles) (Cherry and Dahlbom, 2004).

Correction for partial volume effects can be done by using the lesion size as it was determined using the CT (Hickeson *et al.*, 2002; Erlandsson *et al.*, 2012) or MRI image (Rousset *et al.,* 1998) as the images from these two modalities are assumed to represent the true size of the objects. Van Heijl *et al.* (2010) used a method to calculate the spill-in and spill-out correction factors and applied these factors to the original image and the average background activity to perform PVC. Hickeson *et al.* (2002) applied a method to correct for PVEs and resolution when evaluating lung nodules determines using FDG-PET scans. This was done by measuring the SUV_{max} in a lesion and the actual size of the lesion on the corresponding CT image. A corrected SUV was obtained by using

$$SUV_{cor} = \frac{\frac{activity_{region}(\text{MBq}) - activity_{background}(\text{MBq})}{Lesion\ size_{CTScan}(\text{cm}^3)}}{\frac{Injected\ Dose\,(\text{MBq})}{Body\ mass\ (\text{g})}} \times \frac{1}{decay\ factor\ ^{18}F} \quad \textbf{.....Equation 2-6}$$

Where: $activity_{region}$ = total activity in the RoI, $activity_{background}$ = activity/volume in background × (region's volume – lesion's size on CT scan), $Lesion\ size_{CTScan}$ = size of the lesion as measured on the CT Scanner, *Injected Dose* = dose of ^{18}F administered to the patient, *Body mass* = mass of the patient, and $decay\ factor\ ^{18}F$ = the amount by which the radioactive ^{18}F would have diminished over time.

However if the lesion is not easily identifiable on the CT or MRI, other image-based methods have been proposed by Boussion *et al.* (2006), Boussion *et al.* (2009), Teo *et al.* (2007) and Soret *et al.* (2007) to use deconvolution techniques or wavelet transforms to perform partial volume correction and by Hoetjes *et al.* (2010) by implementing deconvolution methods as well as reconstruction methods. Alkhawaldeh *et al.* (2008)

investigated the combined effect of dual-time-point imaging and partial volume correction when assessing pulmonary nodules and found that it can improve the accuracy in diagnosis of malignant pulmonary nodules and to differentiate between malignancy and inflammation in particular in those nodules that present with a lower SUV. Chang *et al.* (2010) proposed a method to correct for breathing motion and PVE simultaneously which can potentially eliminate the need to measure the blurring motion function while collecting the data. Eventually, the goal of partial volume correction (PVC) is to reverse the effect of the system point spread function (PSF) in a PET image thus restoring the true activity distribution. When a high amount of noise is present in images, partial volume correction cannot be obtained in full and smoothing of the image is desired (Erlandsson *et al.*, 2012).

The factors that influence SUV, viz. respiratory motion, the influence of scatter and random coincidences and the partial volume effect, may be assessed by using PET/CT scans and patients or phantoms or it may be done using Monte Carlo simulations. Using physical PET/CT scans have their advantages, but the ethical considerations and costs may be avoided by using mathematical modelling of the phantoms and Monte Carlo computer simulations to obtain the data. This will be focused upon in the following section.

2.1.4.4 Annihilation Photon Non-colinearity and Positron Range

Two physical effects that lead to errors in determining the line along which the site of annihilation is found are the range of the positron and annihilation photon non-colinearity. Photon annihilation takes place where the positronium is created when a positron and electron meet. The LoR is drawn between the sites of detection and ideally will indicate the site of annihilation. The range the positron travels influences the site where annihilation takes place and thus causes the error in location of the target organ and therefore also the resolution of the PET system. The fact that annihilation photons are almost never emitted at 180 degree directions gives rise to the photon non-colinearity error. This influenced by the residual momentum of the positron before it annihilates with an electron. The LoR is thus deviated from the true site of annihilation and causes

an error in the estimation of where the annihilation occurred. The combined effect of the positron range and the non-colinearity can add up to a few millimetres to system resolution (Cherry *et al.*, 2006; Cherry and Dahlbom, 2004).

2.1.5 Monte Carlo Modelling in PET

Monte Carlo methods are numerical calculation methods based on random variable sampling. The technique of random sampling to solve mathematical problems has been known since 1770 (Buvat and Castiglioni, 2002) and the Monte Carlo method had been useful during the early 20th century when Von Neumann, Fermi and Ulam applied it during the Manhattan Project to solve neutron diffusion problems (Zaidi, 1999). Simulation today involves computer generated phantoms, models of the imaging process, and fast computational methods. Monte Carlo modelling in nuclear medicine is useful to characterise and optimise design of imaging systems, to evaluate dose distributions and to improve the quality and quantitative accuracy of reconstructed images (Andreo, 1991). Mathematical modelling is essential to assess various factors in nuclear medical imaging systems since no solution can be obtained analytically when solving transport equations describing the interaction of photons with body structures that attenuate these photons non-uniformly and photon interaction in complex detector geometry. In nuclear medicine and molecular imaging Monte Carlo simulations are widely applied in planar imaging, SPECT, CT and PET (Zaidi, 1999; Segars *et al.*, 2008; Segars *et al.*, 2010; Buvat *et al.*, 2005; Castiglioni *et al.*, 2005).

Monte Carlo simulation consists mainly of the following components (Zaidi, 1999):

- Probability density functions that describe the physical system.
- Random number generator: a source of random numbers uniformly distributed on the unit interval must be available.
- Sampling rule: a prescription for sampling from the specified probability density functions.
- Scoring: the outcomes must be accumulated into overall tallies or scores for the quantities of interest.

- Error estimation: an estimate of the statistical error (variance) as a function of the number of trials and other quantities must be determined.
- Variance reduction techniques: methods for reducing the variance in the estimated solution to reduce the computational time for Monte Carlo simulation.
- Parallelisation and vectorisation algorithms to allow Monte Carlo methods to be implemented efficiently on advanced computer architectures.

The development of Geant 4 Application for Tomographic Emission (GATE) (Strul, 2003; Assié *et al.*, 2004; Jan *et al.*, 2004; Staelens *et al.*, 2006) has greatly aided users in the nuclear medicine community who desire to perform Monte Carlo simulations. A number of projects with various applications have been successfully completed using GATE. These include the validation of two commercial PET systems viz. Philips Allegro/GEMINI PET (Lamare *et al.,* 2006) and the GE Advance/Discovery (Schmidtlein *et al.*, 2006), the evaluation of the energy resolution and absolute detection efficiency for LSO scintillators by Rothfuss *et al.* (2007), an investigation of sensitivity limits in PET by Eriksson *et al.*.(2007), and Visvikis *et al.* (2006) used GATE for application in dosimetry. With the use of cluster computing i.e. using the combined computing power of a multitude of computer processors, the amount of data that can be generated can be achieved in a shorter time (De Beenhouwer *et al.*, 2007). The GATE code has now been expanded to include improved detector systems, hybrid scanners and Cerenkov radiation and is fast becoming a tool of excellence in the nuclear medical imaging world (Santin *et al.*, 2007; www.opengatecollaboration.org)

Mathematical representation of the human body and other anthropomorphic phantoms are useful when performing radiation transport calculations. These mathematical phantoms are used extensively in the computation of doses delivered to the entire body as well as to specific organs. They are also very useful when image reconstruction algorithms need to be developed and tested. Precise modelling of the human body requires suitable information on the location, shape, density and composition of tissues. In the past software phantoms used in imaging consisted of basic source geometries and the attenuating media. These simple geometries are useful when studying the fundamental

imaging characteristics such as scatter and attenuation, but it is not possible to evaluate clinically realistic distributions by these basic set-ups. (Zaidi, 1999).

A significant advantage of performing simulations is to have a realistic phantom or model of the human anatomy and physiology. Using computer-generated phantoms in simulation studies when the exact anatomy and physiological functions of the phantom are known provides a gold standard from which to evaluate and improve medical imaging devices and image processing and reconstruction techniques. Computer models can be easily modified to assess different medical situations when it might be ethically and practically difficult to evaluate different combinations of parameters under clinical conditions. The computer based phantom that is widely used in Monte Carlo simulations in nuclear medicine is the XCAT phantom (Segars *et al.*, 2008; Segars *et al.*, 2010) and is discussed below.

The XCAT phantom, formerly known as NCAT phantom, was originally developed to provide a realistic and flexible model of the human anatomy and physiology for use in nuclear medicine research in SPECT and PET. The organ models are based on non-uniform rational B-splines (NURBS), as used in computer graphics. NURBS, which define continuous surfaces, allow the phantom to be defined at any spatial resolution. With the addition of the time dimension it is possible to model cardiac and respiratory motions (Segars *et al.*, 2008; Segars *et al.*, 2010).

All the organ and skeletal models with the exception of the heart are based on CT scans from the Visible Human male data set (United States National Library of Medicine, Bethesda, Maryland, 1994). The heart is based on gated MRI cardiac scans of a normal patient.

The phantom is a hybrid between the realism of pixel-based phantoms and the flexibility of geometry-based phantoms. By fitting NURBS to actual patient data, the phantom is more realistic than those based on solid geometry. NURBS give the phantom a mathematical basis allowing the phantom to be very flexible. NURBS surfaces can be altered easily to model realistically variations in anatomy and to simulate patient motion

in SPECT and PET (Segars, 2001). This phantom has been used extensively in various Nuclear Medicine Monte Carlo simulation studies especially where the influence of respiratory motion is investigated (Lamare *et al.,* 2007a; Lamare *et al.,* 2007b; Le Maitre *et al.*, 2009; Hatt *et al.*, 2012, Lamare *et al.*, 2014).

2.1.6 Discussion

In this chapter, the principles of image formation in PET were outlined and the concept of the SUV and the various applications of this quantifier were discussed broadly. Some of the pitfalls of using the SUV under certain conditions were mentioned and the factors that influence the quality of image formation and the consequential influence thereof on the SUV were assessed. From this assessment, it was clear that some of the biggest challenges of using the SUV originate from respiratory motion, the presence of scatter and random coincidences and the partial volume effect. It is possible to compensate or correct for most of the factors that influence the determination of accurate SUVs (Buvat, 2007a; Buvat, 2007b) but it is important to quantify these influences as well.

It is, for instance, possible to correct for breathing motion by using a respiratory-gated acquisition protocol and device to assess the movement of the chest and then to trigger or terminate acquisition at certain pre-determined limits but that does not provide the solution to how lesions behave during the movement of the chest and the concomitant movement of the diaphragm. Consequently, the amount of movement may influence the signal that is recorded in a specific area of the lung which in turn influences the calculation of the SUV and it is therefore also important to determine the influence of breathing movement on the location of the lesions. In addition, the size of the lesions influences their apparent activity concentration as was mentioned before, and by investigating the impact of the partial volume effect as a result of smaller size lesions during breathing, it is then possible to perform corrections more accurately. Assessing the influence of scatter and random coincidences that arise from inside the field-of-view or from the outside on the lesions in the lung will improve the correction for these unwanted coincidences as well as to aid the physician in the interpretation of the PET scan if adequate compensation cannot be implemented.

To assess the influence of these factors under as realistic and controlled conditions as possible, the use of Monte Carlo simulations is an accepted and cost-effective method to obtain reproducible results.

In order to reach the aim of assessing the relative importance of the physical factors that affect the accuracy of a single SUV measurement, the following objectives were set:

2.1.6.1 Partial volume effects

As was demonstrated in the literature, partial volume effects that are due to limited spatial resolution have to be considered when using SUVs especially when monitoring tumour response to therapy. The objective was to assess the relative importance of partial volume effects on SUV accuracy by varying object sizes, varying activity in- and outside the objects of interest and by changes in image sampling.

2.1.6.2 Effects of motion

The objective was to determine the importance of respiratory motion and patient movement on SUV accuracy through simulation of the respiratory motion of a patient.

2.1.6.3 The presence of activity from outside field-of-view

The objective was to assess the influence of activity outside the FoV on the accuracy of the SUVs.

The contribution of true-, scattered and random coincidences to the SUVs were considered in all the objectives. The 2D- and 3D acquisition modes were evaluated throughout.

2.2 References

Adams MC, Turkington TG, Wilson JM, Wong TZ. 2010. A Systematic Review of the Factors Affecting Accuracy of SUV Measurements. *AJR* 195:310-320.

Alkhawaldeh K, Bural G, Kumar R, Alavi A. 2008. Impact of dual-time-point 18-F-FDG PET imaging and partial volume correction in the assessment of solitary pulmonary nodules. *Eur J Nucl Med Mol Imaging* 35:246-252.

Al-Sarraf N, Gately K, Lucey J, Aziz R, Doddakula K, Wilson L, McGovern E, Young V. 2008. Clinical implication and prognostic significance of standardised uptake value of primary non-small cell lung cancer on positron emission tomography: analysis of 176 cases. *Eur J Cardiothorac Surg* 34:892-897.

Andreo P. 1991. Monte Carlo techniques in medical radiation physics. *Phys Med Biol* 36:861-920.

Ashamalla H, Rafla S, Parikh K, Mokhtar B, Goswami G, Kambam S, Abdel-Dayem H, Guirguis A, Ross P, Evola A. 2005. The contribution of integrated PET/CT to the evolving definition of treatment volumes in radiation treatment planning in lung cancer. *Int J Radiation Oncology Biol Phys* 63:1016-1023.

Assié K, Breton V, Buvat I, Comtat C, Jan S, Krieguer M, Lazaro D, Morel C, Rey M, Santin G, Simon L, Staelens S, Strul D, Vieira J-M, van de Walle R. 2004. Monte Carlo simulation in PET and SPECT instrumentation using GATE. *Nucl Instr and Meth A* 527:180-189.

Ay MR and Sarkar S. 2007. Computed Tomography Based Attenuation Correction in PET/CT: Principles, Instrumentation, Protocols, Artifacts and Future Trends. *Iran J Nucl Med* 15:1-29.

Basu S, Kwee TC, Surti S, Akin EA, Yoo D. 2011. Fundamentals of PET and PET/CT imaging. *Ann NY Acad Sci* 1228:1-18.

Basu S, Zaidi H, Houseni M, Bural G, Udupa J, Acton P, Torigian DA, Alavi A. 2007. Novel Quantitative Techniques for Assessing Regional and Global Function

and Structure Based on Modern Imaging Modalities: Implications for Normal Variation, Aging and Diseased States. *Semin Nucl Med* 37:223-239.

Biehl KJ, Kong FM, Dehdashti F, Jin J-Y, Mutic A, El Naqa I,Siegel BA, Bradley JD. 2006. ^{18}F-FDG PET Definition of Gross Tumor Volume for Radiotherapy of Non-Small Cell Lung Cancer: Is a Single Uptake Value Threshold Approach Appropriate? *J Nucl Med* 47:1808-1812.

Boellaard R, Krak NC Hoekstra OS, Lammertsma AA. 2004. Effects of Noise, Image Resolution, and ROI Definition on the Accuracy of Standard Uptake Values: A Simulation Study. *J Nucl Med* 45:1519-1527.

Boussion N, Cheze-le Rest C, Hatt M, Visvikis D. 2009. Incorporation of wavelet-based denoising in iterative deconvolution for partial volume correction in whole-body PET imaging. *Eur J Nucl Med Mol Imaging* 36:1064-1075.

Boussion N, Hatt M, Lamare F, Bizais Y, Turzo A, Cheze-le Rest C, Visvikis D. 2006. A multiresolution image based approach for correction of partial volume effects in emission tomography. *Phys Med Biol* 51:1857-1876.

Boucher L, Rodrigue S, Lecomte R, Bénard F. 2004. Respiratory Gating for 3-Dimensional PET of the Thorax: Feasibility and Initial Results. *J Nucl Med* 45:214-219.

Brasse D, Kinahan PE, Lartizien C, Comtat C, Casey M, Michel C. 2005. Correction Methods for Random Coincidences in Fully 3D whole-body PET: Impact on Data and Image Quality. *J Nucl Med* 46:859-867.

Brooks A and Di Chiro G. 1976. Principles of Computer Assisted Tomography (CAT) in Radiographic and Radioisotopic Imaging. *Phys Med Biol* 21: 689-732.

Bruyant PP, Cheze-le Rest, C, Turzo A, Jarritt P, Carson K, Visvikis D. 2007. A method for synchronizing an external respiratory signal with a list-mode PET acquisition. *Med Phys* 34:4472-4475.

Budinger TF, Brennan KM, Moses WW, Derenzo SE. 1996. Advances in Positron Tomography for Oncology. *Nucl Med Biol* 23:659-667.

Buvat I. 2007a. Quantification in emission tomography: Challenges, solutions, and performance. *Nucl Instr and Meth A* 571:10-13.

Buvat I. 2007b. Les limites du SUV (Understanding the limitations of SUV). *Médecine Nucléaire* 31:165-172.

Buvat I and Castiglioni I. 2002. Monte Carlo simulations in SPET and PET. *Q J Nucl Med* 46:48-61.

Buvat I, Castiglioni I, Feuardent J, Gilardi MC. 2005. Unified description and validation of Monte Carlo simulators in PET. *Phys Med Biol* 50:329-346.

Castiglioni I, Buvat I, Gilardi MC, Feuardent J, Fazio F. 2005. A publicly accessible Monte Carlo database for validation purposes in emission tomography. *Eur J Nucl Med Mol Imaging* 32:1234-1239.

Chang G, Chang T, Pan T, Clark JW, Mawlawi OR. 2010. Joint correction of respiratory motion artifact and partial volume effect in lung/thoracic PET/CT imaging. *Med Phys* 37:6221-6232.

Cherry SR and Dahlbom M. 2004. PET: Physics, Instrumentation and Scanners. In *PET: Molecular Imaging and Its Biological Applications*. Edited by Phelps ME. 1st ed., Springer, New York: 9-12, 97-101.

Cherry SR, Sorenson JA, Phelps MA. 2012. Physics of Nuclear Medicine. 4th ed., Elsevier, Philadelphia: 307- 343.

Chi PM, Mawlawi O, Luo D, Liao Z, Macapinlac HA, Pan T. 2008. Effects of respiration-averaged computed tomography on positron emission tomography/computed tomography quantification and its potential impact on gross tumor volume delineation. *Int J Radiation Oncology Biol Phys* 71:890-899.

Chi PM, Mawlawi O, Nehmeh SA, Erdi YE, Balter PA, Luo D, Mohan R, Pan T. 2007. Design of respiration averaged CT for attenuation correction of the PET data from PET/CT. *Med Phys* 34:2039-2047.

Cormack AM. 1963. Representation of a Function by Its Line Integrals, with Some Radiological Applications. *J Appl Phys* 34: 2722-2727.

Cormack AM. 1964. Representation of a Function by Its Line Integrals, with Some Radiological Applications II. *J Appl Phys* 34: 2908-2913.

Costa DC, Visvikis D, Crosdale, Pigden I, Townsend C, Bomanji J, Prvulovich E, Lonn A, Ell PJ. 2003. Positron emission and computed X-ray tomography: a coming together. *Nucl Med Commun* 24:351-358.

De Beenhouwer J, Staelens S, Kruecker D, Ferrer L, D'Asseler Y, Lemahieu I, Rannou FR. 2007. Cluster computing software for GATE simulations. *Med Phys* 34:1926-1933.

Daouk J, Bailly FP, Meyer M-E. 2009. Respiratory-Gated Positron Emission Tomography and Breath-Hold Computed Tomography Coupling to Reduce the Influence of Respiratory Motion: Methodology and Feasibility. *Acta Radiol* 50:144-155.

Daube-Witherspoon ME and Muehllehner G. 1987. Treatment of Axial Data in Three-Dimensional PET. *J Nucl Med* 28:1717-1724.

Dawood M, Büther F, Lang N, Schober O, Schäfers KP. 2007. Respiratory gating in positron emission tomography: A quantitative comparison of different gating schemes. *Med Phys* 34:3067-3076.

Defrise M, Kinahan PE. Michel CJ. 2005. Image Reconstruction Algorithms in PET. In *Positron Emission Tomography: Basic Sciences*. Edited by Bailey DL, Townsend DW, Valk PE, Maisey MN. 1st ed.. Springer, London :63-89.

Defrise M, Kinahan PE, Townsend DW, Michel C, Sibomana, Newport DF. 1997. Exact and Approximate Rebinning Algorithms for 3-D PET Data. *IEEE Trans Med Imag* 16:145-158.

Di Chiro G and Brooks RA. 1988. PET Quantitation: Blessing and Curse. *J Nucl Med* 29:1603-1604.

Erdi YE, Nehmeh SA, Pan T, Pevsner A, Rosenzweig KE, Mageras G, Yorke ED, Schöder H, Hsiao W, Squire OD, Vernon P, Ashman JB, Mostafavi H, Larson SM, Humm JL. 2004. The CT Motion Quantitation of Lung Lesions and Its Impact on PET-Measured SUVs. *J Nucl Med* 45:1287-1292.

Eriksson L , Townsend D, Cont M, Eriksson M, Rothfuss H, Schmand M, Casey ME, Bendriem B. 2007. An investigation of sensitivity limits in PET scanners. *Nucl Inst and Meth A* 580:836-842.

Erlandsson K, Buvat I, Pretorius PH, Thomas BA, Hutton BF. 2012. A review of partial volume correction techniques for emission tomography and their applications in neurology, cardiology and oncology. *Phys Med Biol* 57:R119-R159.

Fernando S, Kong F, Kessler M, Chetty I, Narayan S, Tatro D, Hayman J, Ten Haken R. 2005. Using FDG-PET to Delineate Gross Tumor and Internal Target Volumes. *Int J Radiation Oncology Biol Phys* 63:S400-S401.

Frey EC, Humm JL, Ljungberg M. 2012. Accuracy and Precision of Radioactivity Quantification in Nuclear Medicine Images. *Semin Nucl Med* 42:208-218.

GATE: Simulations of Preclinical and Clinical Scans in Emission Tomography, Transmission Tomography and Radiation Therapy. Available from: http://www.opengatecollaboration.org/ (Accessed 01 December 2013).

Hatt M, Le Maitre A, Wallach D, Fayad H, Visvikis D. 2012. Comparison of different methods of incorporating respiratory motion for lung cancer tumor volume delineation on PET images: a simulation study. *Phys Med Biol* 57:7409-7430.

Hickeson M, Yun M, Matthies, Zhuang H, Adam L-E, Lacorte L, Alavi A. 2002. Use of a corrected standardized uptake value based on the lesion size on CT permits accurate characterization of lung nodules on FDG-PET. *Eur J Nucl Med* 29:1639-1647.

Hoetjes NJ, van Velden FHP, Hoekstra OS, Hoekstra CJ, Krak NC, Lammertsma AA, Boellaard R. 2010. Partial volume correction strategies for quantitative FDG PET in oncology. *Eur J Nucl Med Mol Imaging* 37:1679-1687.

Hoffman EJ, Huang SC, Phelps ME. 1979. Quantitation in Positron Emission Tomography: 1. Effect of Object Size. *J Comput Assist Tomogr* 3:299-308.

Hounsfield GN. 1973. Computerised transverse axial scanning (tomography). Part I. Description of system. *Br J Radiol* 46:1016-1022.

Hudson HM and Larkin RS. 1994. Accelerated image reconstruction using ordered subsets of projection data. *IEEE Trans Med Imag* 13:601-609.

Jan S, Santin G, Strul D, Staelens S, Assié K, Autret D, Avner S, Barbier R, Bardiès M, Bloomfield PM, Brasse D, Breton V, Bruyndonckx P, Buvat I, Chatziioannou AF, Choi Y, Chung YH, Comtat C, Donnarieix D, Ferrer L, Glick SJ, Groiselle CJ, Guez D, Honore P-F, Kerhoas-Cavata S, Kirov AS, Kohli V, Koole M, Krieguer M, van der Laan DJ, Lamare F, Largeron G, Lartizien C, Lazaro D, Maas MC, Maigne L, Mayet F, Melot F, Merheb C, Pennacchio E, Perez J, Pietrzyk U, Rannou FR, Rey M, Schaart DR, Schmidtlein CR, Simon L, Song TY, Vieira J-M, Visvikis D, Van de Walle R, Wieërs E, Morel C. 2004. GATE: a simulation toolkit for PET and SPET. *Phys Med Biol* 49:4543-4561.

Kawano T, Ohtake E, Inoue T. 2008. Deep-Inspiration Breath-Hold PET/CT of Lung Cancer: Maximum Standardized Uptake Value Analysis of 108 Patients. *J Nucl Med* 49:1223-1231.

Keyes J. 1995. SUV: Standard Uptake or Silly Useless Value? *J Nucl Med* 36:1836-1839.

Lamare F, Cresson T, Savean J, Cheze-le Rest C, Reader AJ, Visvikis D. 2007a. Respiratory motion correction for PET oncology applications using affine transformation of list mode data. *Phys Med Biol* 52:121-140.

Lamare F, Ledesma Carbayo MJ, Cresson T, Kontaxakis G, Santos A, Cheze-le Rest C, Reader AJ, Visvikis D. 2007b. List-mode-based reconstruction for respiratory motion correction in PET using non-rigid body transformations. *Phys Med Biol* 52:5187-5204.

Lamare F, Le Maitre A, Dawood M, Schäfers KP, Fernandez P, Rimoldi OE, Visvikis D. 2014. Evaluation of respiratory and cardiac motion correction schemes in dual gated PET/CT cardiac imaging. *Med Phys* 41:072504-1-13.

Lamare F, Turzo Y, Cheze-Le Rest C, Visvikis D. 2006. Validation of a Monte Carlo simulation of the Philips Allegro/GEMINI PET systems using GATE. *Phys Med Biol* 51:943-962.

Le Maitre A, Segars WP, Marache S, Reilhac A, Hatt M, Tomei S, Lartizien C, Visvikis D. 2009. Incorporating Patient-Specific Variability in the Simulation of Realistic Whole-Body 18-F-FDG Distributions for Oncology Applications. *Proceedings of the IEEE* 97:2026-2038.

Liu C, Pierce LA, Alessio AM, Kinahan PE. 2009. The impact of respiratory motion on tumor quantification and delineation in static PET/CT imaging. *Phys Med Biol* 54:7345-7362.

Lucignani G, Paganelli G, Bombardieri E. 2004. The use of standardized uptake values for assessing FDG uptake with PET in oncology: a clinical perspective. *Nucl Med Commun* 25:651-656.

Marsden PK. 2004. Quantitation in PET: What is it? Can we do it? Do we need it? *Nucl Med Commun* 25:635-636.

Meikle SR and Badawi RD. 2005. Quantitative Techniques. In *Positron Emission Tomography: Basic Sciences*. Edited by Bailey DL, Townsend DW, Valk PE, Maisey MN. 1st ed.. Springer, London :121-123.

Meirelles GSP, Erdi YE, Nehmeh, Squire OD, Larson SM, Humm JL, Schöder H. 2007. Deep-Inspiration Breath-Hold PET/CT: Clinical Findings with a New Technique for Detection and Characterization of Thoracic Lesions. *J Nucl Med* 48:712-719.

Melcher CL. 2000. Scintillation Crystals for PET. *J Nucl Med* 41:1051-1055.

Moses WW. 2011. Fundamental limits of spatial resolution in PET. *Nucl Instr and Meth A* 649:S236-S240.

Nehmeh SA, Erdi YE, Ling CC, Rosenzweig KE, Squire OD, Braban LE, Ford E, Sidhu K, Mageras GS, Larson SM, Humm JL. 2002. Effect of respiratory gating on reducing lung motion artifacts in PET imaging of lung cancer. *Med Phys* 29:366-371.

Nehmeh SA, Erdi YE, Meirelles GSP, Squire OD, Larson SM, Humm JL, Schöder H. 2007. Deep-Inspiration Breath-Hold PET/CT of the Thorax. *J Nucl Med* 48:22-26.

Pan T, Mawlawi O, Nehmeh SA, Erdi YE, Luo D, Liu HH, Castillo R, Mohan R, Liao Z, Macapinlac HA. 2005. Attenuation Correction of PET Images with Respiration-Averaged CT Images in PET/CT. *J Nucl Med* 46:1481-1487.

Phelps, ME (Ed.). 2004. PET: Molecular Imaging and Its Biological Applications. 1st ed.. *Springer, New York* :9-12.

Reader AJ, Erlandsson K, Flower MA, Ott RJ. 1998. Fast accurate iterative reconstruction for low-statistics positron volume imaging. *Phys Med Biol* 43: 835-846.

Reader AJ, Stijn A, Bakatselos F, Manavaki R, Walledge RJ, Jeavons AP, Julyan PJ, Zhao S, Hastings DL, Zweit J. 2002. One-Pass List-Mode EM Algorithm for High-

Resolution 3-D PET Image Reconstruction Into Large Arrays. *IEEE Trans Nucl Sci* 49:693-699.

Rothfuss H, Byars L, Casey ME, Conti M, Eriksson L, Michel C. 2007. Energy resolution and absolute detection efficiency for LSO crystals: A comparison between Monte Carlo simulation and experimental data. *Nucl Instr and Meth A* 580:1087-1092.

Rousset OG, Ma Y, Evans AC. 1998. Correction for Partial Volume Effects in PET: Principle and Validation. *J Nucl Med* 39:904-911.

Saha GB. 2005. Basics of PET Imaging: Physics, Chemistry and Regulations, 1st ed., Springer, New York :196.

Santin G, Staelens S, Taschereau R, Descourt P, Schmidtlein CR, Simon L, Visvikis D, Jan S, Buvat I. 2007. Evolution of the GATE project: new results and developments. *Nucl Phys B (Proc. Suppl.)* 172:101-103.

Schmidtlein CR, Kirov AS, Nehmeh SA, Erdi YE, Humm JL, Amols HI, Bidaut LM, Ganin A, Stearns CW, McDaniel DL, Hamacher KA. 2006. Validation of GATE Monte Carlo simulations of the GE Advance/Discovery LS PET scanners. *Med Phys* 33:198-208.

Segars WP. 2001. Development and Application of the New Dynamic NURBS-based Cardiac-Torso (NCAT) Phantom, Ph.D. Dissertation, The University of North Carolina.

Segars WP, Mahesh M, Beck TJ, Frey EC, Tsui BMW. 2008. Realistic CT simulation using the 4D XCAT phantom. *Med Phys* 35:3800-3808.

Segars WP, Sturgeon G, Mendonca S, Grimes J, Tsui BMW. 2010. 4D XCAT phantom for multimodality imaging research. *Med Phys* 37:4902-4915.

Shepp LA and Vardi Y. 1982. Maximum Likelihood Reconstruction for Emission Tomography. *IEEE Trans Med Imag* MI-1:113-122.

Soret M, Bacharach SL, Buvat I. 2007. Partial-Volume Effect in PET Tumour Imaging. *J Nucl Med* 48:932-945.

Staelens S, De Beenhouwer J, Kruecker D, Maigne L, Rannou F, Ferrer L, d'Asseler Y, Buvat I, Lemahieu I. 2006. GATE: Improving the computational efficiency. *Nucl Instr and Meth A* 569:341-345.

Strul D, Santin G, Lazaro D, Breton V, Morel C. 2003. GATE (Geant4 Application for Tomographic Emission): a PET/SPECT general-purpose simulation platform. *Nucl Phys B (Proc. Suppl.)* 125:75-79.

Sugawara Y, Zasadny KR, Neuhoff AW, Wahl RL. 1999. Reevaluation of the Standardized Uptake Value for FDG: Variations with Body Weight and Methods for Correction. *Radiology* 213:521-525.

Teo BK, Seo, Y, Bacharach SL, Carrasquillo JA, Libutti SK, Shukla H, Hasegawa B, Hawkins RA, Franc BL. 2007. Partial-Volume Correction in PET: Validation of an Iterative Postreconstruction Method with Phantom and Patient Data. *J Nucl Med* 48:802-810.

Townsend DW. 2004. Physical Principles and Technology of Clinical PET Imaging. *Ann Acad Med Singapore* 33:133-145.

Tylski P, Stute S, Grotus N, Doyeux K, Hapdey S, Gardin I, Vanderlinden B, Buvat I. 2010. Comparitive Assessment of Methods for Estimating Tumor Volume and Standardized Uptake Value in 18-F-FDG PET. *J Nucl Med* 51:268-276.

Van Heijl M, Omloo JM, van Berge Henegouwen MI, van Lanschot JJ, Sloof GW, Boellaard R. 2010. Influence of ROI definition, partial volume correction and SUV normalization on SUV-survival correlation in oesophageal cancer. *Nucl Med Commun* 31:652-658.

Visvikis D, Bardies M, Chiavassa, Danford C, Kirov A, Lamare F, Maigne L, Staelens S, Taschereau R. 2006. Use of GATE Monte Carlo package for dosimetry applications. *Nucl Instr and Meth A* 569:335-340.

Visvikis D, Barret O, Fryer TD, Lamare F, Turzo A, Bizais Y, Cheze-le Rest C. 2004a. Evaluation of respiratory motion effects in comparison with other parameters affecting PET image quality. *IEEE TNS and MIC conference records* 6:3668-3672.

Visvikis D, Cheze-Le Rest C, Jarritt P. 2004b. PET technology: current trends and future developments. *Br J Radiol* 77:906-910.

Visvikis D, Costa DC, Croasdale, Lonn AHR, Bomanji J, Gacinovic S, Ell PJ. 2003. CT-based attenuation correction in the calculation of semi-quantitative indices of [^{18}F]FDG uptake in PET. *Eur J Nucl Med Mol Imaging* 30:344-353.

Visvikis D, Turzo A, Bizais Y, Cheze-Le Rest C. 2004c. Technology related parameters affecting quantification in positron emission tomography imaging. *Nucl Med Commun* 25:637-641.

Werner KW, Parker JA, Kolodny GM, English JR, Palmer MR. 2009. Respiratory Gating Enhances Imaging of Pulmonary Nodules and Measurement of Tracer Uptake in FDG PET/CT. *AJR* 193:1640-1645.

Zaidi H. 1999. Relevance of accurate Monte Carlo modeling in nuclear medicine imaging. *Med Phys* 26:574-608.

Zaidi H. 2000. Addendum to "Relevance of accurate Monte Carlo modeling in nuclear medicine imaging". *Med Phys* 27:816-817.

Zaidi H and Alavi A. 2007. Current Trends in PET and Combined (PET/CT and PET/MR) Systems Design. *PET Clin* 2:109-123.

Zanzonico P. 2004. Positron Emission Tomography: A Review of Basic Principles, Scanner Design and Performance, and Current Systems. *Sem Nucl Med* 34(2):87-111.

Zasadny KR and Wahl RL. 1993. Standardized Uptake Values of Normal Tissues at PET with 2-[Fluorine-18]-Fluoro-2-deoxy-D-glucose: Variations with Body Weight and a Method for Correction. *Radiology* 189:847-850.

Chapter III

IEC Body Phantom

Table of Contents

3.1 Introduction

The motivation was given as to why it is important to assess the factors influencing SUV (Chapter 2). It was stated that the major influences on SUV accuracy were the partial volume effect, the presence of scatter and random coincidences and respiratory motion. In this chapter, the influences of the partial volume effect and of contrast and their contribution to the SUV determination were assessed. In the following chapter, the influence of respiratory motion and activity outside the field-of-view was included in the investigation.

This part of the investigation was divided into two sections. The first part was the validation of the simulation software and the second part comprised the evaluation of the parameters that influenced SUV calculation including the assessment of the contribution of the true-, scattered and random coincidences on the SUV determination.

3.1.1 Validation of Simulation Software:

Before using the Monte Carlo simulations of the human equivalent phantom that were needed for the next phase of the investigation and which is the focus of the next chapter, it was important to ensure that the simulation program was performing reliably. The validation of the simulation software consisted of a comparison against an international benchmark and a comparison of phantom studies using a PET/CT scanner and the equivalent set-up by means of simulations using the Monte Carlo software, GATE. To do the comparative simulations included that a voxelised phantom be created as such phantom was neither available commercially nor could it be obtained in the public domain.

3.1.2 Investigation of the Parameters that Influence SUV

The influence of various factors on the calculation of SUV was evaluated by using physical data acquisitions of a readily available phantom under static conditions as well as using a voxelised equivalent of the phantom to perform corresponding simulations. The impact of size of the objects and contrast were assessed in 2D and 3D modes

respectively, the influence of various matrix sizes were investigated and the effect of using various VoIs was studied. Investigation of the relative contribution of the trues, scatters and randoms was done by variation of object size, contrast, matrix size and VoI.

3.2 Methods

3.2.1 Phantom studies using a PET/CT Scanner

Phantom studies were performed to assess the influence of the partial volume effect due to spatial resolution using the General Electric Discovery ST PET/CT scanner (Milwaukee, WI) (See Figure 3-1) at the Free State PET/CT Centre. The Free State PET/CT Centre is situated in the Bloemfontein Mediclinic private hospital and is the only facility of its kind in the central part of South Africa. It receives referrals from three of the country's provinces, mainly patients with private healthcare coverage, but also public healthcare patients. The facility started operation in 2006 and was the third of its kind in the country, and indeed also on the African continent.

Figure 3-1: GE Discovery ST PET/CT Scanner at the Free State PET/CT Centre that was used for the phantom scans in this research.

Phantom data was acquired using the clinical acquisition protocols that are used routinely at the Free State PET/CT Centre. An acquisition time of 900 seconds was used for all studies. The phantom was positioned in such a way that the acquisition required only one bed position. From the CT scout view it was ensured that the first CT image included the lid of the phantom and subsequently an additional 46 image slices were selected for acquisition. The phantom was acquired in 2D and 3D modes using the same set-up each time. The CT images were reconstructed with 2.5 mm slice thicknesses.

The PET projections were reconstructed at the PET/CT acquisition console using iterative reconstruction methods: OSEM for the 2D acquisitions and FORE-Iterative for the 3D acquisitions as these options are normally selected for clinical studies. (OSEM and FORE were discussed in section 2.1.2). The reconstructions comprised of two iterations and twenty-one subsets. This combination of subsets and iterations was the default setting and had also been used in the performance evaluation of this type of PET/CT scanner (Bettinardi *et al.*, 2004). The combination of iterations and subsets also follow the recommendations made by Jaskowiak *et al.* (2005). The data was automatically corrected for attenuation using the CT images that were obtained during the PET/CT acquisition, as well as for scattered and random events by the acquisition software.

3.2.2 Monte Carlo Simulations with GATE

The Monte Carlo simulations were performed on the computer cluster of the High Performance Computing unit situated at the Faculty of Natural and Agricultural Sciences at the University of the Free State. The cluster consists of 17 nodes of forty-eight 2200 MHz cores each with 64 GB RAM, as well as 8 nodes of sixty-four 2200 MHz cores each with 128 GB RAM. The GATE simulations were performed using 400 cores each time. The Geant4 Application for Tomographic Emission (GATE) software version 6.1, released on 01/03/2011, (http://www.opengatecollaboration.org) was used (Jan *et al.*, 2004).

The GE Discovery ST PET scanner used for simulation was defined from the data sheets provided by GE and with the help of Dr Assen Kirov and Dr Ross Schmidtlein of Memorial Sloan Kettering Cancer Center in New York (Du Toit, 2008; Schmidtlein *et al.*, 2006).

For implementation of Monte Carlo simulations, the scanner of choice and the phantom geometries had to be created together with definition of all the physical parameters involved. The main components of a simulation macro (Figure 3-2) are the scanner definition, the description of the structure of the phantom to be imaged as well as the description of the source or spread of activity inside the phantom, the physical processes involved, the detection processes and digitizer, the random number generator model, and the simulation output.

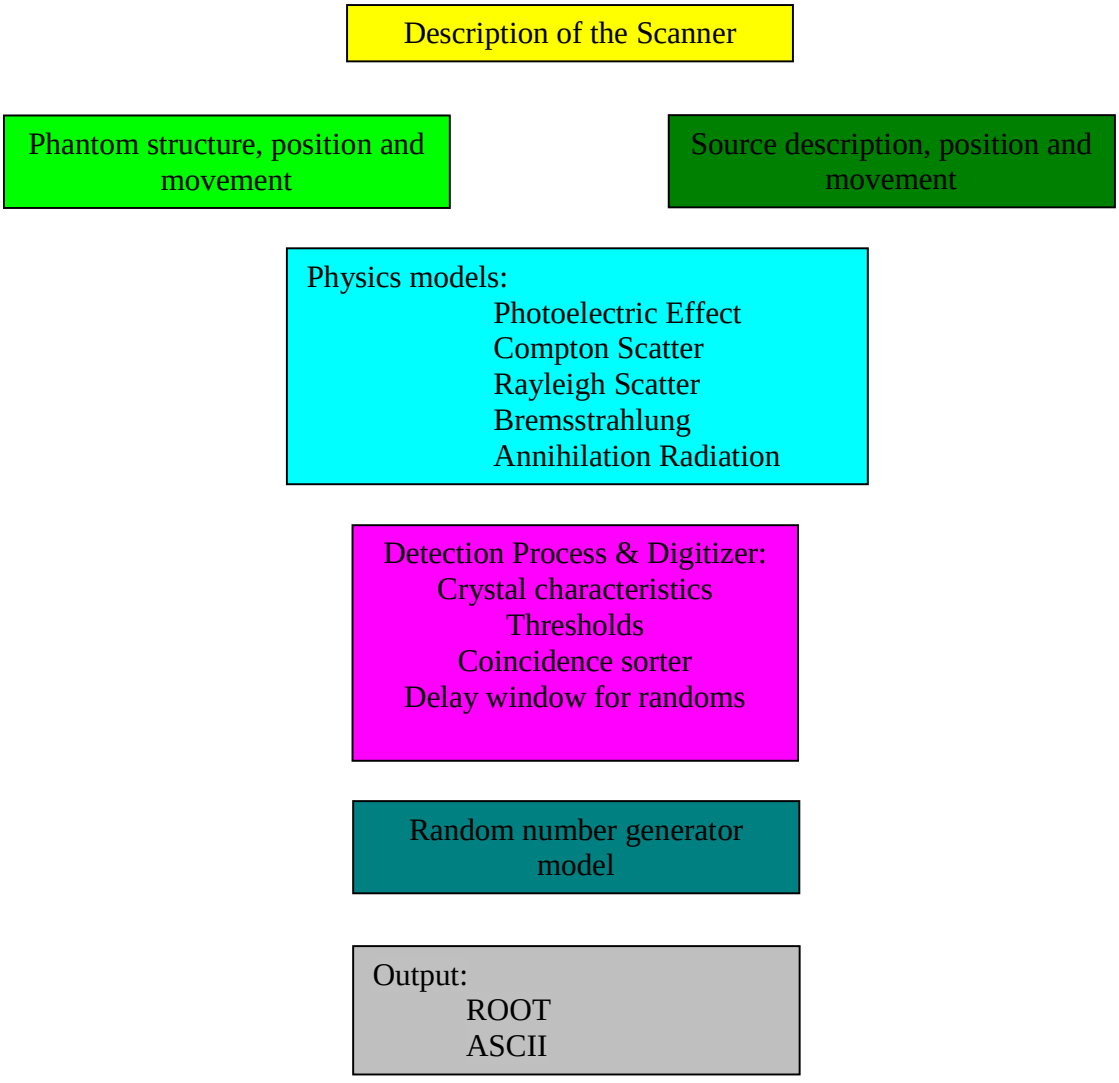

Figure 3-2: A schematic of the components of a typical GATE simulation

The macro was kept the same for all simulations with only minor adjustments for imaging time and defining 2D or 3D imaging modes. An example of a macro can be found in appendix 3.6.2.

Using 400 cores during a simulation created 400 ROOT files containing the saved data. These multiple ROOT files were added after each simulation and the trues, randoms and scatters extracted. The simulated data (comprising of four sets of data giving: combined trues + randoms + scatters data, trues separately, randoms separately and scatters separately) were reconstructed using the OPL-EM algorithm (Reader *et al.*, 2002) using two iterations and twenty-one subsets and corrected for sensitivity and attenuation using the CT data. It should be noted here that the reconstruction algorithm used for the simulation data is different than that used for the phantom data as was discussed in section 3.2.1.

3.2.3 NEMA IEC PET Body Phantom

To assess the validity of the digital simulations, it was necessary to use a phantom that was readily available and often used for quality assurance in PET.

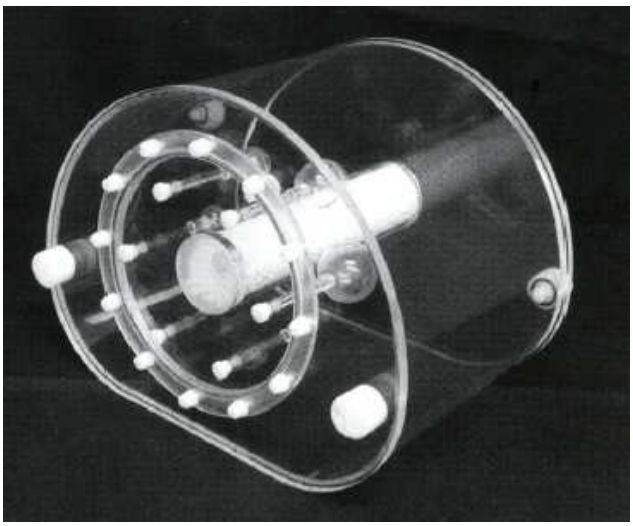

Figure 3-3: NEMA IEC PET BODY PHANTOM™ showing the Poly(methyl methacrylate) (PMMA) outer shell and the sphere inserts with the central lung volume seen as a white cylinder in the centre of the phantom

The NEMA IEC PET Body Phantom™ (Data Spectrum Corporation) (Figure 3-3) was used to acquire images. This phantom consists of a fillable body phantom, a lung insert and a set of six hollow spheres. The volumes of the spheres were designed using an approximately logarithmic progression, Figure 3-4, i.e. each sphere has approximately double the volume of the previous smaller sphere: 0.52 ml (the smallest), 1.15 ml, 2.57 ml, 5.57 ml, 11.49 ml and 26.52 ml (the largest). The diameter of each sphere was 10 mm, 13 mm, 17 mm, 22 mm, 28 mm and 37 mm respectively.

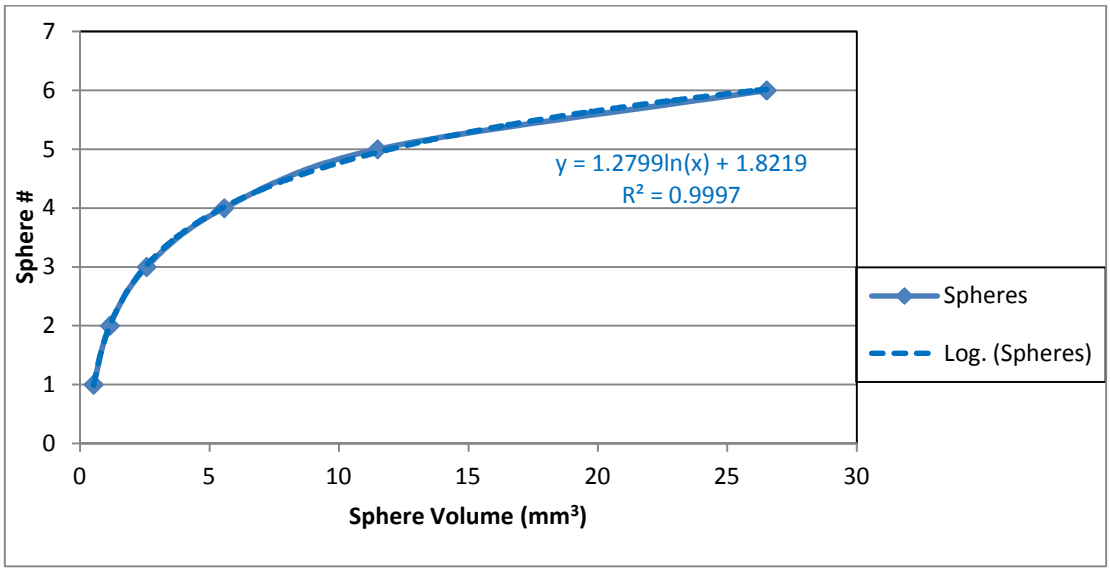

Figure 3-4: Illustration of the logarithmic relation of the volumes of the hollow spheres used in the IEC Body Phantom™

The spheres in each experiment were filled using the same concentration of ^{18}F (as FDG) in water. The activity of ^{18}F was measured in a source calibrator and diluted with water to the exact volume of the combined volume of the spheres. The spheres were then filled with the solution using a thin needle, long enough to ensure that no air remained in the spheres or in the capillary tubes. The background ^{18}F activity concentration and the activity concentration within the set of spheres were varied to create a range of different relative sphere–to–background ratios. The sphere activity–to–background activity ratios that were used were 2:1, 5:1 and 10:1. The activity concentrations to achieve these contrast ratios can be seen in Table 3-1. The lung insert remained non-radioactive throughout the experiments; it was only filled with the polystyrene globules and water.

The capillary tubes of the spheres were filled with the same radioactive concentrations as the spheres.

Table 3-1: Sphere-to-Background activity concentration ratios

Contrast Ratio	Activity concentration in spheres (kBq/ml)	Activity concentration in torso (background) (kBq/ml)
2:1	18.99	9.44
5:1	157.84	31.03
10:1	43.17	4.13

3.2.4 Creation of a Voxelised IEC Body Phantom

GATE allows the input of geometrically described digital phantoms or voxelised phantoms for use in the simulations. A digital model of the NEMA IEC PET Body Phantom™ (hereafter in this chapter "IEC Body Phantom" or "phantom") was used to perform the Monte Carlo Simulations.

The IEC Body Phantom could have been recreated as a digital model either by defining the sizes of the components and materials or by recreating it as a voxelised phantom and a corresponding voxelised source. For this study the voxelised phantom method was used to represent the phantom more accurately (Du Toit *et al.*, 2014a). The phantom was digitized using a CT scanner. The phantom and its inserts were filled with water and scanned with the CT using 120 kV and 380 mA to obtain a set of high resolution images. The CT images were acquired in a 512×512 matrix format and scaled to a 128×128 format in order to be similar to the PET image format. Only 47 images were used to create the input file to correspond with the images that were obtained using the physical PET/CT acquisition phase. The voxelised model uses CT numbers to define the materials of the phantom using a definition file, *range.dat*, as well as the source activity concentrations in the phantom using the definition file, *activityRange.dat*. The CT numbers obtained ranged from –1000 to +1000 and since GATE needs an unsigned

interfile image as input file, the CT numbers of the phantom were scaled linearly to fall within a range of 0 to 255.

The phantom was scanned using water mixed with different concentrations of ^{18}F for the volume within the spheres and the volume as background in the torso part of the phantom; therefore the densities of the material inside and outside the spheres are effectively identical. Thus when the phantom was digitized, the activity concentrations that needed to be assigned according to the densities of the material were the same for within the spheres and background surrounding the spheres. In the *activityRange.dat* file, there is therefore no distinction between water in the spheres and water in the background as the scaled CT numbers would have been in the same range.

To overcome this problem, the spheres needed to be filled with a medium that had different densities than the surrounding water. Two different media were considered, namely alcohol which has a density less than water and Gastrografin® (Bayer) contrast media solution that is usually given to patients undergoing a PET/CT scan and that has a higher density than water. It was therefore possible to segment the spheres and background and thus different activity concentrations based on the scaled CT ranges could be assigned. For attenuation correction purposes the original phantom containing water inside the spheres was used.

Examples of *range.dat* and *activityRange.dat* can be found in the appendices under headings 3.6.3 and 3.6.4 respectively. In these examples, the scaled CT numbers representing different materials in each image are defined as materials with known properties such as density and attenuation coefficients that is used by GATE and that is to be used for attenuation correction during reconstruction. The set-up for using alcohol in the spheres are represented by Table 3-2 and the set-up for using Gastrografin® inside the spheres is shown in Table 3-3. An activity value of 0 was assigned to the voxel values at the upper end of the range to ensure that all values above 156 (in the alcohol scenario) and 220 (in the Gastrografin® case) did not contain any activity that could cause erroneous contamination of the results.

Table 3-2: Assignment of voxel values representing the scaled CT numbers to materials and corresponding activity values for input into GATE for simulation of the IEC Body Phantom using alcohol in the spheres

Scaled CT value	Material	Defined as ...	Activity values
0 – 5	Air	Air	0
6 – 119	Lung equivalent tissue	Lung	0
120 - 135	Alcohol	Water	Sphere activity
136 - 156	Water	Water	Background activity
157 – 255	None	Bone	0

Table 3-3: Assignment of voxel values representing the scaled CT numbers to materials and corresponding activity values for input into GATE for simulation of the IEC Body Phantom using Gastrografin® in the spheres

Scaled CT value	Material	Defined as ...	Activity values
0 – 5	Air	Air	0
6 – 175	Lung equivalent tissue	Lung	0
176 – 191	Water	Water	Background activity
192 – 220	Gastrografin®	Water	Sphere activity
221 – 255	None	Bone	0

By using the newly created voxelised phantom in the simulations, the spheres and background could be allocated similar radionuclide concentrations as were used in the phantom studies. The simulation data were saved in ROOT output format. Files saved in ROOT format allow data to be analysed using the ROOT software. This software was developed to provide a set of object-oriented frameworks with all the functionality that is needed to handle and analyse large amounts of data in an efficient way. The data is defined as a set of objects and by utilising customised storage methods, direct access to the separate attributes of these selected objects is gained without having to go through all of the data (http://root.cern.ch/drupal/content/about). A schematic of the above processes

involving the PET/CT scanner and the physical phantom as well as the GATE Monte Carlo code together with the voxelised phantom, is shown in Figure 3-5:

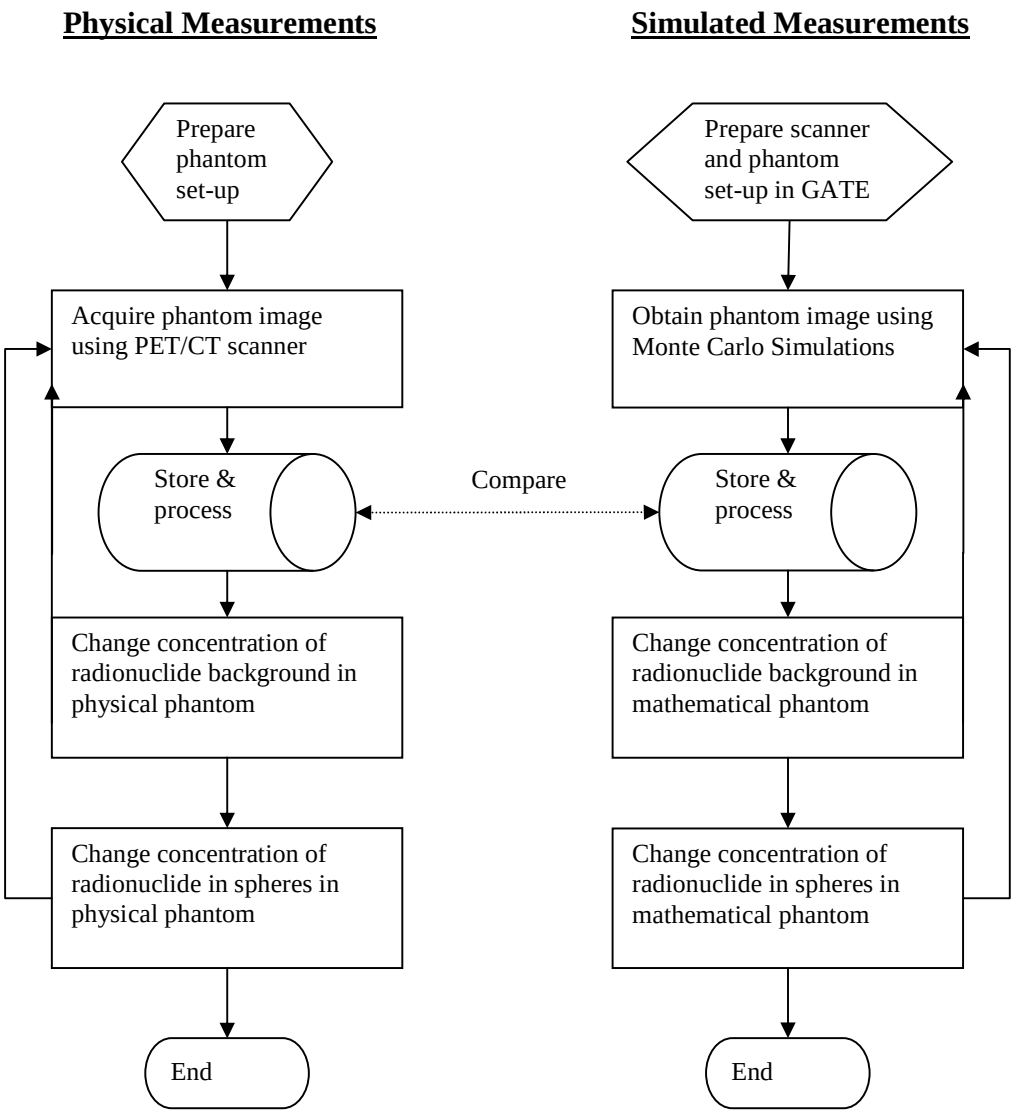

Figure 3-5: Schematic flowchart of phantom study acquisitions of NEMA IEC PET Body Phantom™ using a clinical PET/CT scanner and Monte Carlo simulations

3.2.5 Methods of Evaluation

The data was exported to a PC and the post processing and determination of the SUVs were done using *A Medical Image Data Examiner* (AMIDE) version 1.0.4 that was obtained at http://amide.sourceforge.net (Loening and Gambhir, 2003). SUVs were calculated using Equation 2-5.

The data was filtered using a Gaussian filter with FWHM of 12 mm. The voxel size for all 128×128 measurements performed on the PET data was 5.47 mm x 5.47 mm x 3.27 mm. A logarithmic fit was performed on the SUV data (Pandey *et al.*, 2012) and the correlation coefficients and equations determined.

As was previously performed by Hickeson *et al.*, (2002) the CT images of the spheres were used consistently to determine the sizes of the VoIs (VoI_{CT}) within which the SUV of the spheres were calculated, as is shown in Figure 3-6. This was performed during evaluation of all images obtained from the physical phantom scans as well as for the images that were produced by the simulations. The influence of VoI size on SUV was also investigated by using 90% of the diameter of the actual VoI_{CT} as well as 95%, 105% and 110% of the original diameter in addition to the 100%VoI_{CT}. Thus, 90%VoI_{CT} will represent a volume with a diameter that is 90% of the diameter of original VoI_{CT}. The volumes of the different VoIs as the diameters change are shown in Table 3-4. A visual representation of 90%VoI_{CT} and 110%VoI_{CT} is displayed in Figure 3-7. Throughout the evaluation process the maximum value of the SUV (SUV_{max}) and the mean SUV value (SUV_{mean}) in the VoIs of the spheres/lesions, defined in this way, were determined.

Table 3-4: Relationship between the diameters of VoI_{CT} and the volumes of the VoI_{CT}

	90% VoI_{CT}	95% VoI_{CT}	100% VoI_{CT}	105% VoI_{CT}	110% VoI_{CT}
%Fraction of VoI diameter:	90%	95%	100%	105%	110%
Volume of $VoI_{CT:}$	72.90%	85.74%	100.00%	115.76%	133.10%

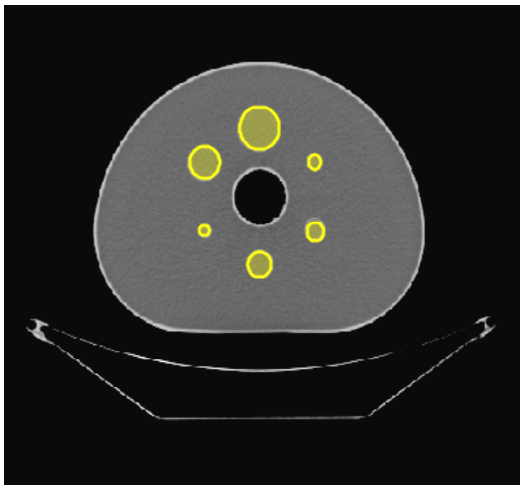

Figure 3-6: Illustration of the VoI sizes based on CT image of spheres (VoI_{CT})

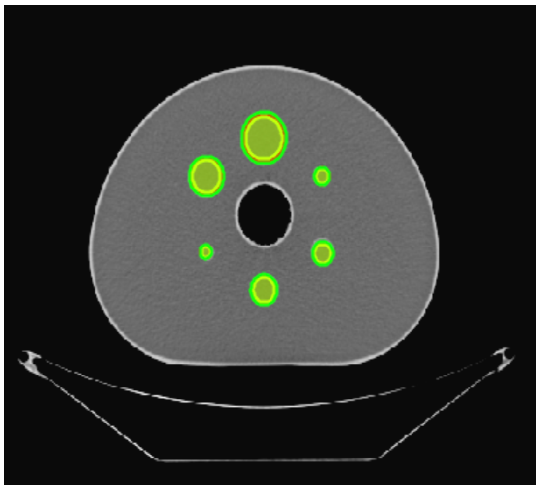

Figure 3-7: Illustration of the 90%VoI_{CT} (yellow) and the 110%VoI_{CT} (green)

The SUVs obtained from the true coincidences from the simulated data (SIM) were compared to the GE reconstructed results (PET) (corrected for scattered and random events) obtained from the phantom studies in all cases. To determine whether the differences were significant, the t-test (*Two-sample testing equality of means assuming Equal Variances and Equal Sample Sizes*) and F-test (*Two-Sample for testing for equal Variances*) were used with a significance level of $p < 0.05$ throughout this work. For all SUV_{mean} calculations, the standard deviation was determined. Error bars on the SUV_{mean} graphs represented one standard deviation from the mean. For each of the SUV_{max} values, the standard error of measurement ε was calculated by Equation 3-1, where σ^2 represents the variance and n represents the amount of voxels in the VoI. The errors bars in the SUV_{max} graphs represented the standard error.

$$\varepsilon = \sqrt{\frac{\sigma^2}{n}}$$

.....Equation 3-1

3.2.6 Validation of GATE

The validation of GATE consisted of two parts: (1) to validate the locally installed software against an international benchmark of the GATE users group; and (2) to validate the Monte Carlo simulations of phantom studies against data obtained from the physical phantom studies that were performed at the clinically used PET/CT scanner in Bloemfontein.

3.2.6.1 Validation of GATE against an international benchmark

Before commencing with the simulations, the GATE simulation program had to be validated using an international benchmark to ensure the software was correctly installed on the local computer system and that the computer system is stable. The PET benchmark was included as part of the GATE software installation package. It contained a number of macros to run simulations, to analyse the output and to generate results. The macros were combined into one macro and converted to be run on the cluster using one core only and also repeated using 400 cores. This was done to eliminate the need for checking and altering the network paths inside the macros. The simulations were run five times each at different times using different input seed values. The output was compared visually and quantitatively against the results that are available on the GATE website: http://www.opengatecollaboration.org/PETBenchmark. The GATE macro of this benchmark can be found in Appendix 3.6.1.

3.2.6.2 Validation of GATE against phantom studies

To assess whether the GATE simulations of the phantom provided an accurate reflection of the scanned phantom, the phantom was scanned on the PET scanner and simulated using various concentrations of sphere-to-background ratios described in 3.2.3. The SUV_{max} and SUV_{mean} were determined for different sphere sizes for the different contrast ratios in 2D and 3D modes. The statistical tests described in 3.2.5 were used to determine whether there were significant differences between the data obtained from physical scans and the simulated data.

3.2.7 Determination of the Parameters influencing SUV calculation

The SUV_{max} and SUV_{mean} were determined for different sphere sizes and for the different contrast ratios described before in 2D and 3D modes.

The following parameters were investigated:

a) Comparison of the SUV_{max} and SUV_{mean} obtained using a PET scanner to the equivalent SUV_{max} and SUV_{mean} that were found using simulations of the same phantom in 2D and 3D modes to assess the influence of the partial volume effect.
b) Comparison of different matrix sizes during simulations of the same contrast ratio in a phantom in 2D and 3D mode to determine the influence of sampling size. To assess the influence of sampling size, the simulations were performed using 64×64, 128×128, 256×256 and 512×512 matrix sizes. A fixed contrast ratio of 10:1 sphere-to-background was used.
c) Assessment of the influence of VoI size when performing the SUV calculations. This was done using different contrast ratios and the varying sphere sizes. The measurements were performed using a 128×128 matrix size.

3.2.8 Determination of the Contribution of True-, Scattered and Random Coincidences

The following investigations were performed to assess the influence of the different coincidence types:

a) Calculation of the contribution of the true-, scatter- and random coincidences respectively to the total image, i.e. the image consisting of all types of coincidences. The assessment was done using different contrast ratios, different sphere sizes and different matrix sizes.
b) Assessment of the influence of VoI size on the contributions of the coincidence fractions. This was done using different contrast ratios and the varying sphere sizes using a 128×128 matrix.

3.3 Results

The results from the simulations involving the IEC Body Phantom are presented here. SUV_{max} and SUV_{mean} values were obtained for the defined VoI for each of the spheres for the following datasets acquired using both the 2D and 3D imaging mode. The SUV_{mean} was calculated using the total coincidences as well as the true coincidences, scattered and random coincidences respectively to assess the contribution of each of these coincidences to the total SUV. This assessment allows for appropriate corrections to be implemented based on the individual findings. The SUV_{max} was determined for the true coincidences only. All results are tabulated in Appendix 3.6.5 for reference purposes

3.3.1 Creation of the Voxelised IEC Body Phantom

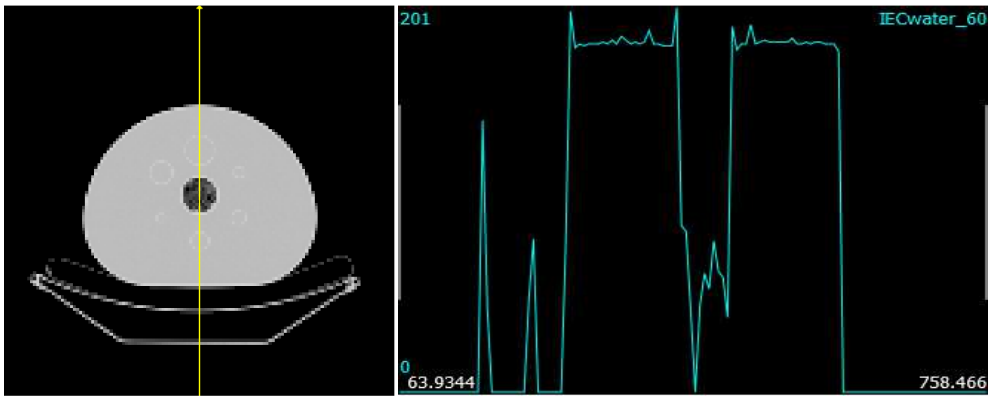

Figure 3-8: Transaxial view of a CT scan of the IEC Body Phantom with all of the spheres and the background filled with water (left); and vertical line profile through the phantom (right). The profile line is drawn from the bottom upwards resulting in the profile to be interpreted from left to right.

In Figure 3-8, a CT scan of IEC Body Phantom's six spheres filled with higher activity than a radioactive background is shown. Since the radioactive liquid inside and outside the spheres is water in both cases, it is noticed that the CT numbers for the activity filled spheres and those of the background cannot be distinguished from each other as is shown in the line profile diagram in Figure 3-8. The vertical line profile is viewed from the bottom upwards. The peaks on the left correspond to the CT numbers of the couch material, while the two broad profiles represent the water inside the phantom as well as inside the spheres. The walls of the spheres are faintly visible. It is therefore not possible for the computer code used to distinguish between the activity in the spheres and the background activity.

Figure 3-9 represents an image of the spheres filled with alcohol in the water-filled torso cavity of the phantom. The vertical line profile through the phantom can be seen in Figure 3-9 and it is evident that the CT numbers for alcohol and water overlapped. The depressions in the profile indicate a lower CT number than that of the water. It was therefore not possible to assign a specific range of CT numbers to the water-filled spheres without including some CT numbers of the background.

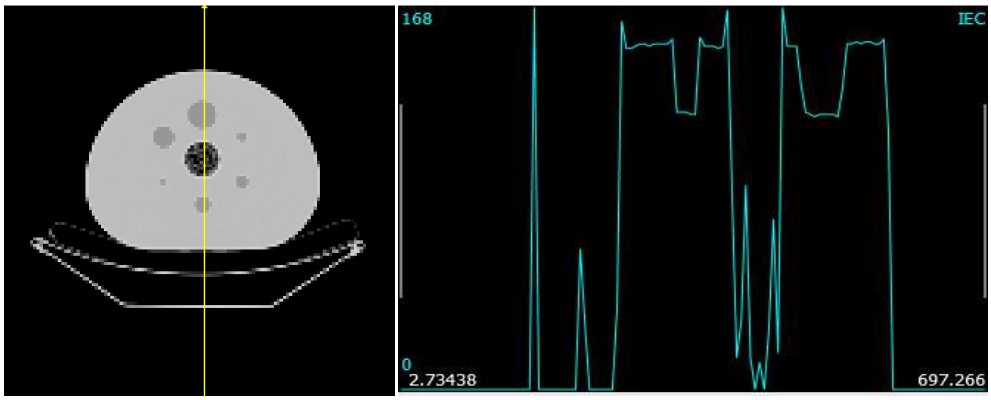

Figure 3-9: Transaxial view of a CT scan of the IEC Body Phantom with the spheres filled with alcohol and background filled with water (left); and with vertical line profile through the phantom (right). The profile line is drawn from the bottom upwards resulting in the profile to be interpreted from left to right.

In Figure 3-10 is an image of the spheres filled with Gastrografin® contrast media. The vertical line profile through the transverse slice of the phantom can be seen in the corresponding line profile diagram Figure 3-10 and it is observed that the CT number ranges for Gastrografin® and water were more distinct.

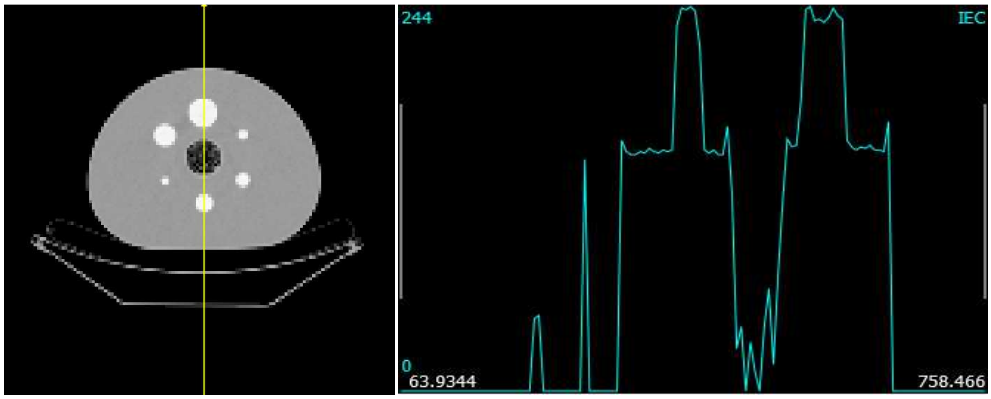

Figure 3-10: Transaxial view of a CT scan of the IEC Body Phantom with the spheres filled with contrast media and background filled with water (left); and with vertical line profile through the phantom (right). The profile line is drawn from the bottom upwards resulting in the profile to be interpreted from left to right.

The Gastrografin® in the profile is represented by the crests protruding from the water-filled background profile. It was therefore possible to assign a specific range of CT numbers to water inside the spheres and a specific range to represent the water in the surrounding cavity.

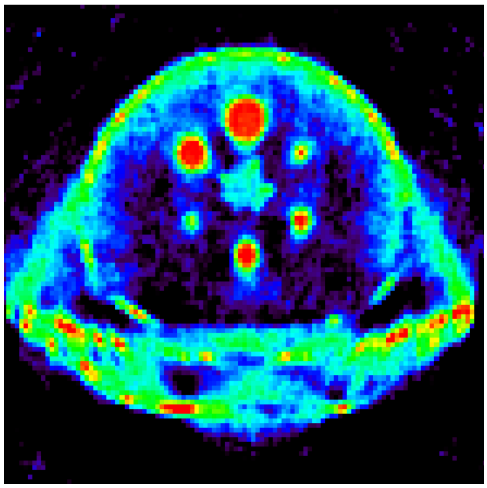

Figure 3-11: Transaxial view of the reconstructed GATE simulated phantom using alcohol in the spheres illustrating incorrect assignment of activity to other voxels in the phantom containing the same voxel values.

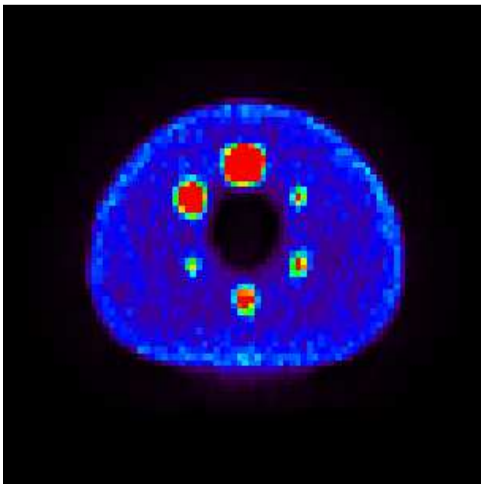

Figure 3-12: Transaxial view of the reconstructed GATE simulated phantom using Gastrografin® in the spheres showing correct assignment of increased activity inside the spheres (10:1 sphere-to-background ratio) and to the background

Figure 3-11 represents the result of a simulated PET scan of the phantom filled with a 10:1 sphere-to-background activity ratio based on the phantom in Figure 3-9. It is

evident that the assignment of CT numbers to represent certain materials resulted in the couch and phantom walls receiving the same activity as those inside the spheres. Incorrect assignment also appears in the lung insert. Figure 3-12 represents the result of the same simulated PET scan based on the phantom in Figure 3-10. In Figure 3-13 the result of the corresponding scan that was repeated physically using the PET/CT scanner is shown.

It is therefore clear that using alcohol to represent water inside the spheres does not provide an exact representation of the physical scan. The Gastrografin® filled spheres in the IEC Body Phantom™ provided CT numbers for the material inside the spheres that were distinguishable from those of the surrounding water making Gastrografin® therefore a more desirable contrast medium to use. As a result a voxelised phantom could be successfully created for use in GATE simulations.

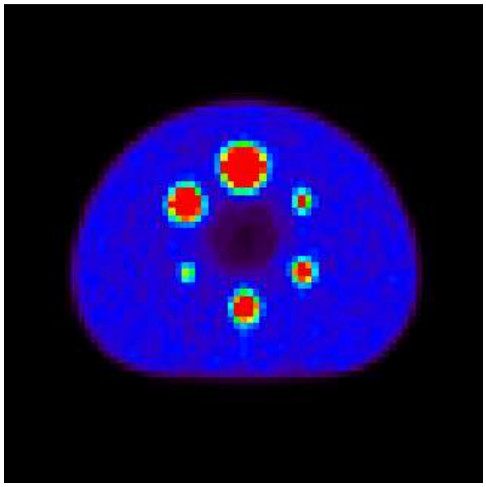

Figure 3-13: Transaxial view of a reconstructed PET scan of the phantom showing 10:1 sphere-to-background activity ratio

3.3.2 Validation of GATE against an international benchmark

The benchmark macro was run on a single processor on the cluster as well as on 400 cores on the cluster using the job-splitter and –merger. The results were compared to the benchmark table provided in the installation manual of GATE v.6.1 (http://wiki.opengatecollaboration.org/index.php/Validating_Installation) and are shown in Table 3-5.

When comparing the results as obtained by running the benchmark on one core to the published benchmark table, it was found that all parameters differ by less than one percent. When the simulation was split over 400 cores, all the parameters differed by less than one percent. The gamma acolinearity results could not be obtained with GATE version 6.1.

The GATE benchmark simulations on the UFS cluster compared favourably with the provided benchmark from the GATE group. The simulations of other scanner-phantom combinations could therefore be run on the UFS computer cluster with confidence.

Table 3-5: Measured benchmark results of GATE run using 1 core and 400 cores respectively on the UFS Computer Cluster compared to the published values (yellow)

	Benchmark	*Std Dev*	*Measured (1 core)*	*Diff. (<1%)*	*Measured (400 cores)*	*Diff. (<1%)*
O-15 decay factor			0.55		0.55	
F-18 decay factor			0.99		0.99	
O-15 initial activity			100000		100000	
F-18 initial activity			100000		100000	
O-15 decays			13113200		13113200	
F-18 decays			23699400		23699400	
Expected total number of decays	36813000		36812600		36812600	
True unscattered coincidences	312725	0.12%	314423	-0.54%	315092	-0.76%
Random coincidences	23536	0.20%	23370	0.71%	23589	-0.23%
Scattered coincidences	370116	0.10%	369099	0.27%	369313	0.22%
Total coincidences	706377		706892	-0.07%	707995	-0.23%
global scatter fraction			0.54		0.54	
Measured O-15 life-time	121.85	0.07%	122.01	-0.13%	122.73	-0.72%
Nominal O-15 life-time	122.4		122.24	0.13%	122.24	0.00%
difference	0.32%		0.19%		0.40%	

3.3.3 Validation of GATE against phantom studies

To assess the validity of the computer simulations with a phantom, the IEC Body Phantom was used to acquire physical PET data and then compared to the equivalent simulated PET data. It was necessary to create a voxelised version of the phantom that would distinguish between the activity inside the spheres and the activity surrounding the spheres, or background. These results are presented together with the results of the assessment of partial volume effect in 3.3.4.1.

3.3.4 Determination of the Parameters influencing SUV calculation

To assess the influences of various parameters on the calculations of the SUVs and whether the GATE simulations of the phantom provided an accurate reflection of the scanned phantom, the phantom was scanned on the PET scanner and simulated using various concentrations of sphere-to-background ratios. On average a set of simulations took 54 hours to complete when splitting the simulation over 400 cores and running 200 split-simulations at one time. Reconstruction of the datasets took on average 14.5 hours to complete all reconstructions for each experimental set-up. The parameters will be discussed forthwith.

3.3.4.1 Comparison of SUV_{max} and SUV_{mean} for different sizes of sphere

In this section, the data from the phantom that were obtained by means of physical scans and simulations are presented. The images from the data of the phantom using a 10:1 sphere-to-background ratio acquired with the PET scanner can be seen in Figure 3-14 (scanned in 2D mode) and Figure 3-15 (scanned using 3D mode).

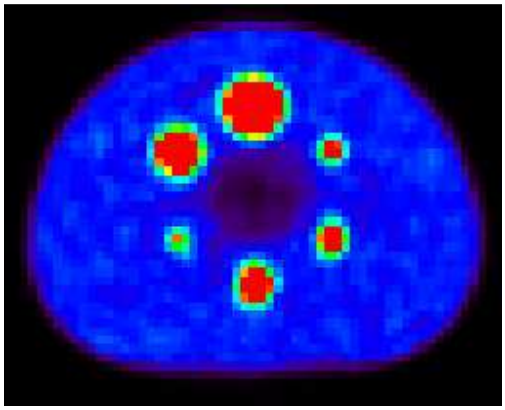

Figure 3-14: Transaxial view of a reconstructed PET scan of the IEC phantom scanned using 2D mode and 10:1 sphere-to-background ratio

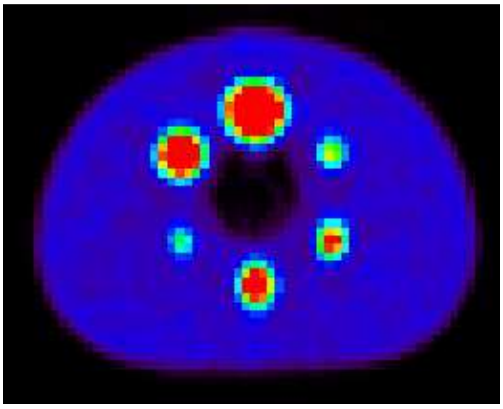

Figure 3-15: Transaxial view of a reconstructed PET scan of the IEC phantom scanned using 3D mode and 10:1 sphere-to-background ratio

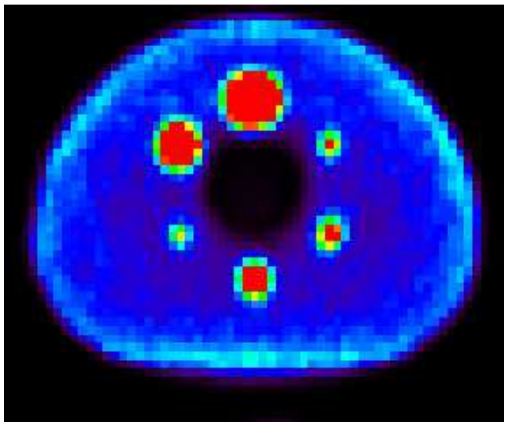

Figure 3-16: Simulated image of IEC phantom scanned using 2D mode and 10:1 sphere-to-background ratio

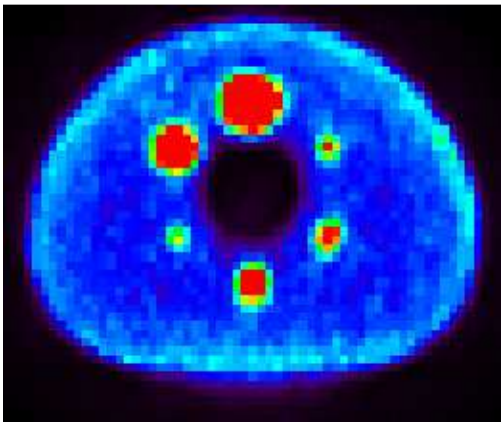

Figure 3-17: Simulated image of IEC phantom scanned using 3D mode and 10:1 sphere-to-background ratio

Image intensity was normalised to an SUV value of 5.5 which represents the SUV_{mean} for the largest sphere in the 10:1 set-up. The same intensity value was used for subsequent images to enable comparison among the images for the other sphere-to-background ratios. The corresponding images from the simulated data are shown in Figure 3-16 (representing 2D mode) and Figure 3-17 (representing 3D mode).

In Figure 3-18, the results of the SUV_{max} from a 10:1 sphere-to-background configuration are displayed. The simulated data (SIM) consists only of the true coincidences and the scanned data (PET) are the coincidences automatically corrected for scattered and random events by the scanner software, therefore supposed to be true coincidences as well. As is evident from Figure 3-18, the data recovered from the three largest spheres have less variation among them than the data acquired from the smallest three spheres. This trend is expected from the partial volume effect. It is noted that the SUVs obtained from the respective 2D and 3D data simulations run concurrently.

The logarithmic fit was applied on the data and is represented by the dotted lines. The respective equations and correlation coefficients are shown on the graphs. The fit to the simulated datasets showed better correlation than that of the scanned data as evidenced by the R^2 values.

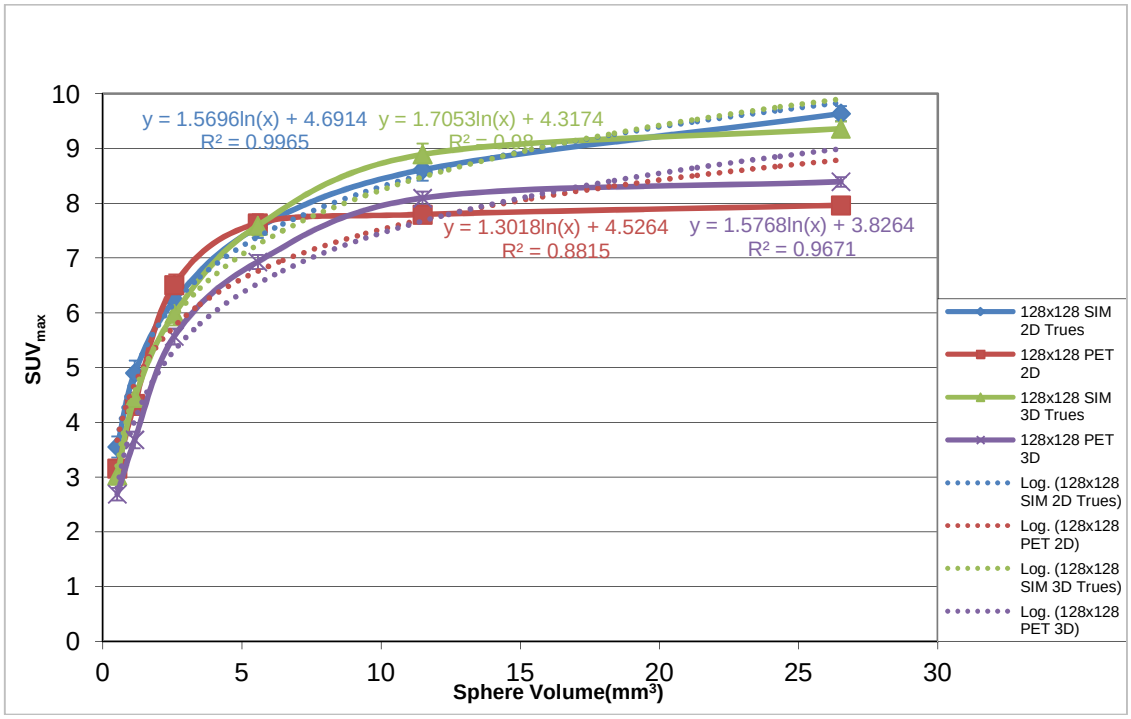

Figure 3-18: SUV_{max} of spheres in IEC Body Phantom (10:1 sphere-to-background ratio) - Comparison of simulated data (SIM) to scanned data (PET) in 2D and 3D modes

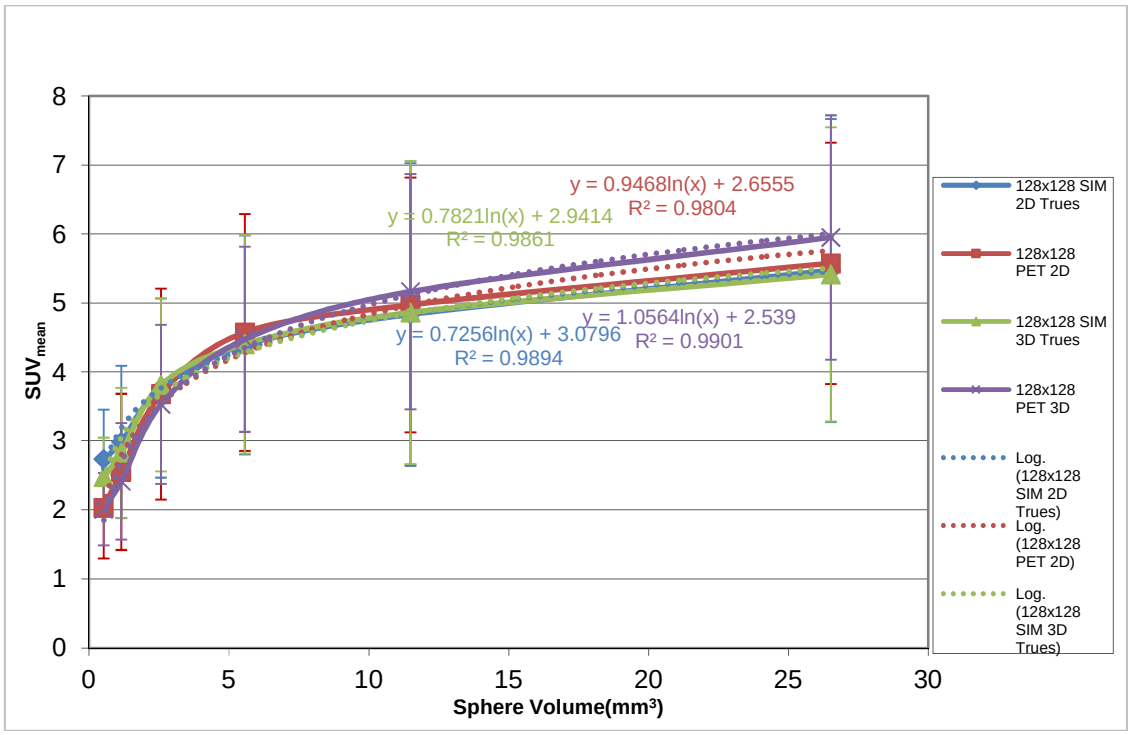

Figure 3-19: SUV_{mean} of spheres in IEC Body Phantom (10:1 sphere-to-background ratio) - Comparison of simulated data (SIM) to scanned data (PET) in 2D and 3D modes

The statistical tests were performed on the raw data points as well as on the fitted data points and the SIM data and PET data did not differ statistically significantly. The test results are given Table 3-6.

Table 3-6: Comparison of SUV_{max} and SUV_{mean} results for the simulated and PET scanned results for different sphere– to-background contrast levels (10:1, 5:1 and 2:1). Simulations and PET scans were performed in 2D and 3D mode. F-test and t-test results are given.

Sphere-to-Background Contrast	Data set	F test: P (F<=f)	t-test (P (T <=t)	Reject H_0? yes / No
10:1	SUV_{max} – 2D	0.39 > 0.05	0.34 > 0.05	No
	SUV_{max} – 3D	0.44 > 0.05	0.32 > 0.05	No
	SUV_{mean} – 2D	0.29 > 0.05	0.43 > 0.05	No
	SUV_{mean} –3D	0.27 > 0.05	0.48 > 0.05	No
5:1	SUV_{max} – 2D	0.43 > 0.05	0.42 > 0.05	No
	SUV_{max} – 3D	0.26 > 0.05	0.22 > 0.05	No
	SUV_{mean} – 2D	0.28 > 0.05	0.43 > 0.05	No
	SUV_{mean} –3D	0.42 > 0.05	0.46 > 0.05	No
2:1	SUV_{max} – 2D	0.12 > 0.05	0.16 > 0.05	No
	SUV_{max} – 3D	0.12 > 0.05	0.14 > 0.05	No
	SUV_{mean} – 2D	0.024 < 0.05	0.37 > 0.05	No
	SUV_{mean} –3D	0.020 < 0.05	0.40 > 0.05	No

In Figure 3-19, the results of the SUV_{mean} from a 10:1 sphere-to-background configuration are presented. The graphs follow a similar trend as was found with SUV_{max}.

The logarithmic fit to the simulated datasets showed good correlation to all data points as is indicated by the correlation coefficients that are shown on the graphs. There is no significant difference between 2D PET and the 2D SIM or 3D SIM data. The data from PET and SIM did not to differ significantly. It is also evident from the overlap in the error bars on the graphs that the data did not differ significantly.

The images from the data of the phantom using a 5:1 sphere-to-background ratio obtained using the PET scanner can be seen in Figure 3-20 (scanned in 2D mode) and in Figure 3-21 (acquired in 3D mode). The corresponding images from the simulated scans are shown in Figure 3-22 (representing 2D mode) and Figure 3-23 (indicating 3D mode). In Figure 3-24, the results of the SUV_{max} for the 5:1 sphere-to-background configuration are shown. The simulated data (SIM) represents the true coincidences extracted from the simulations and the scanned data (PET) are the true corrected coincidences from the scanner.

As was found in the 10:1 scenario, the data follow a similar trend as in Figure 3-18. The logarithmic fitted data show good correlation as is indicated by the coefficients that are shown on the graphs. The statistical tests were performed on the raw data points as well as on the fitted data points and the data were found not to be statistically different.

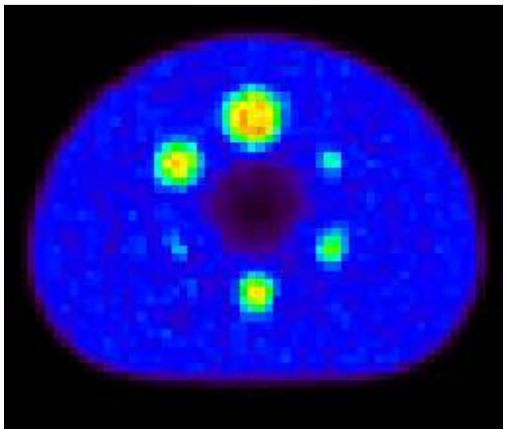

Figure 3-20: Transaxial view of a reconstructed PET scan of the IEC phantom scanned using 2D mode and 5:1 sphere-to-background ratio

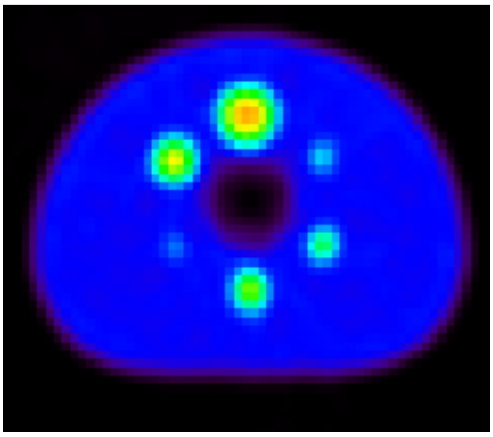

Figure 3-21: Transaxial view of a reconstructed PET scan of the IEC phantom scanned using 3D mode and 5:1 sphere-to-background ratio

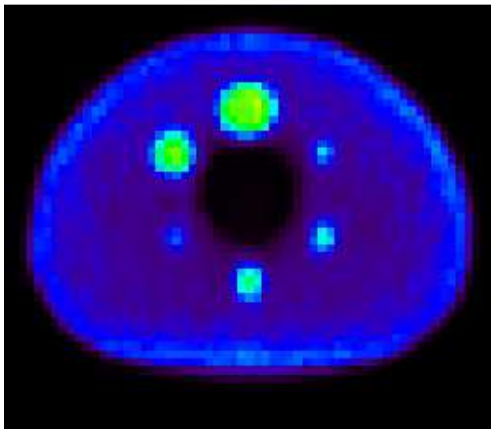

Figure 3-22: Transaxial view of a reconstructed simulated image of IEC phantom scanned using 2D mode and 5:1 sphere-to-background ratio

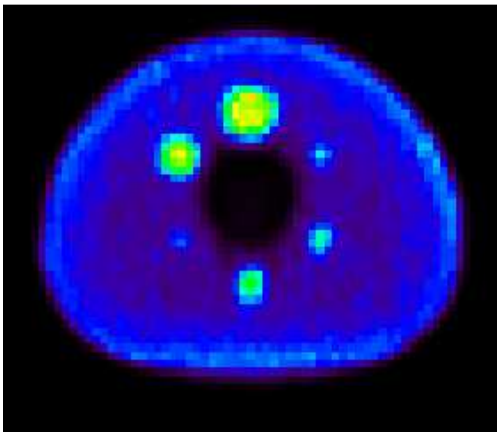

Figure 3-23: Transaxial view of a reconstructed simulated image of IEC phantom scanned using 3D mode and 5:1 sphere-to-background ratio

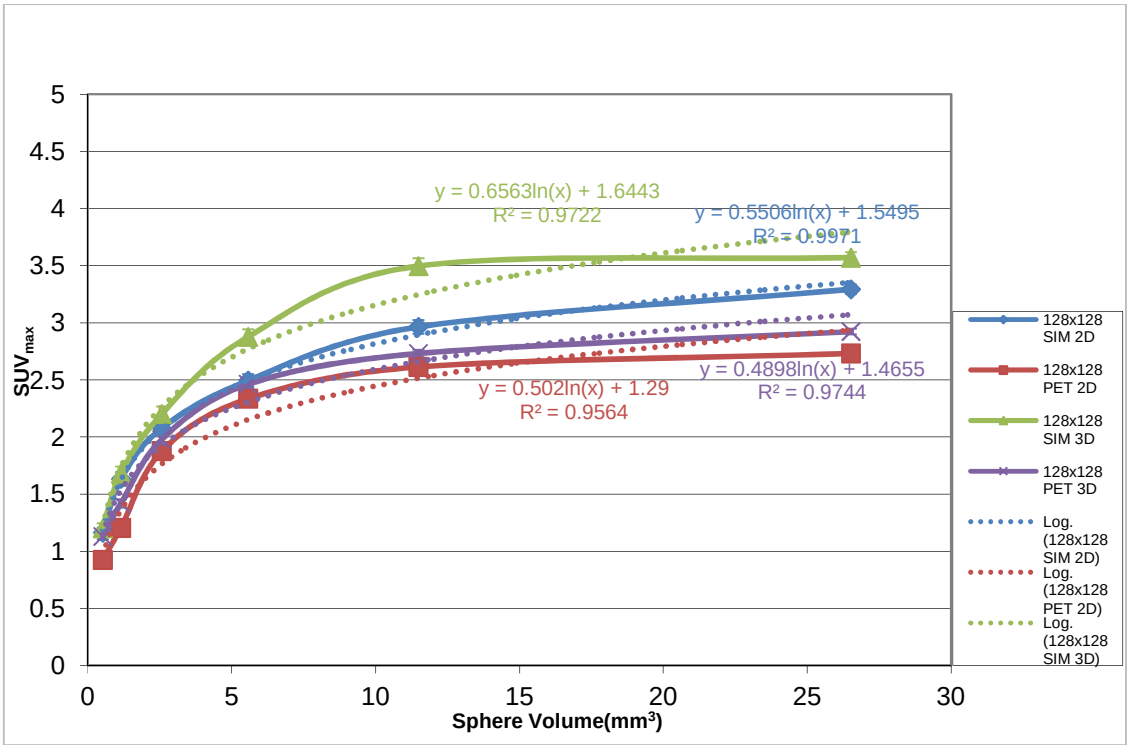

Figure 3-24: SUV_{max} of spheres in IEC Body Phantom (5:1 sphere-to-background ratio) - Comparison of simulated data (SIM) to scanned data (PET) in 2D and 3D modes

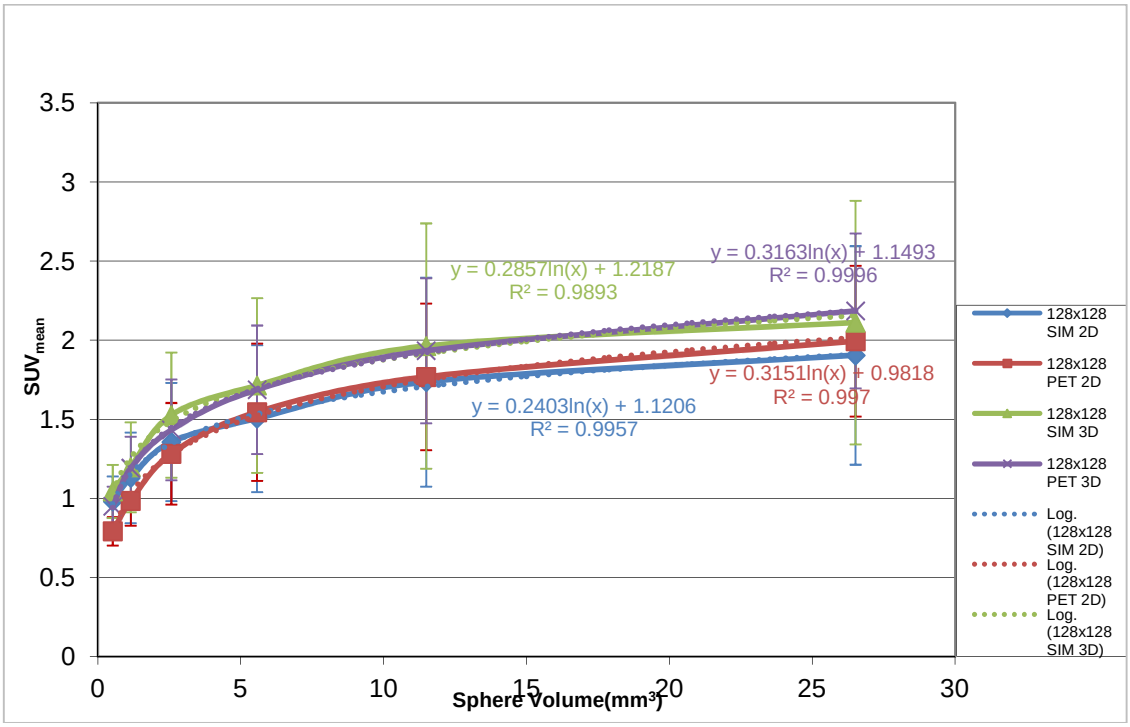

Figure 3-25: SUV_{mean} of spheres in IEC Body Phantom (5:1 sphere-to-background ratio) - Comparison of simulated data (SIM) to scanned data (PET) in 2D and 3D modes

The corresponding results of SUV_{mean} for the 5:1 ratio are found in Figure 3-25. The logarithmic fitted data corresponds well with the SUV_{mean} data points as is visually evident and as well as indicated by the correlation coefficients. From the error bars representing one standard deviation as well as from the statistics, the data do not appear to be significantly different.

The images from the data of the phantom using a 2:1 sphere-to-background ratio obtained with the PET scanner can be seen in Figure 3-26 (scanned in 2D mode) and in Figure 3-27 (acquired in 3D mode). The corresponding images from the simulated scans are shown in Figure 3-28 (representing 2D mode) and Figure 3-29 (indicating 3D mode).

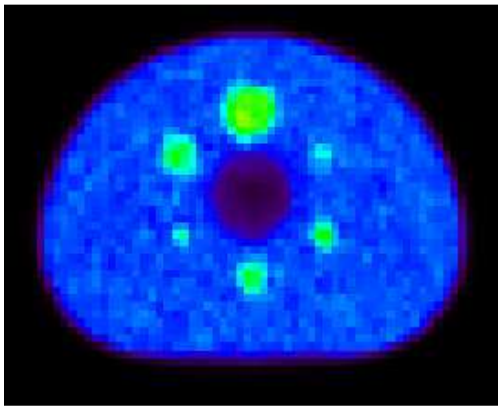

Figure 3-26: Transaxial view of a reconstructed PET scan of the IEC phantom scanned using 2D mode and 2:1 sphere-to-background ratio

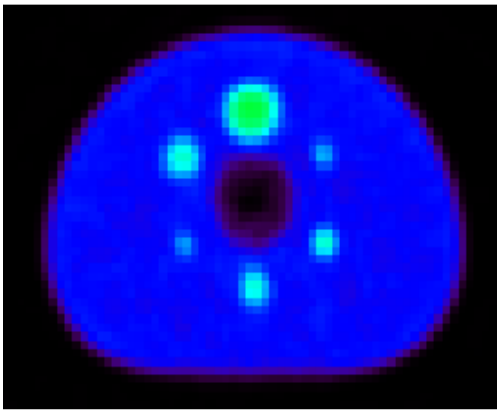

Figure 3-27: Transaxial view of a reconstructed PET scan of the IEC phantom scanned using 3D mode and 2:1 sphere-to-background ratio

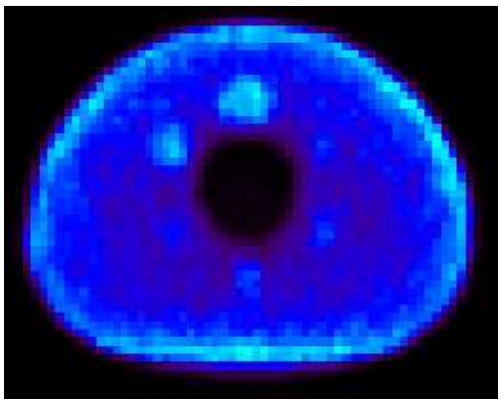

Figure 3-28: Transaxial view of a reconstructed simulated image of IEC phantom scanned using 2D mode and 2:1 sphere-to-background ratio

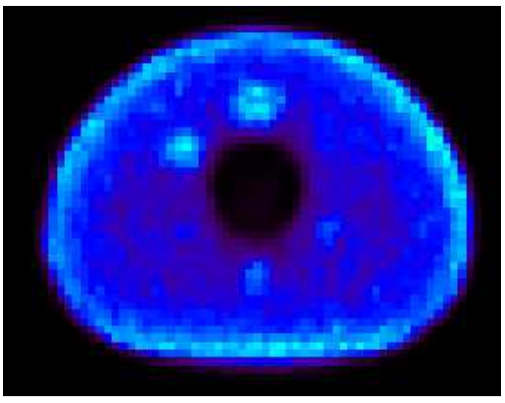

Figure 3-29: Transaxial view of a reconstructed simulated image of IEC phantom scanned using 3D mode and 2:1 sphere-to-background ratio

In Figure 3-30, the results of the SUV_{max} for the 2:1 sphere-to-background configuration are shown. As were found in the 10:1 and the 5:1 scenarios, the data follow a similar trend as in Figure 3-18 and in Figure 3-24. It is observed that the simulated data for 5.57 ml sphere as well as for the two smallest spheres deviate much from the scanned data. When these graphs are analysed by taking into account the images shown in Figure 3-26 to Figure 3-29, it is then clear that the spheres are not clearly visible due to the low contrast. These smaller spheres are susceptible to noise and this may have a large influence on the statistics of these values.

Once again it is noted that the logarithmic fit to the SUVs of the simulated data is not as good. The statistical tests indicated that no statistically significant differences could be found.

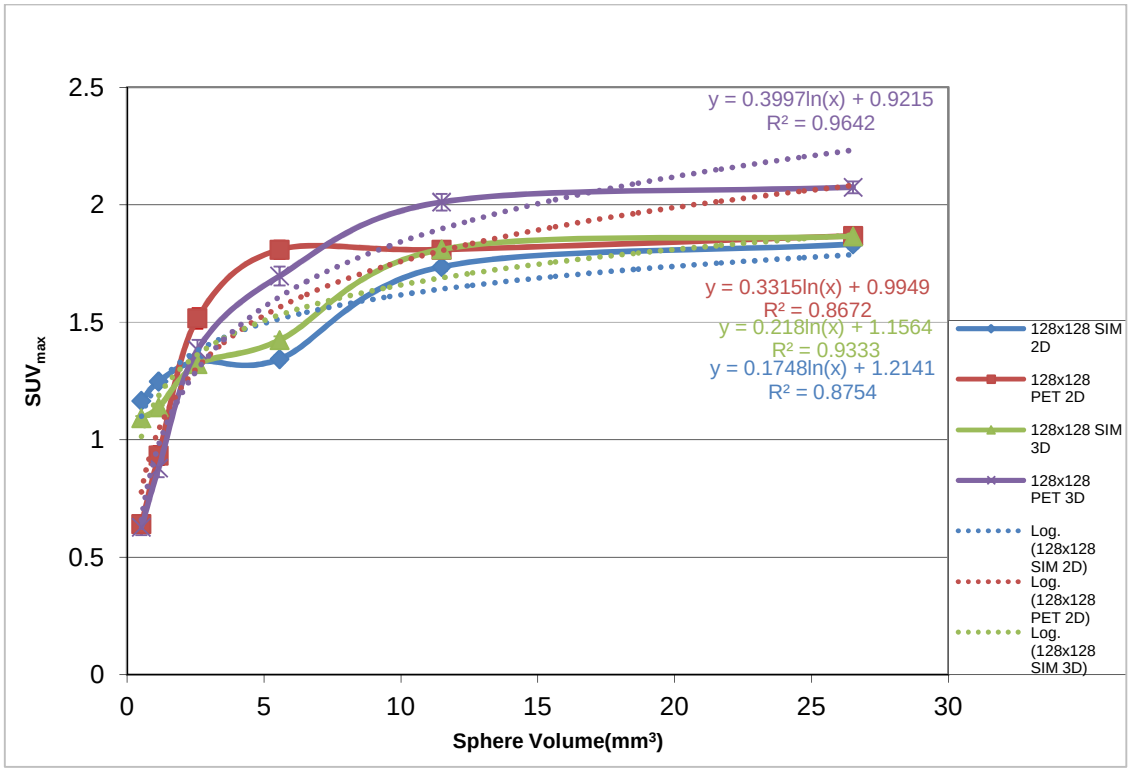

Figure 3-30: SUV_{max} of spheres in IEC Body Phantom (2:1 sphere-to-background ratio) - Comparison of simulated data (SIM) to scanned data (PET) in 2D and 3D modes

The corresponding results of SUV_{mean} for the 2:1 ratio are found in Figure 3-31. The logarithmically fitted data corresponds well with the SUV_{mean} values of the scanned data, but not so well for the simulated data as is visually evident and as are indicated by the correlation coefficients. The data were not significantly different. The F-tests indicated that the variances were different in these analyses and thus a t-test for Unequal Variances was used. Based upon that t-test it was found that the means were the same ($p > 0.05$) and therefore the H_0 could not be rejected. The individual values for the two smallest spheres of the simulated data are however statistically different from the respective data obtained from the scanner. This is once again due to the poor contrast and corresponding increased susceptibility to noise in the image.

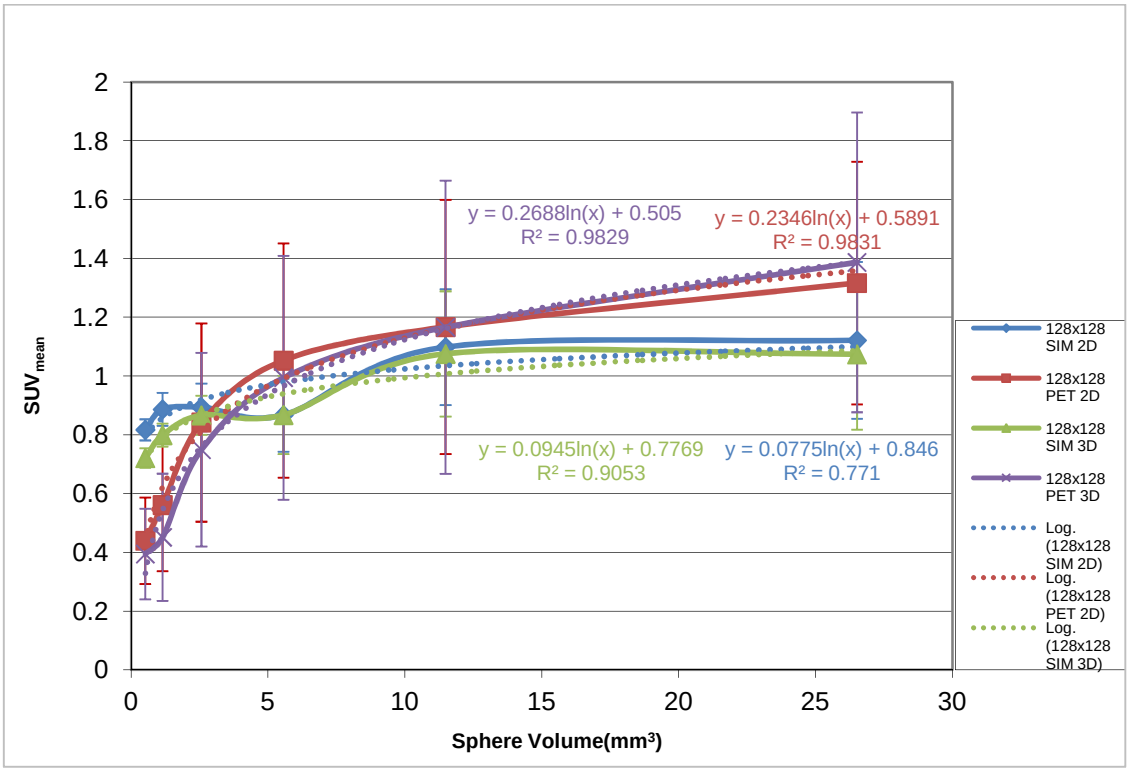

Figure 3-31: SUV_{mean} of spheres in IEC Body Phantom (2:1 sphere-to-background ratio) - Comparison of simulated data (SIM) to scanned data (PET) in 2D and 3D modes

3.3.4.2 Comparison of different matrix sizes to assess sampling size

In this section the results are presented that were obtained from simulation scans using the IEC Body Phantom with a sphere-to-background ratio of 10:1. The matrix sizes were varied to assess the influence of the matrix size on the determination of SUV_{max} and SUV_{mean}.

In Figure 3-32, the image displays the data obtained using a 64×64 matrix in 2D mode and the corresponding 3D mode data is shown in Figure 3-33. It is observed that the voxel sizes are large and the two smallest spheres are barely visible.

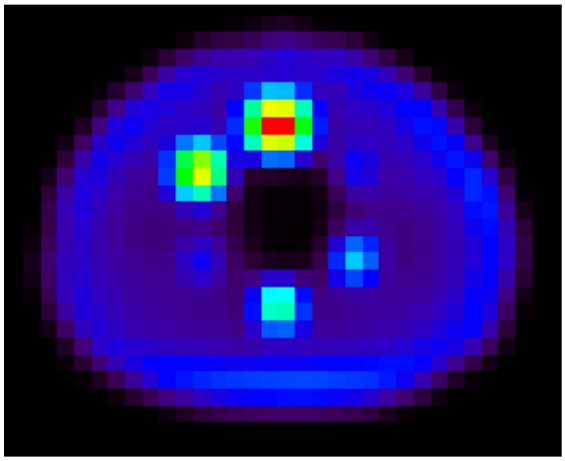

Figure 3-32: Transaxial view of a reconstructed simulated image of the IEC phantom using 2D mode, a 10:1 sphere-to-background ratio and 64×64 matrix

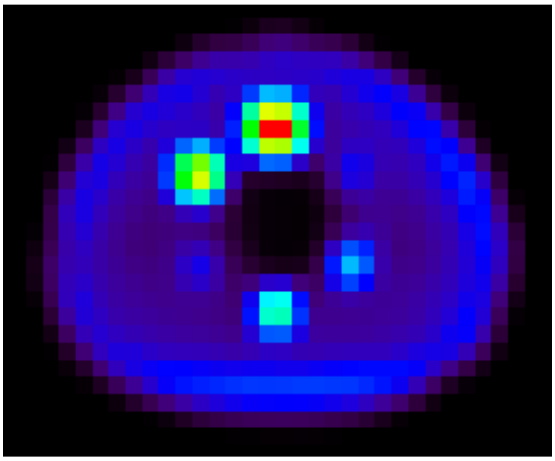

Figure 3-33: Transaxial view of a reconstructed simulated image of the IEC phantom using 3D mode, a 10:1 sphere-to-background ratio and 64×64 matrix

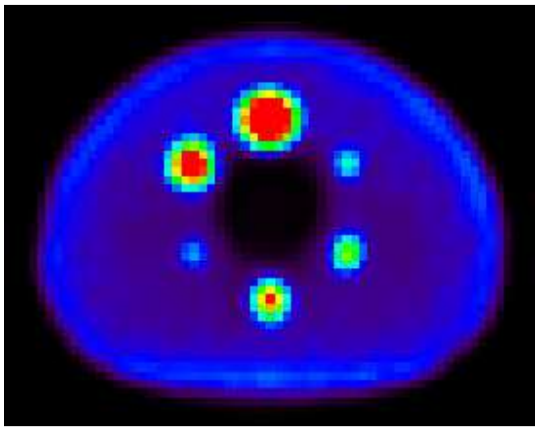

Figure 3-34: Transaxial view of a reconstructed simulated image of the IEC phantom using 2D mode, a 10:1 sphere-to-background ratio and 128×128 matrix

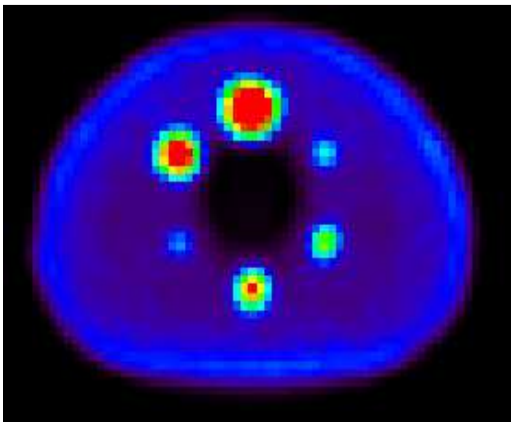

Figure 3-35: Transaxial view of a reconstructed simulated image of the IEC phantom using 3D mode, a 10:1 sphere-to-background ratio and 128×128 matrix

In Figure 3-34, the image portrays the same data, but simulated using a 128×128 matrix in 2D mode with the equivalent image in Figure 3-35 representing the data in 3D mode. The two smallest spheres are more distinct than when comparing them to the 64×64 matrix.

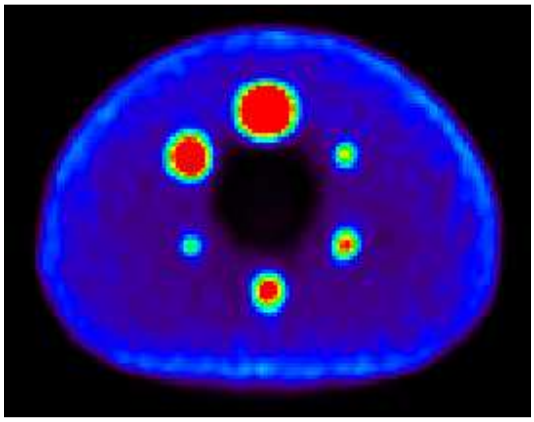

Figure 3-36: Transaxial view of a reconstructed simulated image of the IEC phantom using 2D mode, a 10:1 sphere-to-background ratio and 256×256 matrix

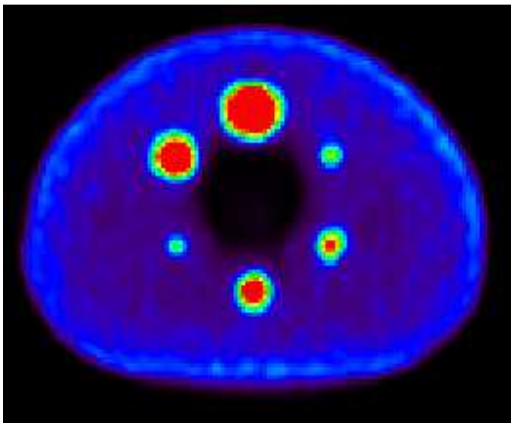

Figure 3-37: Transaxial view of a reconstructed simulated image of the IEC phantom using 3D mode, a 10:1 sphere-to-background ratio and 256×256 matrix

Figure 3-36 represents the data obtained by using a 256×256 matrix in 2D mode whilst Figure 3-37 displays the same data from a 3D acquisition. The edges of the spheres are less prominent as the resolution increases reducing the influence from the background into the sphere VoI.

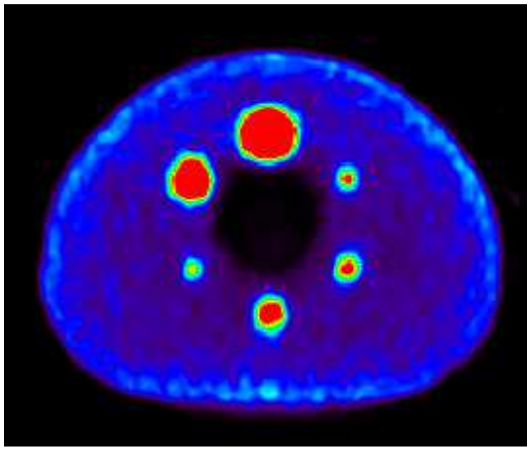

Figure 3-38: Transaxial view of a reconstructed simulated image of the IEC phantom using 2D mode, a 10:1 sphere-to-background ratio and 512×512 matrix

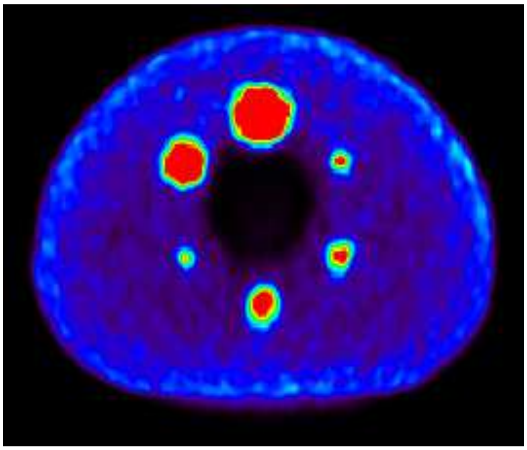

Figure 3-39: Transaxial view of a reconstructed simulated image of the IEC phantom using 3D mode, a 10:1 sphere-to-background ratio and 512×512 matrix

Figure 3-38 and Figure 3-39 represents the data that was acquired by using a 512×512 matrix in 2D and 3D respectively. The edges of the spheres appear smooth and the

intensities of the voxel values have increased when compared to the other matrix size data. The voxel values appear more homogeneous throughout the voxel volume.

The graphs that are depicted in Figure 3-40 represent the influence of the matrix size on SUV_{max} for the phantom scanned in 2D mode with a concentration ratio of 10:1 sphere-to-background. It is noted that SUV_{max} has increased with increase in sphere volume as well as with increase in matrix size. The corresponding graphs for the 3D acquisition are found in Figure 3-41. It is observed that the SUV_{max} for the largest sphere drops when the 256×256 and 512×512 matrices are used. Because the SUV_{max} is a single value determined in the VoI, it has occurred that the values of the maximum SUV are not absolute when using increased matrix sizes for finer sampling. It was more noticeable when performing 3D imaging.

Figure 3-42 and Figure 3-43 represent the SUV_{mean} data obtained when varying the matrix size for 2D- and 3D modes respectively. The logarithmic fit that was performed on each set of data showed good correlation to the original data. It is noted that the increase in SUV_{mean} values between 64×64 matrix and the 128×128 matrix is larger than that between 128×128 and 256×256 matrices. The increase is less when comparing the 256×256 to 512×512 matrices. The statistical tests were used to analyse the statistical differences in the datasets and the statistical results are presented in Table 3-7.

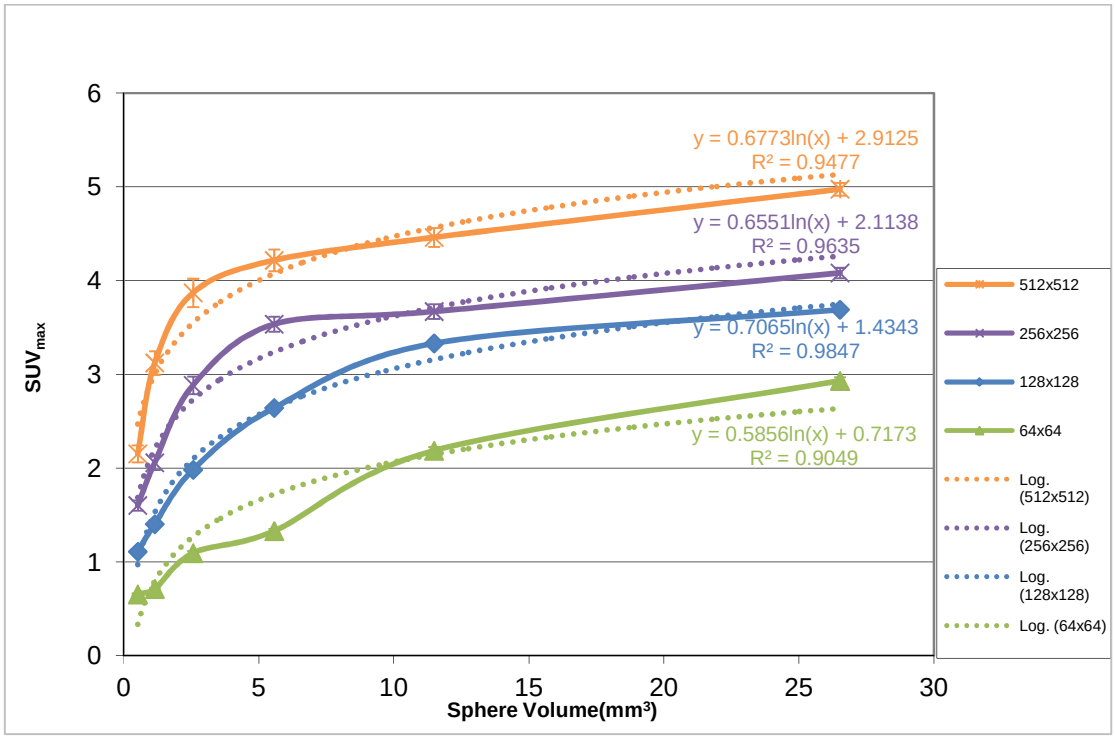

Figure 3-40: SUV_{max} comparison for 10:1 sphere-to-background ratio (2D mode) – Influence of image sampling using different matrix sizes

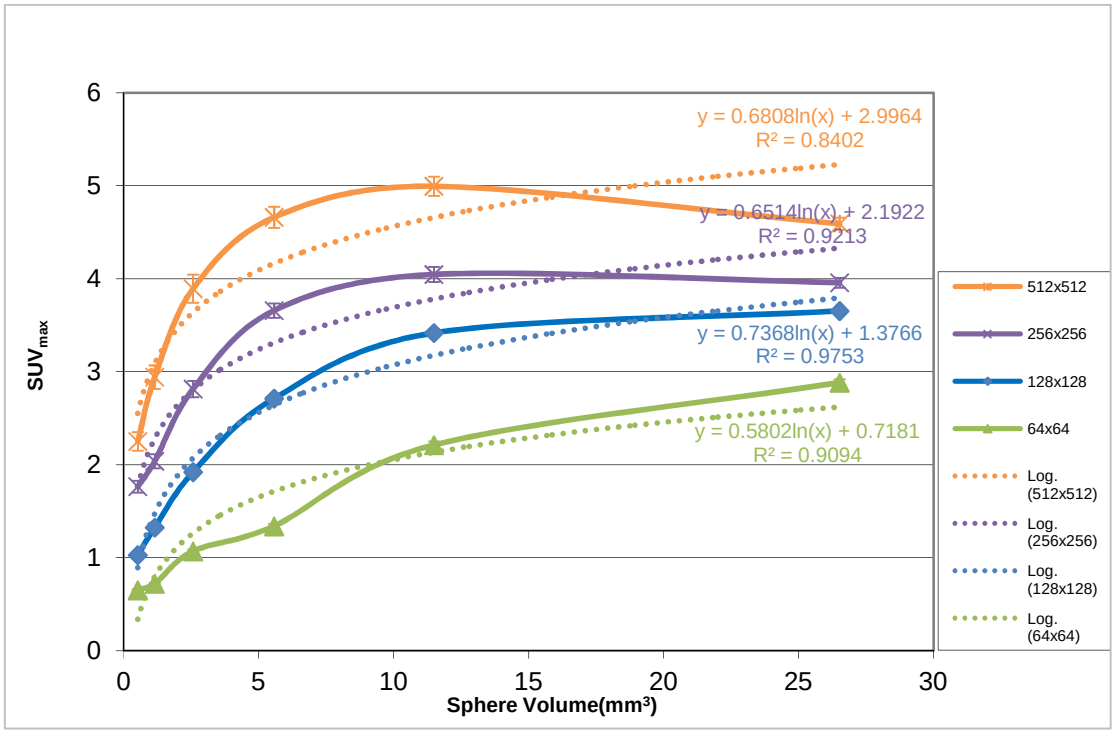

Figure 3-41: SUV_{max} comparison for 10:1 sphere-to-background ratio (3D mode) – Influence of image sampling using different matrix sizes

Table 3-7: Comparison of SUV_{mean} results for the simulated and PET scanned results for different matrix formats levels). Simulations and PET scans were performed in 2D and 3D mode. F-test and t-test results are given.

Matrix Comparison		Data set	F-test: P (F<=f)	t-test (P (T <=t)	Reject H_0? Yes / No
64×64	128×128	SUV_{mean} (2D)	0.38 > 0.05	0.04 < 0.05	Yes
		SUV_{mean} (3D)	0.36 > 0.05	0.04 < 0.05	Yes
128×128	256×256	SUV_{mean} (2D)	0.38 > 0.05	0.12 > 0.05	No
		SUV_{mean} (3D)	0.32 > 0.05	0.11 > 0.05	No
128×128	512×512	SUV_{mean} (2D)	0.19 > 0.05	0.02 < 0.05	Yes
		SUV_{mean} (3D)	0.36 > 0.05	0.04 < 0.05	Yes
256×256	512×512	SUV_{mean} (2D)	0.29 > 0.05	0.13 > 0.05	No
		SUV_{mean} (3D)	0.33 > 0.05	0.15 > 0.05	No

The graphs are a proper representation of what was observed in the images that are displayed in Figure 3-32 to Figure 3-39. The poor image quality and the SUVs obtained by using the 64×64 matrix make it impractical to use this sampling size for quantification of the object sizes. Although there was a small difference between the data of the 256×256 matrix and the 512×512 matrix it does not warrant choosing the 512×512 matrix above the 256×256 matrix since the pixel sizes would be less than one third of the spatial resolution of the PET/CT system causing no real improvement in visual resolution of the images (Saha, 2005). Ideally the 256×256 matrix should then be used since it should optimally provide the best image resolution and accuracy in SUV.

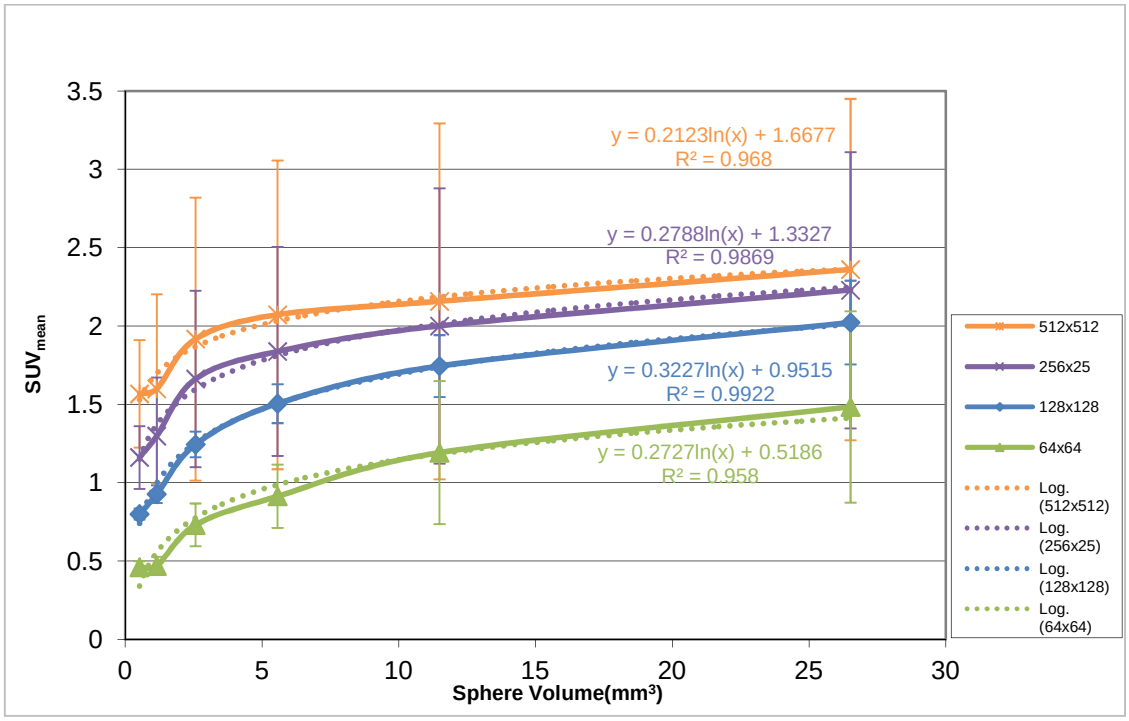

Figure 3-42: SUV_{mean} comparison for 10:1 sphere-to-background ratio (2D mode) – Influence of image sampling using different matrix sizes

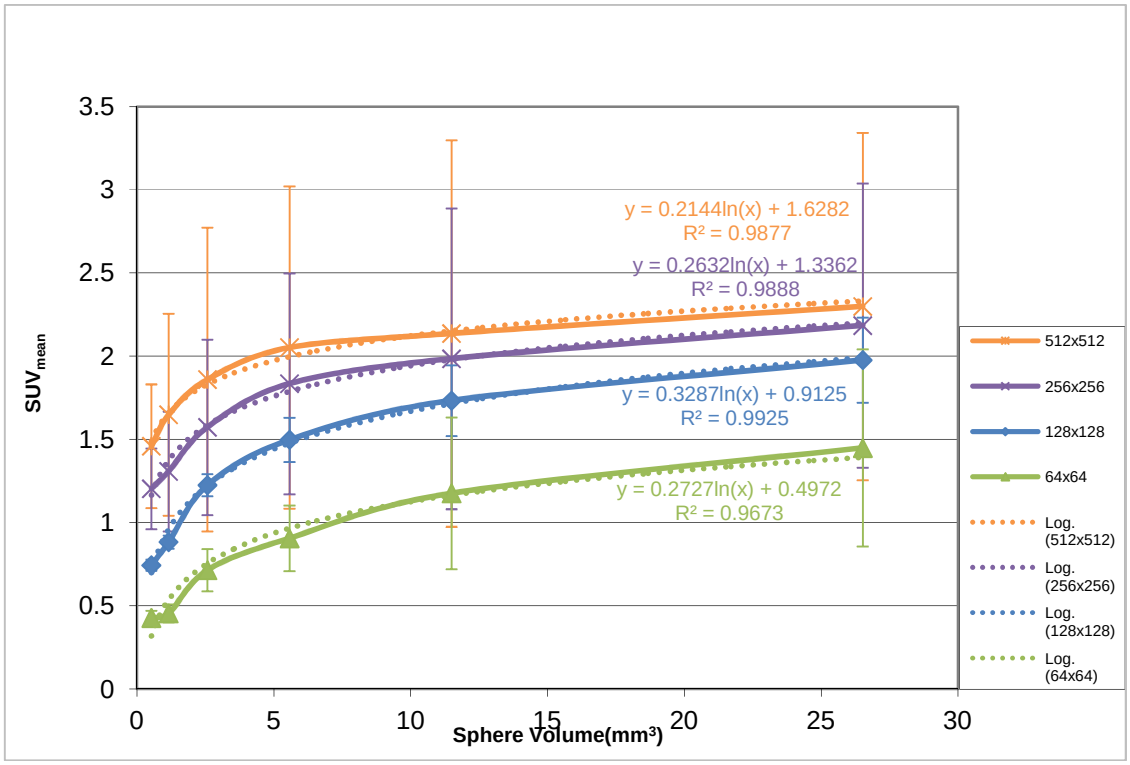

Figure 3-43: SUV_{mean} comparison for 10:1 sphere-to-background ratio (3D mode) – Influence of image sampling using different matrix sizes

3.3.5 Assessment of the Contribution of True-, Scattered and Random coincidences

This section deals with the analyses of how true-, scatter- and random coincidences contribute to the final image. The first part deals with the analyses that were performed on the phantom data comprising of the different sphere-to-background concentrations. The next part of the section describes the influence of the different components of coincidences when a single concentration ratio is used while scanning with various matrix sizes. The ROOT files from the simulations were inspected and the true, scattered and random coincidences were extracted and reconstructed separately.

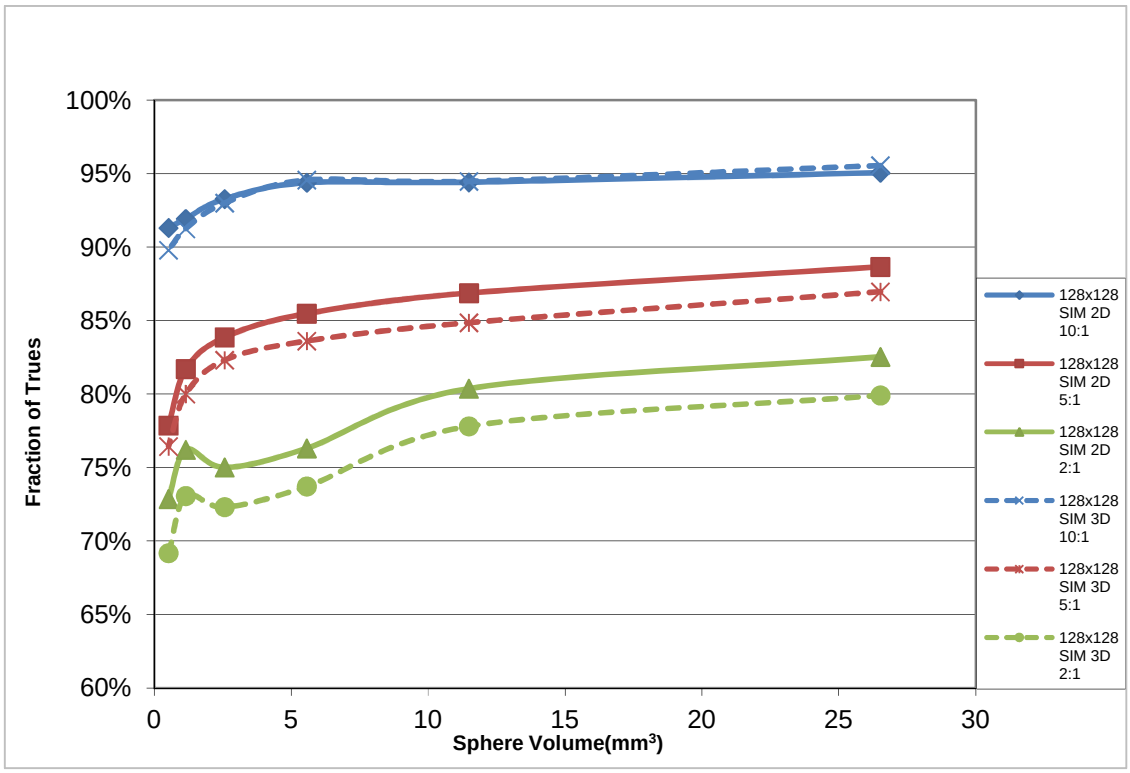

Figure 3-44: Comparison of the Trues Fraction for 10:1, 5:1 and 2:1 sphere-to-background ratios

In Figure 3-44 the contributions of the trues to the total image can be seen for the 10:1, 5:1 and 2:1 sphere-to-background ratios acquired in 2D and 3D modes. It is observed that the maximum contribution of the trues was at 95.55% (3D) at the largest sphere for the 10:1 ratio, while at the 5:1 and 2:1 ratios for the same sphere size it was at 88.66% and 82.54% respectively in 2D mode and 86.96% and 79.91% in 3D mode. The

minimum fraction of trues (69.18%) was found for the smallest sphere for a 2:1 ratio in 3D mode.

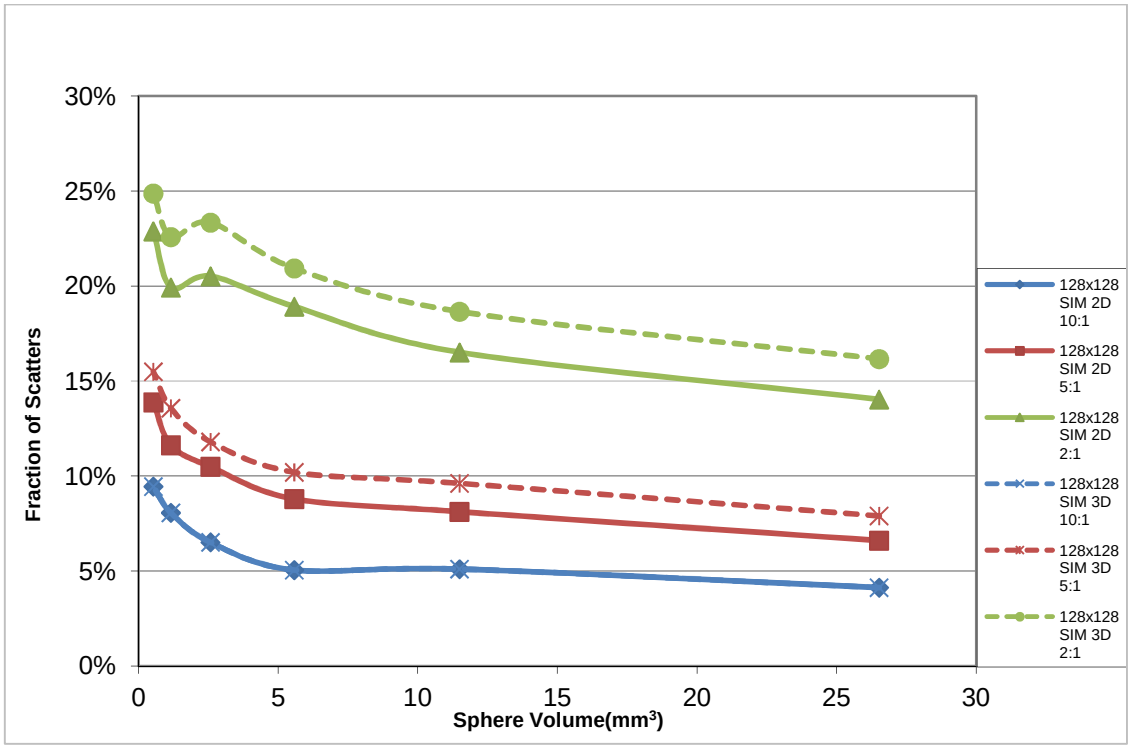

Figure 3-45: Comparison of the Scatters Fraction for 10:1, 5:1 and 2:1 sphere-to-background ratios

The graphs displayed in Figure 3-45 represent the scatters fraction to the total image for the 10:1, 5:1 and 2:1 ratios in 2D and 3D modes. It is observed that the graphs follow an opposite trend to that of the trues fractions.

The maximum amount of scatter was found to be 24.87% at the smallest sphere for the 2:1 ratio scanned in 2D mode. The minimum was found to be 4.13% for the largest sphere filled with a 10:1 concentration ratio.

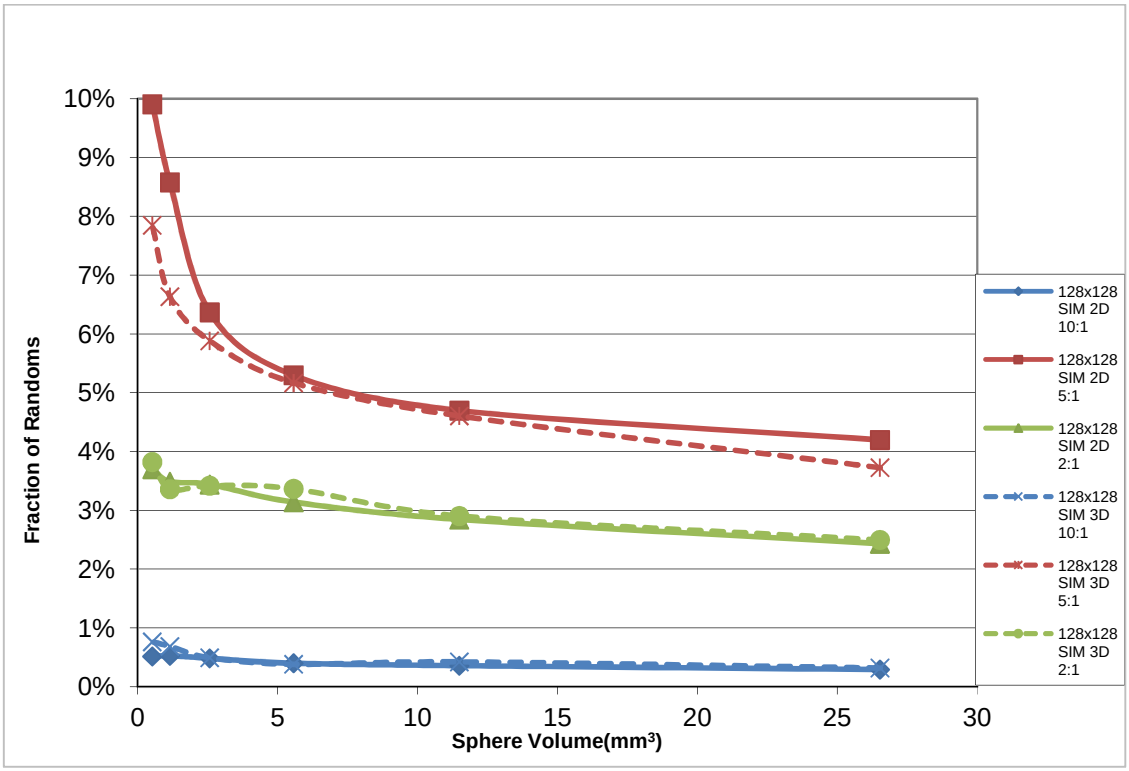

Figure 3-46: Comparison of the Randoms Fraction for 10:1, 5:1 and 2:1 sphere-to-background ratios

In Figure 3-46, the graphs represent the fraction of randoms of the total images for the 10:1, 5:1 and 2:1 sphere-to-background ratios, acquired in 2D and 3D modes. It is once again observed that the randoms follow an opposite trend than that of the trues. The maximum amount of the randoms fraction was found to be 9.91% at the smallest sphere for the 5:1 ratio scanned in 2D mode. The minimum was found to be 0.29% for the smallest sphere filled with a 10:1 concentration ratio and scanned in 2D mode. It would seem that the 5:1 random fraction was more than the same fractions determined for 10:1 and 2:1. It is possible that a process is present where the random fraction peaked at the 5:1 ratio and further investigation is warranted to determine whether there exists a trend when a 3:1 and 7:1 ratio is used.

In Figure 3-47, the contributions of the trues to the total image can be seen for the 10:1, sphere-to-background ratios acquired in 2D and 3D modes with matrix sizes 64×64, 128×128, 256×256 and 512×512.

It is observed that the maximum contribution of the trues 93.56% at the second smallest sphere at a 512×512 matrix scanned in 3D. The minimum trues fraction was found at 68.83% at the smallest sphere scanned using a 64×64 matrix in 3D mode.

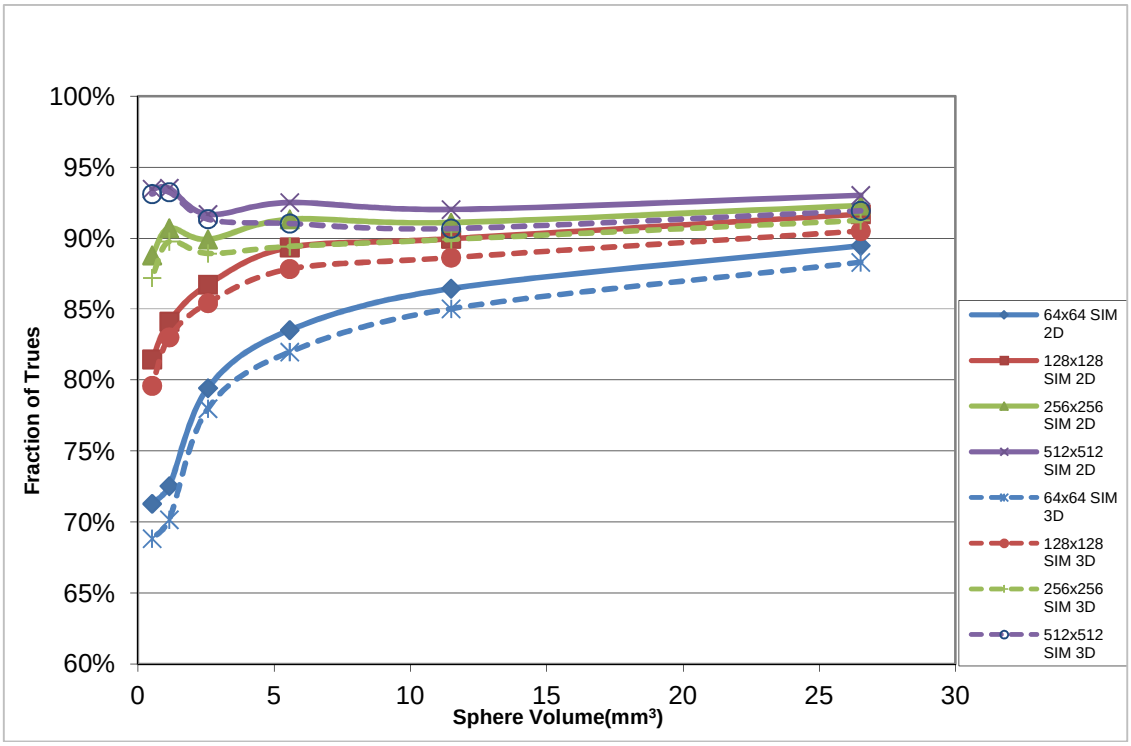

Figure 3-47: Comparison of the Trues Fraction for 10:1 sphere-to-background ratio for variation in matrix size

The graphs displayed in Figure 3-48 represent the scatters fraction to the total image for the various matrix sizes in 2D and 3D modes. It is observed that the graphs follow an opposite trend than that of the trues fractions as before. The maximum amount of scatters was found to be 18.84% at the smallest sphere in the 64×64 matrix scanned in 3D mode. The minimum was found to be 4.04% for the largest sphere acquired in 512×512 matrix size.

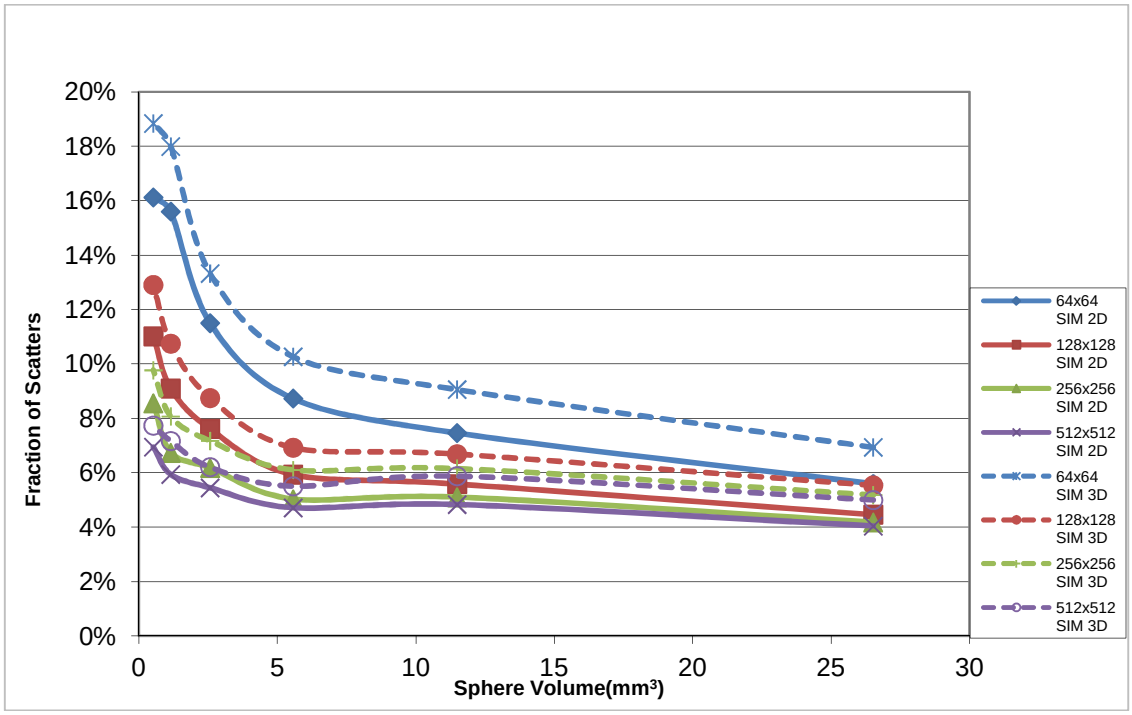

Figure 3-48: Comparison of the Scatters Fraction for 10:1 sphere-to-background ratio for variation in matrix size

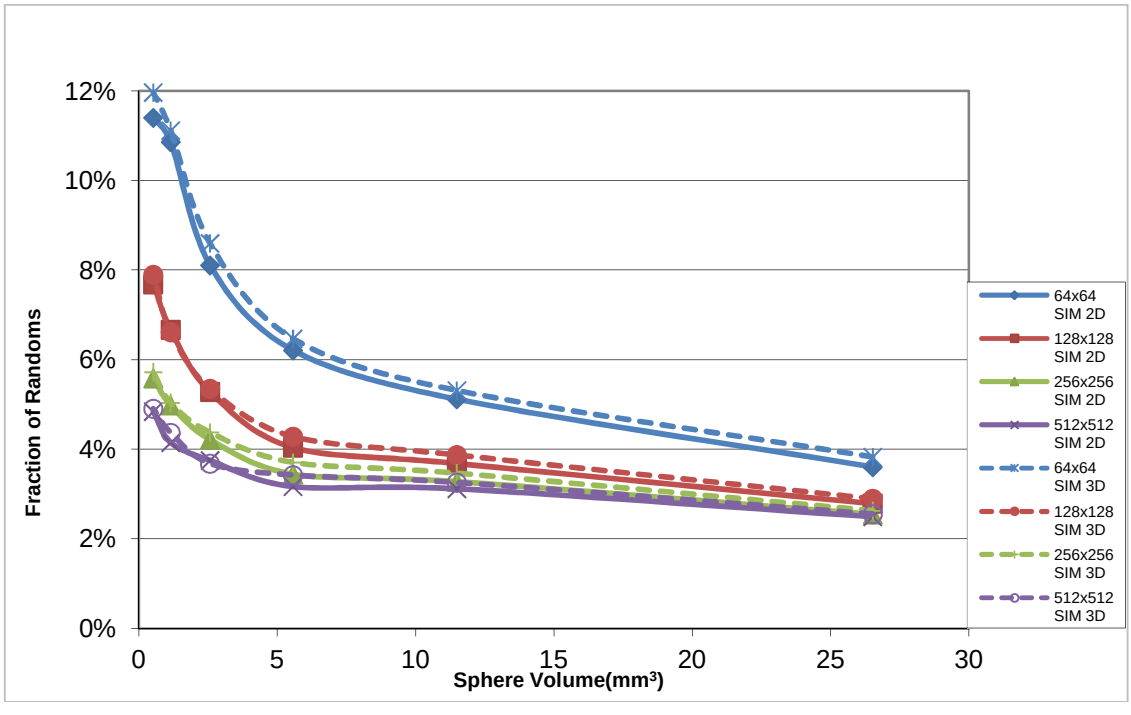

Figure 3-49: Comparison of the Randoms Fraction for 10:1 sphere-to-background ratio for variation in matrix size

In Figure 3-49, the graphs represent the fraction of randoms of the total images for the for the matrix sizes 64×64 up to 512×512 acquired in 2D and 3D modes. It is once again observed that the randoms follow an inverse trend than that of the trues. The maximum amount of the randoms fraction was found to be 11.97% at the smallest sphere scanned in 3D mode with 64×64 matrix. The minimum was found to be 2.50% for the largest sphere scanned in 2D mode using a 512×512 matrix size.

3.3.6 Assessment of the influence of VoI size on SUV calculation and the contribution of true-, scatter and random coincidences

In this section the results of the influence of the different sizes of VoI is presented for data acquired for 10:1, 5:1 and 2:1 sphere-to-background ratios. Table 3-8 depicts the fractional contributions of trues, scatters and randoms to the total image as was obtained using a 90%VoI_{CT} up to 110%VoI_{CT} for the different sphere sizes scanned in 2D mode for a 10:1 ratio. It is observed that as the VoI size decreases, the relative contribution of trues increases. Conversely, the fraction of scatters and randoms decreases with decrease in VoI size.

The SUV_{mean} variations with change in VoI size for the 10:1 ratio can be found in Table 3-9. The SUV decreases with an increase in VoI size. The same trends are observed for the coincidence fractions for 5:1 ratio (2D) as is presented in Table 3-10 as well as for the corresponding SUV_{mean} (Table 3-11), and for the 2:1 concentration ratio (2D) that can be found in Table 3-12 (coincidence fractions) and Table 3-13 (SUV_{mean}). These trends are also observed for the data obtained in 3D mode.

Table 3-8: %Contribution of Trues, Scatters and Randoms in relation to the Total Coincidences with variation in VoI_{CT} size for 10:1 sphere-to-background ratio in 2D mode

2D				*% VOI $_{CT}$*		
Trues		***90%***	***95%***	***100%***	***105%***	***110%***
Sphere no	Volume (ml)					
1	26.52	95.60%	95.35%	95.06%	94.75%	94.41%
2	11.49	94.96%	94.69%	94.41%	94.09%	93.77%
3	5.57	95.12%	94.78%	94.38%	94.01%	93.56%
4	2.57	93.63%	93.46%	93.28%	93.06%	92.75%
5	1.15	92.45%	92.18%	91.93%	91.63%	91.35%
6	0.52	92.09%	91.59%	91.30%	90.94%	90.52%
Scatters						
Sphere no	Volume (ml)					
1	26.52	3.70%	3.90%	4.13%	4.38%	4.66%
2	11.49	4.63%	4.86%	5.10%	5.38%	5.66%
3	5.57	4.55%	4.78%	5.05%	5.31%	5.62%
4	2.57	6.16%	6.35%	6.51%	6.71%	6.97%
5	1.15	7.67%	7.89%	8.07%	8.27%	8.48%
6	0.52	8.99%	9.27%	9.44%	9.65%	9.90%
Randoms						
Sphere no	Volume (ml)					
1	26.52	0.26%	0.27%	0.29%	0.31%	0.33%
2	11.49	0.32%	0.34%	0.36%	0.38%	0.40%
3	5.57	0.36%	0.38%	0.40%	0.42%	0.44%
4	2.57	0.46%	0.47%	0.48%	0.50%	0.52%
5	1.15	0.49%	0.51%	0.52%	0.54%	0.56%
6	0.52	0.48%	0.50%	0.51%	0.53%	0.54%

Table 3-9: SUV_{mean} determined with a variation of VoI_{CT} size for a 10:1 sphere-to-background ratio in 2D mode

				% VOI $_{CT}$		
2D		***90%***	***95%***	***100%***	***105%***	***110%***
Volume (ml)						
26.52		6.22	5.85	5.47	5.10	4.73
11.49		5.40	5.11	4.83	4.55	4.29
5.57		4.90	4.66	4.39	4.17	3.92
2.57		4.00	3.87	3.77	3.65	3.49
1.15		3.17	3.07	2.99	2.90	2.81
0.52		2.89	2.80	2.74	2.68	2.59

Table 3-10: %Contribution of Trues, Scatters and Randoms in relation to the Total Coincidences with variation in VoI_{CT} size for 5:1 sphere-to-background ratio in 2D mode

2D				*% VOI $_{CT}$*		
Trues		***90%***	***95%***	***100%***	***105%***	***110%***
Sphere no	Volume (ml)					
1	26.52	89.70%	89.21%	88.66%	88.08%	87.45%
2	11.49	87.92%	87.40%	86.87%	86.28%	85.72%
3	5.57	86.81%	86.18%	85.48%	84.84%	84.08%
4	2.57	84.66%	84.22%	83.86%	83.43%	82.87%
5	1.15	82.38%	82.00%	81.70%	81.34%	81.00%
6	0.52	78.62%	78.12%	77.86%	77.53%	77.14%
Scatters						
Sphere no	Volume (ml)					
1	26.52	6.00%	6.28%	6.59%	6.93%	7.30%
2	11.49	7.52%	7.81%	8.11%	8.45%	8.78%
3	5.57	8.13%	8.43%	8.78%	9.10%	9.49%
4	2.57	10.09%	10.30%	10.48%	10.70%	10.98%
5	1.15	11.25%	11.45%	11.62%	11.81%	11.98%
6	0.52	13.50%	13.74%	13.87%	14.04%	14.24%
Randoms						
Sphere no	Volume (ml)					
1	26.52	3.84%	4.01%	4.20%	4.41%	4.64%
2	11.49	4.34%	4.52%	4.70%	4.90%	5.09%
3	5.57	6.30%	6.50%	5.30%	6.98%	7.25%
4	2.57	6.21%	6.28%	6.37%	6.51%	6.64%
5	1.15	6.57%	6.63%	8.58%	6.70%	6.72%
6	0.52	9.80%	9.86%	9.91%	9.93%	10.01%

Table 3-11: SUV_{mean} determined with a variation of VoI_{CT} size for a 5:1 sphere-to-background ratio in 2D mode

				%VOI $_{CT}$		
2D		***90%***	***95%***	***100%***	***105%***	***110%***
Volume (ml)						
26.52		2.13	2.02	1.90	1.79	1.68
11.49		1.91	1.82	1.74	1.65	1.57
5.57		1.65	1.58	1.50	1.44	1.37
2.57		1.42	1.39	1.36	1.32	1.28
1.15		1.18	1.15	1.13	1.11	1.08
0.52		1.01	1.00	0.98	0.97	0.95

Table 3-12: %Contribution of Trues, Scatters and Randoms in relation to the Total Coincidences with variation in VoI_{CT} size for 2:1 sphere-to-background ratio in 2D mode

2D				*% VOI $_{CT}$*		
Trues		***90%***	***95%***	***100%***	***105%***	***110%***
Sphere no	Volume (ml)					
1	26.52	83.34%	82.94%	82.54%	82.13%	81.72%
2	11.49	81.04%	80.70%	80.37%	80.02%	79.72%
3	5.57	76.99%	76.68%	76.31%	76.00%	75.64%
4	2.57	75.22%	75.12%	75.01%	74.88%	74.73%
5	1.15	76.35%	76.28%	76.21%	76.14%	76.08%
6	0.52	72.98%	72.91%	72.87%	72.82%	72.74%
Scatters						
Sphere no	Volume (ml)					
1	26.52	13.35%	13.68%	14.03%	14.38%	14.73%
2	11.49	15.99%	16.25%	16.51%	16.78%	17.02%
3	5.57	18.38%	18.63%	18.92%	19.16%	19.46%
4	2.57	20.33%	20.42%	20.51%	20.62%	20.76%
5	1.15	19.82%	19.87%	19.92%	19.98%	20.04%
6	0.52	22.81%	22.85%	22.88%	22.91%	22.97%
Randoms						
Sphere no	Volume (ml)					
1	26.52	2.32%	2.38%	2.43%	2.49%	2.55%
2	11.49	2.75%	2.80%	2.84%	2.89%	2.94%
3	5.57	3.04%	3.09%	3.14%	3.19%	3.24%
4	2.57	3.40%	3.42%	3.44%	3.46%	3.49%
5	1.15	3.47%	3.48%	3.49%	3.50%	3.50%
6	0.52	3.69%	3.69%	3.70%	3.71%	3.72%

Table 3-13: SUV_{mean} determined with a variation of VoI_{CT} size for a 2:1 sphere-to-background ratio in 2D mode

				%VOI $_{CT}$		
2D		***90%***	***95%***	***100%***	***105%***	***110%***
Volume (ml)						
26.52		1.19	1.16	1.12	1.09	1.05
11.49		1.15	1.12	1.10	1.07	1.05
5.57		0.90	0.88	0.87	0.85	0.84
2.57		0.90	0.90	0.89	0.89	0.88
1.15		0.89	0.89	0.89	0.88	0.88
0.52		0.82	0.82	0.82	0.82	0.81

3.4 Discussion

The benchmark to assess the validity of the simulation software was performed and compared favourably to the norm that was provided with the software manual.

A voxelised version of the NEMA IEC Body Phantom™ was created successfully by using a contrast medium inside the spheres to ensure that a difference in CT number existed between the water surrounding the spheres and the volume inside the spheres. Distinct concentrations of radioactive material could thus be allocated to the volumes inside and outside the spheres respectively. This voxelised phantom did not exist before and can therefore be used successfully forthwith and by other researchers using GATE.

The voxelised phantom was evaluated by comparing SUVs obtained from GATE simulations with SUVs obtained from physical scans of the IEC Body phantom using the GE Discovery ST PET/CT scanner. The phantom was filled using concentrations of 10:1, 5:1 and 2:1 sphere-to-background ratios. The same concentrations were used during the simulations. The phantom was scanned using clinical parameters and the results acquired from the simulations compared to those obtained by the scanner. The SUV_{max} and SUV_{mean} were determined for different sizes of spheres and the different concentrations. It was found that the partial volume effect was evident when evaluating the SUVs of the activity in the spheres. A distinct loss in SUV was noted as the spheres became smaller and the data followed a logarithmic curve for SUV_{mean} for all cases as was also noted by Pandey *et al*. (2012) for the recovery coefficients. A sharp drop-off was present in the SUV curves for the spheres with volumes less than 5.57 ml. The implementation of statistical tests indicated no statistical significant difference between the scanned data and the simulated data and it can therefore be concluded that the simulations successfully emulated the physical scans thus validating the GATE simulation software successfully for phantom studies.

Different matrix sizes were used to assess the influence of sampling size on the phantom data. It was found that the 64×64 matrix produced results that were visually poor quantitatively produced SUVs that were statistically significantly different when

compared to using other matrix sizes. The use of the 512×512 matrix delivered the best visual images, but also very large image files that took long to reconstruct making it impractical for clinical use. When compared to the 256×256 matrix size, the improvements gained by using the 512×512, cannot be justified and the 256×256 should be the matrix of choice. There was also statistically no difference between the 256×256 matrix results and those obtained from the 512×512 matrix sampling. Since the 256×256 matrix acquisition is not always an option on commercial PET/CT scanners and since the 128×128 matrix and the 256×256 matrix data did not differ significantly, the 128×128 matrix could still be used with confidence. As Soret *et al.* (2007) has indicated, a 7% change in SUV can be expected when the matrix is increased by 50%. In this work, it was found to be more than 7% depending on the size of the object as well as on the matrix size.

The relative contributions of true-, scatter- and random coincidences demonstrated that the true coincidences were the major contributor when assessing the data from this phantom. This is due to the scatter medium being mainly homogeneous and that the active spheres were all situated relatively in one part of the phantom. There was no activity outside the phantom and no movement was present. The contribution of the trues diminished with decrease in sphere volume as well as with a decrease in relative activity. The randoms and scatters followed an inverse relation to that of the trues. The trues fraction also contributed less to the total image when the matrix size became smaller resulting in an increase in scatter and randoms. The contributions of scatters and randoms were in general greater during the 3D mode acquisitions than when acquisitions were performed in the 2D mode.

Throughout our investigation the volumes-of-interest were based on the sizes of the CT images of the objects to be analysed. The variation in the sizes of the VoIs resulted in the contribution of the trues decreasing with an increase in VoI size as well as showing a decrease in SUV_{mean}. Conversely, the scatters and randoms fractions increased as the VoI increased. This is expected since the size of an object does have an influence on the

amount of scatter and by including surrounding tissue the amount of relative true coincidences will decrease (Phelps, 2004; Soret *et al.*, 2007) .

The parameters assessed in this chapter proved to be conclusive that the GATE simulations could be used accurately to evaluate the performance of a PET/CT scanner in a static phantom situation. In the next chapter, these parameters were investigated in the human phantom in the static status as well as during a simulated breathing cycle.

3.5 References

AMIDE: Amide's a Medical Imaging Data Examiner. Available from: http://amide.sourceforge.net/ (Accessed 12 February 2013).

Bettinardi V, Danna M, Savi A, Lecchi M, Castiglioni I, Gilardi MC, Bammer H, Lucignani G, Fazio F. 2004. Performance evaluation of the new whole-body PET/CT scanner: Discovery ST. *Eur J Nucl Med Mol Imaging* 31:867-881.

Du Toit PD (dutoitpd@nuke.co.za). (20 May 2008 to 27 August 2008). Re: GATE: Discovery ST. Emails to and from Kirov A. (kirova@mskcc.org) and Schmidtlein CR (schmidtr@mskcc.org).

Du Toit PD, Du Raan H, Rae WID. 2014. Verification of Standardised Uptake Values on a GE DST PET/CT Scanner using a Body Phantom: a GATE simulation. Paper presented at the 52nd SAAPMB Congress: Pretoria, South Africa.

Du Toit PD, Du Raan H, Rae WID. 2014. Turning Alcohol into Water when Creating a Mathematical Body Phantom for PET Simulations. Poster presented at the 52nd SAAPMB Congress: Pretoria, South Africa.

GATE InstallationGuideV6.1., Validating Installation, PET Benchmark. Available from http://wiki.opengatecollaboration.org/index.php/Validating_Installation (Accessed 9 September 2014).

GATE: Simulations of Preclinical and Clinical Scans in Emission Tomography, Transmission Tomography and Radiation Therapy. Available from: http://www.opengatecollaboration.org/ (Accessed 01 December 2013).

Hickeson M, Yun M, Matthies, Zhuang H, Adam L-E, Lacorte L, Alavi A. 2002. Use of a corrected standardized uptake value based on the lesion size on CT permits accurate characterization of lung nodules on FDG-PET. *Eur J Nucl Med* 29:1639-1647.

Jan S, Santin G, Strul D, Staelens S, Assié K, Autret D, Avner S, Barbier R, Bardiès M, Bloomfield PM, Brasse D, Breton V, Bruyndonckx P, Buvat I, Chatziioannou AF, Choi Y, Chung YH, Comtat C, Donnarieix D, Ferrer L, Glick SJ, Groiselle CJ, Guez D, Honore P-F, Kerhoas-Cavata S, Kirov AS, Kohli V, Koole M, Krieguer M, van der Laan DJ, Lamare F, Largeron G, Lartizien C, Lazaro D, Maas MC, Maigne L, Mayet F, Melot F, Merheb C, Pennacchio E, Perez J, Pietrzyk U, Rannou FR, Rey M, Schaart DR, Schmidtlein CR, Simon L, Song TY, Vieira J-M, Visvikis D, Van de Walle R, Wieërs E, Morel C. 2004. GATE: a simulation toolkit for PET and SPET. *Phys Med Biol* 49:4543-4561.

Jaskowiak CJ, Bianco JA, Perlman SB, Fine JP. 2005. Influence of Reconstruction Iterations on 18F-FDG PET/CT Standardized Uptake Values. *J Nucl Med* 46:424-428.

Lucignani G, Paganelli G, Bombardieri E. 2004. The use of standardized uptake values for assessing FDG uptake with PET in oncology: a clinical perspective. *Nucl Med Commun* 25:651-656.

Loening AM and Gambhir SS. 2003. AMIDE: A Free Software Tool for Multimodality Medical Image Analysis. *Mol Imaging* 2:131-137.

Pandey AK, Sharma P, Pandey M, Aswathi K K, Malhotra A, Kumar R. 2012. Spreadsheet program for estimating recovery coefficient to get partial volume corrected standardized uptake value in clinical positron emission tomography-computed tomography studies. *Indian J Nucl Med* 27:89-94.

Phelps, ME (Ed.). 2004. PET: Molecular Imaging and Its Biological Applications. 1st ed. *Springer, New York* :37.

Reader AJ, Stijn A, Bakatselos F, Manavaki R, Walledge RJ, Jeavons AP, Julyan PJ, Zhao S, Hastings DL, Zweit J. 2002. One-Pass List-Mode EM Algorithm for High-Resolution 3-D PET Image Reconstruction Into Large Arrays. *IEEE Trans Nucl Sci* 49:693-699.

ROOT: Data Analysis Framework. Available from: http://root.cern.ch/ (Accessed 17 September 2014).

Saha GB. 2005. Basics of PET Imaging: Physics, Chemistry and Regulations, 1st ed., Springer, New York :72.

Schmidtlein C, Turner A, Nehmeh S, Mawlawi O, Erdi Y, Humm J, Amols H, Kirov A. 2006. SU-FF-I-54: A Monte Carlo Model of the Discovery ST PET Scanner. *Med Phys 33:*2009.

Soret M. Bacharach SL, Buvat I. 2007. Partial-Volume Effect in PET Tumor Imaging. *J Nucl Med* 48:932-945.

3.6 Appendices

3.6.1 The PET Benchmark macro

In this macro, the various components are colour-coded as follows:

- scanner definition
- description of the structure of the phantom
- description of the source or spread of activity inside the phantom
- physical processes involved
- detection processes and digitized
- random number generator model
- the output of the simulation

```
/control/verbose 0
/gate/cluster/setTimeSplitHalflife 6600.  s

/vis/disable
#/control/execute visu.mac

/gate/geometry/setMaterialDatabase GateMaterials.db

#  W O R L D
/gate/world/geometry/setXLength 150.  cm
/gate/world/geometry/setYLength 150.  cm
/gate/world/geometry/setZLength 150.  cm

#     CYLINDRICAL
/gate/world/daughters/name cylindricalPET
/gate/world/daughters/insert cylinder
/gate/cylindricalPET/placement/setTranslation 0.0 0.0 0.0 cm
/gate/cylindricalPET/geometry/setRmax 52.0 cm
/gate/cylindricalPET/geometry/setRmin 39.9 cm
/gate/cylindricalPET/geometry/setHeight 40.2 cm
/gate/cylindricalPET/setMaterial Air
/gate/cylindricalPET/vis/forceWireframe
/gate/cylindricalPET/vis/setColor white

#     HEAD
/gate/cylindricalPET/daughters/name head
/gate/cylindricalPET/daughters/insert box
/gate/head/placement/setTranslation 44.0 0.0 0.0 cm
/gate/head/geometry/setXLength 8.0 cm
/gate/head/geometry/setYLength 32.0 cm
/gate/head/geometry/setZLength 40.2 cm
/gate/head/setMaterial Air
/gate/head/vis/setVisible 0

#     END-SHIELDING
```

```
/gate/head/daughters/name endshielding
/gate/head/daughters/insert box
/gate/endshielding/placement/setTranslation 0.0 0.0 0.0 cm
/gate/endshielding/geometry/setXLength 8.0 cm
/gate/endshielding/geometry/setYLength 32.0 cm
/gate/endshielding/geometry/setZLength 1.0 mm
/gate/endshielding/setMaterial Lead
/gate/endshielding/repeaters/insert cubicArray
/gate/endshielding/cubicArray/setRepeatNumberX 1
/gate/endshielding/cubicArray/setRepeatNumberY 1
/gate/endshielding/cubicArray/setRepeatNumberZ 2
/gate/endshielding/cubicArray/setRepeatVector 0.0 0.0 40.1 cm
/gate/endshielding/vis/setColor white

#     SEPTA
/gate/head/daughters/name septa
/gate/head/daughters/insert box
/gate/septa/placement/setTranslation -1.5 0.0 0.0 cm
/gate/septa/geometry/setXLength 5.0 cm
/gate/septa/geometry/setYLength 32.0 cm
/gate/septa/geometry/setZLength .5 mm
/gate/septa/setMaterial Tungsten
/gate/septa/repeaters/insert cubicArray
/gate/septa/cubicArray/setRepeatNumberX 1
/gate/septa/cubicArray/setRepeatNumberY 1
/gate/septa/cubicArray/setRepeatNumberZ 3
/gate/septa/cubicArray/setRepeatVector 0.0 0.0 10.0 cm
/gate/septa/vis/setColor blue

#     MODULE
/gate/head/daughters/name module
/gate/head/daughters/insert box
/gate/module/placement/setTranslation 2.5 0.0 0.0 cm
/gate/module/geometry/setXLength 3.0 cm
/gate/module/geometry/setYLength 8.0 cm
/gate/module/geometry/setZLength 10.0 cm
/gate/module/setMaterial Air
/gate/module/vis/setVisible 0

#     BLOCK
/gate/module/daughters/name block
/gate/module/daughters/insert box
/gate/block/placement/setTranslation 0.0 0.0 0.0 cm
/gate/block/geometry/setXLength 30 mm
/gate/block/geometry/setYLength 15.9 mm
/gate/block/geometry/setZLength 19.9 mm
/gate/block/setMaterial Air
/gate/block/vis/setVisible 0

#     C R Y S T A L
/gate/block/daughters/name crystal
/gate/block/daughters/insert box
```

```
/gate/crystal/placement/setTranslation 0.0 0.0 0.0 cm
/gate/crystal/geometry/setXLength 3.0 cm
/gate/crystal/geometry/setYLength 3.0 mm
/gate/crystal/geometry/setZLength 3.8 mm
/gate/crystal/setMaterial Air
/gate/crystal/vis/setVisible 0


#     LSO layer
/gate/crystal/daughters/name LSO
/gate/crystal/daughters/insert box
/gate/LSO/placement/setTranslation -0.75 0.0 0.0 cm
/gate/LSO/geometry/setXLength 1.5 cm
/gate/LSO/geometry/setYLength 3.0 mm
/gate/LSO/geometry/setZLength 3.8 mm
/gate/LSO/setMaterial LSO
/gate/LSO/vis/setColor green

#     BGO layer
/gate/crystal/daughters/name BGO
/gate/crystal/daughters/insert box
/gate/BGO/placement/setTranslation +0.75 0.0 0.0 cm
/gate/BGO/geometry/setXLength 1.5 cm
/gate/BGO/geometry/setYLength 3.0 mm
/gate/BGO/geometry/setZLength 3.8 mm
/gate/BGO/setMaterial BGO
/gate/BGO/vis/setColor yellow

#     R E P E A T  C R Y S T A L
/gate/crystal/repeaters/insert cubicArray
/gate/crystal/cubicArray/setRepeatNumberX 1
/gate/crystal/cubicArray/setRepeatNumberY 5
/gate/crystal/cubicArray/setRepeatNumberZ 5
/gate/crystal/cubicArray/setRepeatVector 0.0 3.2 4.0 mm


#     R E P E A T  BLOCK
/gate/block/repeaters/insert cubicArray
/gate/block/cubicArray/setRepeatNumberX 1
/gate/block/cubicArray/setRepeatNumberY 5
/gate/block/cubicArray/setRepeatNumberZ 5
/gate/block/cubicArray/setRepeatVector 0.0 1.6 2.0 cm

#     R E P E A T MODULE
/gate/module/repeaters/insert cubicArray
/gate/module/cubicArray/setRepeatNumberX 1
/gate/module/cubicArray/setRepeatNumberY 4
/gate/module/cubicArray/setRepeatNumberZ 4
/gate/module/cubicArray/setRepeatVector 0.0 8.0 10.0 cm

#     R E P E A T HEAD
/gate/head/repeaters/insert ring
```

```
/gate/head/ring/setRepeatNumber 8

/gate/cylindricalPET/moves/insert orbiting
/gate/cylindricalPET/orbiting/setSpeed .1875 deg/s
/gate/cylindricalPET/orbiting/setPoint1 0 0 0 cm
/gate/cylindricalPET/orbiting/setPoint2 0 0 1 cm


#     A T T A C H  S Y S T E M
/gate/systems/cylindricalPET/rsector/attach head
/gate/systems/cylindricalPET/module/attach module
/gate/systems/cylindricalPET/submodule/attach block
/gate/systems/cylindricalPET/crystal/attach crystal
/gate/systems/cylindricalPET/layer0/attach LSO
/gate/systems/cylindricalPET/layer1/attach BGO

#     A T T A C H  C R Y S T A L SD

/gate/LSO/attachCrystalSD
/gate/BGO/attachCrystalSD

/gate/systems/cylindricalPET/describe



#     P H A N T O M
/gate/world/daughters/name NEMACylinder
/gate/world/daughters/insert cylinder
/gate/NEMACylinder/setMaterial Water
/gate/NEMACylinder/geometry/setRmax 10.  cm
/gate/NEMACylinder/geometry/setHeight 70.  cm

/gate/NEMACylinder/vis/forceSolid
/gate/NEMACylinder/vis/setColor red


/gate/NEMACylinder/attachPhantomSD
/gate/endshielding/attachPhantomSD
/gate/septa/attachPhantomSD


#
#   P H Y S I C S
#
/gate/physics/addProcess PhotoElectric
/gate/physics/processes/PhotoElectric/setModel StandardModel

/gate/physics/addProcess Compton
/gate/physics/processes/Compton/setModel StandardModel

/gate/physics/addProcess RayleighScattering
```

```
/gate/physics/processes/RayleighScattering/setModel PenelopeModel

/gate/physics/addProcess ElectronIonisation
/gate/physics/processes/ElectronIonisation/setModel StandardModel
e-
/gate/physics/processes/ElectronIonisation/setModel StandardModel
e+

/gate/physics/addProcess Bremsstrahlung
/gate/physics/processes/Bremsstrahlung/setModel StandardModel e-
/gate/physics/processes/Bremsstrahlung/setModel StandardModel e+

/gate/physics/addProcess PositronAnnihilation

/gate/physics/addProcess MultipleScattering e+
/gate/physics/addProcess MultipleScattering e-

/gate/physics/processList Enabled
/gate/physics/processList Initialized

#
#    C U T S
#


# Cuts for particle in NEMACylinder
#/gate/physics/Gamma/SetCutInRegion   NEMACylinder 1.0 cm
/gate/physics/Electron/SetCutInRegion NEMACylinder 1.0 cm
/gate/physics/Positron/SetCutInRegion NEMACylinder 1.0 cm

# Cuts for particle in NEMACylinder
#/gate/physics/Gamma/SetCutInRegion   LSO 1.0 cm
/gate/physics/Electron/SetCutInRegion LSO 1.0 cm
/gate/physics/Positron/SetCutInRegion LSO 1.0 cm

# Cuts for particle in NEMACylinder
#/gate/physics/Gamma/SetCutInRegion   BGO 1.0 cm
/gate/physics/Electron/SetCutInRegion BGO 1.0 cm
/gate/physics/Positron/SetCutInRegion BGO 1.0 cm



#    I N I T I A L I Z E
/gate/run/initialize

#    D I G I T I Z E R
/gate/digitizer/Singles/insert adder
/gate/digitizer/Singles/insert readout
/gate/digitizer/Singles/readout/setDepth 1
/gate/digitizer/Singles/insert blurring
/gate/digitizer/Singles/blurring/setResolution 0.26
```

```
/gate/digitizer/Singles/blurring/setEnergyOfReference 511.  keV
/gate/digitizer/Singles/insert thresholder
/gate/digitizer/Singles/thresholder/setThreshold 350.  keV
/gate/digitizer/Singles/insert upholder
/gate/digitizer/Singles/upholder/setUphold 650.  keV


#    C O I N C I  S O R T E R
/gate/digitizer/Coincidences/setWindow 120.  ns
/gate/digitizer/Coincidences/MultiplesPolicy takeWinnerOfGoods

/gate/digitizer/name delay
/gate/digitizer/insert coincidenceSorter
/gate/digitizer/delay/setWindow 120.  ns
/gate/digitizer/delay/setOffset 500.  ns

/gate/digitizer/delay/MultiplesPolicy takeWinnerOfGoods



#    S O U R C E

/gate/source/addSource F18LineSource
/gate/source/F18LineSource/setActivity 100000.  becquerel
/gate/source/F18LineSource/gps/particle e+
/gate/source/F18LineSource/setForcedUnstableFlag true
/gate/source/F18LineSource/setForcedHalfLife 6586.2 s
/gate/source/F18LineSource/gps/energytype Fluor18
/gate/source/F18LineSource/gps/type Volume
/gate/source/F18LineSource/gps/shape Cylinder
/gate/source/F18LineSource/gps/radius .5 mm
/gate/source/F18LineSource/gps/halfz 34.0 cm
/gate/source/F18LineSource/gps/angtype iso
/gate/source/F18LineSource/gps/centre 0.  -2.0 0.  cm

/gate/source/addSource O15LineSource
/gate/source/O15LineSource/setActivity 100000.  becquerel
/gate/source/O15LineSource/gps/particle e+
/gate/source/O15LineSource/setForcedUnstableFlag true
/gate/source/O15LineSource/setForcedHalfLife 122.24 s
/gate/source/O15LineSource/gps/energytype Oxygen15
/gate/source/O15LineSource/gps/type Volume
/gate/source/O15LineSource/gps/shape Cylinder
/gate/source/O15LineSource/gps/radius .5 mm
/gate/source/O15LineSource/gps/halfz 34.0 cm
/gate/source/O15LineSource/gps/angtype iso
/gate/source/O15LineSource/gps/centre 0.  2.0 0.  cm

/gate/source/list
```

```
#    V E R B O S I T Y
#/gate/verbose Physic  0
#/gate/verbose Cuts   0
#/gate/verbose Actor  0
#/gate/verbose SD    0
#/gate/verbose Actions 0
#/gate/verbose Step   0
#/gate/verbose Error  0
#/gate/verbose Warning 0
#/gate/verbose Output  0
#/gate/verbose Core   0

/run/verbose 0
/event/verbose 0
/tracking/verbose 0

#    O U T P U T

/gate/output/ascii/setOutFileHitsFlag 0
/gate/output/ascii/setOutFileSinglesFlag 0
/gate/output/ascii/setOutFileCoincidencesFlag 0
/gate/output/ascii/setOutFiledelayFlag 0

#/gate/output/BasicROOT/setFileName test.root

/gate/output/root/enable
/gate/output/root/setFileName benchmarkPET
/gate/output/root/setRootHitFlag 0
/gate/output/root/setRootSinglesFlag 0
/gate/output/root/setRootCoincidencesFlag 1
/gate/output/root/setRootdelayFlag 1


# R A N D O M
# JamesRandom Ranlux64 MersenneTwister
/gate/random/setEngineName Ranlux64
#/gate/random/setEngineSeed default
#/gate/random/setEngineSeed auto
/gate/random/setEngineSeed 123456789
#/gate/random/resetEngineFrom fileName
/gate/random/verbose 1

#    S T A R T
/gate/application/setTimeSlice  120.  s
/gate/application/setTimeStart  0.  s
/gate/application/setTimeStop   240.  s
/gate/application/startDAQ
```

3.6.2 Example of GATE Simulation macro used for IEC Body Phantom

In this macro, the various components are colour-coded as follows:

- scanner definition
- description of the structure of the phantom
- description of the source or spread of activity inside the phantom
- physical processes involved
- detection processes and digitized
- random number generator model
- the output of the simulation

```
/control/verbose 0
/gate/cluster/setTimeSplitHalflife 6600.  s
/gate/geometry/setMaterialDatabase ./GateMaterials.db

#     V I S U A L I S A T I O N
/vis/disable

#  W O R L D
/gate/world/geometry/setXLength 150.  cm
/gate/world/geometry/setYLength 150.  cm
/gate/world/geometry/setZLength 150.  cm

# G E   D I S C O V E R Y   S T   P E T   S C A N N E R

#   1 mm mylar patient window
/gate/world/daughters/name Mwindow
/gate/world/daughters/insert cylinder
/gate/Mwindow/geometry/setRmax 35.1 cm
/gate/Mwindow/geometry/setRmin 35.0 cm
/gate/Mwindow/geometry/setHeight 157.0 mm
/gate/Mwindow/setMaterial Mylar
/gate/Mwindow/vis/forceWireframe
/gate/Mwindow/vis/setColor cyan
/gate/Mwindow/attachPhantomSD

# -------------Lead shields around the detector: 1-Sup 2-inf 3-
steel, 4-Pb,5-steel-shields------
# Note that all Discovery ST shields were made with same widths as
Discovery LS shields
# The lengths were estimated for the Discovery ST to fit the shield
set up of the Discovery LS
#
#           Short Thick PB piece on the left
/gate/world/daughters/name Shield1
/gate/world/daughters/insert cylinder
/gate/Shield1/placement/setTranslation 0.0 0.0 9.75 cm
/gate/Shield1/geometry/setRmax 58.7 cm
#flush with Rmax of Shield 2
/gate/Shield1/geometry/setRmin 44.05 cm
```

```
#flush with Rmin of cylindricalPET
/gate/Shield1/geometry/setHeight 3.8 cm
/gate/Shield1/setMaterial Lead
/gate/Shield1/vis/forceWireframe
/gate/Shield1/vis/setColor grey
/gate/Shield1/attachPhantomSD

#           CORRECTED: Last small L-shaped steel rail piece
superiorly
/gate/world/daughters/name Shield2
/gate/world/daughters/insert cylinder
/gate/Shield2/placement/setTranslation 0.0 0.0 -14.325 cm
#157/2+8gap +10 +27.5+8gap +22.5/2 mm
/gate/Shield2/geometry/setRmax 40.15 cm
#Approximate Length 4 cm
/gate/Shield2/geometry/setRmin 36.15 cm
#measured sticks out 13.5 mm from shield 5
/gate/Shield2/geometry/setHeight 2.25 cm
#measured
/gate/Shield2/setMaterial SS304
#seen as steel
/gate/Shield2/vis/forceWireframe
/gate/Shield2/vis/setColor grey
/gate/Shield2/attachPhantomSD


# Collimator moved to end
#
#           Collimator side NOT USED (if 3D ?)
#/gate/world/daughters/name Shield3          #(Shield 3 is on the
collimator!)
#/gate/world/daughters/insert cylinder
#/gate/Shield3/placement/setTranslation 0.0 0.0 8.25 cm
#/gate/Shield3/geometry/setRmax 43.20 cm
#matches collimator Rmax
#/gate/Shield3/geometry/setRmin 37.8 cm
#matches collimator Rmin
#/gate/Shield3/geometry/setHeight 0.8 cm
#/gate/Shield3/setMaterial SS304
#/gate/Shield3/vis/forceWireframe
#/gate/Shield3/vis/setColor blue
#/gate/Shield3/attachPhantomSD

#           inner 1 cm lead piece
/gate/world/daughters/name Shield4
/gate/world/daughters/insert cylinder
/gate/Shield4/placement/setTranslation 0.0 0.0 -9.15 cm
#157/2 + 8mm gap +10/2 mm
/gate/Shield4/geometry/setRmax 49.2 cm
#Rmin+11.9 cm
/gate/Shield4/geometry/setRmin 37.3 cm
#sticks in 5 mm from collimator Rmin
/gate/Shield4/geometry/setHeight 1.0 cm
/gate/Shield4/setMaterial Lead
```

```
/gate/Shield4/vis/forceWireframe
/gate/Shield4/vis/setColor red
/gate/Shield4/attachPhantomSD

#           outer steel plate
/gate/world/daughters/name Shield5
/gate/world/daughters/insert cylinder
/gate/Shield5/placement/setTranslation 0.0 0.0 -11.025 cm
#78.5+ 8 + 10 + 27.5/2 mm
/gate/Shield5/geometry/setRmax 49.0 cm
#Rmin + 11.5 cm
/gate/Shield5/geometry/setRmin 37.5 cm
#collimator Rmin - 3 mm
/gate/Shield5/geometry/setHeight 2.75 cm
/gate/Shield5/setMaterial SS304
/gate/Shield5/vis/forceWireframe
/gate/Shield5/vis/setColor blue
/gate/Shield5/attachPhantomSD


#  C Y L I N D R I C A L (detector ring, includes 1 mm gap bw each
block)
/gate/world/daughters/name cylindricalPET
/gate/world/daughters/insert cylinder
/gate/cylindricalPET/setMaterial Air
/gate/cylindricalPET/geometry/setRmax 474.58 mm
#extended 5mm from 474.58 to 479.58 to interpolate correctly on vis
/gate/cylindricalPET/geometry/setRmin 440.5 mm
/gate/cylindricalPET/geometry/setHeight 157.0 mm
/gate/cylindricalPET/vis/forceWireframe

#  Al foil
/gate/cylindricalPET/daughters/name Alfoil
/gate/cylindricalPET/daughters/insert box
/gate/Alfoil/placement/setTranslation 455.04 39.85 0 mm
#translated 2.5mm less to account for cylindricalPET widening
/gate/Alfoil/geometry/setXLength 34.08 mm
/gate/Alfoil/geometry/setYLength 0.1 mm
#Sits on top of Rsector
/gate/Alfoil/geometry/setZLength 157.0 mm
/gate/Alfoil/setMaterial Aluminium
/gate/Alfoil/vis/setColor yellow
#/gate/Alfoil/vis/forceWireframe
/gate/Alfoil/attachPhantomSD

#  R S E C T O R (GE's module)
/gate/cylindricalPET/daughters/name rsector
/gate/cylindricalPET/daughters/insert box
/gate/rsector/placement/setTranslation 455.04 0 0 mm     #translated
2.5mm less to account for cylindricalPET widening
/gate/rsector/geometry/setXLength 34.08 mm
/gate/rsector/geometry/setYLength 78.52 mm
#Houses two blocks and W foil
/gate/rsector/geometry/setZLength 157.0 mm
```

```
/gate/rsector/setMaterial Air
/gate/rsector/vis/forceWireframe

#  W foil
/gate/rsector/daughters/name Wfoil
/gate/rsector/daughters/insert box
/gate/Wfoil/geometry/setXLength 34.08 mm
/gate/Wfoil/geometry/setYLength 0.4 mm
#Sits between blocks (modules)
/gate/Wfoil/geometry/setZLength 157.0 mm
/gate/Wfoil/setMaterial Tungsten
/gate/Wfoil/vis/setColor red
/gate/Wfoil/vis/forceWireframe
/gate/Wfoil/attachPhantomSD

#   M O D U L E (GE's block)
/gate/rsector/daughters/name module
/gate/rsector/daughters/insert box
/gate/module/geometry/setXLength 34.08 mm
#contains a .8mm teflon layer, 30mm crystal, and 3.28mm RTV+glass
/gate/module/geometry/setYLength 38.56 mm
/gate/module/geometry/setZLength 38.56 mm
/gate/module/setMaterial PTFE
/gate/module/vis/forceWireframe
/gate/module/vis/setColor gray

#   C R Y S T A L (10 micron teflon around each crystal)
/gate/module/daughters/name crystal
/gate/module/daughters/insert box
/gate/crystal/placement/setTranslation -1.24 0 0 mm
/gate/crystal/geometry/setXLength 30.00 mm
/gate/crystal/geometry/setYLength 6.3 mm
/gate/crystal/geometry/setZLength 6.3 mm
/gate/crystal/setMaterial BGO
/gate/crystal/vis/forceWireframe
/gate/crystal/vis/setColor green

#   Glass 3 mm + 0.28 mm RTV
/gate/module/daughters/name PMTGlass
/gate/module/daughters/insert box
/gate/PMTGlass/placement/setTranslation 15.4 0 0 mm
/gate/PMTGlass/geometry/setXLength 3.28 mm
/gate/PMTGlass/geometry/setYLength 38.56 mm
/gate/PMTGlass/geometry/setZLength 38.56 mm
/gate/PMTGlass/setMaterial Glass
/gate/PMTGlass/vis/forceWireframe
/gate/PMTGlass/vis/setColor blue
/gate/PMTGlass/attachPhantomSD

#   R E P E A T  C R Y S T A L
/gate/crystal/repeaters/insert cubicArray
/gate/crystal/cubicArray/setRepeatNumberX 1
/gate/crystal/cubicArray/setRepeatNumberY 6
/gate/crystal/cubicArray/setRepeatNumberZ 6
```

```
/gate/crystal/cubicArray/setRepeatVector 0.  6.31 6.31 mm

#   R E P E A T  M O D U L E
/gate/module/repeaters/insert cubicArray
/gate/module/cubicArray/setRepeatNumberY 2
/gate/module/cubicArray/setRepeatNumberZ 4
/gate/module/cubicArray/setRepeatVector 0.  39.96 39.25 mm

#   R E P E A T  R S E C T O R
/gate/rsector/repeaters/insert ring
/gate/rsector/ring/setRepeatNumber 35

#   R E P E A T  Al foil
/gate/Alfoil/repeaters/insert ring
/gate/Alfoil/ring/setRepeatNumber 35

#   A T T A C H  S Y S T E M
/gate/systems/cylindricalPET/rsector/attach rsector
/gate/systems/cylindricalPET/module/attach module
/gate/systems/cylindricalPET/crystal/attach crystal


#   Add Collimator in 3D mode
#
#           Holds: shield, septa column, shield, shield
/gate/world/daughters/name Advcol
/gate/world/daughters/insert cylinder
# 2D mode translation
#/gate/Advcol/placement/setTranslation 0.0 0.0 46.825 mm
/gate/Advcol/placement/setTranslation 0.0 0.0 210.175 mm
/gate/Advcol/geometry/setRmax 43.20 cm
/gate/Advcol/geometry/setRmin 37.8 cm
/gate/Advcol/geometry/setHeight 263.35 mm
/gate/Advcol/setMaterial Air
/gate/Advcol/vis/forceWireframe
/gate/Advcol/vis/setColor white

#    fiber carbon cylinder centered with ring at Z=0
/gate/Advcol/daughters/name Fibercyl
/gate/Advcol/daughters/insert cylinder
/gate/Fibercyl/placement/setTranslation 0.0 0.0 -46.825 mm
/gate/Fibercyl/geometry/setRmax 43.20 cm
/gate/Fibercyl/geometry/setRmin 37.8 cm
/gate/Fibercyl/geometry/setHeight 157.0 mm
/gate/Fibercyl/setMaterial CarbonFiber
/gate/Fibercyl/vis/forceWireframe
/gate/Fibercyl/vis/setColor yellow
/gate/Fibercyl/attachPhantomSD

#           Collimator inferior (R) side
/gate/Advcol/daughters/name ShieldR
/gate/Advcol/daughters/insert cylinder
/gate/ShieldR/placement/setTranslation 0.0 0.0 -126.5 mm
```

```
/gate/ShieldR/geometry/setRmax 43.20 cm
/gate/ShieldR/geometry/setRmin 37.8 cm
/gate/ShieldR/geometry/setHeight 6.35 mm
/gate/ShieldR/setMaterial SS304
#/gate/ShieldR/vis/forceWireframe
/gate/ShieldR/vis/setColor blue
/gate/ShieldR/attachPhantomSD

#           Collimator sup left side Steel 81.5-46.825 = 3.4675 cm
/gate/Advcol/daughters/name ShieldL
/gate/Advcol/daughters/insert cylinder
/gate/ShieldL/placement/setTranslation 0.0 0.0 36.7 mm
/gate/ShieldL/geometry/setRmax 43.20 cm
/gate/ShieldL/geometry/setRmin 37.8 cm
/gate/ShieldL/geometry/setHeight 1.0 cm
/gate/ShieldL/setMaterial SS304
# /gate/ShieldL/vis/forceWireframe
/gate/ShieldL/vis/setColor blue
/gate/ShieldL/attachPhantomSD

#           Collimator sup side Pb 131.5-46.825 = 84.675 cm
/gate/Advcol/daughters/name ShieldL2
/gate/Advcol/daughters/insert cylinder
/gate/ShieldL2/placement/setTranslation 0.0 0.0 86.7 mm
/gate/ShieldL2/geometry/setRmax 43.201 cm
/gate/ShieldL2/geometry/setRmin 34.701 cm
/gate/ShieldL2/geometry/setHeight 9.0 cm
/gate/ShieldL2/setMaterial Lead
/gate/ShieldL2/vis/forceWireframe
/gate/ShieldL2/vis/setColor gray
/gate/ShieldL2/attachPhantomSD

#    Air centered in Fibercyl
/gate/Fibercyl/daughters/name Colair
/gate/Fibercyl/daughters/insert cylinder
/gate/Colair/placement/setTranslation 0.0 0.0 0.0 mm
/gate/Colair/geometry/setRmax 43.2 cm
/gate/Colair/geometry/setRmin 37.8 cm
/gate/Colair/geometry/setHeight 157.0 mm
/gate/Colair/setMaterial Air
/gate/Colair/vis/forceWireframe
/gate/Colair/vis/setColor white

#    Tungsten plates in Fibercyl
/gate/Fibercyl/daughters/name Wplate
/gate/Fibercyl/daughters/insert cylinder
/gate/Wplate/placement/setTranslation 0.0 0.0 0.0 mm
/gate/Wplate/geometry/setRmax 43.2 cm
/gate/Wplate/geometry/setRmin 37.8 cm
/gate/Wplate/geometry/setHeight 0.8 mm
/gate/Wplate/setMaterial Tungsten
#/gate/Wplate/vis/forceWireframe
/gate/Wplate/vis/setColor red
/gate/Wplate/attachPhantomSD
```

```
#   R E P E A T  W plate
/gate/Wplate/repeaters/insert linear
/gate/Wplate/linear/setRepeatNumber 23
/gate/Wplate/linear/setRepeatVector 0.  0.  6.542 mm

#   A T T A C H  crystalSD
/gate/crystal/attachCrystalSD

#/gate/geometry/rebuild

# V O X E L I Z E D  M A T R I X  I E C  B O D Y  P H A N T O M
/gate/world/daughters/name IEC
/gate/world/daughters/insert compressedMatrix
/gate/IEC/geometry/insertReader interfile
/gate/IEC/verbose 0
/gate/IEC/interfileReader/insertTranslator range
/gate/IEC/interfileReader/rangeTranslator/readTable
/auto/home/mount/dutoitpd/IEC2D60_420_10_1_128/range.dat
/gate/IEC/interfileReader/rangeTranslator/describe 1
/gate/IEC/interfileReader/readFile
/auto/home/mount/dutoitpd/IEC2D60_420_10_1_128/IECwater_60.h33
/gate/IEC/placement/setTranslation 0.  0.  0.  mm
/gate/IEC/placement/setRotationAxis 1 0 0
/gate/IEC/placement/setRotationAngle 0 deg
/gate/IEC/attachVoxelPhantomSD
#/gate/geometry/update
/gate/IEC/interfileReader/describe 1
#/gate/IEC/addOutput doseOutput
#/gate/output/doseOutput/saveUncertainty true
#/gate/output/doseOutput/setFileName IEC_paraDose.bin

#=====================================================
# PHYSICS
#=====================================================

/gate/physics/addProcess PhotoElectric
/gate/physics/processes/PhotoElectric/setModel StandardModel

/gate/physics/addProcess Compton
/gate/physics/processes/Compton/setModel StandardModel

/gate/physics/addProcess RayleighScattering
/gate/physics/processes/RayleighScattering/setModel PenelopeModel

/gate/physics/addProcess ElectronIonisation
/gate/physics/processes/ElectronIonisation/setModel StandardModel e-
/gate/physics/processes/ElectronIonisation/setModel StandardModel e+

/gate/physics/addProcess Bremsstrahlung
/gate/physics/processes/Bremsstrahlung/setModel StandardModel e-
/gate/physics/processes/Bremsstrahlung/setModel StandardModel e+

/gate/physics/addProcess PositronAnnihilation
```

```
/gate/physics/addProcess MultipleScattering e+
/gate/physics/addProcess MultipleScattering e-

#/gate/physics/setEMin 0.1 keV
#/gate/physics/setEMax 2 MeV
#/gate/physics/setDEDXBinning 220
#/gate/physics/setLambdaBinning 220

/gate/physics/processList Enabled
/gate/physics/processList Initialized

#=====================================================
# CUTS
#=====================================================

#
#   C U T S
#
# Cuts for particle in NEMACylinder
#/gate/physics/Gamma/SetCutInRegion   BGO 1.0 cm
#/gate/physics/Electron/SetCutInRegion BGO 1.0 cm
#/gate/physics/Positron/SetCutInRegion BGO 1.0 cm

# Cuts for particle in NEMACylinder
#/gate/physics/Gamma/SetCutInRegion   LSO 1.0 cm
#/gate/physics/Electron/SetCutInRegion LSO 1.0 cm
#/gate/physics/Positron/SetCutInRegion LSO 1.0 cm


# Cuts for particle in IEC phantom
/gate/physics/Gamma/SetCutInRegion   IEC 0.1 mm
/gate/physics/Electron/SetCutInRegion IEC 0.1 mm
/gate/physics/Positron/SetCutInRegion IEC 0.1 mm
/gate/physics/SetMaxStepSizeInRegion  IEC 0.01 mm


#    I N I T I A L I Z E
#/gate/systems/cylindricalPET/verbose 0
#/gate/geometry/enableAutoUpdate
/gate/run/initialize
#/geometry/test/recursive_test


#    D I G I T I Z E R
/gate/digitizer/Singles/insert adder
/gate/digitizer/Singles/insert readout
/gate/digitizer/Singles/readout/setDepth 2

/gate/digitizer/Singles/insert crystalblurring
/gate/digitizer/Singles/crystalblurring/setCrystalResolutionMin 0.15
/gate/digitizer/Singles/crystalblurring/setCrystalResolutionMax 0.35
/gate/digitizer/Singles/crystalblurring/setCrystalQE 0.9
```

```
/gate/digitizer/Singles/crystalblurring/setCrystalEnergyOfReference
511 keV

/gate/digitizer/Singles/insert thresholder
/gate/digitizer/Singles/thresholder/setThreshold 375 keV
/gate/digitizer/Singles/insert upholder
/gate/digitizer/Singles/upholder/setUphold 650 keV

#
#
#   C O I N C I D E N C E S O R T E R
/gate/digitizer/Coincidences/setWindow 5.85 ns
/gate/digitizer/Coincidences/MultiplesPolicy takeWinnerOfGoods

/gate/digitizer/name delay
/gate/digitizer/insert coincidenceSorter
/gate/digitizer/delay/setWindow 5.85 ns
/gate/digitizer/delay/setOffset 500 ns
/gate/digitizer/delay/MultiplesPolicy takeWinnerOfGoods

# V O X E L  S O U R C E  B A S E D  O N  T H E  I E C  B O D Y  P H
A N T O M

/gate/source/addSource voxel voxel
/gate/source/voxel/reader/insert interfile
/gate/source/voxel/interfileReader/translator/insert range
/gate/source/voxel/interfileReader/rangeTranslator/readTable
/auto/home/mount/dutoitpd/IEC2D60_420_10_1_128/activityRange.dat
/gate/source/voxel/interfileReader/rangeTranslator/describe 1
/gate/source/voxel/interfileReader/readFile
/auto/home/mount/dutoitpd/IEC2D60_420_10_1_128/IEC.h33
/gate/source/voxel/gps/particle e+
/gate/source/voxel/setForcedUnstableFlag true
/gate/source/voxel/gps/energytype Fluor18
/gate/source/voxel/setForcedHalfLife 6586.2 s
/gate/source/voxel/setPosition -256.  -256.  -30.  mm
/gate/source/voxel/gps/confine NULL
/gate/source/voxel/gps/angtype iso
/gate/source/voxel/dump 1
/gate/source/voxel/visualize 1000 cyan 2
#/gate/source/voxel/verbose 0

/gate/source/list


#    V E R B O S I T Y
/control/verbose 0
/run/verbose 0
/event/verbose 0
/tracking/verbose 0
/gate/application/verbose 0
/gate/generator/verbose 0
/gate/source/verbose 0
```

```
#     O U T P U T

/gate/output/verbose 1

/gate/output/root/enable
/gate/output/root/setFileName IEC2D
/gate/output/root/setRootHitFlag 0
/gate/output/root/setRootSinglesFlag 1
/gate/output/root/setRootCoincidencesFlag 1
/gate/output/root/setRootdelayFlag 1
/gate/output/root/setRootNtupleFlag 0
/gate/random/setEngineName JamesRandom
/gate/random/setEngineSeed auto
/gate/random/verbose 1


#     S T A R T
/gate/application/setTimeSlice  1 s
/gate/application/setTimeStart  0 s
/gate/application/setTimeStop   900 s

/gate/application/startDAQ
```

3.6.3 Example of *range.dat*

```
5
0  5   Air    true 0.0 0.0 0.0 0.2
6  175  Lung   true 0.0 0.0 0.0 0.2
176 191  Water   true 1.0 0.0 0.0 0.2
192 220  Water   true 0.0 1.0 0.0 0.2
221 255  Bone   true 0.0 0.0 1.0 0.2
```

3.6.4 Example of *activityRange.dat*

```
5
0 5 0
6 175 0
176 191 37.77
192 220 377.70
221 255 0.
```

3.6.5 Tables of Results

The SUV data for the IEC Body Phantom are listed in the following tables:

Table a 1: SUVs of 100%VoI of the Body Phantom spheres acquired with a 10:1 sphere-to-background contrast by simulation (SIM) and PET scanner (PET)

All

2D				SIM						PET					
		Diameter (mm)	Volume (ml)	min	max	mean	std dev	variance	std error	min	max	mean	std dev	variance	std error
ROI:	1	37	26.52	1.085	10.049	5.755	2.204	6.159	0.138						
	2	28	11.49	1.108	9.033	5.120	2.195	6.108	0.197						
	3	22	5.57	1.345	7.780	4.653	1.557	3.075	0.185						
	4	17	2.57	1.567	6.583	4.037	1.311	2.181	0.219						
	5	13	1.15	1.503	5.161	3.248	1.090	1.507	0.227						
	6	10	0.52	1.612	3.764	2.998	0.671	0.571	0.179						
3D															
		Diameter (mm)	Volume (ml)	min	max	mean	std dev	variance	std error	min	max	mean	std dev	variance	std error
ROI:	1	37	26.52	1.039	9.707	5.666	2.166	5.950	0.136						
	2	28	11.49	1.093	9.317	5.147	2.230	6.306	0.200						
	3	22	5.57	1.466	7.904	4.658	1.606	3.271	0.191						
	4	17	2.57	1.427	6.307	4.100	1.278	2.073	0.213						
	5	13	1.15	1.651	4.770	3.099	0.971	1.196	0.202						
	6	10	0.52	1.700	3.326	2.760	0.593	0.445	0.158						

Trues

2D															
		Diameter (mm)	Volume (ml)	min	max	mean	std dev	variance	std error	min	max	mean	std dev	variance	
ROI:	1	37	26.52	0.823	9.641	5.471	2.197	6.123	0.138	1.079	7.963	5.575	1.748	4.879	0.088
	2	28	11.49	0.872	8.616	4.834	2.194	6.103	0.197	0.990	7.796	4.971	1.848	5.453	0.131
	3	22	5.57	1.094	7.558	4.392	1.588	3.200	0.189	1.249	7.634	4.572	1.716	4.703	0.167
	4	17	2.57	1.214	6.226	3.766	1.297	2.135	0.216	1.079	6.510	3.681	1.529	3.733	0.196
	5	13	1.15	1.203	4.901	2.986	1.104	1.546	0.230	0.728	4.341	2.552	1.132	2.047	0.203
	6	10	0.52	1.244	3.553	2.737	0.718	0.654	0.192	0.915	3.155	2.030	0.732	0.855	0.160
3D															
		Diameter (mm)	Volume (ml)	min	max	mean	std dev	variance	std error	min	max	mean	std dev	variance	
ROI:	1	37	26.52	0.877	9.367	5.414	2.133	5.949	0.134	1.018	8.395	5.950	1.771	3.135	0.089
	2	28	11.49	0.883	8.897	4.862	2.199	6.305	0.197	1.158	8.095	5.164	1.706	2.911	0.121
	3	22	5.57	1.240	7.597	4.405	1.586	3.271	0.188	1.396	6.931	4.474	1.342	1.800	0.131
	4	17	2.57	1.212	5.984	3.813	1.256	2.072	0.209	1.220	5.570	3.529	1.153	1.329	0.148
	5	13	1.15	1.400	4.447	2.828	0.944	1.195	0.197	0.855	3.681	2.416	0.844	0.712	0.152
	6	10	0.52	1.435	3.027	2.478	0.570	0.445	0.152	0.985	2.689	2.011	0.523	0.274	0.114

Scatters

2D															
		Diameter (mm)	Volume (ml)	min	max	mean	std dev	variance	std error	min	max	mean	std dev	variance	
ROI:	1	37	26.52	0.159	0.319	0.238	0.029	0.001	0.002						
	2	28	11.49	0.201	0.365	0.261	0.025	0.001	0.002						
	3	22	5.57	0.196	0.277	0.235	0.017	0.000	0.002						
	4	17	2.57	0.222	0.305	0.263	0.019	0.000	0.003						
	5	13	1.15	0.218	0.321	0.262	0.027	0.001	0.006						
	6	10	0.52	0.234	0.309	0.283	0.023	0.001	0.006						
3D															
		Diameter (mm)	Volume (ml)	min	max	mean	std dev	variance	std error	min	max	mean	std dev	variance	
ROI:	1	37	26.52	0.152	0.308	0.234	0.029	0.001	0.002						
	2	28	11.49	0.198	0.376	0.263	0.025	0.001	0.002						
	3	22	5.57	0.213	0.281	0.235	0.017	0.000	0.002						
	4	17	2.57	0.202	0.292	0.267	0.019	0.000	0.003						
	5	13	1.15	0.239	0.297	0.250	0.024	0.001	0.005						
	6	10	0.52	0.247	0.273	0.261	0.020	0.001	0.005						

Randoms

2D															
		Diameter (mm)	Volume (ml)	min	max	mean	std dev	variance	std error	min	max	mean	std dev	variance	
ROI:	1	37	26.52	0.010	0.030	0.017	0.004	0.000	0.000						
	2	28	11.49	0.013	0.030	0.018	0.003	0.000	0.000						
	3	22	5.57	0.011	0.027	0.018	0.004	0.000	0.000						
	4	17	2.57	0.015	0.025	0.020	0.003	0.000	0.000						
	5	13	1.15	0.012	0.022	0.017	0.003	0.000	0.001						
	6	10	0.52	0.011	0.024	0.015	0.004	0.000	0.001						
3D															
		Diameter (mm)	Volume (ml)	min	max	mean	std dev	variance	std error	min	max	mean	std dev	variance	
ROI:	1	37	26.52	0.010	0.032	0.018	0.004	0.000	0.000						
	2	28	11.49	0.011	0.044	0.022	0.006	0.000	0.001						
	3	22	5.57	0.013	0.026	0.018	0.003	0.000	0.000						
	4	17	2.57	0.013	0.031	0.020	0.004	0.000	0.001						
	5	13	1.15	0.012	0.026	0.021	0.004	0.000	0.001						
	6	10	0.52	0.018	0.026	0.021	0.002	0.000	0.001						

Table a 2: SUVs of 90%VoI of the Body Phantom spheres acquired with a 10:1 sphere-to-background contrast by simulation (SIM) and PET scanner (PET)

All

2D

		Diameter (mm)	Volume (ml)	min	max	mean	std dev	variance	std error	min	max	mean	std dev	variance	std error
ROI:	1	37	26.52	1.579	10.049	6.505	1.965	4.895	0.140						
	2	28	11.49	1.174	9.033	5.688	2.098	5.584	0.214						
	3	22	5.57	1.731	7.780	5.150	1.428	2.588	0.194						
	4	17	2.57	1.991	6.583	4.270	1.325	2.227	0.250						
	5	13	1.15	1.703	5.161	3.429	1.073	1.460	0.246						
	6	10	0.52	1.702	3.764	3.144	0.615	0.480	0.185						

3D

		Diameter (mm)	Volume (ml)	min	max	mean	std dev	variance	std error	min	max	mean	std dev	variance	std error
ROI:	1	37	26.52	1.435	9.707	6.412	1.938	4.763	0.138						
	2	28	11.49	1.093	9.317	5.714	2.142	5.817	0.219						
	3	22	5.57	1.717	7.904	5.165	1.487	2.805	0.202						
	4	17	2.57	1.836	6.307	4.344	1.273	2.055	0.241						
	5	13	1.15	1.683	4.770	3.272	0.955	1.157	0.219						
	6	10	0.52	1.700	3.326	2.898	0.544	0.375	0.164						

Trues

2D

		Diameter (mm)	Volume (ml)	min	max	mean	std dev	variance	std error	min	max	mean	std dev	variance	
ROI:	1	37	26.52	1.289	9.641	6.219	1.957	4.855	0.139	1.604	7.963	6.202	1.348	2.900	0.077
	2	28	11.49	0.906	8.616	5.401	2.096	5.571	0.214	1.197	7.796	5.562	1.602	4.101	0.131
	3	22	5.57	1.440	7.558	4.898	1.457	2.693	0.198	1.549	7.634	5.115	1.574	3.955	0.173
	4	17	2.57	1.673	6.226	3.997	1.302	2.151	0.246	1.137	6.510	4.042	1.480	3.499	0.214
	5	13	1.15	1.434	4.901	3.170	1.088	1.500	0.250	0.853	4.341	2.690	1.106	1.953	0.226
	6	10	0.52	1.346	3.553	2.895	0.660	0.553	0.199	0.915	3.155	2.150	0.750	0.899	0.194

3D

		Diameter (mm)	Volume (ml)	min	max	mean	std dev	variance	std error	min	max	mean	std dev	variance	
ROI:	1	37	26.52	1.215	9.367	6.128	1.908	4.762	0.136	1.888	8.395	6.594	1.423	2.026	0.081
	2	28	11.49	0.883	8.897	5.401	2.111	5.816	0.215	1.559	8.095	5.715	1.492	2.228	0.122
	3	22	5.57	1.454	7.597	4.887	1.468	2.804	0.200	1.812	6.931	4.904	1.201	1.444	0.132
	4	17	2.57	1.563	5.984	4.041	1.251	2.055	0.236	1.345	5.570	3.803	1.091	1.190	0.157
	5	13	1.15	1.427	4.447	2.987	0.928	1.156	0.213	0.887	3.681	2.518	0.816	0.666	0.167
	6	10	0.52	1.435	3.027	2.604	0.523	0.375	0.158	1.213	2.689	2.101	0.522	0.272	0.135

Scatters

2D

		Diameter (mm)	Volume (ml)	min	max	mean	std dev	variance	std error	min	max	mean	std dev	variance	
ROI:	1	37	26.52	0.159	0.319	0.241	0.028	0.001	0.002						
	2	28	11.49	0.201	0.365	0.263	0.023	0.001	0.002						
	3	22	5.57	0.208	0.277	0.234	0.016	0.000	0.002						
	4	17	2.57	0.222	0.305	0.263	0.019	0.000	0.004						
	5	13	1.15	0.218	0.321	0.263	0.027	0.001	0.006						
	6	10	0.52	0.234	0.309	0.283	0.023	0.001	0.007						

3D

		Diameter (mm)	Volume (ml)	min	max	mean	std dev	variance	std error	min	max	mean	std dev	variance	
ROI:	1	37	26.52	0.211	0.308	0.265	0.026	0.001	0.002						
	2	28	11.49	0.198	0.376	0.292	0.024	0.001	0.002						
	3	22	5.57	0.250	0.281	0.261	0.016	0.000	0.002						
	4	17	2.57	0.260	0.292	0.283	0.018	0.000	0.003						
	5	13	1.15	0.244	0.297	0.264	0.023	0.001	0.005						
	6	10	0.52	0.247	0.273	0.274	0.019	0.000	0.006						

Randoms

2D

		Diameter (mm)	Volume (ml)	min	max	mean	std dev	variance	std error	min	max	mean	std dev	variance	
ROI:	1	37	26.52	0.010	0.030	0.017	0.003	0.000	0.000						
	2	28	11.49	0.013	0.030	0.018	0.003	0.000	0.000						
	3	22	5.57	0.011	0.027	0.018	0.004	0.000	0.001						
	4	17	2.57	0.015	0.025	0.020	0.002	0.000	0.000						
	5	13	1.15	0.012	0.022	0.017	0.003	0.000	0.001						
	6	10	0.52	0.011	0.024	0.015	0.004	0.000	0.001						

3D

		Diameter (mm)	Volume (ml)	min	max	mean	std dev	variance	std error	min	max	mean	std dev	variance	
ROI:	1	37	26.52	0.010	0.032	0.018	0.005	0.000	0.000						
	2	28	11.49	0.011	0.044	0.022	0.006	0.000	0.001						
	3	22	5.57	0.013	0.026	0.018	0.003	0.000	0.000						
	4	17	2.57	0.013	0.031	0.020	0.004	0.000	0.001						
	5	13	1.15	0.012	0.026	0.021	0.003	0.000	0.001						
	6	10	0.52	0.018	0.026	0.021	0.002	0.000	0.001						

Table a 3: SUVs of 95%VoI of the Body Phantom spheres acquired with a 10:1 sphere-to-background contrast by simulation (SIM) and PET scanner (PET)

All

2D

		Diameter (mm)	Volume (ml)	min	max	mean	std dev	variance	std error	min	max	mean	std dev	variance	std error
ROI:	1	37	26.52	1.579	10.049	6.139	2.088	5.530	0.142						
	2	28	11.49	1.108	9.033	5.396	2.157	5.900	0.203						
	3	22	5.57	1.626	7.780	4.912	1.488	2.808	0.189						
	4	17	2.57	1.567	6.583	4.143	1.307	2.165	0.218						
	5	13	1.15	1.677	5.161	3.328	1.073	1.460	0.234						
	6	10	0.52	1.612	3.764	3.056	0.647	0.531	0.179						

3D

		Diameter (mm)	Volume (ml)	min	max	mean	std dev	variance	std error	min	max	mean	std dev	variance	std error
ROI:	1	37	26.52	1.435	9.707	6.046	2.055	5.355	0.139						
	2	28	11.49	1.093	9.317	5.423	2.197	6.120	0.207						
	3	22	5.57	1.676	7.904	4.919	1.544	3.023	0.196						
	4	17	2.57	1.427	6.307	4.209	1.267	2.036	0.211						
	5	13	1.15	1.683	4.770	3.172	0.960	1.170	0.210						
	6	10	0.52	1.700	3.326	2.815	0.567	0.408	0.157						

Trues

2D

		Diameter (mm)	Volume (ml)	min	max	mean	std dev	variance	std error	min	max	mean	std dev	variance	
ROI:	1	37	26.52	1.289	9.641	5.854	2.081	5.494	0.141	1.097	7.963	5.899	1.560	3.886	0.083
	2	28	11.49	0.872	8.616	5.110	2.156	5.892	0.203	1.197	7.796	5.276	1.731	4.783	0.132
	3	22	5.57	1.299	7.558	4.655	1.518	2.923	0.193	1.249	7.634	4.841	1.649	4.342	0.170
	4	17	2.57	1.214	6.226	3.872	1.289	2.107	0.215	1.137	6.510	3.863	1.513	3.658	0.206
	5	13	1.15	1.419	4.901	3.068	1.087	1.498	0.237	0.728	4.341	2.619	1.130	2.039	0.214
	6	10	0.52	1.244	3.553	2.799	0.694	0.611	0.193	0.915	3.155	2.090	0.744	0.883	0.180

3D

		Diameter (mm)	Volume (ml)	min	max	mean	std dev	variance	std error	min	max	mean	std dev	variance	
ROI:	1	37	26.52	1.215	9.367	5.779	2.023	5.354	0.137	1.337	8.395	6.279	1.605	2.577	0.086
	2	28	11.49	0.883	8.897	5.125	2.166	6.119	0.204	1.184	8.095	5.450	1.599	2.556	0.122
	3	22	5.57	1.419	7.597	4.653	1.524	3.023	0.194	1.470	6.931	4.689	1.274	1.623	0.131
	4	17	2.57	1.212	5.984	3.915	1.244	2.035	0.207	1.332	5.570	3.668	1.130	1.277	0.154
	5	13	1.15	1.427	4.447	2.895	0.933	1.169	0.204	0.887	3.681	2.465	0.840	0.705	0.159
	6	10	0.52	1.435	3.027	2.528	0.546	0.408	0.151	1.213	2.689	2.055	0.523	0.274	0.127

Scatters

2D

		Diameter (mm)	Volume (ml)	min	max	mean	std dev	variance	std error	min	max	mean	std dev	variance	
ROI:	1	37	26.52	0.159	0.319	0.239	0.028	0.001	0.002						
	2	28	11.49	0.201	0.365	0.262	0.024	0.001	0.002						
	3	22	5.57	0.208	0.277	0.235	0.016	0.000	0.002						
	4	17	2.57	0.222	0.305	0.263	0.019	0.000	0.003						
	5	13	1.15	0.218	0.321	0.263	0.027	0.001	0.006						
	6	10	0.52	0.234	0.309	0.283	0.023	0.001	0.006						

3D

		Diameter (mm)	Volume (ml)	min	max	mean	std dev	variance	std error	min	max	mean	std dev	variance	
ROI:	1	37	26.52	0.211	0.308	0.250	0.027	0.001	0.002						
	2	28	11.49	0.198	0.376	0.277	0.025	0.001	0.002						
	3	22	5.57	0.244	0.281	0.248	0.017	0.000	0.002						
	4	17	2.57	0.202	0.292	0.274	0.018	0.000	0.003						
	5	13	1.15	0.244	0.297	0.256	0.024	0.001	0.005						
	6	10	0.52	0.247	0.273	0.266	0.019	0.000	0.005						

Randoms

2D

		Diameter (mm)	Volume (ml)	min	max	mean	std dev	variance	std error	min	max	mean	std dev	variance	
ROI:	1	37	26.52	0.010	0.030	0.017	0.003	0.000	0.000						
	2	28	11.49	0.013	0.030	0.018	0.003	0.000	0.000						
	3	22	5.57	0.011	0.027	0.018	0.004	0.000	0.000						
	4	17	2.57	0.015	0.025	0.020	0.002	0.000	0.000						
	5	13	1.15	0.012	0.022	0.017	0.003	0.000	0.001						
	6	10	0.52	0.011	0.024	0.015	0.004	0.000	0.001						

3D

		Diameter (mm)	Volume (ml)	min	max	mean	std dev	variance	std error	min	max	mean	std dev	variance	
ROI:	1	37	26.52	0.010	0.032	0.018	0.004	0.000	0.000						
	2	28	11.49	0.011	0.044	0.022	0.006	0.000	0.001						
	3	22	5.57	0.013	0.026	0.018	0.003	0.000	0.000						
	4	17	2.57	0.013	0.031	0.020	0.004	0.000	0.001						
	5	13	1.15	0.012	0.026	0.021	0.004	0.000	0.001						
	6	10	0.52	0.018	0.026	0.021	0.002	0.000	0.001						

Table a 4: SUVs of 105%VoI of the Body Phantom spheres acquired with a 10:1 sphere-to-background contrast by simulation (SIM) and PET scanner (PET)

All

2D

		Diameter (mm)	Volume (ml)	min	max	mean	std dev	variance	std error	min	max	mean	std dev	variance	std error
ROI:	1	37	26.52	0.900	10.049	5.382	2.307	6.750	0.134						
	2	28	11.49	0.957	9.033	4.835	2.224	6.274	0.184						
	3	22	5.57	1.182	7.780	4.432	1.603	3.260	0.176						
	4	17	2.57	1.171	6.583	3.917	1.323	2.220	0.209						
	5	13	1.15	1.503	5.161	3.160	1.078	1.473	0.220						
	6	10	0.52	1.612	3.764	2.943	0.668	0.566	0.178						

3D

		Diameter (mm)	Volume (ml)	min	max	mean	std dev	variance	std error	min	max	mean	std dev	variance	std error
ROI:	1	37	26.52	1.009	9.707	5.303	2.262	6.486	0.131						
	2	28	11.49	0.953	9.317	4.862	2.256	6.454	0.187						
	3	22	5.57	1.220	7.904	4.438	1.646	3.434	0.181						
	4	17	2.57	1.175	6.307	3.975	1.297	2.135	0.205						
	5	13	1.15	1.468	4.770	3.017	0.960	1.170	0.196						
	6	10	0.52	1.700	3.326	2.707	0.592	0.444	0.158						

Trues

2D

		Diameter (mm)	Volume (ml)	min	max	mean	std dev	variance	std error	min	max	mean	std dev	variance	
ROI:	1	37	26.52	0.653	9.641	5.100	2.300	6.710	0.134	0.982	7.963	5.228	1.919	5.879	0.090
	2	28	11.49	0.728	8.616	4.549	2.224	6.272	0.184	0.990	7.796	4.681	1.928	5.936	0.130
	3	22	5.57	0.910	7.558	4.167	1.635	3.389	0.179	0.991	7.634	4.316	1.764	4.972	0.160
	4	17	2.57	0.871	6.226	3.645	1.313	2.188	0.208	1.033	6.510	3.495	1.544	3.806	0.190
	5	13	1.15	1.203	4.901	2.896	1.092	1.512	0.223	0.728	4.341	2.479	1.141	2.078	0.199
	6	10	0.52	1.244	3.553	2.676	0.716	0.650	0.191	0.915	3.155	1.961	0.721	0.831	0.150

3D

		Diameter (mm)	Volume (ml)	min	max	mean	std dev	variance	std error	min	max	mean	std dev	variance	
ROI:	1	37	26.52	0.852	9.367	5.066	2.227	6.485	0.129	0.928	8.395	5.602	1.929	3.722	0.090
	2	28	11.49	0.770	8.897	4.593	2.225	6.453	0.184	0.889	8.095	4.890	1.786	3.191	0.120
	3	22	5.57	1.030	7.596	4.196	1.625	3.434	0.178	1.192	6.931	4.266	1.398	1.953	0.127
	4	17	2.57	0.995	5.984	3.696	1.274	2.134	0.201	1.220	5.570	3.384	1.177	1.386	0.145
	5	13	1.15	1.244	4.446	2.752	0.933	1.169	0.190	0.855	3.681	2.361	0.858	0.736	0.149
	6	10	0.52	1.435	3.027	2.430	0.569	0.443	0.152	0.985	2.689	1.958	0.523	0.274	0.109

Scatters

2D

		Diameter (mm)	Volume (ml)	min	max	mean	std dev	variance	std error	min	max	mean	std dev	variance
ROI:	1	37	26.52	0.150	0.319	0.236	0.030	0.001	0.002					
	2	28	11.49	0.201	0.365	0.260	0.026	0.001	0.002					
	3	22	5.57	0.196	0.277	0.235	0.017	0.000	0.002					
	4	17	2.57	0.222	0.305	0.263	0.019	0.000	0.003					
	5	13	1.15	0.218	0.321	0.261	0.027	0.001	0.006					
	6	10	0.52	0.234	0.309	0.284	0.022	0.001	0.006					

3D

		Diameter (mm)	Volume (ml)	min	max	mean	std dev	variance	std error	min	max	mean	std dev	variance
ROI:	1	37	26.52	0.148	0.308	0.219	0.030	0.001	0.002					
	2	28	11.49	0.173	0.376	0.248	0.026	0.001	0.002					
	3	22	5.57	0.178	0.281	0.224	0.018	0.000	0.002					
	4	17	2.57	0.166	0.292	0.259	0.019	0.000	0.003					
	5	13	1.15	0.213	0.297	0.243	0.024	0.001	0.005					
	6	10	0.52	0.247	0.273	0.256	0.020	0.001	0.005					

Randoms

2D

		Diameter (mm)	Volume (ml)	min	max	mean	std dev	variance	std error	min	max	mean	std dev	variance
ROI:	1	37	26.52	0.010	0.030	0.017	0.004	0.000	0.000					
	2	28	11.49	0.013	0.030	0.018	0.003	0.000	0.000					
	3	22	5.57	0.011	0.027	0.018	0.004	0.000	0.000					
	4	17	2.57	0.011	0.025	0.019	0.003	0.000	0.000					
	5	13	1.15	0.012	0.022	0.017	0.003	0.000	0.001					
	6	10	0.52	0.011	0.024	0.016	0.004	0.000	0.001					

3D

		Diameter (mm)	Volume (ml)	min	max	mean	std dev	variance	std error	min	max	mean	std dev	variance
ROI:	1	37	26.52	0.009	0.032	0.018	0.004	0.000	0.000					
	2	28	11.49	0.010	0.044	0.021	0.006	0.000	0.000					
	3	22	5.57	0.013	0.026	0.018	0.003	0.000	0.000					
	4	17	2.57	0.013	0.031	0.020	0.004	0.000	0.001					
	5	13	1.15	0.012	0.028	0.021	0.004	0.000	0.001					
	6	10	0.52	0.018	0.026	0.021	0.002	0.000	0.001					

Table a 5: SUVs of 110%VoI of the Body Phantom spheres acquired with a 10:1 sphere-to-background contrast by simulation (SIM) and PET scanner (PET)

All

2D

		Diameter (mm)	Volume (ml)	min	max	mean	std dev	variance	std error	min	max	mean	std dev	variance	std error
ROI:	1	37	26.52	0.808	10.049	5.010	2.395	7.273	0.132						
	2	28	11.49	0.888	9.033	4.579	2.231	6.315	0.179						
	3	22	5.57	1.177	7.780	4.188	1.635	3.389	0.170						
	4	17	2.57	1.086	6.583	3.764	1.343	2.287	0.198						
	5	13	1.15	1.133	5.161	3.071	1.059	1.422	0.208						
	6	10	0.52	1.539	3.764	2.865	0.695	0.612	0.179						

3D

		Diameter (mm)	Volume (ml)	min	max	mean	std dev	variance	std error	min	max	mean	std dev	variance	std error
ROI:	1	37	26.52	0.841	9.707	4.942	2.343	6.961	0.129						
	2	28	11.49	0.926	9.317	4.606	2.260	6.479	0.182						
	3	22	5.57	1.062	7.904	4.191	1.672	3.543	0.174						
	4	17	2.57	1.028	6.307	3.814	1.324	2.224	0.195						
	5	13	1.15	1.285	4.770	2.936	0.943	1.126	0.185						
	6	10	0.52	1.297	3.326	2.640	0.614	0.478	0.159						

Trues

2D

		Diameter (mm)	Volume (ml)	min	max	mean	std dev	variance	std error	min	max	mean	std dev	variance	
ROI:	1	37	26.52	0.563	9.641	4.730	2.387	7.227	0.132	0.884	7.963	4.881	2.051	6.720	0.090
	2	28	11.49	0.659	8.616	4.294	2.231	6.312	0.179	0.887	7.796	4.391	1.990	6.323	0.126
	3	22	5.57	0.883	7.558	3.918	1.666	3.519	0.174	0.991	7.634	4.070	1.802	5.184	0.155
	4	17	2.57	0.771	6.226	3.491	1.337	2.268	0.197	0.785	6.510	3.326	1.546	3.818	0.180
	5	13	1.15	0.853	4.901	2.805	1.072	1.457	0.210	0.728	4.341	2.390	1.148	2.103	0.184
	6	10	0.52	1.224	3.553	2.593	0.743	0.700	0.192	0.915	3.155	1.900	0.702	0.787	0.140

3D

		Diameter (mm)	Volume (ml)	min	max	mean	std dev	variance	std error	min	max	mean	std dev	variance	
ROI:	1	37	26.52	0.710	9.367	4.721	2.308	6.959	0.127	0.793	8.395	5.253	2.060	4.242	0.090
	2	28	11.49	0.747	8.897	4.350	2.229	6.479	0.179	0.889	8.095	4.614	1.854	3.439	0.118
	3	22	5.57	0.895	7.596	3.962	1.650	3.543	0.172	1.110	6.931	4.063	1.447	2.094	0.125
	4	17	2.57	0.869	5.984	3.545	1.301	2.223	0.192	0.874	5.570	3.247	1.194	1.425	0.139
	5	13	1.15	1.086	4.446	2.678	0.915	1.126	0.180	0.855	3.681	2.293	0.868	0.754	0.139
	6	10	0.52	1.095	3.027	2.370	0.591	0.477	0.153	0.985	2.689	1.911	0.518	0.269	0.104

Scatters

2D

		Diameter (mm)	Volume (ml)	min	max	mean	std dev	variance	std error	min	max	mean	std dev	variance	
ROI:	1	37	26.52	0.150	0.319	0.234	0.030	0.001	0.002						
	2	28	11.49	0.199	0.365	0.259	0.026	0.001	0.002						
	3	22	5.57	0.194	0.277	0.235	0.017	0.000	0.002						
	4	17	2.57	0.206	0.305	0.262	0.020	0.000	0.003						
	5	13	1.15	0.218	0.321	0.260	0.027	0.001	0.005						
	6	10	0.52	0.234	0.309	0.284	0.023	0.001	0.006						

3D

		Diameter (mm)	Volume (ml)	min	max	mean	std dev	variance	std error	min	max	mean	std dev	variance	
ROI:	1	37	26.52	0.123	0.308	0.204	0.031	0.001	0.002						
	2	28	11.49	0.168	0.376	0.235	0.026	0.001	0.002						
	3	22	5.57	0.155	0.281	0.212	0.018	0.000	0.002						
	4	17	2.57	0.146	0.292	0.248	0.019	0.000	0.003						
	5	13	1.15	0.186	0.297	0.237	0.023	0.001	0.005						
	6	10	0.52	0.188	0.273	0.249	0.021	0.001	0.005						

Randoms

2D

		Diameter (mm)	Volume (ml)	min	max	mean	std dev	variance	std error	min	max	mean	std dev	variance	
ROI:	1	37	26.52	0.009	0.030	0.017	0.004	0.000	0.000						
	2	28	11.49	0.013	0.030	0.018	0.003	0.000	0.000						
	3	22	5.57	0.011	0.027	0.019	0.004	0.000	0.000						
	4	17	2.57	0.011	0.025	0.019	0.003	0.000	0.000						
	5	13	1.15	0.012	0.022	0.017	0.003	0.000	0.001						
	6	10	0.52	0.011	0.024	0.016	0.004	0.000	0.001						

3D

		Diameter (mm)	Volume (ml)	min	max	mean	std dev	variance	std error	min	max	mean	std dev	variance	
ROI:	1	37	26.52	0.008	0.032	0.018	0.004	0.000	0.000						
	2	28	11.49	0.010	0.044	0.021	0.006	0.000	0.000						
	3	22	5.57	0.013	0.026	0.018	0.003	0.000	0.000						
	4	17	2.57	0.013	0.031	0.020	0.004	0.000	0.001						
	5	13	1.15	0.012	0.028	0.021	0.004	0.000	0.001						
	6	10	0.52	0.014	0.026	0.021	0.002	0.000	0.001						

Table a 6: SUVs of 100%VoI of the Body Phantom spheres acquired with a 5:1 sphere-to-background contrast by simulation (SIM) and PET scanner (PET)

All

2D				min	max	mean	std dev	variance	std error	min	max	mean	std dev	variance	std error
		Diameter (mm)	Volume (ml)												
ROI:	1	37	26.52	0.603	3.591	2.148	0.695	0.613	0.044						
	2	28	11.49	0.722	3.242	1.998	0.657	0.548	0.059						
	3	22	5.57	0.715	2.712	1.760	0.447	0.253	0.053						
	4	17	2.57	0.980	2.307	1.618	0.358	0.163	0.060						
	5	13	1.15	0.890	1.892	1.384	0.284	0.102	0.059						
	6	10	0.52	0.941	1.422	1.261	0.147	0.028	0.039						
3D				min	max	mean	std dev	variance	std error	min	max	mean	std dev	variance	std error
		Diameter (mm)	Volume (ml)												
ROI:	1	37	26.52	0.649	3.940	2.429	0.779	0.770	0.049						
	2	28	11.49	0.822	3.950	2.314	0.789	0.790	0.071						
	3	22	5.57	0.954	3.169	2.050	0.543	0.374	0.064						
	4	17	2.57	1.039	2.480	1.855	0.382	0.185	0.064						
	5	13	1.15	1.049	1.941	1.498	0.262	0.087	0.055						
	6	10	0.52	1.021	1.520	1.368	0.147	0.028	0.039						

Trues

2D				min	max	mean	std dev	variance	std error	min	max	mean	std dev	variance	
		Diameter (mm)	Volume (ml)												
ROI:	1	37	26.52	0.392	3.294	1.904	0.691	0.605	0.043	0.846	2.733	1.994	0.476	0.362	0.024
	2	28	11.49	0.521	2.965	1.736	0.660	0.553	0.059	0.752	2.615	1.769	0.463	0.342	0.033
	3	22	5.57	0.505	2.495	1.505	0.464	0.273	0.055	0.646	2.336	1.546	0.434	0.301	0.042
	4	17	2.57	0.668	2.078	1.357	0.374	0.177	0.062	0.642	1.877	1.282	0.321	0.165	0.041
	5	13	1.15	0.646	1.634	1.131	0.286	0.104	0.060	0.643	1.205	0.985	0.157	0.040	0.028
	6	10	0.52	0.656	1.164	0.982	0.158	0.031	0.042	0.554	0.925	0.793	0.090	0.013	0.020
3D				min	max	mean	std dev	variance	std error	min	max	mean	std dev	variance	
		Diameter (mm)	Volume (ml)												
ROI:	1	37	26.52	0.395	3.571	2.112	0.770	0.751	0.048	0.929	2.923	2.185	0.489	0.382	0.024
	2	28	11.49	0.547	3.497	1.963	0.775	0.762	0.070	0.839	2.732	1.934	0.458	0.335	0.032
	3	22	5.57	0.606	2.877	1.714	0.552	0.387	0.066	0.746	2.463	1.688	0.406	0.263	0.040
	4	17	2.57	0.682	2.201	1.527	0.395	0.198	0.066	0.716	1.979	1.434	0.318	0.162	0.041
	5	13	1.15	0.752	1.682	1.198	0.284	0.102	0.059	0.728	1.419	1.192	0.198	0.063	0.036
	6	10	0.52	0.721	1.201	1.045	0.168	0.036	0.045	0.649	1.130	0.951	0.123	0.024	0.027

Scatters

2D				min	max	mean	std dev	variance	std error	min	max	mean	std dev	variance	
		Diameter (mm)	Volume (ml)												
ROI:	1	37	26.52	0.094	0.205	0.142	0.016	0.000	0.001						
	2	28	11.49	0.131	0.195	0.162	0.013	0.000	0.001						
	3	22	5.57	0.125	0.175	0.155	0.009	0.000	0.001						
	4	17	2.57	0.148	0.205	0.170	0.011	0.000	0.002						
	5	13	1.15	0.141	0.185	0.161	0.012	0.000	0.002						
	6	10	0.52	0.153	0.192	0.175	0.012	0.000	0.003						
3D				min	max	mean	std dev	variance	std error	min	max	mean	std dev	variance	
		Diameter (mm)	Volume (ml)												
ROI:	1	37	26.52	0.134	0.243	0.192	0.021	0.001	0.001						
	2	28	11.49	0.168	0.272	0.222	0.019	0.000	0.002						
	3	22	5.57	0.167	0.250	0.209	0.015	0.000	0.002						
	4	17	2.57	0.169	0.256	0.219	0.020	0.001	0.003						
	5	13	1.15	0.184	0.234	0.203	0.013	0.000	0.003						
	6	10	0.52	0.188	0.261	0.212	0.017	0.000	0.005						

Randoms

2D				min	max	mean	std dev	variance	std error	min	max	mean	std dev	variance	
		Diameter (mm)	Volume (ml)												
ROI:	1	37	26.52	0.043	0.174	0.090	0.021	0.001	0.001						
	2	28	11.49	0.044	0.143	0.094	0.023	0.001	0.002						
	3	22	5.57	0.071	0.174	0.119	0.023	0.001	0.003						
	4	17	2.57	0.061	0.159	0.103	0.023	0.001	0.004						
	5	13	1.15	0.044	0.142	0.092	0.029	0.001	0.006						
	6	10	0.52	0.088	0.143	0.125	0.016	0.000	0.004						
3D				min	max	mean	std dev	variance	std error	min	max	mean	std dev	variance	
		Diameter (mm)	Volume (ml)												
ROI:	1	37	26.52	0.063	0.119	0.090	0.011	0.000	0.001						
	2	28	11.49	0.082	0.141	0.107	0.011	0.000	0.001						
	3	22	5.57	0.081	0.129	0.106	0.009	0.000	0.001						
	4	17	2.57	0.082	0.139	0.109	0.010	0.000	0.002						
	5	13	1.15	0.092	0.111	0.099	0.005	0.000	0.001						
	6	10	0.52	0.087	0.130	0.107	0.008	0.000	0.002						

Table a 7: SUVs of 90%VoI of the Body Phantom spheres acquired with a 5:1 sphere-to-background contrast by simulation (SIM) and PET scanner (PET)

All

2D

		Diameter (mm)	Volume (ml)	min	max	mean	std dev	variance	std error	min	max	mean	std dev	variance	std error
ROI:	1	37	26.52	0.789	3.591	2.378	0.630	0.503	0.045						
	2	28	11.49	0.802	3.242	2.171	0.628	0.500	0.064						
	3	22	5.57	0.902	2.712	1.900	0.410	0.213	0.056						
	4	17	2.57	1.084	2.307	1.675	0.365	0.169	0.069						
	5	13	1.15	0.933	1.892	1.427	0.276	0.097	0.063						
	6	10	0.52	0.941	1.422	1.289	0.134	0.023	0.041						

3D

		Diameter (mm)	Volume (ml)	min	max	mean	std dev	variance	std error	min	max	mean	std dev	variance	std error
ROI:	1	37	26.52	0.874	3.940	2.690	0.708	0.635	0.050						
	2	28	11.49	0.822	3.950	2.515	0.761	0.735	0.078						
	3	22	5.57	1.026	3.169	2.219	0.504	0.322	0.069						
	4	17	2.57	1.162	2.480	1.927	0.380	0.183	0.072						
	5	13	1.15	1.049	1.941	1.545	0.254	0.082	0.058						
	6	10	0.52	1.132	1.520	1.401	0.132	0.022	0.040						

Trues

2D

		Diameter (mm)	Volume (ml)	min	max	mean	std dev	variance	std error	min	max	mean	std dev	variance	
ROI:	1	37	26.52	0.575	3.294	2.133	0.624	0.493	0.044	1.031	2.733	2.189	0.374	0.224	0.021
	2	28	11.49	0.551	2.965	1.909	0.631	0.506	0.064	0.900	2.615	1.938	0.397	0.252	0.033
	3	22	5.57	0.618	2.495	1.650	0.428	0.232	0.058	0.710	2.336	1.683	0.401	0.257	0.044
	4	17	2.57	0.782	2.078	1.418	0.378	0.182	0.072	0.770	1.877	1.369	0.305	0.149	0.044
	5	13	1.15	0.677	1.634	1.176	0.279	0.099	0.064	0.659	1.205	1.021	0.147	0.035	0.030
	6	10	0.52	0.679	1.164	1.013	0.145	0.027	0.044	0.628	0.925	0.817	0.082	0.011	0.021

3D

		Diameter (mm)	Volume (ml)	min	max	mean	std dev	variance	std error	min	max	mean	std dev	variance	
ROI:	1	37	26.52	0.578	3.571	2.370	0.695	0.613	0.050	1.235	2.923	2.389	0.383	0.235	0.022
	2	28	11.49	0.547	3.497	2.161	0.747	0.708	0.076	1.052	2.732	2.106	0.386	0.237	0.032
	3	22	5.57	0.687	2.877	1.886	0.514	0.336	0.070	0.820	2.463	1.821	0.363	0.210	0.040
	4	17	2.57	0.809	2.201	1.602	0.394	0.196	0.074	0.871	1.979	1.521	0.293	0.137	0.042
	5	13	1.15	0.752	1.682	1.249	0.278	0.098	0.064	0.728	1.419	1.237	0.180	0.052	0.037
	6	10	0.52	0.735	1.201	1.083	0.154	0.030	0.046	0.714	1.130	0.983	0.113	0.020	0.029

Scatters

2D

		Diameter (mm)	Volume (ml)	min	max	mean	std dev	variance	std error	min	max	mean	std dev	variance	
ROI:	1	37	26.52	0.094	0.205	0.143	0.015	0.000	0.001						
	2	28	11.49	0.135	0.195	0.163	0.013	0.000	0.001						
	3	22	5.57	0.125	0.175	0.155	0.008	0.000	0.001						
	4	17	2.57	0.148	0.197	0.169	0.010	0.000	0.002						
	5	13	1.15	0.141	0.185	0.161	0.012	0.000	0.003						
	6	10	0.52	0.153	0.192	0.174	0.012	0.000	0.004						

3D

		Diameter (mm)	Volume (ml)	min	max	mean	std dev	variance	std error	min	max	mean	std dev	variance	
ROI:	1	37	26.52	0.134	0.243	0.193	0.021	0.001	0.001						
	2	28	11.49	0.179	0.272	0.225	0.018	0.000	0.002						
	3	22	5.57	0.175	0.250	0.210	0.015	0.000	0.002						
	4	17	2.57	0.169	0.256	0.219	0.020	0.001	0.004						
	5	13	1.15	0.184	0.234	0.203	0.013	0.000	0.003						
	6	10	0.52	0.195	0.247	0.211	0.016	0.000	0.005						

Randoms

2D

		Diameter (mm)	Volume (ml)	min	max	mean	std dev	variance	std error	min	max	mean	std dev	variance	
ROI:	1	37	26.52	0.043	0.150	0.091	0.022	0.001	0.002						
	2	28	11.49	0.047	0.143	0.094	0.023	0.001	0.002						
	3	22	5.57	0.077	0.174	0.120	0.022	0.001	0.003						
	4	17	2.57	0.061	0.159	0.104	0.025	0.001	0.005						
	5	13	1.15	0.048	0.142	0.094	0.030	0.001	0.007						
	6	10	0.52	0.088	0.143	0.126	0.015	0.000	0.004						

3D

		Diameter (mm)	Volume (ml)	min	max	mean	std dev	variance	std error	min	max	mean	std dev	variance	
ROI:	1	37	26.52	0.063	0.119	0.091	0.011	0.000	0.001						
	2	28	11.49	0.086	0.141	0.107	0.010	0.000	0.001						
	3	22	5.57	0.086	0.129	0.106	0.008	0.000	0.001						
	4	17	2.57	0.082	0.139	0.109	0.010	0.000	0.002						
	5	13	1.15	0.092	0.110	0.099	0.005	0.000	0.001						
	6	10	0.52	0.098	0.121	0.107	0.008	0.000	0.002						

Table a 8: SUVs of 95%VoI of the Body Phantom spheres acquired with a 5:1 sphere-to-background contrast by simulation (SIM) and PET scanner (PET)

All

2D

		Diameter (mm)	Volume (ml)	min	max	mean	std dev	variance	std error	min	max	mean	std dev	variance	std error
ROI:	1	37	26.52	0.789	3.591	2.265	0.664	0.560	0.045						
	2	28	11.49	0.722	3.242	2.082	0.645	0.528	0.061						
	3	22	5.57	0.808	2.712	1.833	0.427	0.231	0.054						
	4	17	2.57	0.980	2.307	1.645	0.358	0.163	0.060						
	5	13	1.15	0.933	1.892	1.403	0.277	0.098	0.061						
	6	10	0.52	0.941	1.422	1.274	0.139	0.025	0.039						

3D

		Diameter (mm)	Volume (ml)	min	max	mean	std dev	variance	std error	min	max	mean	std dev	variance	std error
ROI:	1	37	26.52	0.872	3.940	2.561	0.745	0.704	0.051						
	2	28	11.49	0.822	3.950	2.412	0.779	0.769	0.073						
	3	22	5.57	0.994	3.169	2.137	0.523	0.347	0.066						
	4	17	2.57	1.039	2.480	1.888	0.378	0.182	0.063						
	5	13	1.15	1.049	1.941	1.517	0.258	0.084	0.056						
	6	10	0.52	1.021	1.520	1.383	0.137	0.024	0.038						

Trues

2D

		Diameter (mm)	Volume (ml)	min	max	mean	std dev	variance	std error	min	max	mean	std dev	variance	
ROI:	1	37	26.52	0.554	3.294	2.021	0.659	0.551	0.045	0.921	2.733	2.092	0.430	0.295	0.023
	2	28	11.49	0.521	2.965	1.820	0.649	0.534	0.061	0.890	2.615	1.854	0.432	0.298	0.033
	3	22	5.57	0.543	2.495	1.580	0.444	0.250	0.056	0.694	2.336	1.612	0.421	0.283	0.043
	4	17	2.57	0.668	2.078	1.385	0.373	0.176	0.062	0.710	1.877	1.330	0.312	0.155	0.042
	5	13	1.15	0.677	1.634	1.151	0.280	0.099	0.061	0.652	1.205	1.003	0.154	0.038	0.029
	6	10	0.52	0.656	1.164	0.995	0.151	0.029	0.042	0.554	0.925	0.808	0.083	0.011	0.020

3D

		Diameter (mm)	Volume (ml)	min	max	mean	std dev	variance	std error	min	max	mean	std dev	variance	
ROI:	1	37	26.52	0.578	3.571	2.243	0.734	0.683	0.050	1.099	2.923	2.288	0.440	0.309	0.024
	2	28	11.49	0.547	3.497	2.060	0.765	0.742	0.072	0.979	2.732	2.021	0.423	0.286	0.032
	3	22	5.57	0.641	2.877	1.802	0.533	0.360	0.068	0.807	2.463	1.752	0.387	0.240	0.040
	4	17	2.57	0.682	2.201	1.561	0.392	0.194	0.065	0.785	1.979	1.482	0.304	0.147	0.041
	5	13	1.15	0.752	1.682	1.219	0.280	0.100	0.061	0.728	1.419	1.215	0.191	0.058	0.036
	6	10	0.52	0.721	1.201	1.061	0.160	0.032	0.044	0.649	1.130	0.971	0.114	0.021	0.028

Scatters

2D

		Diameter (mm)	Volume (ml)	min	max	mean	std dev	variance	std error	min	max	mean	std dev	variance	
ROI:	1	37	26.52	0.094	0.205	0.142	0.016	0.000	0.001						
	2	28	11.49	0.131	0.195	0.163	0.013	0.000	0.001						
	3	22	5.57	0.125	0.175	0.155	0.009	0.000	0.001						
	4	17	2.57	0.148	0.205	0.169	0.011	0.000	0.002						
	5	13	1.15	0.141	0.185	0.161	0.012	0.000	0.003						
	6	10	0.52	0.153	0.192	0.175	0.012	0.000	0.003						

3D

		Diameter (mm)	Volume (ml)	min	max	mean	std dev	variance	std error	min	max	mean	std dev	variance	
ROI:	1	37	26.52	0.134	0.243	0.193	0.021	0.001	0.001						
	2	28	11.49	0.168	0.272	0.224	0.019	0.000	0.002						
	3	22	5.57	0.169	0.250	0.210	0.015	0.000	0.002						
	4	17	2.57	0.169	0.256	0.219	0.020	0.001	0.003						
	5	13	1.15	0.184	0.234	0.203	0.013	0.000	0.003						
	6	10	0.52	0.188	0.261	0.212	0.017	0.000	0.005						

Randoms

2D

		Diameter (mm)	Volume (ml)	min	max	mean	std dev	variance	std error	min	max	mean	std dev	variance	
ROI:	1	37	26.52	0.043	0.150	0.091	0.021	0.001	0.001						
	2	28	11.49	0.044	0.143	0.094	0.023	0.001	0.002						
	3	22	5.57	0.077	0.174	0.119	0.023	0.001	0.003						
	4	17	2.57	0.061	0.159	0.103	0.024	0.001	0.004						
	5	13	1.15	0.048	0.142	0.093	0.029	0.001	0.006						
	6	10	0.52	0.088	0.143	0.126	0.015	0.000	0.004						

3D

		Diameter (mm)	Volume (ml)	min	max	mean	std dev	variance	std error	min	max	mean	std dev	variance	
ROI:	1	37	26.52	0.063	0.119	0.091	0.011	0.000	0.001						
	2	28	11.49	0.082	0.141	0.107	0.010	0.000	0.001						
	3	22	5.57	0.081	0.129	0.106	0.009	0.000	0.001						
	4	17	2.57	0.082	0.139	0.109	0.010	0.000	0.002						
	5	13	1.15	0.092	0.111	0.099	0.005	0.000	0.001						
	6	10	0.52	0.087	0.130	0.108	0.008	0.000	0.002						

Table a 9: SUVs of 105%VoI of the Body Phantom spheres acquired with a 5:1 sphere-to-background contrast by simulation (SIM) and PET scanner (PET)

All

2D				min	max	mean	std dev	variance	std error	min	max	mean	std dev	variance	std error
		Diameter (mm)	Volume (ml)												
ROI:	1	37	26.52	0.538	3.591	2.035	0.724	0.664	0.042						
	2	28	11.49	0.681	3.242	1.912	0.667	0.564	0.055						
	3	22	5.57	0.701	2.712	1.698	0.461	0.269	0.051						
	4	17	2.57	0.770	2.307	1.587	0.361	0.165	0.057						
	5	13	1.15	0.890	1.892	1.362	0.282	0.101	0.058						
	6	10	0.52	0.941	1.422	1.252	0.147	0.027	0.039						
3D				min	max	mean	std dev	variance	std error	min	max	mean	std dev	variance	std error
		Diameter (mm)	Volume (ml)												
ROI:	1	37	26.52	0.615	3.940	2.304	0.809	0.829	0.047						
	2	28	11.49	0.737	3.950	2.214	0.797	0.806	0.066						
	3	22	5.57	0.845	3.169	1.978	0.556	0.391	0.061						
	4	17	2.57	0.861	2.480	1.818	0.389	0.192	0.061						
	5	13	1.15	1.040	1.941	1.476	0.261	0.086	0.053						
	6	10	0.52	1.021	1.520	1.356	0.148	0.028	0.040						

Trues

2D				min	max	mean	std dev	variance	std error	min	max	mean	std dev	variance	
		Diameter (mm)	Volume (ml)												
ROI:	1	37	26.52	0.328	3.294	1.792	0.719	0.655	0.042	0.758	2.733	1.889	0.524	0.438	0.024
	2	28	11.49	0.447	2.965	1.650	0.669	0.568	0.055	0.748	2.615	1.680	0.490	0.384	0.033
	3	22	5.57	0.453	2.495	1.441	0.477	0.288	0.052	0.618	2.336	1.479	0.446	0.318	0.041
	4	17	2.57	0.518	2.078	1.324	0.377	0.180	0.060	0.642	1.877	1.238	0.327	0.171	0.040
	5	13	1.15	0.646	1.634	1.108	0.284	0.102	0.058	0.642	1.205	0.964	0.163	0.042	0.028
	6	10	0.52	0.656	1.164	0.971	0.157	0.031	0.042	0.554	0.925	0.785	0.090	0.013	0.019
3D				min	max	mean	std dev	variance	std error	min	max	mean	std dev	variance	
		Diameter (mm)	Volume (ml)												
ROI:	1	37	26.52	0.365	3.571	1.988	0.800	0.811	0.046	0.826	2.923	2.076	0.542	0.469	0.025
	2	28	11.49	0.435	3.497	1.865	0.783	0.778	0.065	0.757	2.732	1.843	0.491	0.385	0.033
	3	22	5.57	0.509	2.877	1.641	0.564	0.404	0.062	0.644	2.463	1.621	0.424	0.287	0.039
	4	17	2.57	0.556	2.201	1.488	0.402	0.205	0.064	0.716	1.979	1.389	0.328	0.172	0.040
	5	13	1.15	0.708	1.682	1.174	0.282	0.101	0.057	0.701	1.419	1.165	0.207	0.069	0.036
	6	10	0.52	0.721	1.201	1.032	0.168	0.036	0.045	0.649	1.130	0.940	0.124	0.025	0.026

Scatters

2D				min	max	mean	std dev	variance	std error	min	max	mean	std dev	variance	
		Diameter (mm)	Volume (ml)												
ROI:	1	37	26.52	0.094	0.205	0.141	0.016	0.000	0.001						
	2	28	11.49	0.129	0.195	0.162	0.014	0.000	0.001						
	3	22	5.57	0.122	0.175	0.155	0.009	0.000	0.001						
	4	17	2.57	0.148	0.205	0.170	0.011	0.000	0.002						
	5	13	1.15	0.141	0.185	0.161	0.012	0.000	0.002						
	6	10	0.52	0.153	0.192	0.176	0.012	0.000	0.003						
3D				min	max	mean	std dev	variance	std error	min	max	mean	std dev	variance	
		Diameter (mm)	Volume (ml)												
ROI:	1	37	26.52	0.134	0.243	0.191	0.021	0.001	0.001						
	2	28	11.49	0.156	0.272	0.221	0.020	0.001	0.002						
	3	22	5.57	0.167	0.265	0.209	0.016	0.000	0.002						
	4	17	2.57	0.169	0.256	0.219	0.020	0.001	0.003						
	5	13	1.15	0.184	0.234	0.203	0.013	0.000	0.003						
	6	10	0.52	0.188	0.261	0.213	0.017	0.000	0.005						

Randoms

2D				min	max	mean	std dev	variance	std error	min	max	mean	std dev	variance	
		Diameter (mm)	Volume (ml)												
ROI:	1	37	26.52	0.043	0.174	0.090	0.021	0.001	0.001						
	2	28	11.49	0.044	0.143	0.094	0.023	0.001	0.002						
	3	22	5.57	0.071	0.174	0.118	0.023	0.001	0.002						
	4	17	2.57	0.061	0.159	0.103	0.023	0.001	0.004						
	5	13	1.15	0.044	0.142	0.091	0.029	0.001	0.006						
	6	10	0.52	0.088	0.143	0.124	0.016	0.000	0.004						
3D				min	max	mean	std dev	variance	std error	min	max	mean	std dev	variance	
		Diameter (mm)	Volume (ml)												
ROI:	1	37	26.52	0.058	0.119	0.090	0.011	0.000	0.001						
	2	28	11.49	0.076	0.141	0.106	0.011	0.000	0.001						
	3	22	5.57	0.081	0.129	0.106	0.009	0.000	0.001						
	4	17	2.57	0.082	0.139	0.109	0.010	0.000	0.002						
	5	13	1.15	0.092	0.111	0.100	0.005	0.000	0.001						
	6	10	0.52	0.087	0.130	0.108	0.009	0.000	0.002						

Table a 10: SUVs of 110%VoI of the Body Phantom spheres acquired with a 5:1 sphere-to-background contrast by simulation (SIM) and PET scanner (PET)

All

2D				min	max	mean	std dev	variance	std error	min	max	mean	std dev	variance	std error
		Diameter (mm)	Volume (ml)												
ROI:	1	37	26.52	0.432	3.591	1.922	0.748	0.710	0.041						
	2	28	11.49	0.681	3.242	1.835	0.670	0.569	0.054						
	3	22	5.57	0.701	2.712	1.629	0.471	0.281	0.049						
	4	17	2.57	0.762	2.307	1.547	0.369	0.172	0.054						
	5	13	1.15	0.730	1.892	1.339	0.279	0.099	0.055						
	6	10	0.52	0.900	1.422	1.234	0.155	0.030	0.040						
3D				min	max	mean	std dev	variance	std error	min	max	mean	std dev	variance	std error
		Diameter (mm)	Volume (ml)												
ROI:	1	37	26.52	0.529	3.940	2.179	0.834	0.883	0.046						
	2	28	11.49	0.737	3.950	2.124	0.798	0.808	0.064						
	3	22	5.57	0.789	3.169	1.897	0.564	0.403	0.059						
	4	17	2.57	0.842	2.480	1.769	0.400	0.203	0.059						
	5	13	1.15	0.949	1.941	1.453	0.258	0.084	0.051						
	6	10	0.52	0.891	1.520	1.339	0.157	0.031	0.041						

Trues

2D				min	max	mean	std dev	variance	std error	min	max	mean	std dev	variance	
		Diameter (mm)	Volume (ml)												
ROI:	1	37	26.52	0.260	3.294	1.681	0.743	0.700	0.041	0.689	2.733	1.784	0.563	0.507	0.025
	2	28	11.49	0.446	2.965	1.573	0.671	0.571	0.054	0.669	2.615	1.596	0.510	0.416	0.032
	3	22	5.57	0.453	2.495	1.369	0.486	0.299	0.051	0.618	2.336	1.417	0.455	0.330	0.039
	4	17	2.57	0.492	2.078	1.282	0.383	0.186	0.057	0.642	1.877	1.200	0.332	0.176	0.039
	5	13	1.15	0.494	1.634	1.085	0.280	0.100	0.055	0.642	1.205	0.945	0.167	0.045	0.027
	6	10	0.52	0.641	1.164	0.952	0.164	0.034	0.042	0.554	0.925	0.775	0.093	0.014	0.019
3D				min	max	mean	std dev	variance	std error	min	max	mean	std dev	variance	
		Diameter (mm)	Volume (ml)												
ROI:	1	37	26.52	0.292	3.571	1.865	0.825	0.863	0.045	0.763	2.923	1.965	0.587	0.551	0.026
	2	28	11.49	0.435	3.497	1.776	0.784	0.779	0.063	0.753	2.732	1.755	0.517	0.427	0.033
	3	22	5.57	0.466	2.877	1.558	0.572	0.415	0.060	0.626	2.463	1.558	0.438	0.306	0.038
	4	17	2.57	0.516	2.201	1.437	0.412	0.215	0.061	0.716	1.979	1.348	0.338	0.182	0.039
	5	13	1.15	0.623	1.682	1.150	0.277	0.097	0.054	0.701	1.419	1.141	0.214	0.073	0.034
	6	10	0.52	0.613	1.201	1.012	0.176	0.039	0.045	0.626	1.130	0.927	0.128	0.026	0.026

Scatters

2D				min	max	mean	std dev	variance	std error	min	max	mean	std dev	variance	
		Diameter (mm)	Volume (ml)												
ROI:	1	37	26.52	0.094	0.205	0.140	0.017	0.000	0.001						
	2	28	11.49	0.129	0.195	0.161	0.014	0.000	0.001						
	3	22	5.57	0.122	0.175	0.155	0.010	0.000	0.001						
	4	17	2.57	0.138	0.205	0.170	0.012	0.000	0.002						
	5	13	1.15	0.141	0.185	0.160	0.012	0.000	0.002						
	6	10	0.52	0.153	0.192	0.176	0.012	0.000	0.003						
3D				min	max	mean	std dev	variance	std error	min	max	mean	std dev	variance	
		Diameter (mm)	Volume (ml)												
ROI:	1	37	26.52	0.134	0.243	0.191	0.022	0.001	0.001						
	2	28	11.49	0.156	0.272	0.219	0.020	0.001	0.002						
	3	22	5.57	0.167	0.265	0.208	0.016	0.000	0.002						
	4	17	2.57	0.169	0.256	0.218	0.021	0.001	0.003						
	5	13	1.15	0.184	0.234	0.203	0.013	0.000	0.003						
	6	10	0.52	0.176	0.261	0.213	0.018	0.000	0.005						

Randoms

2D				min	max	mean	std dev	variance	std error	min	max	mean	std dev	variance	
		Diameter (mm)	Volume (ml)												
ROI:	1	37	26.52	0.043	0.174	0.089	0.021	0.001	0.001						
	2	28	11.49	0.044	0.143	0.093	0.023	0.001	0.002						
	3	22	5.57	0.071	0.174	0.118	0.023	0.001	0.002						
	4	17	2.57	0.061	0.159	0.103	0.022	0.001	0.003						
	5	13	1.15	0.044	0.142	0.090	0.028	0.001	0.006						
	6	10	0.52	0.088	0.143	0.124	0.016	0.000	0.004						
3D				min	max	mean	std dev	variance	std error	min	max	mean	std dev	variance	
		Diameter (mm)	Volume (ml)												
ROI:	1	37	26.52	0.058	0.119	0.090	0.011	0.000	0.001						
	2	28	11.49	0.076	0.141	0.106	0.011	0.000	0.001						
	3	22	5.57	0.081	0.129	0.106	0.009	0.000	0.001						
	4	17	2.57	0.082	0.139	0.109	0.011	0.000	0.002						
	5	13	1.15	0.092	0.111	0.100	0.005	0.000	0.001						
	6	10	0.52	0.087	0.130	0.108	0.009	0.000	0.002						

Table a 11: SUVs of 100%VoI of the Body Phantom spheres acquired with a 2:1 sphere-to-background contrast by simulation (SIM) and PET scanner (PET)

All

2D

		Diameter (mm)	Volume (ml)	min	max	mean	std dev	variance	std error	min	max	mean	std dev	variance	std error
ROI:	1	37	26.52	0.629	1.831	1.359	0.260	0.068	0.016						
	2	28	11.49	0.920	1.736	1.367	0.192	0.037	0.017						
	3	22	5.57	0.832	1.344	1.136	0.118	0.014	0.014						
	4	17	2.57	1.044	1.335	1.191	0.083	0.007	0.014						
	5	13	1.15	1.014	1.249	1.163	0.062	0.004	0.013						
	6	10	0.52	1.021	1.166	1.122	0.041	0.002	0.011						

3D

		Diameter (mm)	Volume (ml)	min	max	mean	std dev	variance	std error	min	max	mean	std dev	variance	std error
ROI:	1	37	26.52	0.591	1.866	1.344	0.257	0.066	0.016						
	2	28	11.49	0.907	1.810	1.382	0.219	0.048	0.020						
	3	22	5.57	0.835	1.424	1.177	0.135	0.018	0.016						
	4	17	2.57	0.973	1.322	1.198	0.074	0.005	0.012						
	5	13	1.15	0.981	1.139	1.094	0.035	0.001	0.007						
	6	10	0.52	0.954	1.093	1.043	0.039	0.002	0.010						

Trues

2D

		Diameter (mm)	Volume (ml)	min	max	mean	std dev	variance	std error	min	max	mean	std dev	variance	
ROI:	1	37	26.52	0.413	1.623	1.122	0.267	0.071	0.017	0.292	1.867	1.317	0.413	0.943	0.021
	2	28	11.49	0.627	1.458	1.099	0.197	0.039	0.018	0.233	1.809	1.167	0.432	1.036	0.031
	3	22	5.57	0.539	1.074	0.867	0.124	0.015	0.015	0.233	1.809	1.053	0.399	0.882	0.039
	4	17	2.57	0.740	1.029	0.894	0.081	0.007	0.014	0.292	1.517	0.842	0.337	0.631	0.043
	5	13	1.15	0.741	0.962	0.887	0.056	0.003	0.012	0.175	0.934	0.561	0.225	0.279	0.040
	6	10	0.52	0.733	0.858	0.817	0.036	0.001	0.010	0.233	0.642	0.440	0.147	0.119	0.032

3D

		Diameter (mm)	Volume (ml)	min	max	mean	std dev	variance	std error	min	max	mean	std dev	variance	
ROI:	1	37	26.52	0.371	1.567	1.074	0.256	0.065	0.016	0.189	2.074	1.387	0.510	1.151	0.026
	2	28	11.49	0.602	1.483	1.076	0.213	0.046	0.019	0.189	2.011	1.166	0.499	1.101	0.035
	3	22	5.57	0.527	1.106	0.868	0.133	0.018	0.016	0.251	1.697	0.994	0.415	0.763	0.041
	4	17	2.57	0.653	0.972	0.867	0.066	0.004	0.011	0.189	1.383	0.750	0.330	0.481	0.042
	5	13	1.15	0.675	0.841	0.799	0.039	0.002	0.008	0.189	0.880	0.452	0.216	0.207	0.039
	6	10	0.52	0.629	0.762	0.721	0.033	0.001	0.009	0.189	0.629	0.395	0.154	0.105	0.034

Scatters

2D

		Diameter (mm)	Volume (ml)	min	max	mean	std dev	variance	std error	min	max	mean	std dev	variance	
ROI:	1	37	26.52	0.145	0.232	0.191	0.016	0.000	0.001						
	2	28	11.49	0.184	0.253	0.226	0.016	0.000	0.001						
	3	22	5.57	0.193	0.236	0.215	0.009	0.000	0.001						
	4	17	2.57	0.226	0.264	0.244	0.009	0.000	0.002						
	5	13	1.15	0.213	0.245	0.232	0.006	0.000	0.001						
	6	10	0.52	0.237	0.277	0.257	0.008	0.000	0.002						

3D

		Diameter (mm)	Volume (ml)	min	max	mean	std dev	variance	std error	min	max	mean	std dev	variance	
ROI:	1	37	26.52	0.175	0.263	0.217	0.016	0.000	0.001						
	2	28	11.49	0.224	0.294	0.258	0.017	0.000	0.001						
	3	22	5.57	0.212	0.267	0.246	0.010	0.000	0.001						
	4	17	2.57	0.232	0.303	0.280	0.014	0.000	0.002						
	5	13	1.15	0.222	0.266	0.247	0.010	0.000	0.002						
	6	10	0.52	0.238	0.282	0.259	0.010	0.000	0.003						

Randoms

2D

		Diameter (mm)	Volume (ml)	min	max	mean	std dev	variance	std error	min	max	mean	std dev	variance	
ROI:	1	37	26.52	0.025	0.041	0.033	0.003	0.000	0.000						
	2	28	11.49	0.031	0.048	0.039	0.004	0.000	0.000						
	3	22	5.57	0.030	0.042	0.036	0.002	0.000	0.000						
	4	17	2.57	0.038	0.046	0.041	0.002	0.000	0.000						
	5	13	1.15	0.035	0.045	0.041	0.002	0.000	0.000						
	6	10	0.52	0.037	0.045	0.042	0.001	0.000	0.000						

3D

		Diameter (mm)	Volume (ml)	min	max	mean	std dev	variance	std error	min	max	mean	std dev	variance	
ROI:	1	37	26.52	0.025	0.041	0.034	0.003	0.000	0.000						
	2	28	11.49	0.032	0.047	0.040	0.003	0.000	0.000						
	3	22	5.57	0.035	0.044	0.040	0.002	0.000	0.000						
	4	17	2.57	0.033	0.046	0.041	0.003	0.000	0.000						
	5	13	1.15	0.032	0.043	0.037	0.003	0.000	0.001						
	6	10	0.52	0.035	0.044	0.040	0.002	0.000	0.000						

Table a 12: SUVs of 90%VoI of the Body Phantom spheres acquired with a 2:1 sphere-to-background contrast by simulation (SIM) and PET scanner (PET)

All

2D

		Diameter (mm)	Volume (ml)	min	max	mean	std dev	variance	std error	min	max	mean	std dev	variance	std error
ROI:	1	37	26.52	0.709	1.831	1.433	0.238	0.055	0.017						
	2	28	11.49	0.960	1.736	1.420	0.179	0.031	0.018						
	3	22	5.57	0.902	1.344	1.167	0.108	0.011	0.015						
	4	17	2.57	1.064	1.335	1.202	0.083	0.007	0.016						
	5	13	1.15	1.014	1.249	1.171	0.058	0.003	0.013						
	6	10	0.52	1.021	1.166	1.128	0.038	0.001	0.011						

3D

		Diameter (mm)	Volume (ml)	min	max	mean	std dev	variance	std error	min	max	mean	std dev	variance	std error
ROI:	1	37	26.52	0.713	1.866	1.417	0.234	0.054	0.017						
	2	28	11.49	0.948	1.810	1.438	0.210	0.043	0.021						
	3	22	5.57	0.896	1.424	1.215	0.122	0.014	0.017						
	4	17	2.57	1.008	1.322	1.212	0.071	0.005	0.013						
	5	13	1.15	0.981	1.139	1.101	0.033	0.001	0.008						
	6	10	0.52	0.954	1.093	1.049	0.036	0.001	0.011						

Trues

2D

		Diameter (mm)	Volume (ml)	min	max	mean	std dev	variance	std error	min	max	mean	std dev	variance	
ROI:	1	37	26.52	0.493	1.623	1.195	0.246	0.059	0.017	0.408	1.867	1.465	0.324	0.583	0.018
	2	28	11.49	0.673	1.458	1.151	0.185	0.034	0.019	0.350	1.809	1.298	0.388	0.833	0.032
	3	22	5.57	0.611	1.074	0.899	0.114	0.013	0.015	0.350	1.809	1.171	0.374	0.776	0.041
	4	17	2.57	0.766	1.029	0.904	0.082	0.007	0.015	0.292	1.517	0.918	0.330	0.604	0.048
	5	13	1.15	0.741	0.962	0.894	0.052	0.003	0.012	0.233	0.934	0.589	0.219	0.266	0.045
	6	10	0.52	0.738	0.858	0.823	0.034	0.001	0.010	0.233	0.642	0.467	0.150	0.124	0.039

3D

		Diameter (mm)	Volume (ml)	min	max	mean	std dev	variance	std error	min	max	mean	std dev	variance	
ROI:	1	37	26.52	0.473	1.567	1.145	0.234	0.054	0.017	0.314	2.074	1.535	0.440	0.856	0.025
	2	28	11.49	0.631	1.483	1.129	0.205	0.041	0.021	0.189	2.011	1.284	0.466	0.962	0.038
	3	22	5.57	0.576	1.106	0.904	0.120	0.014	0.016	0.251	1.697	1.077	0.397	0.698	0.044
	4	17	2.57	0.715	0.972	0.879	0.064	0.004	0.012	0.251	1.383	0.789	0.328	0.475	0.047
	5	13	1.15	0.675	0.841	0.806	0.037	0.001	0.008	0.189	0.880	0.460	0.210	0.196	0.043
	6	10	0.52	0.629	0.762	0.727	0.031	0.001	0.009	0.189	0.629	0.407	0.158	0.111	0.041

Scatters

2D

		Diameter (mm)	Volume (ml)	min	max	mean	std dev	variance	std error	min	max	mean	std dev	variance	
ROI:	1	37	26.52	0.145	0.232	0.191	0.015	0.000	0.001						
	2	28	11.49	0.184	0.253	0.227	0.015	0.000	0.002						
	3	22	5.57	0.193	0.236	0.215	0.009	0.000	0.001						
	4	17	2.57	0.226	0.259	0.244	0.009	0.000	0.002						
	5	13	1.15	0.213	0.245	0.232	0.006	0.000	0.001						
	6	10	0.52	0.237	0.277	0.257	0.007	0.000	0.002						

3D

		Diameter (mm)	Volume (ml)	min	max	mean	std dev	variance	std error	min	max	mean	std dev	variance	
ROI:	1	37	26.52	0.175	0.263	0.218	0.016	0.000	0.001						
	2	28	11.49	0.227	0.294	0.260	0.016	0.000	0.002						
	3	22	5.57	0.225	0.263	0.248	0.009	0.000	0.001						
	4	17	2.57	0.232	0.303	0.280	0.013	0.000	0.003						
	5	13	1.15	0.222	0.263	0.247	0.009	0.000	0.002						
	6	10	0.52	0.238	0.277	0.260	0.010	0.000	0.003						

Randoms

2D

		Diameter (mm)	Volume (ml)	min	max	mean	std dev	variance	std error	min	max	mean	std dev	variance	
ROI:	1	37	26.52	0.025	0.041	0.033	0.003	0.000	0.000						
	2	28	11.49	0.032	0.048	0.039	0.004	0.000	0.000						
	3	22	5.57	0.030	0.042	0.036	0.002	0.000	0.000						
	4	17	2.57	0.038	0.046	0.041	0.002	0.000	0.000						
	5	13	1.15	0.035	0.045	0.041	0.002	0.000	0.001						
	6	10	0.52	0.037	0.045	0.042	0.001	0.000	0.000						

3D

		Diameter (mm)	Volume (ml)	min	max	mean	std dev	variance	std error	min	max	mean	std dev	variance	
ROI:	1	37	26.52	0.027	0.041	0.034	0.003	0.000	0.000						
	2	28	11.49	0.033	0.047	0.041	0.003	0.000	0.000						
	3	22	5.57	0.035	0.044	0.040	0.002	0.000	0.000						
	4	17	2.57	0.034	0.046	0.041	0.003	0.000	0.000						
	5	13	1.15	0.032	0.043	0.037	0.003	0.000	0.001						
	6	10	0.52	0.039	0.042	0.040	0.002	0.000	0.000						

Table a 13: SUVs of 95%VoI of the Body Phantom spheres acquired with a 2:1 sphere-to-background contrast by simulation (SIM) and PET scanner (PET)

All

2D

		Diameter (mm)	Volume (ml)	min	max	mean	std dev	variance	std error	min	max	mean	std dev	variance	std error
ROI:	1	37	26.52	0.709	1.831	1.396	0.251	0.061	0.017						
	2	28	11.49	0.960	1.736	1.393	0.187	0.034	0.018						
	3	22	5.57	0.834	1.344	1.153	0.112	0.012	0.014						
	4	17	2.57	1.044	1.335	1.197	0.083	0.007	0.014						
	5	13	1.15	1.014	1.249	1.167	0.059	0.003	0.013						
	6	10	0.52	1.021	1.166	1.125	0.039	0.001	0.011						

3D

		Diameter (mm)	Volume (ml)	min	max	mean	std dev	variance	std error	min	max	mean	std dev	variance	std error
ROI:	1	37	26.52	0.705	1.866	1.381	0.247	0.059	0.017						
	2	28	11.49	0.948	1.810	1.409	0.216	0.045	0.020						
	3	22	5.57	0.835	1.424	1.197	0.128	0.016	0.016						
	4	17	2.57	0.973	1.322	1.204	0.072	0.005	0.012						
	5	13	1.15	0.981	1.139	1.096	0.035	0.001	0.008						
	6	10	0.52	0.954	1.093	1.046	0.037	0.001	0.010						

Trues

2D

		Diameter (mm)	Volume (ml)	min	max	mean	std dev	variance	std error	min	max	mean	std dev	variance	
ROI:	1	37	26.52	0.493	1.623	1.158	0.258	0.065	0.017	0.350	1.867	1.394	0.370	0.758	0.020
	2	28	11.49	0.673	1.458	1.124	0.192	0.036	0.018	0.292	1.809	1.234	0.412	0.939	0.031
	3	22	5.57	0.539	1.074	0.884	0.118	0.014	0.015	0.350	1.809	1.113	0.386	0.825	0.040
	4	17	2.57	0.740	1.029	0.899	0.081	0.006	0.013	0.292	1.517	0.880	0.335	0.621	0.046
	5	13	1.15	0.741	0.962	0.890	0.054	0.003	0.012	0.233	0.934	0.580	0.221	0.271	0.042
	6	10	0.52	0.738	0.858	0.820	0.035	0.001	0.010	0.233	0.642	0.451	0.148	0.122	0.036

3D

		Diameter (mm)	Volume (ml)	min	max	mean	std dev	variance	std error	min	max	mean	std dev	variance	
ROI:	1	37	26.52	0.461	1.567	1.109	0.246	0.059	0.017	0.251	2.074	1.462	0.477	1.007	0.025
	2	28	11.49	0.631	1.483	1.101	0.210	0.043	0.020	0.189	2.011	1.226	0.483	1.032	0.037
	3	22	5.57	0.527	1.106	0.887	0.126	0.016	0.016	0.251	1.697	1.037	0.408	0.736	0.042
	4	17	2.57	0.653	0.972	0.872	0.064	0.004	0.011	0.251	1.383	0.769	0.330	0.481	0.045
	5	13	1.15	0.675	0.841	0.802	0.039	0.001	0.008	0.189	0.880	0.455	0.213	0.201	0.040
	6	10	0.52	0.629	0.762	0.724	0.032	0.001	0.009	0.189	0.629	0.400	0.153	0.104	0.037

Scatters

2D

		Diameter (mm)	Volume (ml)	min	max	mean	std dev	variance	std error	min	max	mean	std dev	variance	
ROI:	1	37	26.52	0.145	0.232	0.191	0.016	0.000	0.001						
	2	28	11.49	0.184	0.253	0.226	0.016	0.000	0.001						
	3	22	5.57	0.193	0.236	0.215	0.009	0.000	0.001						
	4	17	2.57	0.226	0.264	0.244	0.009	0.000	0.001						
	5	13	1.15	0.213	0.245	0.232	0.006	0.000	0.001						
	6	10	0.52	0.237	0.277	0.257	0.007	0.000	0.002						

3D

		Diameter (mm)	Volume (ml)	min	max	mean	std dev	variance	std error	min	max	mean	std dev	variance	
ROI:	1	37	26.52	0.175	0.263	0.218	0.016	0.000	0.001						
	2	28	11.49	0.224	0.294	0.259	0.016	0.000	0.002						
	3	22	5.57	0.212	0.263	0.247	0.010	0.000	0.001						
	4	17	2.57	0.232	0.303	0.280	0.014	0.000	0.002						
	5	13	1.15	0.222	0.266	0.247	0.009	0.000	0.002						
	6	10	0.52	0.238	0.282	0.260	0.010	0.000	0.003						

Randoms

2D

		Diameter (mm)	Volume (ml)	min	max	mean	std dev	variance	std error	min	max	mean	std dev	variance	
ROI:	1	37	26.52	0.025	0.041	0.033	0.003	0.000	0.000						
	2	28	11.49	0.032	0.048	0.039	0.004	0.000	0.000						
	3	22	5.57	0.030	0.042	0.036	0.002	0.000	0.000						
	4	17	2.57	0.038	0.046	0.041	0.002	0.000	0.000						
	5	13	1.15	0.035	0.045	0.041	0.002	0.000	0.000						
	6	10	0.52	0.037	0.045	0.042	0.001	0.000	0.000						

3D

		Diameter (mm)	Volume (ml)	min	max	mean	std dev	variance	std error	min	max	mean	std dev	variance	
ROI:	1	37	26.52	0.027	0.041	0.034	0.003	0.000	0.000						
	2	28	11.49	0.032	0.047	0.040	0.003	0.000	0.000						
	3	22	5.57	0.035	0.044	0.040	0.002	0.000	0.000						
	4	17	2.57	0.033	0.046	0.041	0.003	0.000	0.000						
	5	13	1.15	0.032	0.043	0.037	0.003	0.000	0.001						
	6	10	0.52	0.035	0.044	0.040	0.002	0.000	0.000						

Table a 14: SUVs of 105%VoI of the Body Phantom spheres acquired with a 2:1 sphere-to-background contrast by simulation (SIM) and PET scanner (PET)

All

2D

		Diameter (mm)	Volume (ml)	min	max	mean	std dev	variance	std error	min	max	mean	std dev	variance	std error
ROI:	1	37	26.52	0.433	1.831	1.323	0.270	0.071	0.016						
	2	28	11.49	0.827	1.736	1.341	0.197	0.038	0.016						
	3	22	5.57	0.831	1.344	1.122	0.122	0.015	0.013						
	4	17	2.57	0.923	1.335	1.185	0.084	0.007	0.013						
	5	13	1.15	1.014	1.249	1.160	0.063	0.004	0.013						
	6	10	0.52	1.021	1.166	1.119	0.040	0.002	0.011						

3D

		Diameter (mm)	Volume (ml)	min	max	mean	std dev	variance	std error	min	max	mean	std dev	variance	std error
ROI:	1	37	26.52	0.433	1.866	1.310	0.266	0.069	0.015						
	2	28	11.49	0.812	1.810	1.355	0.223	0.048	0.018						
	3	22	5.57	0.834	1.424	1.161	0.139	0.019	0.015						
	4	17	2.57	0.961	1.322	1.191	0.077	0.006	0.012						
	5	13	1.15	0.981	1.139	1.091	0.036	0.001	0.007						
	6	10	0.52	0.954	1.093	1.041	0.040	0.002	0.011						

Trues

2D

		Diameter (mm)	Volume (ml)	min	max	mean	std dev	variance	std error	min	max	mean	std dev	variance	
ROI:	1	37	26.52	0.271	1.623	1.087	0.276	0.074	0.016	0.233	1.867	1.238	0.448	1.111	0.021
	2	28	11.49	0.553	1.458	1.073	0.202	0.040	0.017	0.233	1.809	1.100	0.450	1.124	0.030
	3	22	5.57	0.539	1.074	0.853	0.129	0.016	0.014	0.233	1.809	0.996	0.407	0.918	0.037
	4	17	2.57	0.627	1.029	0.887	0.083	0.007	0.013	0.233	1.517	0.803	0.339	0.638	0.042
	5	13	1.15	0.741	0.962	0.883	0.057	0.003	0.012	0.175	0.934	0.552	0.227	0.285	0.039
	6	10	0.52	0.733	0.858	0.815	0.036	0.001	0.010	0.233	0.642	0.428	0.143	0.114	0.030

3D

		Diameter (mm)	Volume (ml)	min	max	mean	std dev	variance	std error	min	max	mean	std dev	variance	
ROI:	1	37	26.52	0.264	1.567	1.041	0.265	0.068	0.015	0.189	2.074	1.309	0.539	1.285	0.025
	2	28	11.49	0.529	1.483	1.049	0.217	0.046	0.018	0.189	2.011	1.110	0.509	1.148	0.034
	3	22	5.57	0.519	1.106	0.852	0.137	0.018	0.015	0.251	1.697	0.953	0.420	0.782	0.038
	4	17	2.57	0.643	0.972	0.860	0.069	0.005	0.011	0.189	1.383	0.729	0.334	0.492	0.041
	5	13	1.15	0.675	0.841	0.796	0.040	0.002	0.008	0.189	0.880	0.444	0.216	0.207	0.038
	6	10	0.52	0.629	0.762	0.720	0.034	0.001	0.009	0.189	0.629	0.390	0.152	0.102	0.032

Scatters

2D

		Diameter (mm)	Volume (ml)	min	max	mean	std dev	variance	std error	min	max	mean	std dev	variance	
ROI:	1	37	26.52	0.138	0.232	0.190	0.016	0.000	0.001						
	2	28	11.49	0.179	0.253	0.225	0.016	0.000	0.001						
	3	22	5.57	0.193	0.236	0.215	0.010	0.000	0.001						
	4	17	2.57	0.226	0.264	0.244	0.009	0.000	0.001						
	5	13	1.15	0.213	0.248	0.232	0.006	0.000	0.001						
	6	10	0.52	0.237	0.277	0.256	0.008	0.000	0.002						

3D

		Diameter (mm)	Volume (ml)	min	max	mean	std dev	variance	std error	min	max	mean	std dev	variance	
ROI:	1	37	26.52	0.151	0.263	0.217	0.017	0.000	0.001						
	2	28	11.49	0.214	0.294	0.257	0.017	0.000	0.001						
	3	22	5.57	0.212	0.281	0.246	0.010	0.000	0.001						
	4	17	2.57	0.232	0.303	0.279	0.015	0.000	0.002						
	5	13	1.15	0.222	0.266	0.247	0.010	0.000	0.002						
	6	10	0.52	0.238	0.282	0.259	0.011	0.000	0.003						

Randoms

2D

		Diameter (mm)	Volume (ml)	min	max	mean	std dev	variance	std error	min	max	mean	std dev	variance	
ROI:	1	37	26.52	0.023	0.041	0.033	0.003	0.000	0.000						
	2	28	11.49	0.031	0.048	0.039	0.004	0.000	0.000						
	3	22	5.57	0.030	0.042	0.036	0.002	0.000	0.000						
	4	17	2.57	0.038	0.046	0.041	0.002	0.000	0.000						
	5	13	1.15	0.035	0.045	0.041	0.002	0.000	0.000						
	6	10	0.52	0.037	0.045	0.042	0.002	0.000	0.000						

3D

		Diameter (mm)	Volume (ml)	min	max	mean	std dev	variance	std error	min	max	mean	std dev	variance	
ROI:	1	37	26.52	0.020	0.041	0.033	0.003	0.000	0.000						
	2	28	11.49	0.030	0.047	0.040	0.003	0.000	0.000						
	3	22	5.57	0.035	0.044	0.040	0.002	0.000	0.000						
	4	17	2.57	0.033	0.047	0.041	0.003	0.000	0.000						
	5	13	1.15	0.032	0.043	0.037	0.003	0.000	0.001						
	6	10	0.52	0.035	0.044	0.040	0.002	0.000	0.000						

Table a 15: SUVs of 110%VoI of the Body Phantom spheres acquired with a 2:1 sphere-to-background contrast by simulation (SIM) and PET scanner (PET)

All

2D

		Diameter (mm)	Volume (ml)	min	max	mean	std dev	variance	std error	min	max	mean	std dev	variance	std error
ROI:	1	37	26.52	0.394	1.831	1.287	0.281	0.077	0.015						
	2	28	11.49	0.827	1.736	1.318	0.200	0.039	0.016						
	3	22	5.57	0.831	1.344	1.107	0.126	0.015	0.013						
	4	17	2.57	0.923	1.335	1.177	0.089	0.008	0.013						
	5	13	1.15	0.941	1.249	1.155	0.064	0.004	0.013						
	6	10	0.52	1.021	1.166	1.116	0.042	0.002	0.011						

3D

		Diameter (mm)	Volume (ml)	min	max	mean	std dev	variance	std error	min	max	mean	std dev	variance	std error
ROI:	1	37	26.52	0.405	1.866	1.275	0.277	0.075	0.015						
	2	28	11.49	0.812	1.810	1.330	0.224	0.049	0.018						
	3	22	5.57	0.789	1.424	1.143	0.143	0.020	0.015						
	4	17	2.57	0.919	1.322	1.181	0.082	0.007	0.012						
	5	13	1.15	0.981	1.139	1.088	0.037	0.001	0.007						
	6	10	0.52	0.903	1.093	1.037	0.043	0.002	0.011						

Trues

2D

		Diameter (mm)	Volume (ml)	min	max	mean	std dev	variance	std error	min	max	mean	std dev	variance	
ROI:	1	37	26.52	0.246	1.623	1.052	0.285	0.079	0.016	0.233	1.867	1.157	0.478	1.269	0.021
	2	28	11.49	0.553	1.458	1.050	0.204	0.041	0.016	0.233	1.809	1.033	0.465	1.196	0.029
	3	22	5.57	0.539	1.074	0.837	0.132	0.017	0.014	0.233	1.809	0.942	0.412	0.942	0.035
	4	17	2.57	0.627	1.029	0.879	0.087	0.007	0.013	0.233	1.517	0.767	0.339	0.637	0.039
	5	13	1.15	0.669	0.962	0.879	0.059	0.003	0.012	0.175	0.934	0.529	0.227	0.287	0.036
	6	10	0.52	0.733	0.858	0.812	0.037	0.001	0.010	0.175	0.642	0.415	0.140	0.109	0.028

3D

		Diameter (mm)	Volume (ml)	min	max	mean	std dev	variance	std error	min	max	mean	std dev	variance	
ROI:	1	37	26.52	0.240	1.567	1.008	0.274	0.073	0.015	0.189	2.074	1.232	0.561	1.396	0.025
	2	28	11.49	0.529	1.483	1.026	0.218	0.046	0.017	0.189	2.011	1.056	0.517	1.181	0.033
	3	22	5.57	0.487	1.106	0.835	0.141	0.019	0.015	0.251	1.697	0.912	0.422	0.789	0.036
	4	17	2.57	0.596	0.972	0.851	0.074	0.005	0.011	0.189	1.383	0.708	0.334	0.493	0.039
	5	13	1.15	0.671	0.841	0.793	0.041	0.002	0.008	0.189	0.880	0.437	0.218	0.211	0.035
	6	10	0.52	0.623	0.762	0.716	0.036	0.001	0.009	0.189	0.629	0.385	0.149	0.099	0.030

Scatters

2D

		Diameter (mm)	Volume (ml)	min	max	mean	std dev	variance	std error	min	max	mean	std dev	variance	
ROI:	1	37	26.52	0.136	0.232	0.190	0.017	0.000	0.001						
	2	28	11.49	0.179	0.253	0.224	0.016	0.000	0.001						
	3	22	5.57	0.191	0.236	0.215	0.010	0.000	0.001						
	4	17	2.57	0.211	0.264	0.244	0.010	0.000	0.001						
	5	13	1.15	0.213	0.248	0.232	0.007	0.000	0.001						
	6	10	0.52	0.237	0.277	0.256	0.009	0.000	0.002						

3D

		Diameter (mm)	Volume (ml)	min	max	mean	std dev	variance	std error	min	max	mean	std dev	variance	
ROI:	1	37	26.52	0.151	0.263	0.216	0.017	0.000	0.001						
	2	28	11.49	0.214	0.294	0.256	0.017	0.000	0.001						
	3	22	5.57	0.212	0.281	0.246	0.011	0.000	0.001						
	4	17	2.57	0.232	0.303	0.279	0.015	0.000	0.002						
	5	13	1.15	0.218	0.267	0.247	0.010	0.000	0.002						
	6	10	0.52	0.223	0.282	0.259	0.011	0.000	0.003						

Randoms

2D

		Diameter (mm)	Volume (ml)	min	max	mean	std dev	variance	std error	min	max	mean	std dev	variance	
ROI:	1	37	26.52	0.021	0.041	0.033	0.003	0.000	0.000						
	2	28	11.49	0.031	0.048	0.039	0.004	0.000	0.000						
	3	22	5.57	0.030	0.042	0.036	0.002	0.000	0.000						
	4	17	2.57	0.037	0.046	0.041	0.002	0.000	0.000						
	5	13	1.15	0.035	0.045	0.040	0.002	0.000	0.000						
	6	10	0.52	0.037	0.045	0.042	0.002	0.000	0.000						

3D

		Diameter (mm)	Volume (ml)	min	max	mean	std dev	variance	std error	min	max	mean	std dev	variance	
ROI:	1	37	26.52	0.020	0.041	0.033	0.003	0.000	0.000						
	2	28	11.49	0.030	0.047	0.039	0.003	0.000	0.000						
	3	22	5.57	0.035	0.045	0.040	0.002	0.000	0.000						
	4	17	2.57	0.033	0.047	0.041	0.003	0.000	0.000						
	5	13	1.15	0.031	0.043	0.037	0.003	0.000	0.001						
	6	10	0.52	0.035	0.044	0.040	0.002	0.000	0.000						

Table a 16: SUVs of 100%VoI of the Body Phantom spheres acquired with a 10:1 sphere-to-background contrast by simulation (SIM) and 64 ×64 matrix

All

2D		Diameter (mm)	Volume (ml)	min	max	mean	std dev	variance
ROI:	1	37	26.52	0.428	2.932	1.660	0.620	0.384
	2	28	11.49	0.472	2.186	1.380	0.460	0.211
	3	22	5.57	0.534	1.329	1.095	0.204	0.042
	4	17	2.57	0.665	1.094	0.921	0.144	0.021
	5	13	1.15	0.522	0.713	0.649	0.058	0.003
	6	10	0.52	0.547	0.655	0.649	0.034	0.001

3D		Diameter (mm)	Volume (ml)	min	max	mean	std dev	variance
ROI:	1	37	26.52	0.433	2.882	1.641	0.601	0.361
	2	28	11.49	0.485	2.211	1.384	0.462	0.214
	3	22	5.57	0.564	1.339	1.106	0.199	0.039
	4	17	2.57	0.686	1.069	0.917	0.130	0.017
	5	13	1.15	0.531	0.721	0.648	0.053	0.003
	6	10	0.52	0.518	0.651	0.621	0.042	0.002

Trues

2D		Diameter (mm)	Volume (ml)	min	max	mean	std dev	variance
ROI:	1	37	26.52	0.272	2.743	1.485	0.611	0.373
	2	28	11.49	0.289	1.991	1.193	0.457	0.209
	3	22	5.57	0.351	1.146	0.914	0.202	0.041
	4	17	2.57	0.498	0.896	0.732	0.137	0.019
	5	13	1.15	0.342	0.539	0.470	0.058	0.003
	6	10	0.52	0.349	0.471	0.462	0.039	0.001

3D		Diameter (mm)	Volume (ml)	min	max	mean	std dev	variance
ROI:	1	37	26.52	0.272	2.676	1.449	0.593	0.351
	2	28	11.49	0.284	1.983	1.176	0.455	0.207
	3	22	5.57	0.360	1.135	0.906	0.197	0.039
	4	17	2.57	0.496	0.865	0.715	0.127	0.016
	5	13	1.15	0.335	0.529	0.455	0.053	0.003
	6	10	0.52	0.314	0.453	0.427	0.042	0.002

Scatters

2D		Diameter (mm)	Volume (ml)	min	max	mean	std dev	variance
ROI:	1	37	26.52	0.074	0.104	0.093	0.007	0.000
	2	28	11.49	0.089	0.109	0.103	0.005	0.000
	3	22	5.57	0.089	0.100	0.096	0.002	0.000
	4	17	2.57	0.095	0.111	0.106	0.005	0.000
	5	13	1.15	0.092	0.104	0.101	0.003	0.000
	6	10	0.52	0.103	0.111	0.105	0.002	0.000

3D		Diameter (mm)	Volume (ml)	min	max	mean	std dev	variance
ROI:	1	37	26.52	0.088	0.134	0.114	0.009	0.000
	2	28	11.49	0.105	0.141	0.125	0.009	0.000
	3	22	5.57	0.100	0.128	0.114	0.008	0.000
	4	17	2.57	0.100	0.132	0.122	0.007	0.000
	5	13	1.15	0.102	0.123	0.117	0.008	0.000
	6	10	0.52	0.114	0.127	0.117	0.005	0.000

Randoms

2D		Diameter (mm)	Volume (ml)	min	max	mean	std dev	variance
ROI:	1	37	26.52	0.049	0.067	0.060	0.004	0.000
	2	28	11.49	0.061	0.076	0.071	0.003	0.000
	3	22	5.57	0.064	0.072	0.068	0.002	0.000
	4	17	2.57	0.067	0.081	0.075	0.003	0.000
	5	13	1.15	0.064	0.072	0.070	0.002	0.000
	6	10	0.52	0.073	0.078	0.074	0.002	0.000

3D		Diameter (mm)	Volume (ml)	min	max	mean	std dev	variance
ROI:	1	37	26.52	0.050	0.076	0.063	0.005	0.000
	2	28	11.49	0.061	0.080	0.074	0.004	0.000
	3	22	5.57	0.064	0.085	0.072	0.004	0.000
	4	17	2.57	0.064	0.085	0.079	0.005	0.000
	5	13	1.15	0.067	0.074	0.072	0.003	0.000
	6	10	0.52	0.072	0.081	0.074	0.003	0.000

Table a 17: SUVs of 100%VoI of the Body Phantom spheres acquired with a 10:1 sphere-to-background contrast by simulation (SIM) and 128 ×128 matrix

All

2D		Diameter (mm)	Volume (ml)	min	max	mean	std dev	variance
ROI:	1	37	26.52	0.530	3.691	2.207	0.778	0.606
	2	28	11.49	0.556	3.332	1.940	0.723	0.523
	3	22	5.57	0.632	2.643	1.685	0.455	0.207
	4	17	2.57	0.724	1.984	1.436	0.313	0.098
	5	13	1.15	0.680	1.404	1.103	0.191	0.037
	6	10	0.52	0.743	1.110	0.983	0.112	0.012

3D		Diameter (mm)	Volume (ml)	min	max	mean	std dev	variance
ROI:	1	37	26.52	0.548	3.653	2.184	0.762	0.581
	2	28	11.49	0.579	3.417	1.956	0.740	0.548
	3	22	5.57	0.674	2.711	1.705	0.466	0.217
	4	17	2.57	0.700	1.921	1.435	0.294	0.087
	5	13	1.15	0.701	1.325	1.064	0.169	0.029
	6	10	0.52	0.705	1.029	0.934	0.097	0.009

Trues

2D		Diameter (mm)	Volume (ml)	min	max	mean	std dev	variance
ROI:	1	37	26.52	0.351	3.484	2.023	0.771	0.594
	2	28	11.49	0.389	3.123	1.745	0.718	0.516
	3	22	5.57	0.439	2.479	1.505	0.462	0.213
	4	17	2.57	0.509	1.793	1.245	0.317	0.101
	5	13	1.15	0.496	1.232	0.928	0.195	0.038
	6	10	0.52	0.535	0.934	0.801	0.116	0.013

3D		Diameter (mm)	Volume (ml)	min	max	mean	std dev	variance
ROI:	1	37	26.52	0.343	3.391	1.977	0.751	0.564
	2	28	11.49	0.387	3.163	1.733	0.728	0.530
	3	22	5.57	0.453	2.495	1.498	0.465	0.216
	4	17	2.57	0.487	1.723	1.225	0.298	0.089
	5	13	1.15	0.501	1.157	0.883	0.177	0.031
	6	10	0.52	0.488	0.850	0.744	0.103	0.011

Scatters

2D		Diameter (mm)	Volume (ml)	min	max	mean	std dev	variance
ROI:	1	37	26.52	0.070	0.117	0.098	0.008	0.000
	2	28	11.49	0.088	0.122	0.108	0.007	0.000
	3	22	5.57	0.087	0.108	0.100	0.004	0.000
	4	17	2.57	0.101	0.121	0.109	0.004	0.000
	5	13	1.15	0.093	0.110	0.100	0.004	0.000
	6	10	0.52	0.100	0.115	0.108	0.003	0.000

3D		Diameter (mm)	Volume (ml)	min	max	mean	std dev	variance
ROI:	1	37	26.52	0.093	0.147	0.121	0.010	0.000
	2	28	11.49	0.108	0.149	0.131	0.009	0.000
	3	22	5.57	0.106	0.128	0.118	0.005	0.000
	4	17	2.57	0.104	0.135	0.126	0.007	0.000
	5	13	1.15	0.107	0.122	0.114	0.003	0.000
	6	10	0.52	0.111	0.126	0.121	0.005	0.000

Randoms

2D		Diameter (mm)	Volume (ml)	min	max	mean	std dev	variance
ROI:	1	37	26.52	0.049	0.073	0.062	0.004	0.000
	2	28	11.49	0.061	0.080	0.072	0.004	0.000
	3	22	5.57	0.063	0.076	0.068	0.002	0.000
	4	17	2.57	0.070	0.083	0.076	0.003	0.000
	5	13	1.15	0.066	0.080	0.074	0.003	0.000
	6	10	0.52	0.069	0.082	0.076	0.002	0.000

3D		Diameter (mm)	Volume (ml)	min	max	mean	std dev	variance
ROI:	1	37	26.52	0.050	0.076	0.063	0.005	0.000
	2	28	11.49	0.063	0.084	0.076	0.004	0.000
	3	22	5.57	0.064	0.080	0.073	0.004	0.000
	4	17	2.57	0.065	0.083	0.077	0.004	0.000
	5	13	1.15	0.066	0.077	0.070	0.003	0.000
	6	10	0.52	0.066	0.078	0.074	0.003	0.000

Table a 18: SUVs of 100%VoI of the Body Phantom spheres acquired with a 10:1 sphere-to-background contrast by simulation (SIM) and 256 ×256 matrix

All

2D				min	max	mean	std dev	variance
		Diameter (mm)	Volume (ml)					
ROI:	1	37	26.52	0.514	4.082	2.415	0.890	0.793
	2	28	11.49	0.503	3.671	2.196	0.884	0.781
	3	22	5.57	0.555	3.536	2.013	0.668	0.446
	4	17	2.57	0.782	2.885	1.849	0.550	0.302
	5	13	1.15	0.714	2.059	1.432	0.352	0.124
	6	10	0.52	0.862	1.603	1.308	0.171	0.029

3D				min	max	mean	std dev	variance
		Diameter (mm)	Volume (ml)					
ROI:	1	37	26.52	0.495	3.958	2.394	0.865	0.748
	2	28	11.49	0.489	4.046	2.207	0.917	0.841
	3	22	5.57	0.655	3.658	2.052	0.674	0.455
	4	17	2.57	0.765	2.814	1.769	0.506	0.256
	5	13	1.15	0.742	2.038	1.457	0.329	0.109
	6	10	0.52	0.882	1.765	1.380	0.218	0.048

Trues

2D				min	max	mean	std dev	variance
		Diameter (mm)	Volume (ml)					
ROI:	1	37	26.52	0.328	3.826	2.229	0.881	0.776
	2	28	11.49	0.327	3.413	2.001	0.878	0.772
	3	22	5.57	0.426	3.311	1.838	0.667	0.445
	4	17	2.57	0.603	2.745	1.662	0.563	0.317
	5	13	1.15	0.541	1.966	1.299	0.375	0.140
	6	10	0.52	0.665	1.515	1.162	0.200	0.040

3D				min	max	mean	std dev	variance
		Diameter (mm)	Volume (ml)					
ROI:	1	37	26.52	0.301	3.657	2.184	0.855	0.731
	2	28	11.49	0.322	3.705	1.984	0.903	0.816
	3	22	5.57	0.452	3.328	1.835	0.664	0.441
	4	17	2.57	0.551	2.649	1.573	0.527	0.278
	5	13	1.15	0.585	1.959	1.308	0.360	0.129
	6	10	0.52	0.661	1.644	1.203	0.242	0.059

Scatters

2D				min	max	mean	std dev	variance
		Diameter (mm)	Volume (ml)					
ROI:	1	37	26.52	0.071	0.134	0.101	0.011	0.000
	2	28	11.49	0.083	0.139	0.112	0.010	0.000
	3	22	5.57	0.069	0.122	0.101	0.009	0.000
	4	17	2.57	0.089	0.128	0.114	0.008	0.000
	5	13	1.15	0.083	0.113	0.096	0.008	0.000
	6	10	0.52	0.103	0.125	0.112	0.004	0.000

3D				min	max	mean	std dev	variance
		Diameter (mm)	Volume (ml)					
ROI:	1	37	26.52	0.092	0.150	0.124	0.012	0.000
	2	28	11.49	0.101	0.179	0.136	0.014	0.000
	3	22	5.57	0.093	0.153	0.125	0.013	0.000
	4	17	2.57	0.087	0.156	0.127	0.010	0.000
	5	13	1.15	0.092	0.140	0.118	0.012	0.000
	6	10	0.52	0.105	0.149	0.135	0.008	0.000

Randoms

2D				min	max	mean	std dev	variance
		Diameter (mm)	Volume (ml)					
ROI:	1	37	26.52	0.047	0.082	0.062	0.006	0.000
	2	28	11.49	0.057	0.090	0.072	0.006	0.000
	3	22	5.57	0.049	0.086	0.069	0.006	0.000
	4	17	2.57	0.063	0.090	0.078	0.005	0.000
	5	13	1.15	0.060	0.082	0.071	0.006	0.000
	6	10	0.52	0.067	0.084	0.073	0.003	0.000

3D				min	max	mean	std dev	variance
		Diameter (mm)	Volume (ml)					
ROI:	1	37	26.52	0.047	0.081	0.063	0.006	0.000
	2	28	11.49	0.058	0.098	0.077	0.007	0.000
	3	22	5.57	0.056	0.093	0.076	0.009	0.000
	4	17	2.57	0.051	0.095	0.077	0.007	0.000
	5	13	1.15	0.060	0.086	0.073	0.007	0.000
	6	10	0.52	0.065	0.088	0.079	0.005	0.000

Table a 19: SUVs of 100%VoI of the Body Phantom spheres acquired with a 10:1 sphere-to-background contrast by simulation (SIM) and 512 ×512 matrix

All

2D				min	max	mean	std dev	variance
		Diameter (mm)	Volume (ml)					
ROI:	1	37	26.52	0.379	4.976	2.538	1.091	1.191
	2	28	11.49	0.374	4.462	2.346	1.128	1.272
	3	22	5.57	0.374	4.217	2.240	0.961	0.924
	4	17	2.57	0.582	3.871	2.092	0.855	0.730
	5	13	1.15	0.460	3.123	1.710	0.545	0.297
	6	10	0.52	0.923	2.154	1.677	0.287	0.082
3D				min	max	mean	std dev	variance
		Diameter (mm)	Volume (ml)					
ROI:	1	37	26.52	0.395	4.591	2.501	1.041	1.083
	2	28	11.49	0.347	4.995	2.356	1.171	1.370
	3	22	5.57	0.442	4.661	2.254	0.956	0.914
	4	17	2.57	0.570	3.893	2.036	0.867	0.752
	5	13	1.15	0.620	2.943	1.768	0.534	0.286
	6	10	0.52	0.858	2.251	1.567	0.315	0.099

Trues

2D				min	max max	mean	std dev	variance
		Diameter (mm)	Volume (ml)					
ROI:	1	37	26.52	0.243	4.627	2.361	1.089	1.187
	2	28	11.49	0.237	4.232	2.158	1.136	1.290
	3	22	5.57	0.246	3.967	2.072	0.985	0.971
	4	17	2.57	0.426	3.680	1.917	0.902	0.814
	5	13	1.15	0.326	3.202	1.599	0.604	0.365
	6	10	0.52	0.703	2.183	1.568	0.343	0.118
3D				min	max max	mean	std dev	variance
		Diameter (mm)	Volume (ml)					
ROI:	1	37	26.52	0.224	4.394	2.299	1.043	1.089
	2	28	11.49	0.204	4.612	2.137	1.162	1.349
	3	22	5.57	0.266	4.293	2.052	0.969	0.939
	4	17	2.57	0.413	3.750	1.860	0.912	0.832
	5	13	1.15	0.435	3.033	1.648	0.607	0.369
	6	10	0.52	0.638	2.261	1.459	0.372	0.138

Scatters

2D				min	max	mean	std dev	variance
		Diameter (mm)	Volume (ml)					
ROI:	1	37	26.52	0.066	0.161	0.103	0.015	0.000
	2	28	11.49	0.072	0.177	0.113	0.014	0.000
	3	22	5.57	0.066	0.137	0.106	0.012	0.000
	4	17	2.57	0.079	0.151	0.114	0.011	0.000
	5	13	1.15	0.062	0.127	0.102	0.012	0.000
	6	10	0.52	0.096	0.136	0.116	0.007	0.000
3D				min	max	mean	std dev	variance
		Diameter (mm)	Volume (ml)					
ROI:	1	37	26.52	0.082	0.182	0.125	0.017	0.000
	2	28	11.49	0.088	0.213	0.139	0.021	0.000
	3	22	5.57	0.085	0.163	0.124	0.018	0.000
	4	17	2.57	0.066	0.163	0.126	0.015	0.000
	5	13	1.15	0.095	0.154	0.127	0.011	0.000
	6	10	0.52	0.103	0.144	0.121	0.009	0.000

Randoms

2D				min	max	mean	std dev	variance
		Diameter (mm)	Volume (ml)					
ROI:	1	37	26.52	0.037	0.103	0.063	0.010	0.000
	2	28	11.49	0.051	0.118	0.073	0.009	0.000
	3	22	5.57	0.045	0.093	0.071	0.008	0.000
	4	17	2.57	0.052	0.108	0.078	0.008	0.000
	5	13	1.15	0.048	0.088	0.071	0.008	0.000
	6	10	0.52	0.063	0.095	0.081	0.006	0.000
3D				min	max	mean	std dev	variance
		Diameter (mm)	Volume (ml)					
ROI:	1	37	26.52	0.044	0.093	0.064	0.009	0.000
	2	28	11.49	0.046	0.118	0.077	0.011	0.000
	3	22	5.57	0.046	0.106	0.077	0.012	0.000
	4	17	2.57	0.045	0.102	0.075	0.009	0.000
	5	13	1.15	0.061	0.098	0.077	0.006	0.000
	6	10	0.52	0.059	0.088	0.077	0.006	0.000

Chapter IV

XCAT Phantom

Table of Contents

4.1 Introduction

In the previous chapter, the influence of partial volume and matrix size on the calculation of SUVs was assessed in a static phantom. The individual contributions of true-, scattered- and random-coincidences to the SUV were also investigated. In this chapter, the influence of the partial volume effect and its contribution to the SUV determination were assessed, but now under the influence of respiratory motion as well as in the presence of activity outside the field-of-view using Monte Carlo simulations of a human phantom.

This chapter is divided into two main sections. The first section presents the evaluation of the parameters that influence SUV calculation in the human phantom as well as an assessment of the contribution of the true-, scattered- and random-coincidences on the determination of SUV. Investigation of the relative contribution of the true-, scattered and random coincidences was done by variation of object size, lesion placement in the lungs and lesion-to-lung contrast.

The second part consists of evaluation of the influence of activity outside the field-of-view on the determination of the SUV. All parameters that were evaluated in the first section were re-assessed in the second section under the differing circumstances.

The influence of the various factors on the calculation of SUVs of pulmonary lesions was evaluated by simulating an anthropomorphic phantom under static conditions as well as during breathing. The impact of the size of the objects, the placement of the objects and different lesion-to-lung contrast was assessed in 2D and 3D modes respectively.

4.2 Methods

4.2.1 XCAT Phantom

The XCAT Phantom V1 (Segars *et al.*, 2008; Segars *et al.*, 2010; XCAT, 2011) was used to assess the influences on the determination of SUV in a human-like configuration. The phantom was described in Chapter 2. For the purposes of the simulations in this chapter

the phantom consisted of slices from the clavicle bones to just below the diaphragm to include the upper part of the liver (Figure 4-1). The phantom was set-up to simulate movement in the thorax during breathing. Twenty frames of 0.25 seconds each were created to simulate a five second breathing cycle. The average image of these frames was obtained and used as input in the simulations. Sixty transaxial slices were initially created using the XCAT program. Since the sixty slices would have been larger than the FoV of the PET scanner, they were compressed to 48 slices by averaging for input into the GATE simulations so that the full extent of the lungs would fit into a single FoV. A log file of the phantom set-up including all the parameters is found in Appendix 4.6.1.

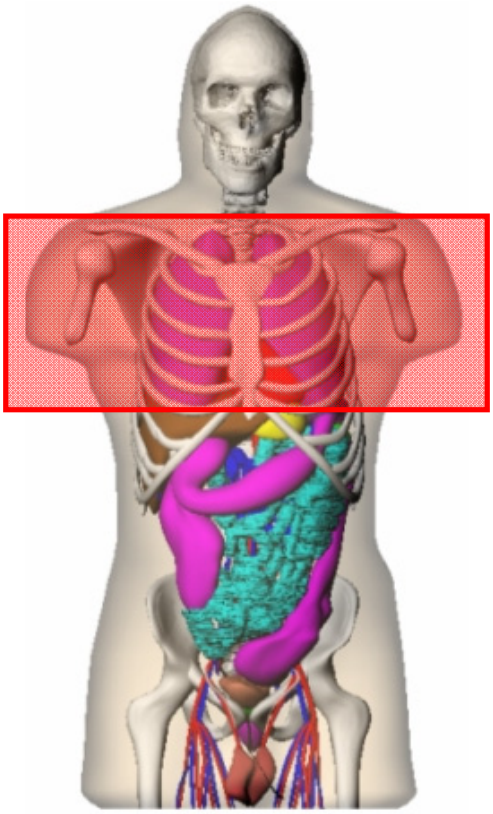

Figure 4-1: The upper part of the XCAT phantom with the area of interest for this study shaded in red (http://www.hopkinsradiology.org/DMIP/Research/xcat). Activity was not allocated to the regions outside the field of view, except for the liver.

Activity images as well as attenuation images (mu-maps) were created for each slice. The activity images contained different intensity values for each tissue type ("Activity ratios" in Appendix 4.6.1), as can be seen in Table 4-1 which was also needed as input for the simulation study (Appendix 4.6.3). Six spherical lesions were placed inside the

lungs, three in the left lung and three in the right lung. These lesions were superimposed on the background structures and did not replace these structures. The lesions were created separately using the XCAT code and added to the already created phantom. Two of the lesions (one in each lung) were placed in the apical region of the lungs where minimal movement and minimal influence from other organs such as scattered photons originating from the liver or heart were expected. Two lesions were placed near the centre of each lung at approximately the same distance from the heart. It was expected that the lesion in the left lung would be influenced by the nearby cardiac activity, and that movement for the right as well as left central lesion would be more than for the apical lesions. Two lesions were placed at the basal areas of the lungs where the maximum amount of lung movement due to breathing was expected (Hallet, 2004). The left lesion would be exposed to scattered photons emanating from the heart whereas the right lesion would be influenced by activity from the liver. Bronchi were avoided as far as possible when placing the lesions. Figures 4.2 – 4.4 show the positioning of these lesions on the activity as well as the attenuation map images. Based on work performed by Hickeson *et al.* (2002) the influence of size of the lesions was assessed by using three sets of lesions with different diameters, viz. 10 mm, 20 mm and 30 mm.

Table 4-1: Voxel values in the activity map of the XCAT Phantom representing different tissue types

Intensity values	Tissue Type
0	Air
1 — 2	Body
3 — 4	Lung
5 — 5	Rib Bone
6 — 6	Spine Bone
7 — 24	Breast (Lesions)
25 — 40	Liver
41 — 75	Heart

To create a realistic representation of the spread of ^{18}F-FDG activity in the XCAT phantom, six PET/CT scans of patients with confirmed pulmonary lesions were selected and the activity concentrations were determined for each of the tissue types and organs.

The average activity concentrations that were found were used in the set-up of the simulations and can be seen in Table 4-2 and an example input file for the simulations is found in Appendix 4.6.4. The activity concentrations assigned to the lesions varied to create a range of different lesion:background ratios. The lesion activity:background activity ratios that were used were 2:1, 5:1 and 10:1. The activity concentrations to achieve these contrast ratios can be seen in Table 4-3 and Appendix 4.6.4.

Table 4-2: Activity concentration values that were assigned to different tissue types according to the intensity values in the activity map of the XCAT phantom

Voxel values	Assigned activity concentration (Bq/voxel)
0 — 0	0
1 — 2	177
3 — 4	163
5 — 5	288
6 — 6	331
7 — 24	1630
25 — 35	530
36 — 75	1986

Table 4-3: Lesion-to-Background activity concentration corresponding to the different contrast ratios

Contrast Ratio	Activity concentration in lesions (Bq/voxel)	Activity concentration in lungs (background) (Bq/voxel)
2:1	326	163
5:1	815	163
10:1	1630	163

The total activity in the XCAT phantom (thoracic area) varied based upon the activity concentrations listed in Table 4-3 and also upon the size of the lesions and a summary of the different total activities can be found in Appendix 4.6.5.

4.2.2 Monte Carlo Simulations with GATE

The Monte Carlo simulations were performed on the computer cluster of the High Performance Computing unit at the University of the Free State. The composition was described in section 3.2.2. The Geant4 Application for Tomographic Emission (GATE) software version 6.1, released on 01/03/2011, was used (http://www.opengatecollaboration.org; Jan *et al.*, 2004).

The GE Discovery ST PET scanner (Du Toit, 2008; Schmidtlein *et al.*, 2006) was used for the simulations, as described in Chapter 3. The macro was kept the same for all simulations with only minor adjustments for imaging time, movement of the phantom partly out of the field-of-view and defining 2D or 3D imaging modes. An example of a macro can be found in Appendix 4.6.2.

The 400 ROOT (http://root.cern.ch/drupal/content/about) files containing the saved data that came about by using 400 cores during a simulation were added after each simulation and the trues, randoms and scatters extracted. The simulated data (comprising of four sets of data giving: (i) combined trues + randoms + scatters data; (ii) trues separately; (iii) randoms separately and (iv) scatters separately) were reconstructed using the OPL-EM algorithm (Reader *et al.*, 2002) (section 2.1.2, Equation 2-4) using two iterations and twenty-one subsets and corrected for sensitivity and attenuation using the attenuation mu-map file.

4.2.3 Methods of Evaluation

The data was exported to a PC and the post processing and determination of the SUVs were done using *A Medical Image Data Examiner* (AMIDE) version 1.0.4 that was obtained at http://amide.sourceforge.net (Loening and Gambhir, 2003). The data was filtered using a Gaussian filter with FWHM of 12 mm. The voxel size was 5.47 mm x 5.47 mm x 3.27 mm for all images using a 128 x 128 matrix. The VoIs were chosen according to the size of the lesions on the activity map images for each set of simulations.

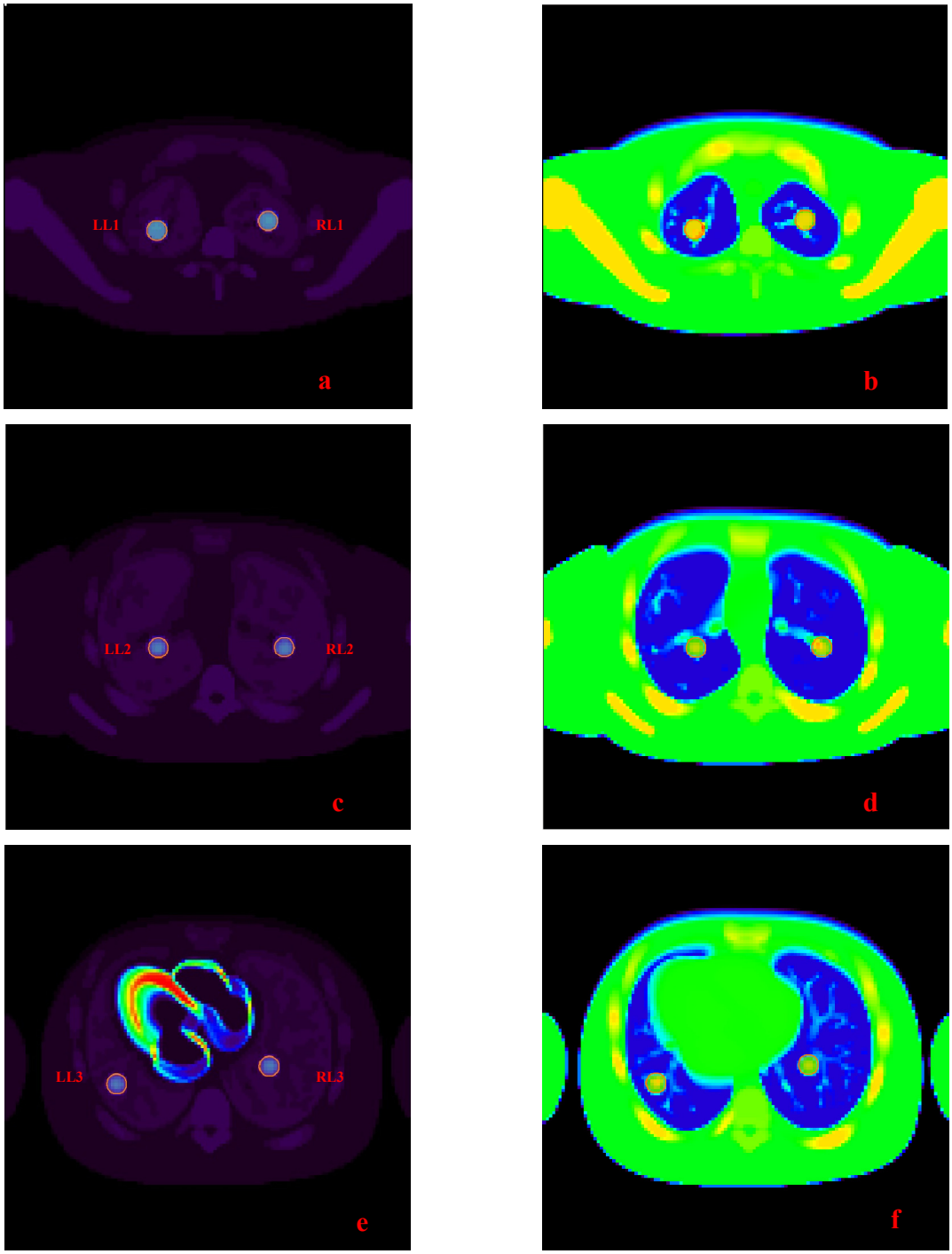

Figure 4-2: Transaxial views of the XCAT phantom showing the lesions and VoIs in the apical region (a & b, with a being the activity image and b the attenuation image), central region (c & d, with c the activity image and d the attenuation image, and basal region near the diaphragm and heart (e & f, with e being the activity image and f the attenuation image). Lesions in the left lung are referred to as LL1 (apical region), LL2 (central region) and LL3 (basal region). Similarly the lesions in the right lung are referred to as RL1, RL2 and RL3.

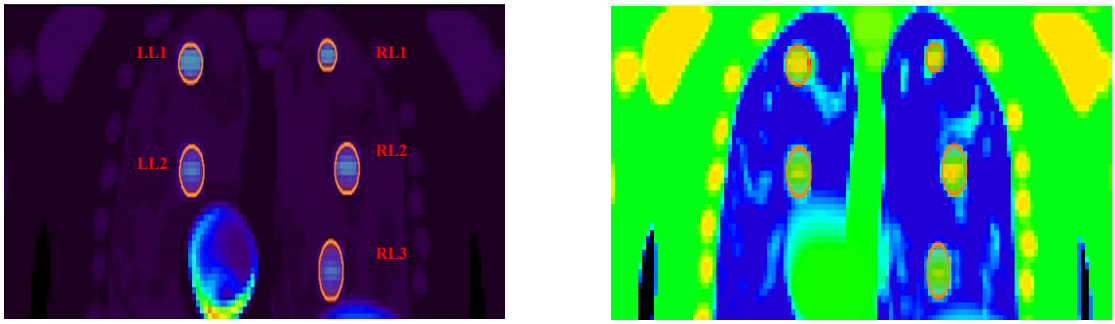

Figure 4-3: Coronal views of the XCAT phantom showing the lesions and VoIs from top to bottom in the apical region, central region and basal region near the diaphragm and heart with the activity image on the left and the attenuation image on the right. Lesions in the left lung are referred to as LL1 (apical region), LL2 (central region) and LL3 (basal region). Similarly the lesions in the right lung are referred to as RL1, RL2 and RL3. The lesion LL3 is not visible on these coronal views.

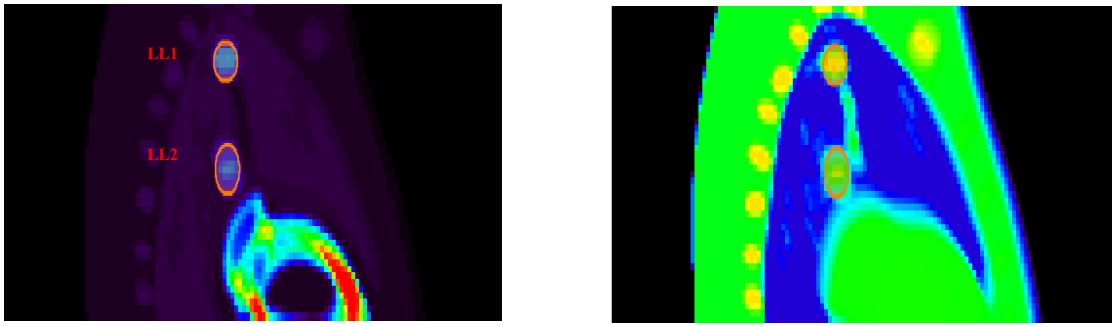

Figure 4-4: Sagittal views of the XCAT phantom showing the lesions and VoIs from top to bottom in the apical region and central region and with the activity image on the left and the attenuation image on the right. The basal lesions are not visible on this section. Lesions in the left lung are referred to as LL1 (apical region) and LL2 (central region). Similarly the lesions in the right lung are referred to as RL1 and RL2.

Examples of the VoIs around the various lesions can be seen in Figure 4-2 representing the transaxial views, Figure 4-3 depicting a coronal view of the three sets of lesions all at once, and Figure 4-4 showing a sagittal view of two of the lesions. The apical lesions are labelled LL1 (left lung) and RL1 (right lung), the lesions in the central area are LL2 (left lung) and RL2 (right lung), and the basal lesions are labelled LL3 (left lung) and RL3 right lung). The activity maps are displayed on the left of each figure while the attenuation images are located on the right. SUVs in each VoI were calculated using Equation 2-5. The weight of the torso of an average sized man (USAARL Report

No 88-5, 1988) was used in the calculation of the SUV throughout this work adjusting only for the variation in weight of the lesions.

4.2.4 Determination of the Parameters influencing SUV calculation

The SUV_{max} and SUV_{mean} were determined for different sphere sizes and for the different contrast ratios described previously for 2D and 3D modes.
The following parameters were investigated:

a) Comparison of the SUV_{max} and SUV_{mean} obtained using simulations of the XCAT phantom in 2D and 3D modes to assess the influence of the partial volume effect by variation of the size of the lesions, by variation of the contrast ratios as was shown in Table 4-3 and by placing the lesions in different areas in the left and right lung during breathing (the average image) and static conditions (at full inspiration and full expiration) respectively.
b) Comparison of the SUV_{max} and SUV_{mean} that were obtained using simulations of the XCAT phantom in 2D and 3D modes after repositioning part of the phantom out of the FoV to assess the influence of activity from the liver lying outside the FoV.

To determine the influence of breathing on the SUV, three different simulations were performed for each configuration. As mentioned in section 4.2.1, the initial simulation used the average of all the breathing frames as input file. The subsequent simulation was performed using the set of images with only frame one, which was the frame of full expiration with all lesions at their "rest position" and where the liver was also partly inside the FoV. The last simulation was done using the set of images consisting of frame ten that was representative of the frame of full inspiration. All lesions would then have moved maximally and the liver was outside the FoV. An illustration of the size and movement of the VoIs around these lesions can be seen in Figure 4-5. For each of the simulations the SUVs in the VoIs were determined and compared.

The influence of activity lying outside the FoV was determined by repositioning the set of images, consisting of the average of all the breathing frames, six slices (19.62 mm) axially outside the FoV. The liver would then have been completely outside the imaging FoV and only scattered radiation and random events were supposed to have an influence on the image inside the FoV. The SUVs for each of the lesions were determined and compared to the corresponding SUVs obtained from the simulation where no axial movement had taken place.

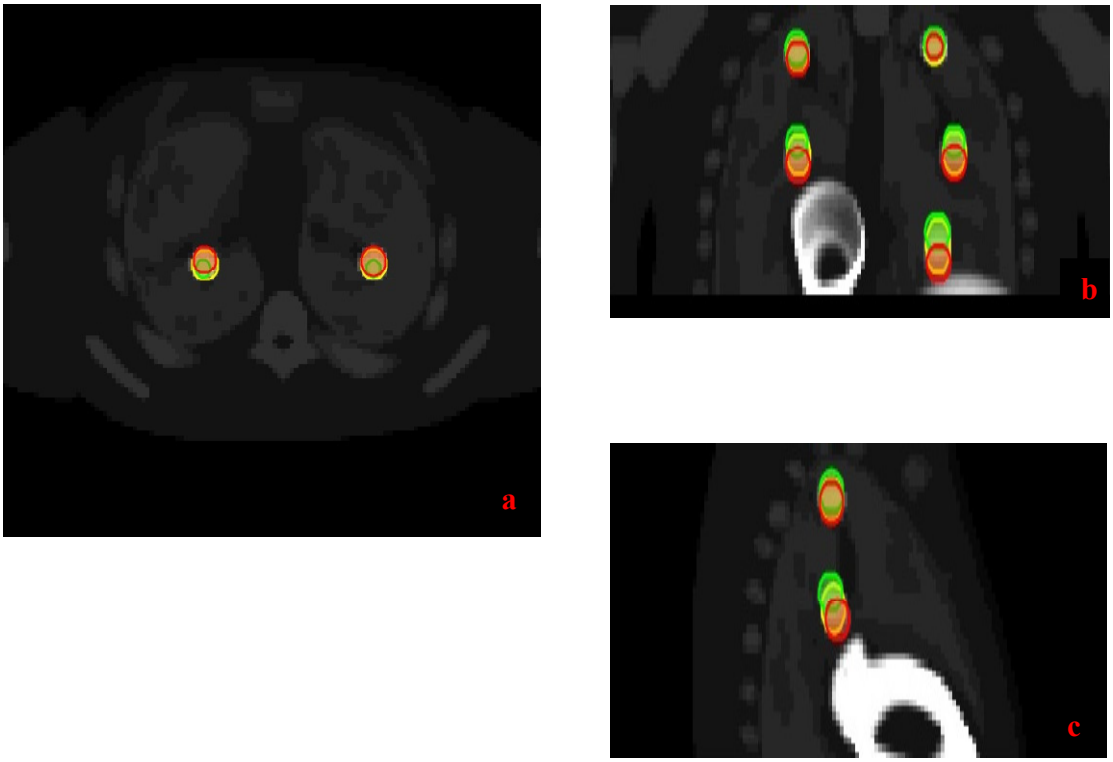

Figure 4-5: Illustration of the size and movement of the VoI during breathing (yellow), full expiration (green) and full inspiration (red) in the transaxial view (a), coronal view (b) and sagittal view (c).

4.2.5 Determination of the Contribution of True-, Scattered- and Random-Coincidences

Calculations of the fractional contribution of the true-, scatter- and random-coincidences respectively to the total image were done to assess the influence of each of these different coincidence types. Normally in the clinical situation corrections are applied for scatter and randoms but it is important to know whether these corrections can be applied

holistically and are properly done, or whether there exists a need to assess the different contributions of the variety of coincidences in diverse areas of the body–in this case, the lung area– and then to apply corrections based on this information. The assessment was done using different contrast ratios, different lesion sizes and varied placement of the lesions in the lung areas during static and breathing conditions.

4.2.6 Statistical Analysis

To determine whether the differences that were found in the comparison of the various SUVs were statistically significant, the F-test (*Two-Sample for Variances*) was first used to determine whether the variances were equal or not. Depending on the outcome of the F-test, the appropriate t-test (*Two-sample testing equality of means assuming Equal or Unequal Variances and Equal Sample Sizes*) was used. A significance level of $p < 0.05$ was used (Nuzzo, 2014). For all SUV_{mean} calculations, the standard deviation in each lesion VoI was determined. Error bars on the SUV_{mean} graphs represented one standard deviation from the mean. For each of the SUV_{max} values which represents a single value in a VoI, the standard error of measurement, ε, was calculated using Equation 3-1.

4.3 Results

The results from the simulations involving the XCAT phantom are presented here. SUV_{max} and SUV_{mean} values were obtained for the defined VoI for each of the six lung lesions for the following datasets acquired using both the 2D and 3D imaging mode. The SUV_{mean} was calculated using the total coincidences as well as the true coincidences, scattered and random coincidences respectively to assess the contribution of each of these coincidences to the total SUV. This assessment allows for appropriate corrections to be implemented based on the individual findings. The SUV_{max} was determined for the true coincidences only.

All results are tabulated in Appendix 4.6.6 for reference purposes and the legend in Table 4-4 can be used to access the results effortlessly.

Table 4-4: Summary of the datasets that were generated and the list of tables in the Appendix where the SUV results can be obtained

Phantom inside FoV				
		Lesion – background contrast level		
Breathing mode	*Lesion diameter*	*10:1*	*5:1*	*2:1*
Average	10 mm	Table A1	Table A2	Table A3
	20 mm	Table A4	Table A5	Table A6
	30 mm	Table A7	Table A8	Table A9
Full Expiration	20 mm	Table A10	Table A11	Table A12
Full Inspiration	20 mm	Table A13	Table A14	Table A15
Repositioned phantom				
Breathing mode	*Lesion diameter*			
Average	10 mm	Table A16		
	20 mm	Table A17	Table A18	Table A19
	30 mm	Table A20		

From these results several graphs were generated in order to evaluate the influence of the various parameters on the SUV calculation.

4.3.1 Determination of the influence of breathing on SUV calculation

The results presented below were obtained by comparing the SUVs in lung lesions that were calculated on the average image obtained during a full breathing cycle to those that were calculated when the lesions remain static during full expiration and full inspiration respectively. Only the 20 mm lesions were included to determine the effect of breathing on SUV since partial volume effects should not have a large influence on that lesion size from experience in Chapter 3. Figure 4-6 represents the comparison of the SUV_{mean} using all coincidences for the 10:1, 5:1 and 2:1 lung-to-lesion contrast ratio for imaging in 2D and 3D modes. It is noted that the SUVs decrease as the contrast ratio decreases and the patterns of the graphs remain visually the same with just a variation in magnitude of the SUV. The SUV comparisons for the true coincidences are shown in Figure 4-7,

representing SUV_{mean} and Figure 4-8, representing SUV_{max}. It is noted that differentiation is found in SUV between the different lesions at various locations in the lungs with the most prominent being the expiration SUVs obtained in 3D mode. Using SUV_{max} tends to render SUVs of similar order since it is less susceptible to pixel intensity variation in the VoIs.

The comparison of SUVs determined from lesions at full inspiration and at full expiration (using the true coincidences only) was statistically significant except for those listed in Table 4-5. For the 10:1 contrast ratio imaged in 2D, it is noted that because movement was little in the apical area (highlighted), the differences are insignificant. When 3D imaging was used, there is a change at RL1.

The differences when comparing the SUV_{mean} using the true coincidences from the averaged breathing images to the SUV_{mean} using the image at full expiration and at full inspiration were statistically significant except for those that are listed in Table 4-6. It is interesting to observe that when the statistical differences in SUV, calculated using the true coincidences only that are shown in Table 4-6, are compared to those differences in SUV, calculated with all coincidences as listed in Table 4-7 and also when comparing these entries to those in Table 4-5, that there is little correlation between the entries in the tables. It would have been expected that most insignificant differences that are listed in Table 4-5, would follow through to those in Table 4-7 and also to Table 4-6.

If the scattered and random coincidences are brought into the picture – as can be observed in Figure 4-9 and Figure 4-10 – and those are viewed together with Figure 4-6 and Figure 4-7, the role of the scattered and random coincidences become more significant during breathing and that these coincidences determine the significant changes, especially when the contrast ratio changes. It was therefore necessary to calculate the SUVs for all lesions using scattered and random coincidences as well during the assessments to follow.

Table 4-5: Statistical analysis of differences obtained between SUV_{mean} calculated for lesions at full expiration and full inspiration. SUV_{mean} was calculated for true coincidences. Results are only given where the H_o ($p < 0.05$) could not be rejected.

Lesion	Image Comparison		F test: P(F<=f)	T-test P(T <=t)
10:1 Lesion-to-Lung contrast ratio				
LL1 (2D)	Expiration	Inspiration	0.452	0.508
LL1 (3D)	Expiration	Inspiration	0.969	0.551
LL2 (2D)	Expiration	Inspiration	0.643	0.746
LL2 (3D)	Expiration	Inspiration	0.268	0.135
LL3 (3D)	Expiration	Inspiration	0.740	0.291
RL1 (2D)	Expiration	Inspiration	0.000	0.191
RL2 (2D)	Expiration	Inspiration	0.136	0.781
RL2 (3D)	Expiration	Inspiration	0.703	0.294
5:1 Lesion-to-Lung contrast ratio				
LL1 (2D)	Expiration	Inspiration	0.408	0.612
RL2 (2D)	Expiration	Inspiration	0.500	0.364
RL3 (3D)	Expiration	Inspiration	0.000	0.745
2:1 Lesion-to-Lung contrast Ratio				
LL3 (2D)	Expiration	Inspiration	0.000	0.084
LL3 (3D)	Expiration	Inspiration	0.062	0.097
RL1 (2D)	Expiration	Inspiration	0.000	0.760
RL1 (3D)	Expiration	Inspiration	0.641	0.515
RL2 (2D)	Expiration	Inspiration	0.733	0.538

Table 4-6: Statistical analysis of differences obtained between SUV_{mean} calculated for average breathing images and the static images (at expiration and inspiration). SUV_{mean} was calculated for true coincidences. Results are only given where the H_o ($p < 0.05$) could not be rejected.

Lesion	Image Comparison		F test: P(F<=f)	T-test P(T <=t)
10:1 Lesion-to-Lung contrast ratio				
LL2 (2D)	Average Breathing	Expiration	0.062	0.152
LL2 (2D)	Average Breathing	Inspiration	0.018	0.290
RL2 (2D)	Average Breathing	Expiration	0.027	0.664
RL2 (2D)	Average Breathing	Inspiration	0.508	0.491
RL2 (3D)	Average Breathing	Inspiration	0.810	0.365
5:1 Lesion-to-Lung contrast ratio				
LL1 (3D)	Average Breathing	Expiration	0.000	0.287
RL2 (3D)	Average Breathing	Inspiration	0.092	0.070
LL1 (2D)	Average Breathing	Inspiration	0.025	0.071
2:1 Lesion-to-Lung contrast Ratio				
LL1 (2D)	Average Breathing	Expiration	0.003	0.168
LL1 (3D)	Average Breathing	Inspiration	0.164	0.872

Table 4-7: Statistical analysis of differences obtained between SUV_{mean} calculated for average breathing images and the static images (at expiration and inspiration). SUV_{mean} was calculated for all coincidences. Results are only given where the H_o ($p < 0.05$) could not be rejected.

Lesion	Image Comparison		F test: P(F<=f)	T-test P(T <=t)
10:1 Lesion-to-Lung contrast ratio				
LL1 (2D)	Average Breathing	Expiration	0.043	0.419
LL1 (3D)	Average Breathing	Inspiration	0.868	0.924
RL1 (2D)	Average Breathing	Expiration	0.502	0.688
RL1 (2D)	Average Breathing	Inspiration	0.000	0.217
RL1 (3D)	Average Breathing	Expiration	0.589	0.083
5:1 Lesion-to-Lung contrast ratio				
LL1 (2D)	Average Breathing	Inspiration	0.219	0.202
LL1 (3D)	Average Breathing	Inspiration	0.632	0.335
RL1 (3D)	Average Breathing	Expiration	0.284	0.088
2:1 Lesion-to-Lung contrast Ratio				
LL1 (2D)	Average Breathing	Expiration	0.648	0.083
LL1 (3D)	Average Breathing	Inspiration	0.722	0.290
RL1 (2D)	Average Breathing	Inspiration	0.064	0.088
RL1 (3D)	Average Breathing	Expiration	0.693	0.538

It is noted that the magnitude of the SUV_{mean} using scattered and random coincidences remains of the same order regardless of the variation in contrast ratio for the 20 mm lesion. It should be noted that the standard deviation for the SUVs calculated from the scattered and random coincidences seem to be quite large when looking at the different contrast ratios (Figure 4-9 and Figure 4-10), but that the relative standard deviation to the mean SUV remains of the same order.

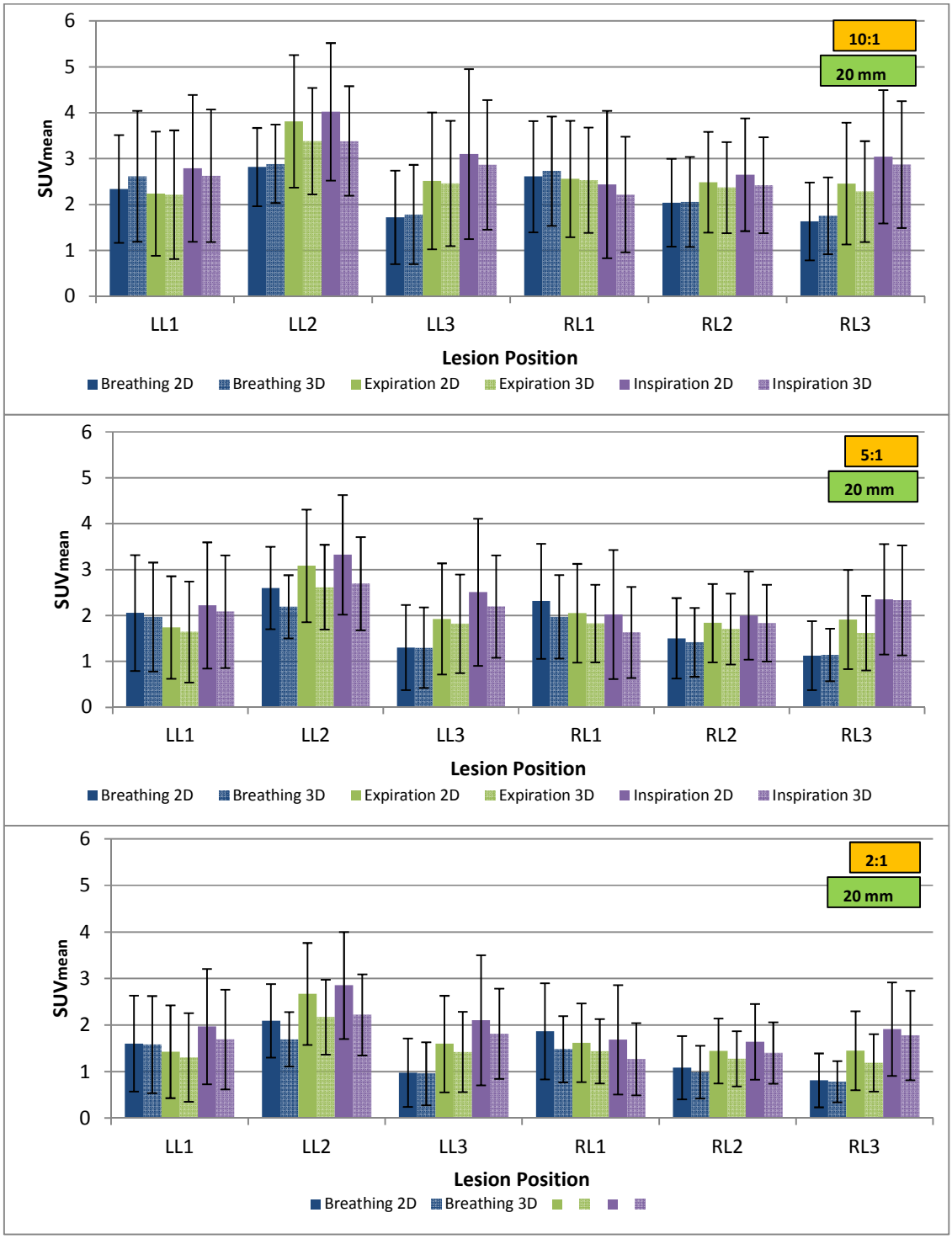

Figure 4-6: SUV_{mean} determined using <u>all coincidences</u> for 20 mm lesions (10:1, 5:1 and 2:1 contrast ratio) in 2D and 3D-imaging for the left lung lesions (LL1 - LL3) and right lung lesions (RL1 - RL3) to determine the effect of breathing motion versus the static conditions at full expiration and full inspiration. SUV_{mean} is shown for averaged breathing images, images obtained at full expiration and at full inspiration.

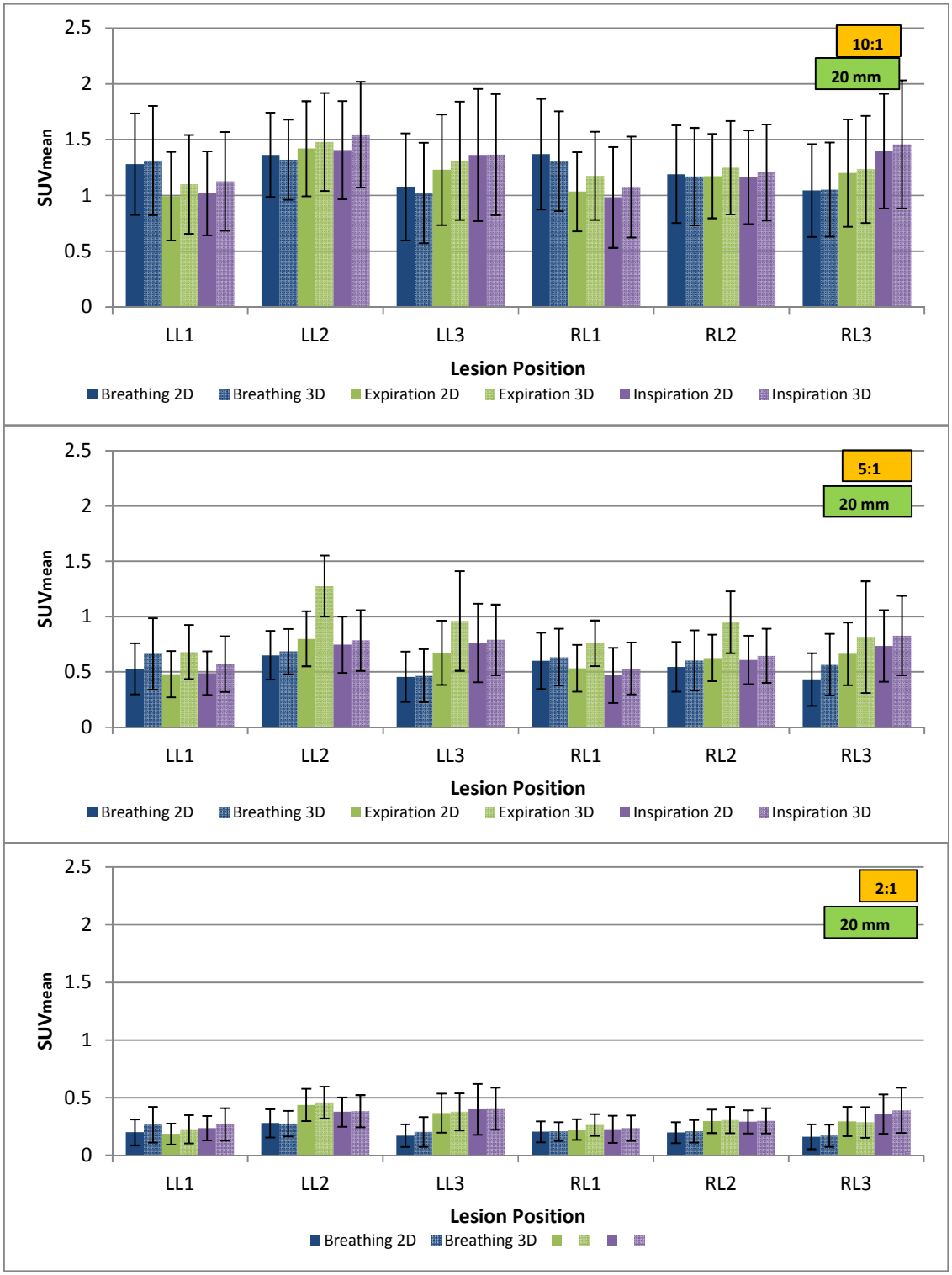

Figure 4-7: SUV_{mean} determined using <u>true coincidences</u> for 20 mm lesions (10:1, 5:1 and 2:1 contrast ratio) in 2D and 3D-imaging for the left lung lesions (LL1 - LL3) and right lung lesions (RL1 - RL3) to determine the effect of breathing motion versus the static conditions at full expiration and full inspiration. SUV_{mean} is shown for averaged breathing images, images obtained at full expiration and at full inspiration.

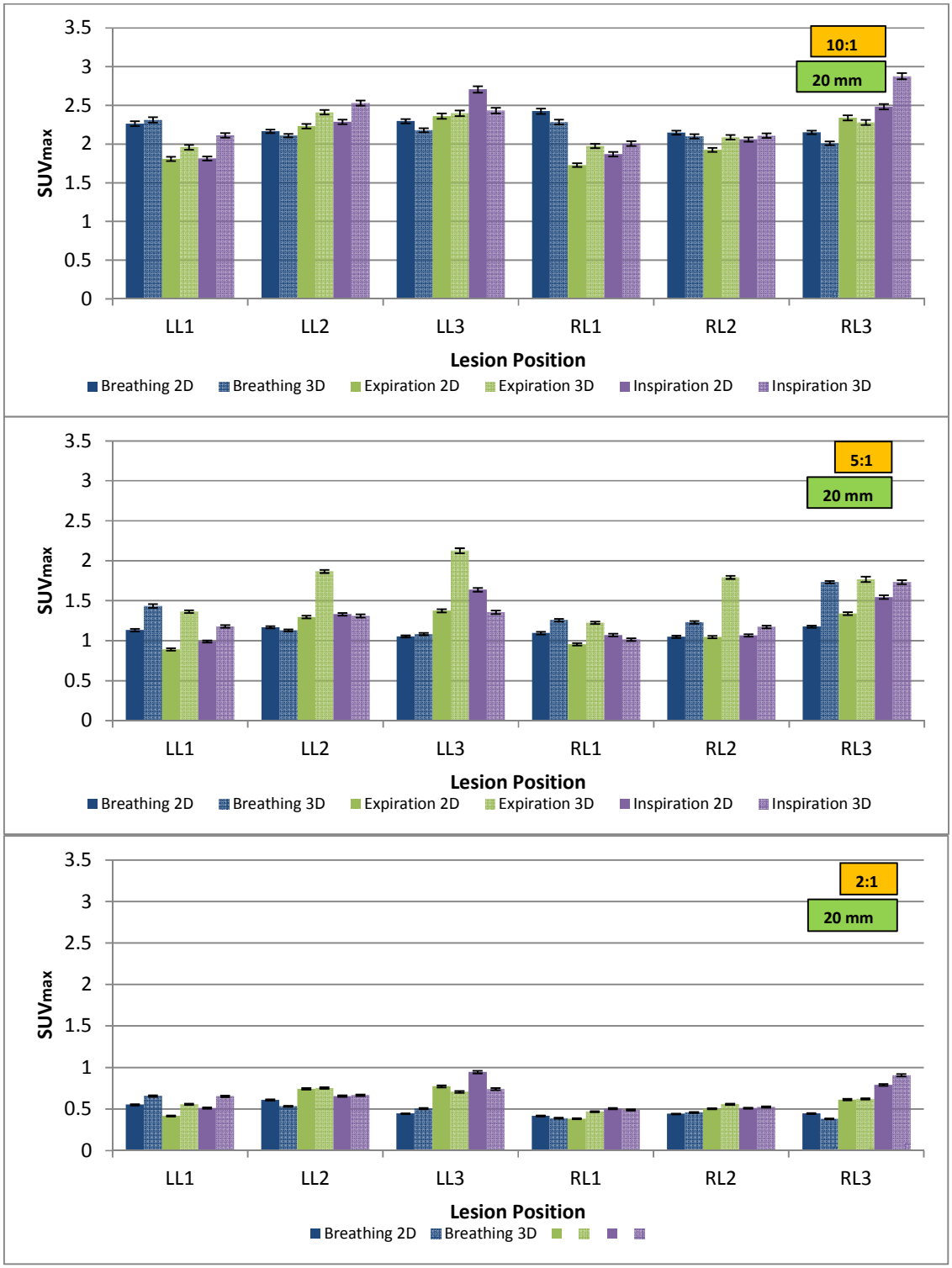

Figure 4-8: SUV_{max} determined using <u>true coincidences</u> for 20 mm lesions (10:1, 5:1 and 2:1 contrast ratio) in 2D and 3D-imaging for the left lung lesions (LL1 - LL3) and right lung lesions (RL1 - RL3) to determine the effect of breathing motion versus the static conditions at full expiration and full inspiration. SUV_{max} is shown for averaged breathing images, images obtained at full expiration and at full inspiration.

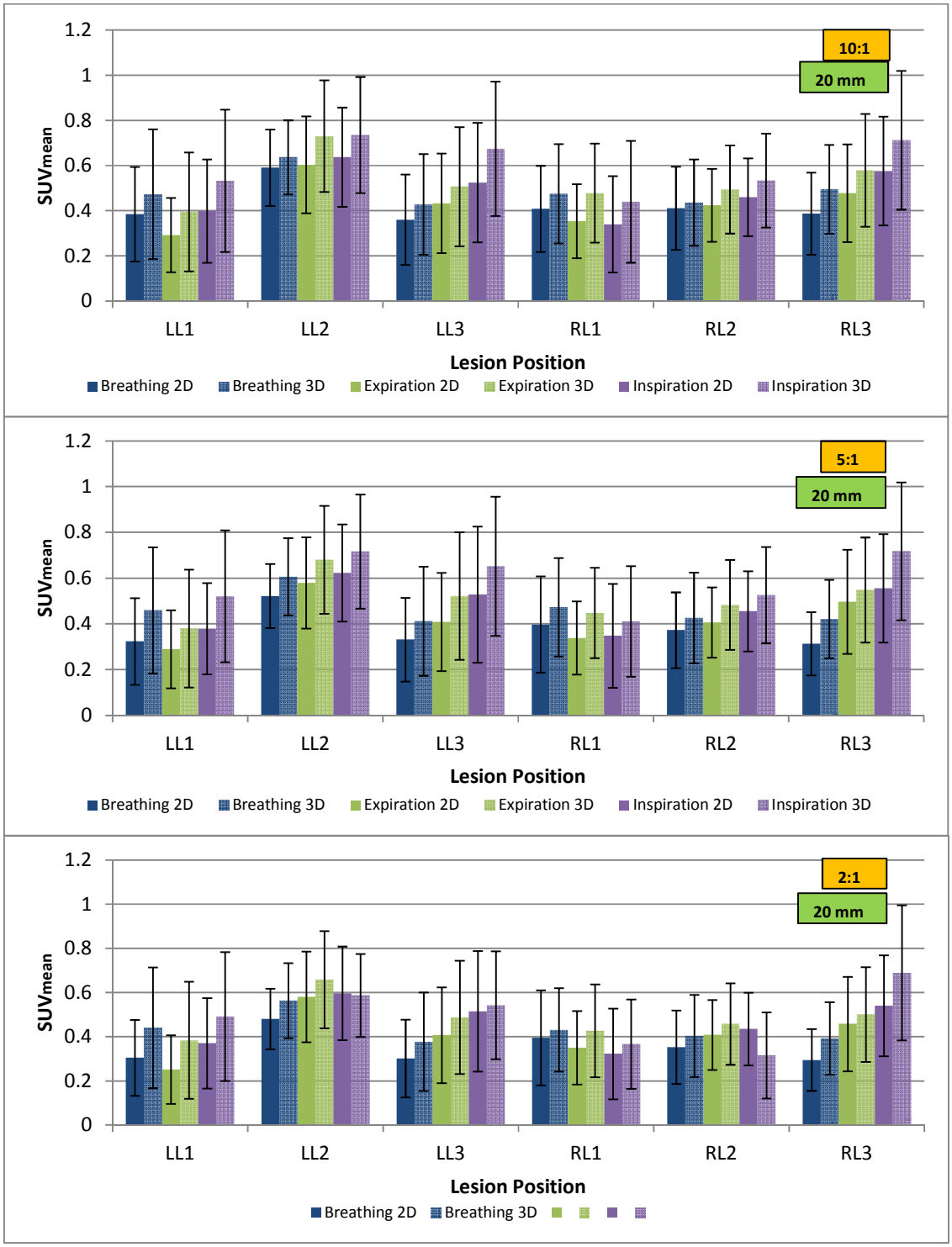

Figure 4-9: SUV_{mean} determined using scattered coincidences for 20 mm lesions (10:1, 5:1 and 2:1 contrast ratio) in 2D and 3D-imaging for the left lung lesions (LL1 - LL3) and right lung lesions (RL1 - RL3) to determine the effect of breathing motion versus the static conditions at full expiration and full inspiration. SUV_{mean} is shown for averaged breathing images, images obtained at full expiration and at full inspiration.

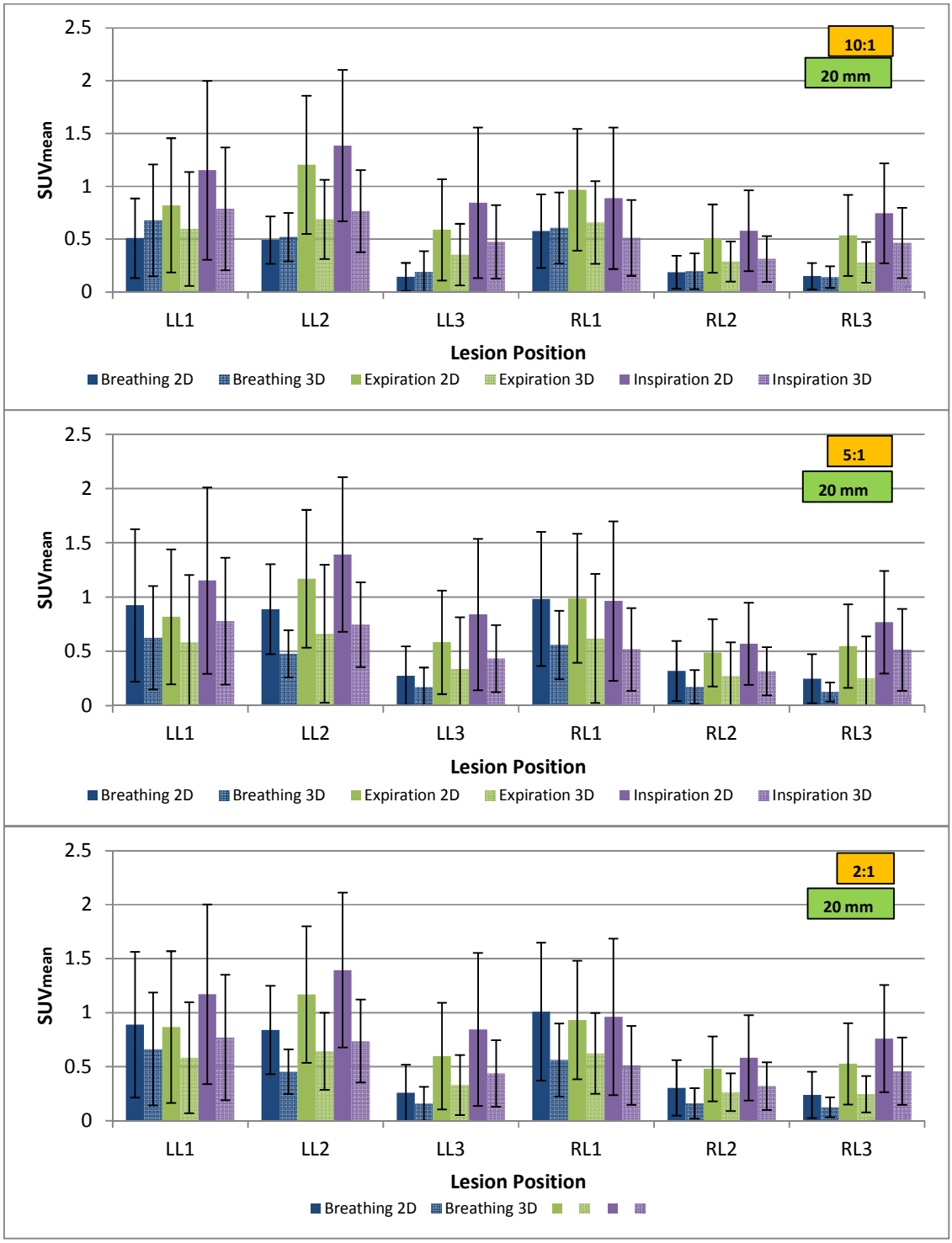

Figure 4-10: SUV_{mean} determined using <u>random coincidences</u> for 20 mm lesions (10:1, 5:1 and 2:1 contrast ratio) in 2D and 3D-imaging for the left lung lesions (LL1 - LL3) and right lung lesions (RL1 - RL3) to determine the effect of breathing motion versus the static conditions at full expiration and full inspiration. SUV_{mean} is shown for averaged breathing images, images obtained at full expiration and at full inspiration.

4.3.2 Determination of the influence of breathing and the variation in lesion-to-lung contrast on SUV calculation

The influence of movement during breathing and the variation in the lesion-to-lung contrast on the determination of the SUV for a specific lesion size is presented in this section. Since it was already established in the previous section that differences exist between the SUVs of the average breathing image and those that were obtained at full inspiration and full expiration, the SUV dependence on lesion contrast variation was not assessed again on the two static images. In Figure 4-11 the comparison of SUV_{mean} for the different contrast ratios are shown when including all coincidences in the analysis. With a decrease in contrast ratio, a decrease in SUV_{mean} is noted for all lesions.

When only the true coincidences are extracted (Figure 4-12 for SUV_{mean}), the decrease in SUV between the different contrast ratios is more pronounced. A similar pattern is noted when examining the SUV_{max} in Figure 4-13. All differences between the SUV_{mean} involving the true coincidences calculated for the various contrast ratios for each lesion location were statistically significant $P(F<=f) = 0.000 < 0.05$ and $P(T<=t) = 0.000 < 0.05$, and therefore the H_0 was rejected.

An analysis of the scattered coincidences as depicted in Figure 4-14 demonstrated that the differences between the SUVs of lesions at various locations in the lungs with various contrast ratios were statistically significant with the exception of those listed in Table 4-8. The variation in lesion location also seems to have little effect on the amount of scattered coincidences, although the largest amount of scatter is found at LL2, which is the lesion closest to the heart.

The analysis of the random coincidences as displayed in Figure 4-15 demonstrated that the differences between the SUVs of lesions at various locations in the lungs with various contrast ratios were statistically significant with the exception of those listed in Table 4-9. There is a larger variation in SUV_{mean} determined from random coincidences when changing the contrast ratio as well as when changing the location of the lesions. The randoms tend to be increased in the apical regions.

Table 4-8: Statistical analysis of differences between SUV_{mean} calculated for average breathing images and different contrast ratios. SUV_{mean} was calculated for scattered coincidences. Results are only given where the H_o ($p < 0.05$) could not be rejected.

Lesion	Contrast Comparison		F test: P(F<=f)	T-test P(T <=t)
LL1 (2D)	5:1	2:1	0.166	0.295
LL1 (3D)	10:1	5:1	0.577	0.601
	5:1	2:1	0.885	0.446
	10:1	2:1	0.484	0.233
LL3 (2D)	10:1	5:1	0.111	0.066
LL3 (3D)	10:1	5:1	0.238	0.375
	5:1	2:1	0.250	0.070
RL1 (2D)	10:1	5:1	0.148	0.569
	5:1	2:1	0.785	0.928
	10:1	2:1	0.086	0.510
RL1 (3D)	10:1	5:1	0.744	0.906
RL2 (3D)	10:1	5:1	0.548	0.552
	5:1	2:1	0.286	0.181
RL3 (2D)	5:1	2:1	0.854	0.097

Table 4-9: Statistical analysis of differences between SUV_{mean} calculated for average breathing images and different contrast ratios. SUV_{mean} was calculated for random coincidences. Results are only given where the H_o ($p < 0.05$) could not be rejected.

Lesion	Contrast Comparison		F test: P(F<=f)	T-test P(T <=t)
LL1 (2D)	5:1	2:1	0.564	0.593
LL1 (3D)	10:1	5:1	0.141	0.282
	5:1	2:1	0.169	0.394
	10:1	2:1	0.859	0.758
LL2 (2D)	5:1	2:1	0.845	0.168
LL2 (3D)	5:1	2:1	0.440	0.182
LL3 (2D)	5:1	2:1	0.534	0.376
LL3 (3D)	10:1	5:1	0.094	0.250
	5:1	2:1	0.014	0.282
RL1 (2D)	5:1	2:1	0.639	0.681
RL1 (3D)	10:1	5:1	0.332	0.146
	5:1	2:1	0.309	0.952
	10:1	2:1	0.962	0.178
RL2 (2D)	5:1	2:1	0.232	0.515
RL2 (3D)	10:1	5:1	0.154	0.106
	5:1	2:1	0.127	0.282
RL3 (2D)	5:1	2:1	0.369	0.588
RL3 (3D)	5:1	2:1	0.517	0.785

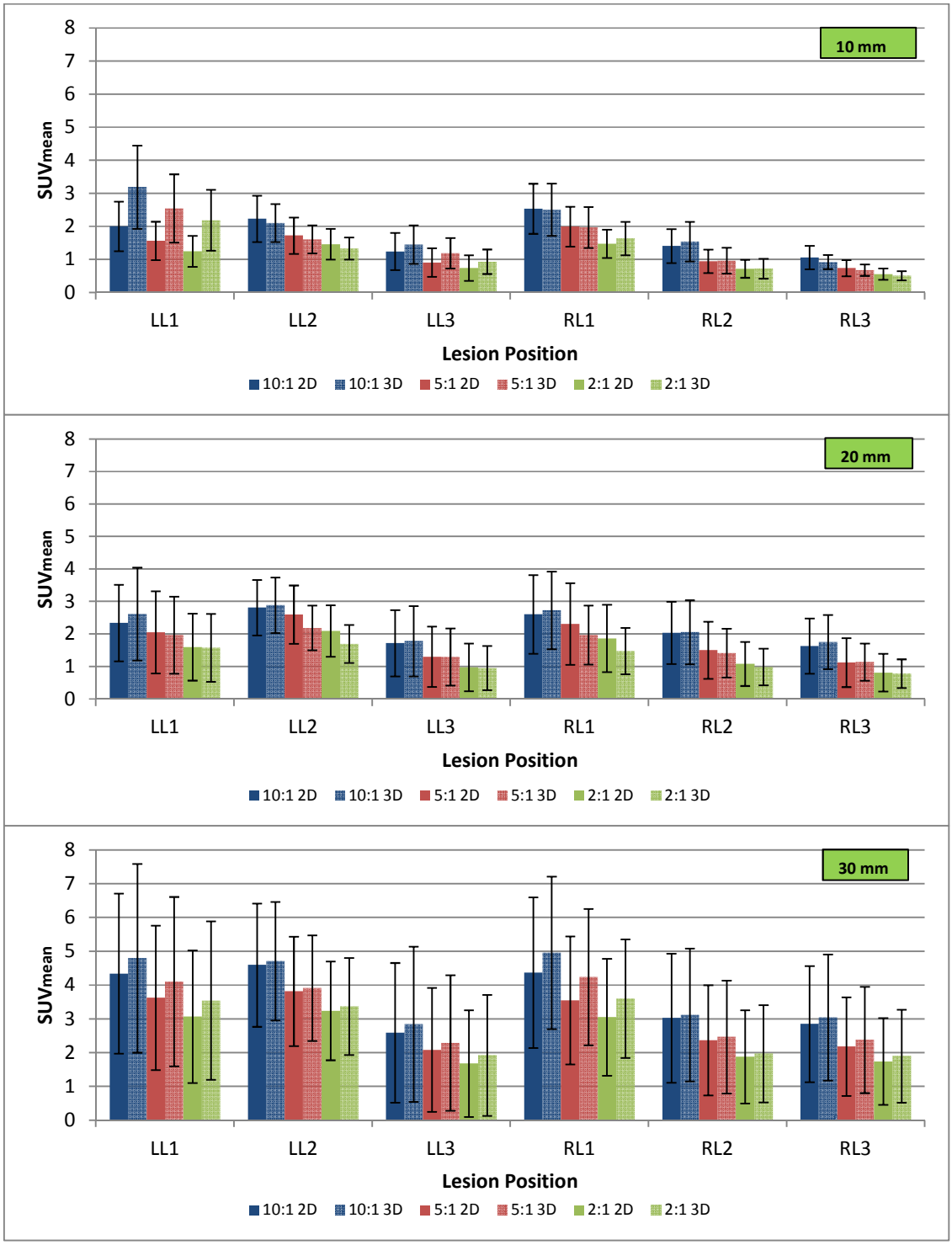

Figure 4-11: SUV_{mean} determined using <u>all coincidences</u> for 10 mm, 20 mm and 30 mm lesions (10:1, 5:1 and 2:1 contrast ratio) in 2D and 3D-imaging for the left lung lesions (LL1 - LL3) and right lung lesions (RL1 - RL3) to determine the effect of lesion-to-lung contrast ratio and lesion size on SUV_{mean}. SUV_{mean} is shown for averaged breathing images.

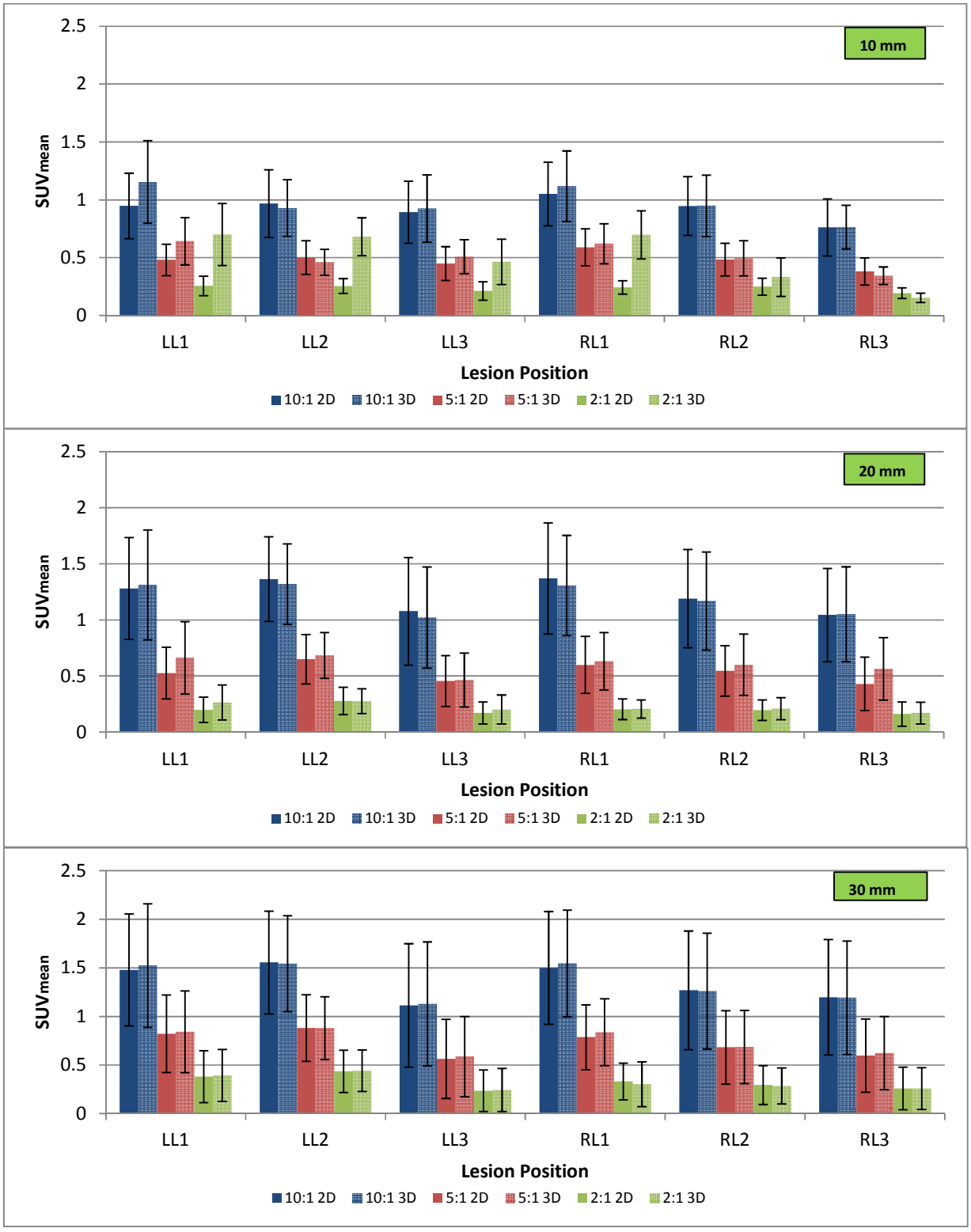

Figure 4-12: SUV_{mean} determined using <u>true coincidences</u> for 10 mm, 20 mm and 30 mm lesions (10:1, 5:1 and 2:1 contrast ratio) in 2D and 3D-imaging for the left lung lesions (LL1 - LL3) and right lung lesions (RL1 - RL3) to determine the effect of lesion-to-lung contrast ratio and lesion size on SUV_{mean}. SUV_{mean} is shown for averaged breathing images.

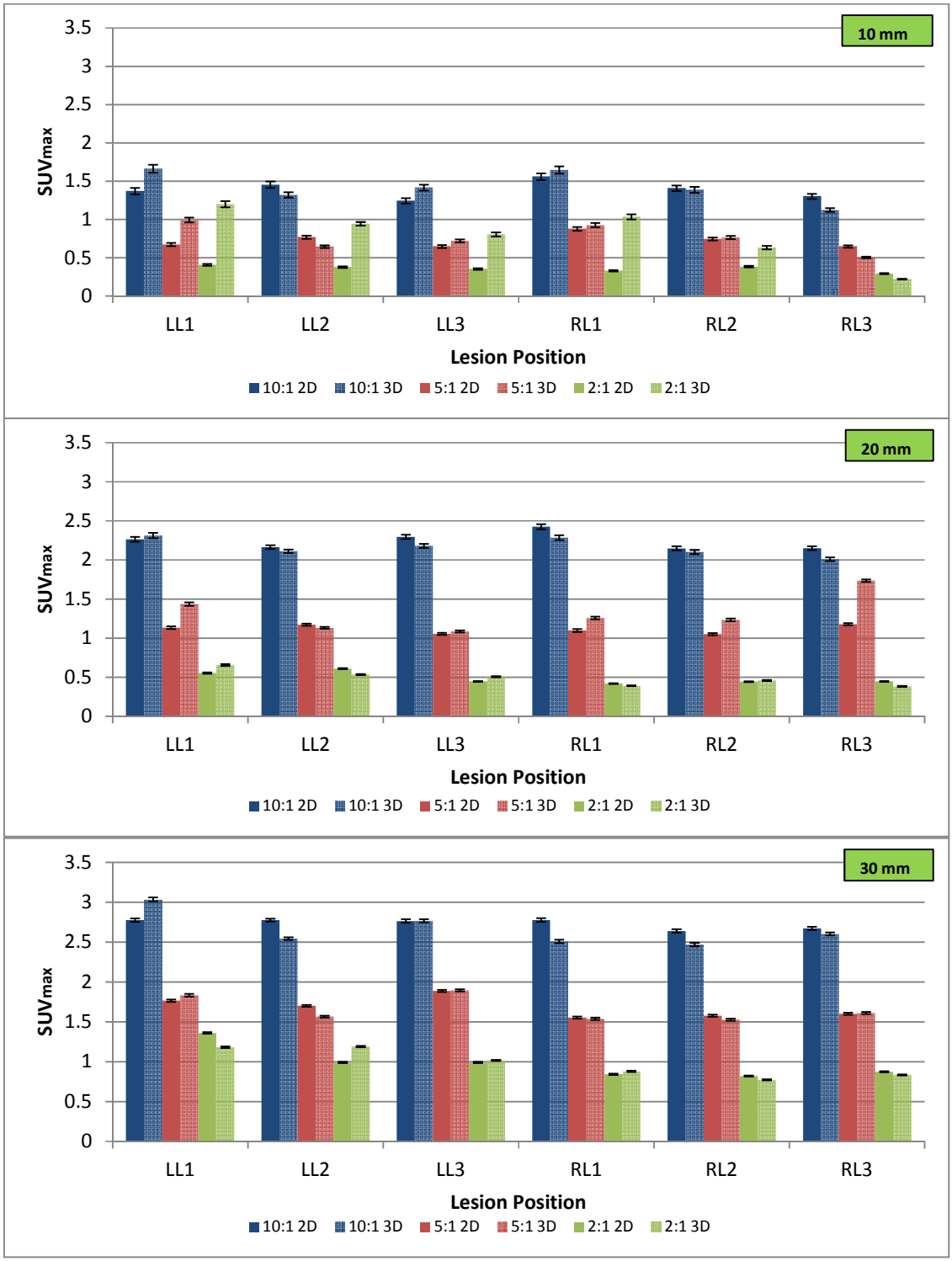

Figure 4-13: SUV_{max} determined using <u>true coincidences</u> for 10 mm, 20 mm and 30 mm lesions (10:1, 5:1 and 2:1 contrast ratio) in 2D and 3D-imaging for the left lung lesions (LL1 - LL3) and right lung lesions (RL1 - RL3) to determine the effect of lesion-to-lung contrast ratio and lesion size on SUV_{max}. SUV_{max} is shown for averaged breathing images.

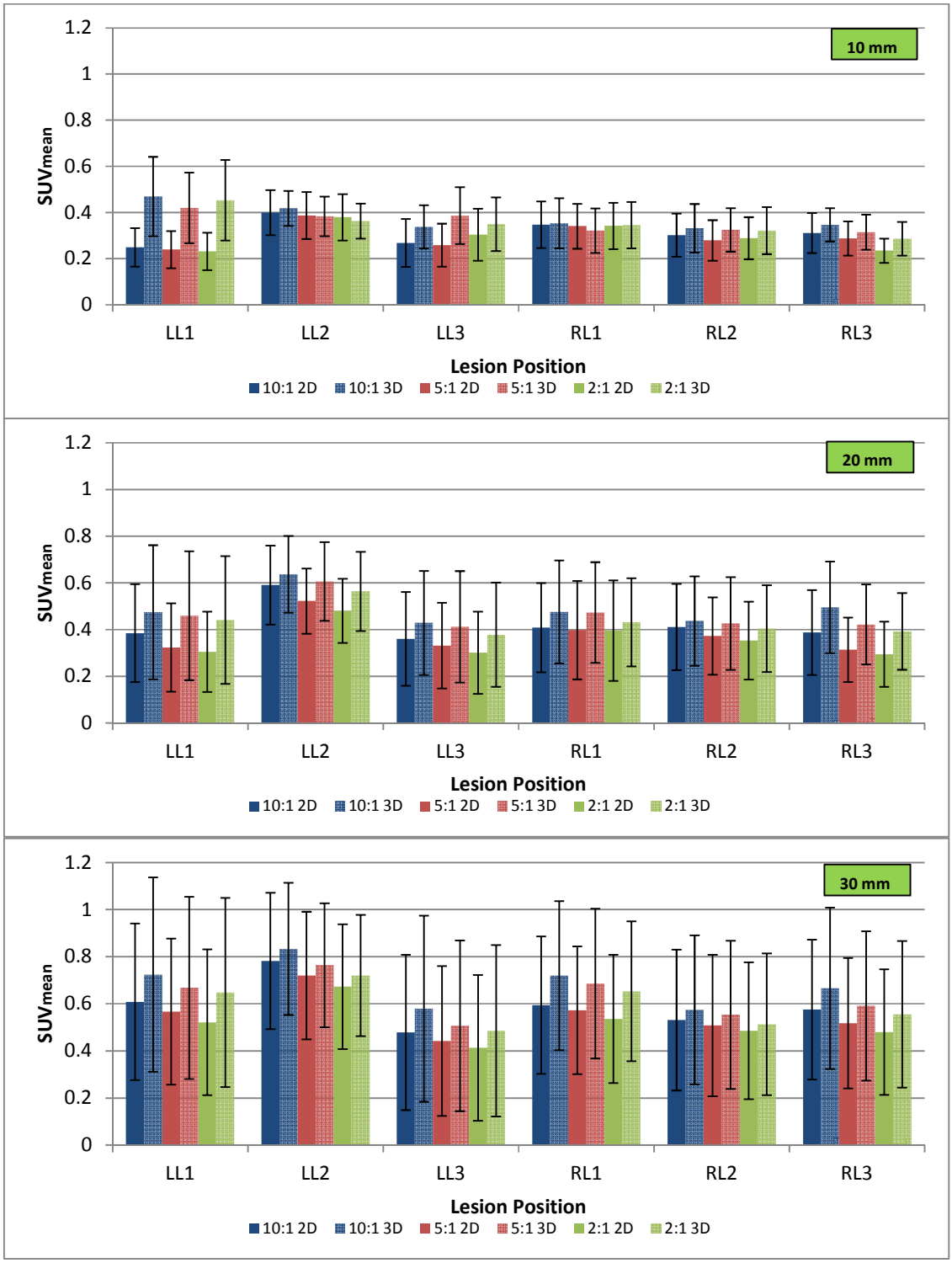

Figure 4-14: SUV_{mean} determined using <u>scattered coincidences</u> for 10 mm, 20 mm and 30 mm lesions (10:1, 5:1 and 2:1 contrast ratio) in 2D and 3D-imaging for the left lung lesions (LL1 - LL3) and right lung lesions (RL1 - RL3) to determine the effect of lesion-to-lung contrast ratio and lesion size on SUV_{mean}. SUV_{mean} is shown for averaged breathing images.

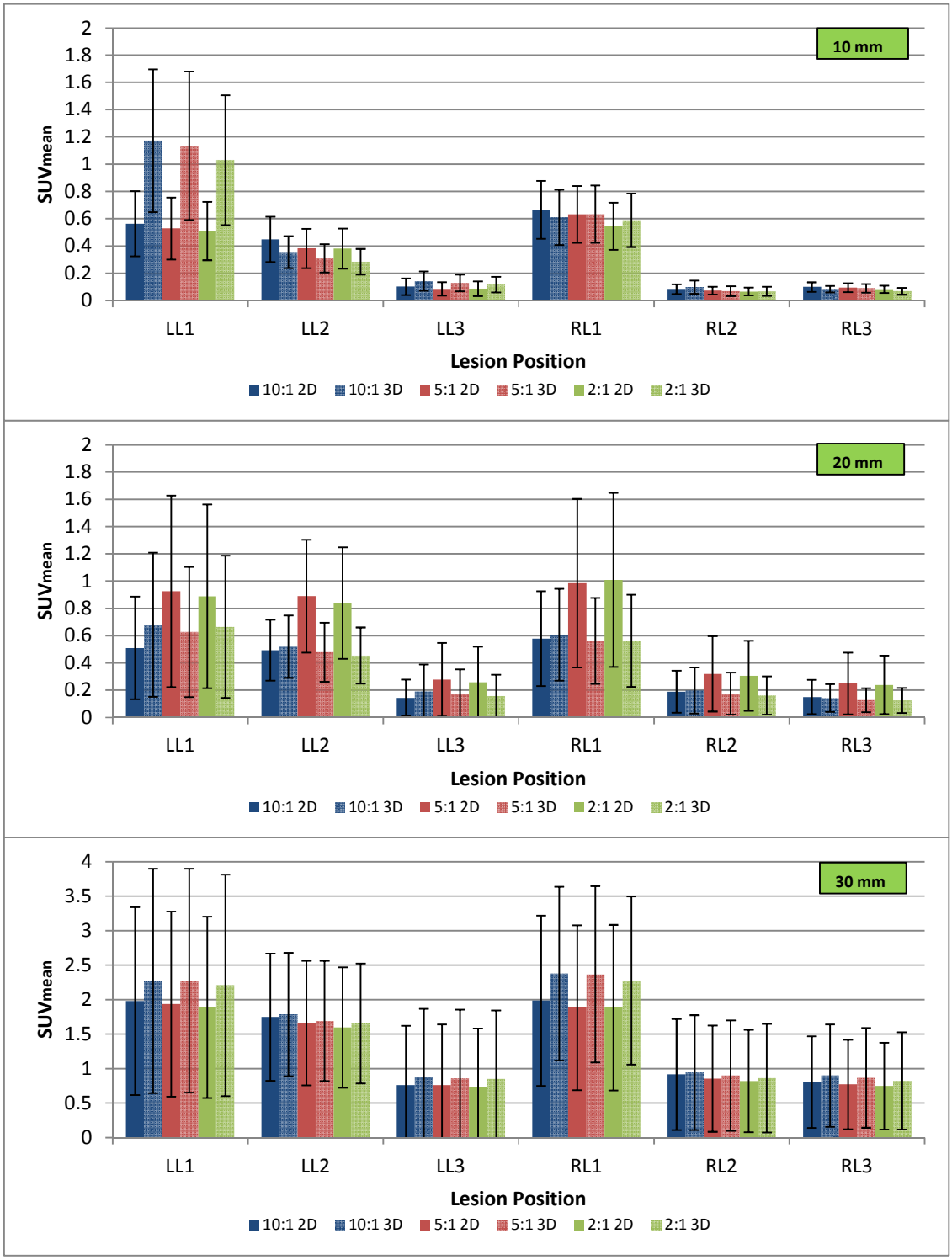

Figure 4-15: SUV_{mean} determined using <u>random coincidences</u> for 10 mm, 20 mm and 30 mm lesions (10:1, 5:1 and 2:1 contrast ratio) in 2D and 3D-imaging for the left lung lesions (LL1 - LL3) and right lung lesions (RL1 - RL3) to determine the effect of lesion-to-lung contrast ratio and lesion size on SUV_{mean}. SUV_{mean} is shown for averaged breathing images. (Note the difference in scale on the y-axes).

A direct comparison of the percentage true-to-total coincidences, scattered-to-total coincidences and random-to-total coincidences for all the lesions and different contrast ratios can be seen in Figure 4-16, Figure 4-17 and Figure 4-18 respectively. The %trues-to-total follow a downward trend with a decrease in contrast ratio except for the increase found at 2:1 contrast (3D) at the 10 mm lesion. Comparing this element in the graph with those in Figure 4-11 and Figure 4-12, it is evident that for the smallest lesion, the relative amount of trues to all coincidences is higher.

It is noted that the scattered coincidences have a more significant contribution when the contrast is less and the lesion is closer to the diaphragm (LL3 and RL3). The contribution in 3D mode is also more when compared to 2D mode. Scatter is minimised by using the septa during 2D imaging.

The relative amount of random coincidences is more increased in the apical region than in the other lung regions in particular where the contrast is less and when the lesions are large. Overall the percentage random-to-total coincidences tends to be higher during 3D acquisition when compared to the 2D acquisition. Since the random sensitivity rate is inversely proportional to the length of the septa[2], it therefore increases the amount of randoms that can be detected in 3D mode, inside the FoV and from outside the FoV (Bailey *et al.*, 2005). It is observed that the fraction of true coincidences-to-total coincidences increases when the lesions become smaller, but the relative amount of scattered events increases along with it. The difference is not as pronounced between the 20 mm and 30 mm lesions as it is between the 20 mm lesions and the 10 mm lesions. The partial volume effect is absent at the 30 mm lesions and present at the 10 mm lesions; thus it is probable that the PVE contributes to the differences found. Conversely, the amount of random coincidences relative to the total number of coincidences increases with an increase in lesion size.

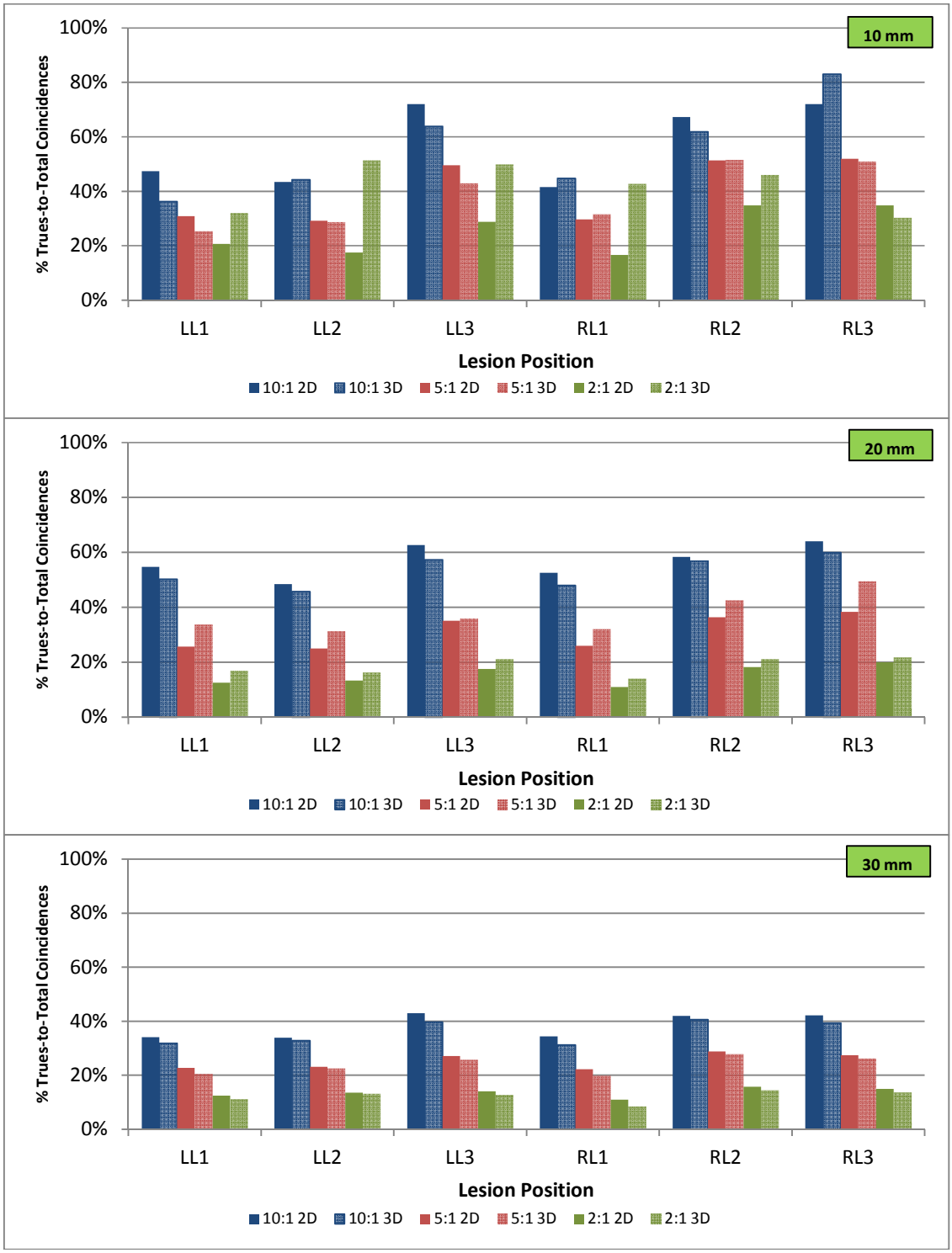

Figure 4-16: Comparison of %True-to-Total Coincidences for 10 mm, 20 mm and 30 mm lesions in the left lung (LL1 - LL3) and right lung (RL1 - RL3) using 10:1, 5:1 and 2:1 contrast ratios in 2D- and 3D modes. Average breathing images were evaluated

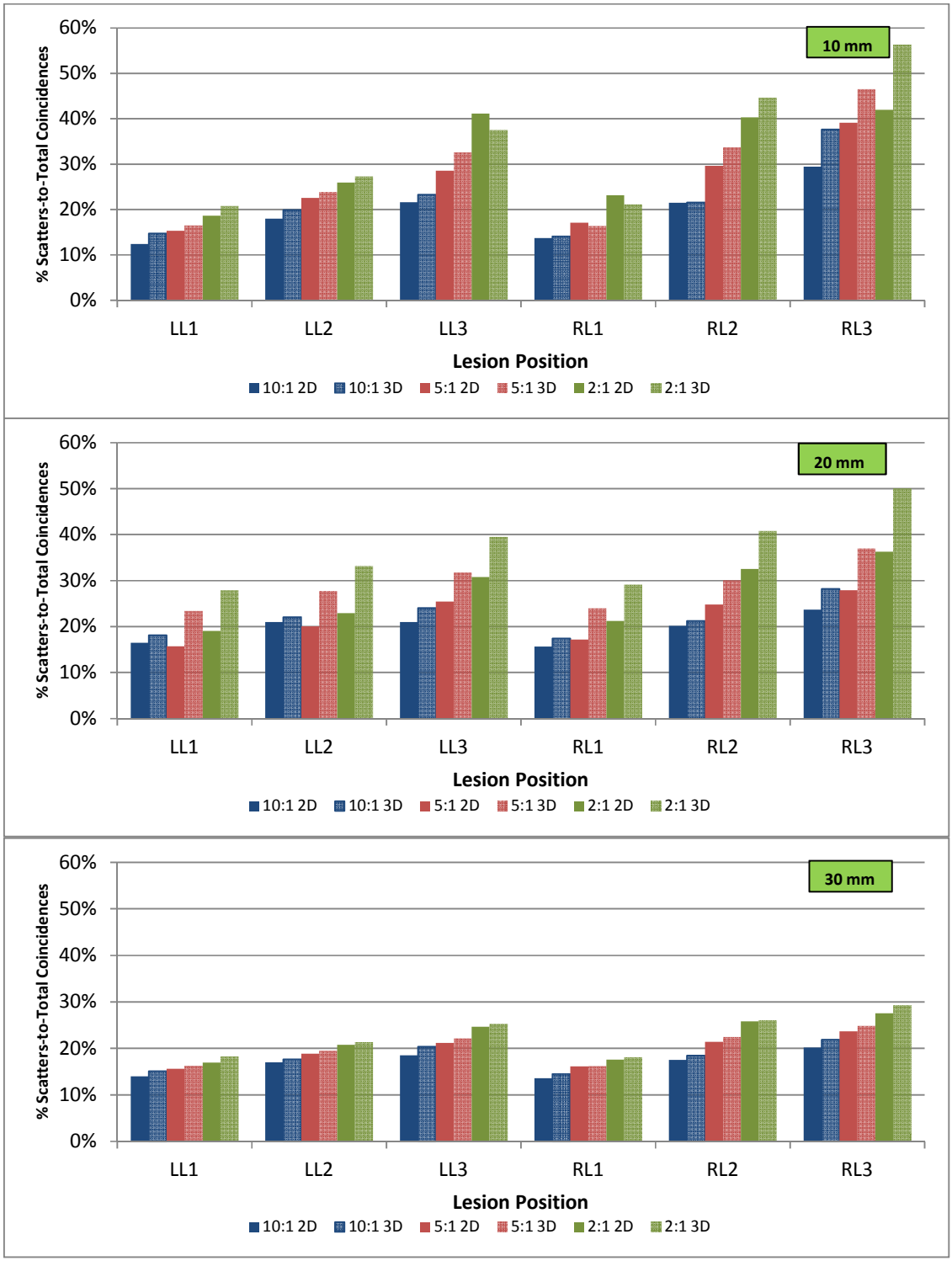

Figure 4-17: Comparison of %Scattered-to-Total Coincidences for 10 mm, 20 mm and 30 mm lesions in the left lung (LL1 - LL3) and right lung (RL1 - RL3) using 10:1, 5:1 and 2:1 contrast ratios in 2D- and 3D modes. Average breathing images were evaluated

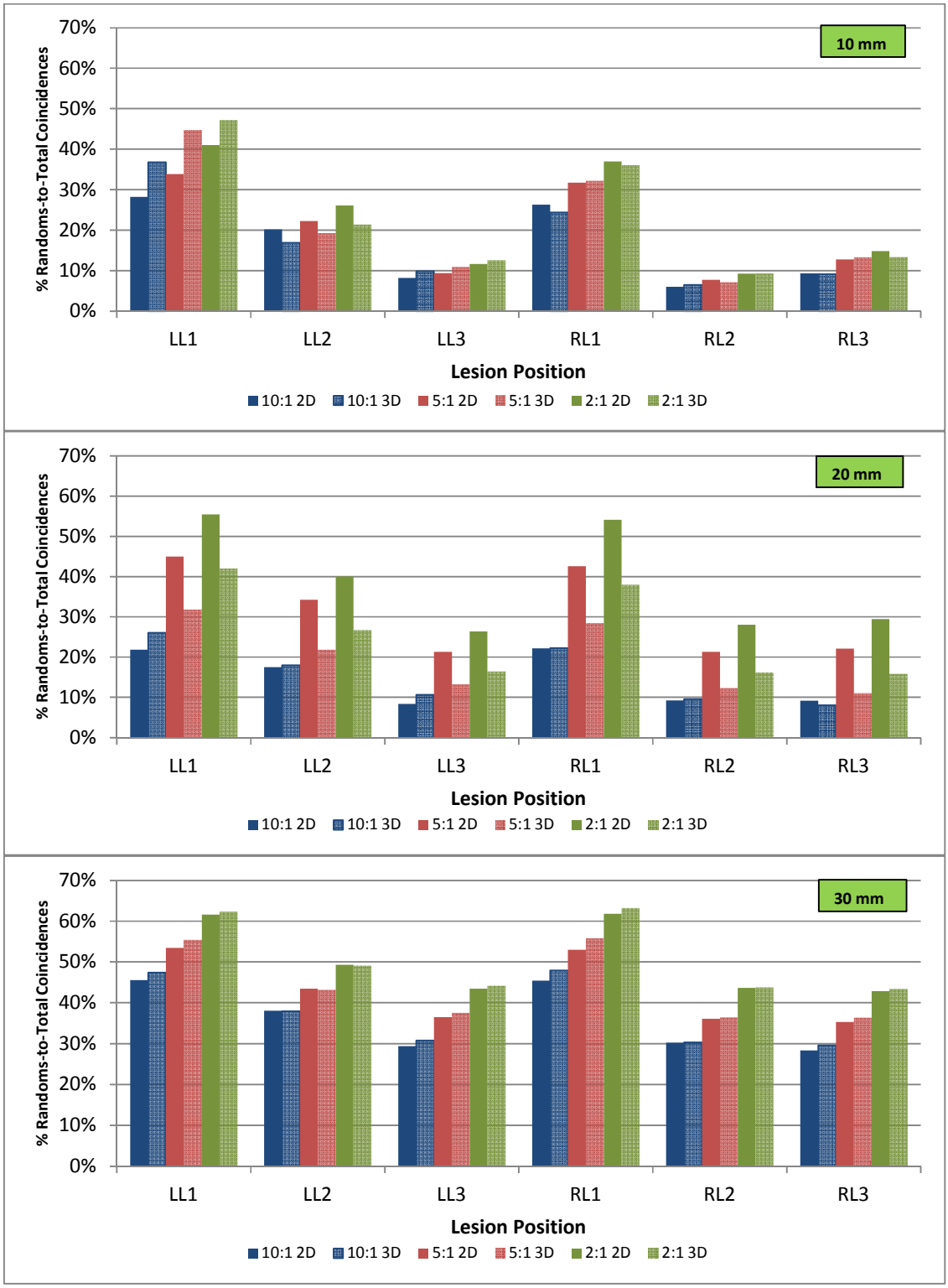

Figure 4-18: Comparison of %Random-to-Total Coincidences for 10 mm, 20 mm and 30 mm lesions in the left lung (LL1 - LL3) and right lung (RL1 - RL3) using 10:1, 5:1 and 2:1 contrast ratios in 2D- and 3D modes. Average breathing images were evaluated.

4.3.3 Determination of the influence of breathing and the variation in lesion size on the SUV calculation

The influence of movement during breathing and the variation in the lesion size with a fixed lesion contrast on the determination of the SUV is presented below. The figures in the previous section are applicable to this section. The focus in this section is on the variation in lesion size and how SUV is influenced. In Figure 4-11 the comparison is shown for SUV_{mean} when all the coincidences are included in the analysis while in Figure 4-12 only the true coincidences are used. It is noted that the SUV_{mean} for the lesions in all lung regions increases when larger lesions are imaged. This is also true for SUV_{max} (Figure 4-13). Almost all differences in SUV_{mean} calculated for true coincidences for the various lesion sizes were statistically significant different with $P(F<=f) = 0.000 < 0.05$ and $P(T<=t) = 0.000 < 0.05$, and therefore the H_0 was rejected. The only difference that was not significantly different is shown in Table 4-10.

Table 4-10: Statistical analysis of differences between SUV_{mean} calculated for average breathing images and different lesion sizes ratios. SUV_{mean} was calculated for true coincidences. Results are only given where the H_o ($p < 0.05$) could not be rejected.

Lesion	Lesion Size Comparison		F test: P(F<=f)	T-test P(T <=t)
LL3 (2D)	20 mm	30 mm	0.000	0.298

The comparison of SUV_{mean} calculated using scattered coincidences can be seen in Figure 4-14 and it is noted that the SUV gradually increases with object size for all of the lesions. The only difference in SUV_{mean} that was not significantly different is shown in Table 4-11. The remainder of the differences in SUVs measured at different lesion sizes were statistically significant.

Table 4-11: Statistical analysis of differences between SUV_{mean} calculated for average breathing images and different lesion sizes ratios. SUV_{mean} was calculated for scattered coincidences. Results are only given where the H_o ($p < 0.05$) could not be rejected.

Lesion	Lesion Size Comparison		F test: P(F<=f)	T-test P(T <=t)
LL3 (2D)	10 mm	20 mm	0.000	0.931

The SUV_{mean} of random coincidences vary little for the smaller lesions, but increases significantly when the 30 mm lesions are analysed as can be seen in Figure 4-15. The differences in SUV_{mean} for the randoms that were not significantly different are shown in Table 4-12.

Table 4-12: Statistical analysis of differences between SUV_{mean} calculated for average breathing images and different lesion sizes ratios. SUV_{mean} was calculated for random coincidences. Results are only given where the H_o ($p < 0.05$) could not be rejected.

Lesion	Lesion Size Comparison		F test: P(F<=f)	T-test P(T <=t)
LL1 (2D)	10 mm	20 mm	0.001	0.231
LL2 (2D)	10 mm	20 mm	0.015	0.113
RL1 (3D)	10 mm	20 mm	0.000	0.928

The percentage true-to-total coincidences is presented in Figure 4-16, the percentage scattered-to-total coincidences in Figure 4-17 while the percentage of random-to-total coincidences is shown in Figure 4-18. The amount of trues-to-total is highest at the 10 mm lesions especially in the basal area, while the fraction of scattered coincidences varied little for all lesion sizes except for the increase in scatter that was noted for the 10 mm lesion in basal area on the right, although it is still below 40%. The amount of random-to-total coincidences is most when imaging the 30 mm lesions in the apical region.

4.3.4 Determination of the influence of activity outside the FoV on the SUV calculation

The influence of repositioning the phantom so that the inferior part consisting mainly of the liver lies outside the FoV was investigated and the results are presented here. In this particular section the influence on the calculation of SUV by repositioning of the breathing phantom with varying lesion-background contrast ratios is presented and compared to the results of the lesion images averaged during breathing that were presented in section 4.3.1. In Figure 4-19 the comparisons are made for SUV_{mean} calculated using all coincidences obtained using a 10:1 contrast ratio and lesion sizes of 10 mm, 20 mm and 30 mm. The equivalent representations involving the true coincidences can be seen in Figure 4-20 (SUV_{mean}) and in Figure 4-21 for SUV_{max}. SUVs were calculated for lesions obtained from the original phantom ("Breathing" on the legends) as well as the repositioned phantom. The difference between the results of these two datasets were analysed for statistical significance were statistically significant except for those presented in Table 4-13.

Table 4-13: Statistical analysis of differences between SUV_{mean} calculated for average breathing images of the original and the repositioned phantom. The 10 mm, 20 mm and 30 mm lesions were assessed. SUV_{mean} was calculated for true coincidences. Results are only given where the H_o ($p < 0.05$) could not be rejected.

Lesion	Comparison		F test: P(F<=f)	T-test P(T <=t)
10 mm				
10:1 lesion-to-lung contrast ratio				
LL2 (3D)	Inside FoV	Repositioned	0.000	0.196
20 mm				
10:1 lesion-to-lung contrast ratio				
LL2 (2D)	Inside FoV	Repositioned	0.000	0.704
LL2 (3D)	Inside FoV	Repositioned	0.000	0.231
5:1 lesion-to-lung contrast ratio				
LL2 (3D)	Inside FoV	Repositioned	0.000	0.089
30 mm				
10:1 lesion-to-lung contrast ratio				
LL2 (2D)	Inside FoV	Repositioned	0.025	0.394
LL2 (3D)	Inside FoV	Repositioned	0.001	0.272

Table 4-14: Statistical analysis of differences between SUV_{mean} calculated for average breathing images of the original and the repositioned phantom. The 10 mm, 20 mm and 30 mm lesions were assessed. SUV_{mean} was calculated for scattered coincidences. Results are only given where the H_o ($p < 0.05$) could not be rejected.

Lesion	Comparison		F test: P(F<=f)	T-test P(T <=t)
10 mm				
10:1 lesion-to-lung contrast ratio				
RL1 (2D)	Inside FoV	Repositioned	0.000	0.622
20 mm				
10:1 lesion-to-lung contrast ratio				
LL1 (3D)	Inside FoV	Repositioned	0.249	0.554
RL1 (2D)	Inside FoV	Repositioned	0.499	0.183
RL1 (3D)	Inside FoV	Repositioned	0.008	0.096
RL2 (2D)	Inside FoV	Repositioned	0.511	0.460
RL2 (3D)	Inside FoV	Repositioned	0.133	0.825
RL3 (2D)	Inside FoV	Repositioned	0.000	0.217
RL3 (3D)	Inside FoV	Repositioned	0.001	0.209
30 mm				
10:1 lesion-to-lung contrast ratio				
LL1 (2D)	Inside FoV	Repositioned	0.630	0.187
LL1 (3D)	Inside FoV	Repositioned	0.474	0.942
RL1 (2D)	Inside FoV	Repositioned	0.750	0.244
RL1 (3D)	Inside FoV	Repositioned	0.393	0.978
RL2 (2D)	Inside FoV	Repositioned	0.611	0.245
RL3 (2D)	Inside FoV	Repositioned	0.657	0.083

Figure 4-22 and Figure 4-23 represents the SUVs calculated from the scattered and random coincidences respectively. It is noted that the repositioning of the phantom had fewer significant effects on the SUVs calculated from scattered and random coincidences as is evident from Table 4-14 and Table 4-15, than the effect it had on the true coincidences. The effects of repositioning were more significant at the 10 mm lesions than on the 20 mm and 30 mm lesions, indicating that the PVE played a more significant role.

Table 4-15: Statistical analysis of differences between SUV_{mean} calculated for average breathing images of the original and the repositioned phantom. The 10 mm, 20 mm and 30 mm lesions were assessed. SUV_{mean} was calculated for random coincidences. Results are only given where the H_o ($p < 0.05$) could not be rejected.

Lesion	Comparison		F test: P(F<=f)	T-test P(T <=t)
10 mm				
10:1 lesion-to-lung contrast ratio				
LL1 (3D)	Inside FoV	Repositioned	0.257	0.345
RL1 (2D)	Inside FoV	Repositioned	0.000	0.830
20 mm				
10:1 lesion-to-lung contrast ratio				
LL1 (3D)	Inside FoV	Repositioned	0.302	0.871
LL2 (3D)	Inside FoV	Repositioned	0.000	0.154
RL1 (2D)	Inside FoV	Repositioned	0.121	0.052
RL1 (3D)	Inside FoV	Repositioned	0.000	0.097
RL3 (2D)	Inside FoV	Repositioned	0.744	0.203
30 mm				
10:1 lesion-to-lung contrast ratio				
LL1 (2D)	Inside FoV	Repositioned	0.911	0.615
LL2 (2D)	Inside FoV	Repositioned	0.394	0.881
RL1 (2D)	Inside FoV	Repositioned	0.433	0.868
RL3 (2D)	Inside FoV	Repositioned	0.560	0.410
LL1 (3D)	Inside FoV	Repositioned	0.207	0.599
LL2(3D)	Inside FoV	Repositioned	0.061	0.623
RL1 (3D)	Inside FoV	Repositioned	0.221	0.222
RL3 (3D)	Inside FoV	Repositioned	0.160	0.354

In all of the above scenarios where the phantom was partly moved outside the FoV and where the comparisons in SUV_{mean} were significantly different, the SUV_{mean} involving the true coincidences increased for all lesions except for the lesion closest to the liver (RL3) where a lower SUV was recorded in each case. This was true for all the lesion sizes that were evaluated.

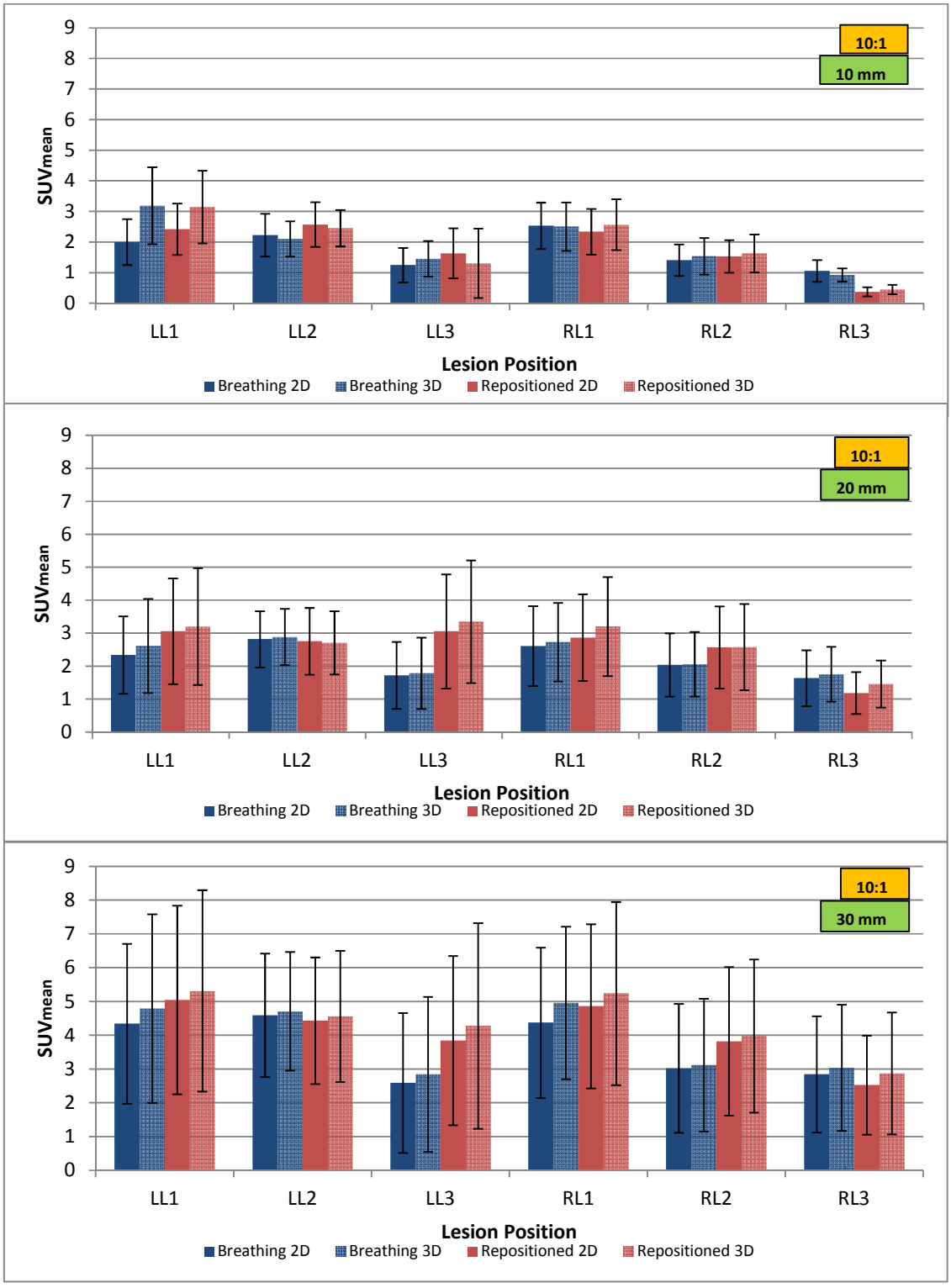

Figure 4-19: SUV_{mean} determined using <u>all coincidences</u> for 10 mm, 20 mm and 30 mm lesions (10:1 contrast ratio) in 2D and 3D-imaging for the left lung lesions (LL1 - LL3) and right lung lesions (RL1 - RL3) by repositioning the phantom partly outside the FoV to determine the effect of activity outside the FoV on SUV_{mean}. SUV_{mean} is shown for averaged breathing images.

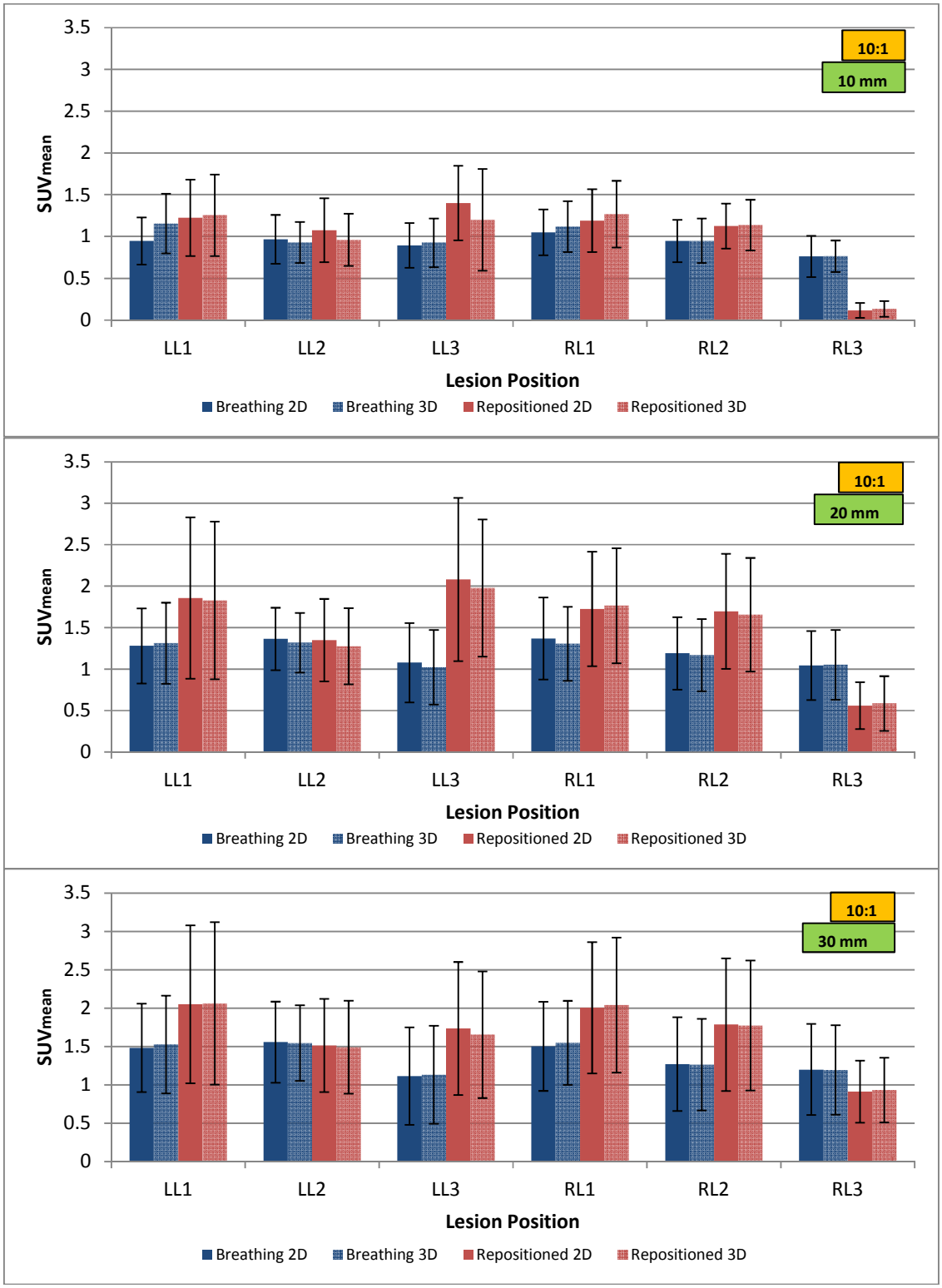

Figure 4-20: SUV_{mean} determined using <u>true coincidences</u> for 10 mm, 20 mm and 30 mm lesions (10:1 contrast ratio) in 2D and 3D-imaging for the left lung lesions (LL1 - LL3) and right lung lesions (RL1 - RL3) by repositioning the phantom partly outside the FoV to determine the effect of activity outside the FoV on SUV_{mean}. SUV_{mean} is shown for averaged breathing images.

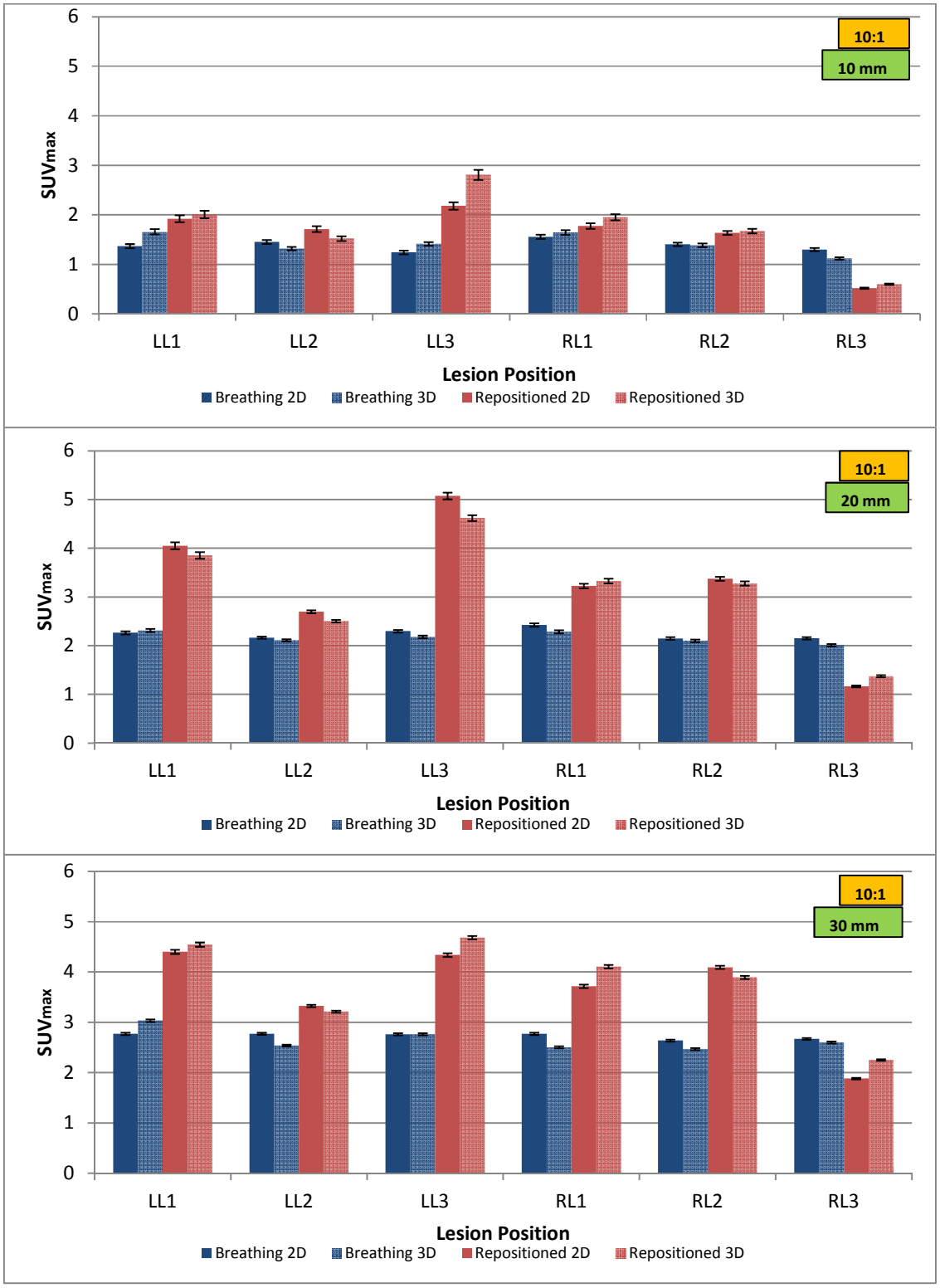

Figure 4-21: SUV_{max} determined using true coincidences for 10 mm, 20 mm and 30 mm lesions (10:1 contrast ratio) in 2D and 3D-imaging for the left lung lesions (LL1 - LL3) and right lung lesions (RL1 - RL3) by repositioning the phantom partly outside the FoV to determine the effect of activity outside the FoV on SUV_{max}. SUV_{max} is shown for averaged breathing images.

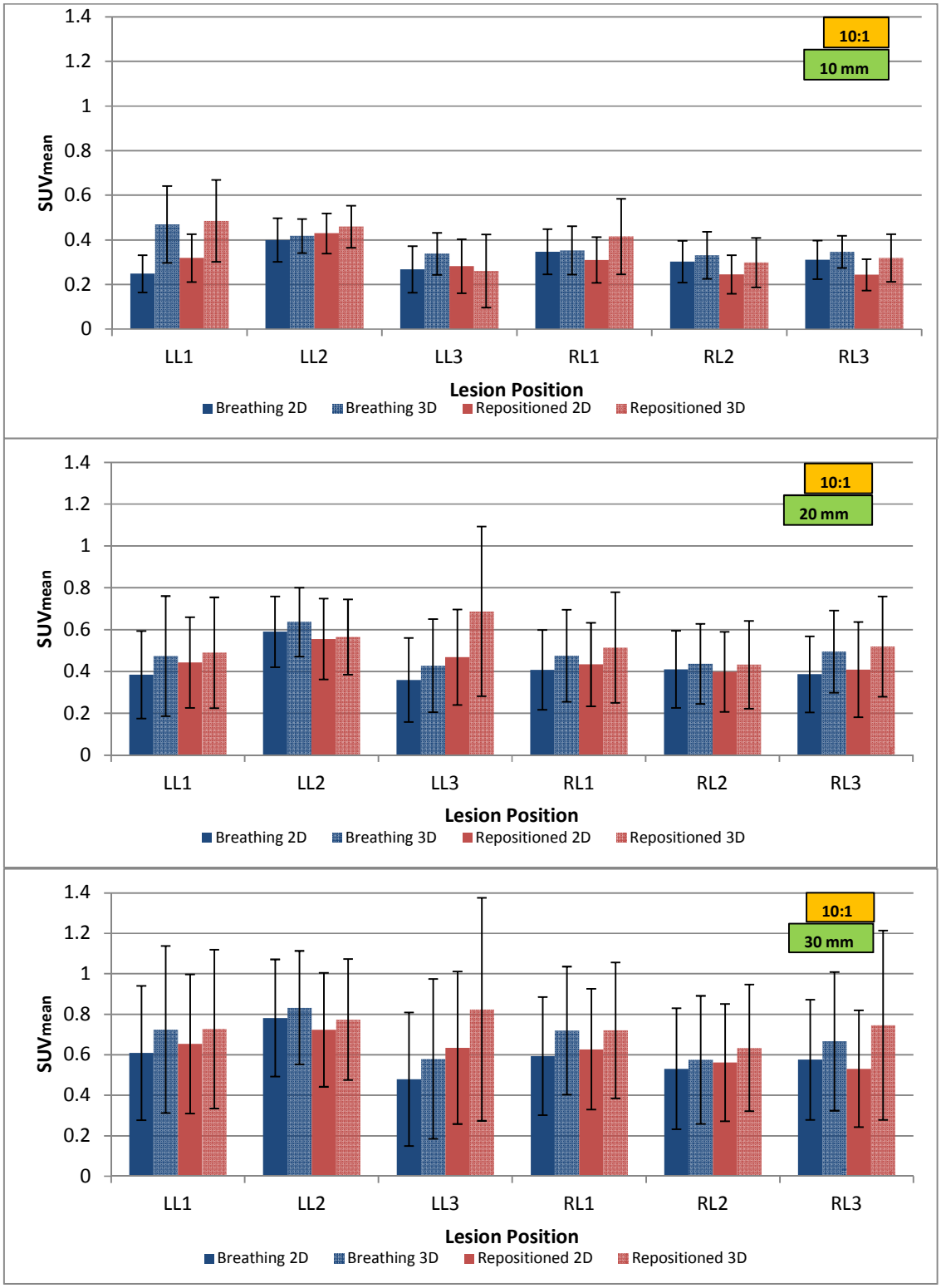

Figure 4-22: SUV_{mean} determined using <u>scattered coincidences</u> for 10 mm, 20 mm and 30 mm lesions (10:1 contrast ratio) in 2D and 3D-imaging for the left lung lesions (LL1 - LL3) and right lung lesions (RL1 - RL3) by repositioning the phantom partly outside the FoV to determine the effect of activity outside the FoV on SUV_{mean}. SUV_{mean} is shown for averaged breathing images.

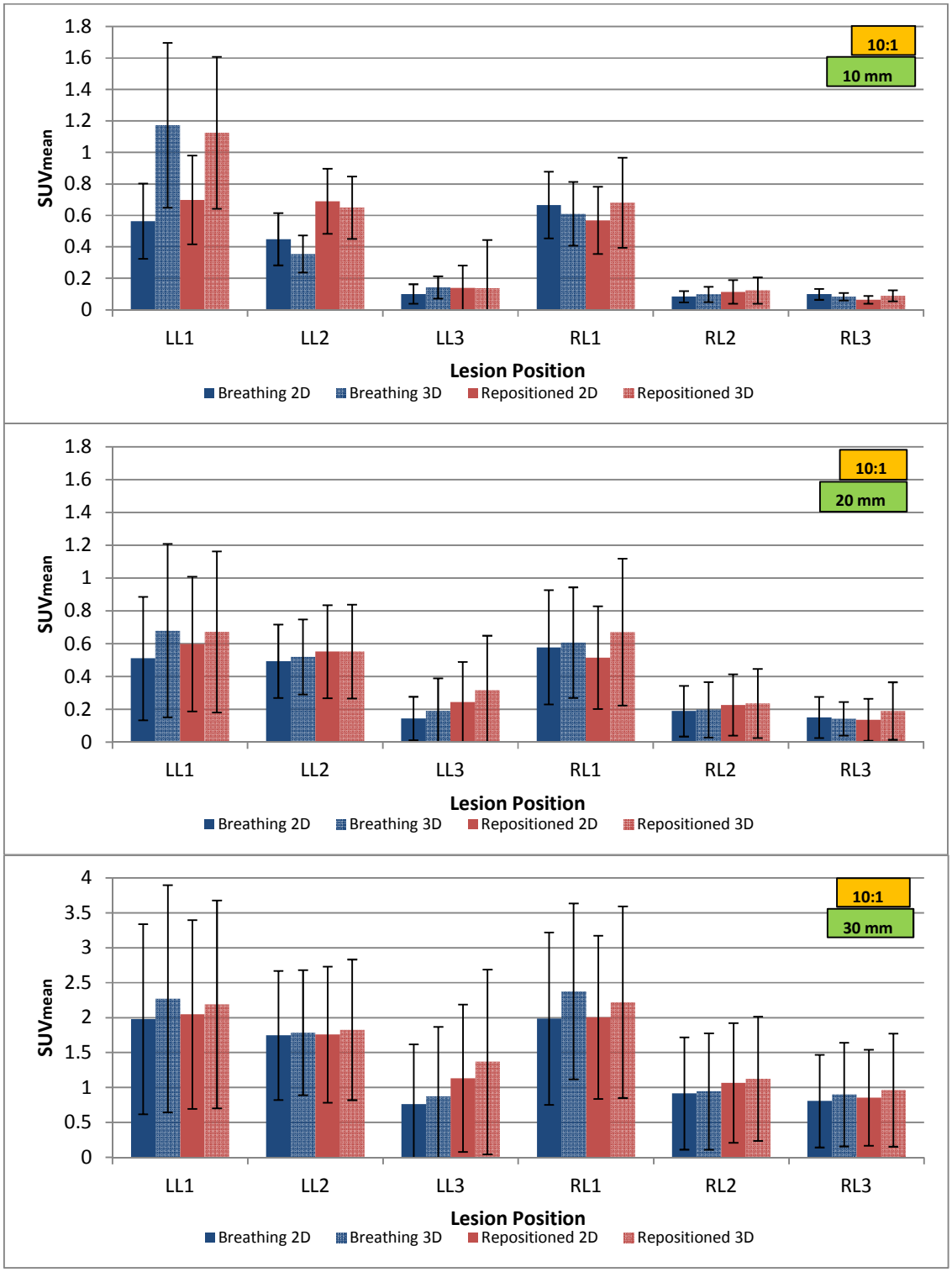

Figure 4-23: SUV_{mean} determined using <u>random coincidences</u> for 10 mm, 20 mm and 30 mm lesions (10:1 contrast ratio) in 2D and 3D-imaging for the left lung lesions (LL1 - LL3) and right lung lesions (RL1 - RL3) by repositioning the phantom partly outside the FoV to determine the effect of activity outside the FoV on SUV_{mean}. SUV_{mean} is shown for averaged breathing images. (Note the difference in scale on the y-axes).

4.3.5 Determination of the influence of activity outside the FoV and the variation in lesion-to-lung contrast on the SUV calculation

The influence of movement during breathing and the variation in the lesion-to-lung contrast on the determination of the SUV for a specific lesion size while the phantom is repositioned partly outside the FoV, is presented in this section. In Figure 4-24 the comparison of SUV_{mean} for the different contrast ratios are shown when including all coincidences in the analysis. With a decrease in contrast ratio, a decrease in SUV_{mean} is noted for all lesions.

Analysing the SUV_{mean} and SUV_{max} for the true coincidences as is displayed in Figure 4-25 and Figure 4-26 respectively, the decrease in SUV between the different contrast ratios is more noticeable as was seen in section 4.3.2. Again, all differences between the SUV_{mean} calculated for the various contrast ratios for each lesion location were statistically significant $P(F<=f) = 0.000 < 0.05$ and $P(T<=t) = 0.000 < 0.05$, and therefore the H_0 was rejected.

Table 4-16: Statistical analysis of differences between SUV_{mean} calculated for average breathing images, using various contrast ratios and by repositioning the phantom outside the FoV. A 20 mm lesion was assessed. SUV_{mean} was calculated for scattered coincidences. Results are only given where the H_o ($p < 0.05$) could not be rejected.

Lesion	Contrast Comparison		F test: P(F<=f)	T-test P(T <=t)
LL1 (2D)	5:1	2:1	0.645	0.447
LL1 (3D)	10:1	5:1	0.689	0.718
	5:1	2:1	0.449	0.130
	10:1	2:1	0.746	0.082
LL3 (2D)	5:1	2:1	0.522	0.118
LL3 (3D)	10:1	5:1	0.005	0.252
	10:1	2:1	0.102	0.177
RL1 (2D)	5:1	2:1	0.663	0.561
RL1 (3D)	10:1	5:1	0.449	0.475
	5:1	2:1	0.772	0.730
	10:1	2:1	0.640	0.297
RL2 (2D)	5:1	2:1	0.649	0.531
RL2 (3D)	10:1	5:1	0.744	0.259
	5:1	2:1	0.895	0.932
	10:1	2:1	0.846	0.227
RL3 (2D)	5:1	2:1	0.151	0.281
RL3 (3D)	5:1	2:1	0.917	0.807

The analysis of the scattered coincidences as depicted in Figure 4-27 demonstrated that very few of the differences between the SUVs of lesions with various contrast ratios were statistically significant with the exception of those listed in Table 4-16. The absolute amount of scatter remains of the same order of magnitude for both the 2D and the 3D acquisitions.

Using the random coincidences to calculate the SUV_{mean} produced the results that can be seen in Figure 4-28. Differences in SUVs were statistically significant except those listed in Table 4-17.

Table 4-17: Statistical analysis of differences between SUV_{mean} calculated for average breathing images, using various contrast ratios and by repositioning the phantom outside the FoV. A 20 mm lesion was assessed. SUV_{mean} was calculated for random coincidences. Results are only given where the H_o ($p < 0.05$) could not be rejected.

Lesion	Contrast Comparison		F test: P(F<=f)	T-test P(T <=t)
LL1 (2D)	5:1	2:1	0.970	0.830
LL1 (3D)	10:1	5:1	0.465	0.470
	5:1	2:1	0.697	0.682
	10:1	2:1	0.269	0.277
LL2 (2D)	5:1	2:1	0.417	0.301
LL2 (3D)	10:1	5:1	0.825	0.218
	5:1	2:1	0.075	0.126
LL3 (2D)	5:1	2:1	0.070	0.058
LL3 (3D)	10:1	5:1	0.079	0.520
	5:1	2:1	0.000	0.062
RL1 (2D)	5:1	2:1	0.507	0.887
RL1 (3D)	10:1	5:1	0.156	0.226
	5:1	2:1	0.793	0.775
	10:1	2:1	0.248	0.141
RL2 (2D)	5:1	2:1	0.815	0.553
RL2 (3D)	10:1	5:1	0.083	0.176
	5:1	2:1	0.408	0.791
	10:1	2:1	0.366	0.283
RL3 (3D)	5:1	2:1	0.271	0.591

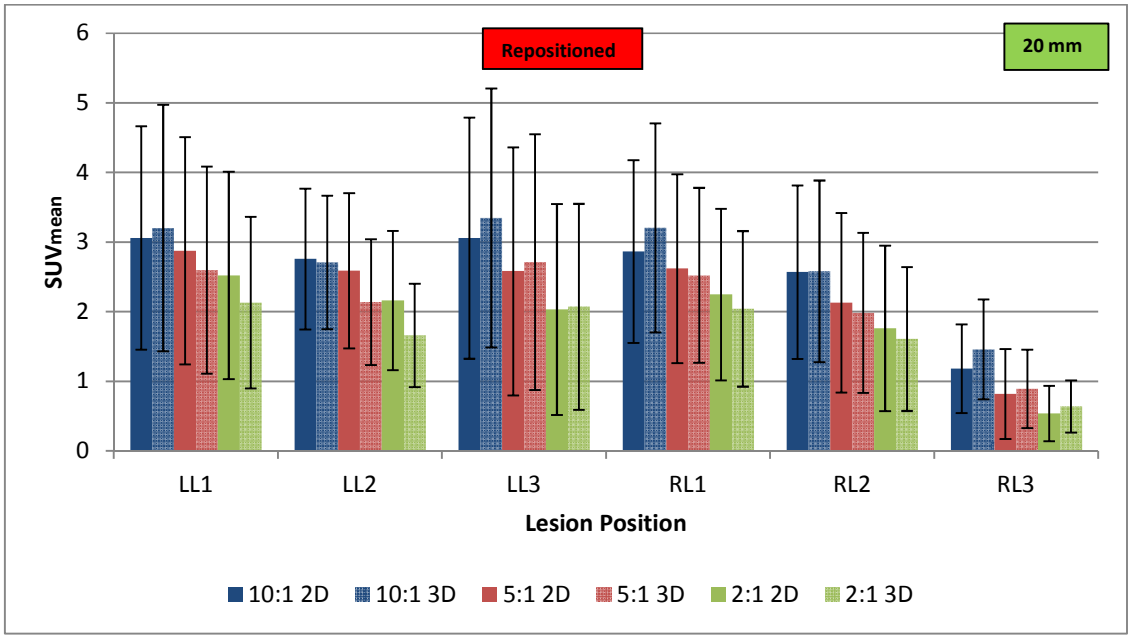

Figure 4-24: SUV_{mean} determined using <u>all coincidences</u> for 20 mm lesions in 2D and 3D-imaging for the left lung lesions (LL1 - LL3) and right lung lesions (RL1 - RL3) using 10:1, 5:1 and 2:1 contrast and by repositioning the phantom partly outside the FoV to determine the effect of lesion-to-lung contrast ratio and activity outside the FoV on SUV_{mean}. SUV_{mean} is shown for averaged breathing images.

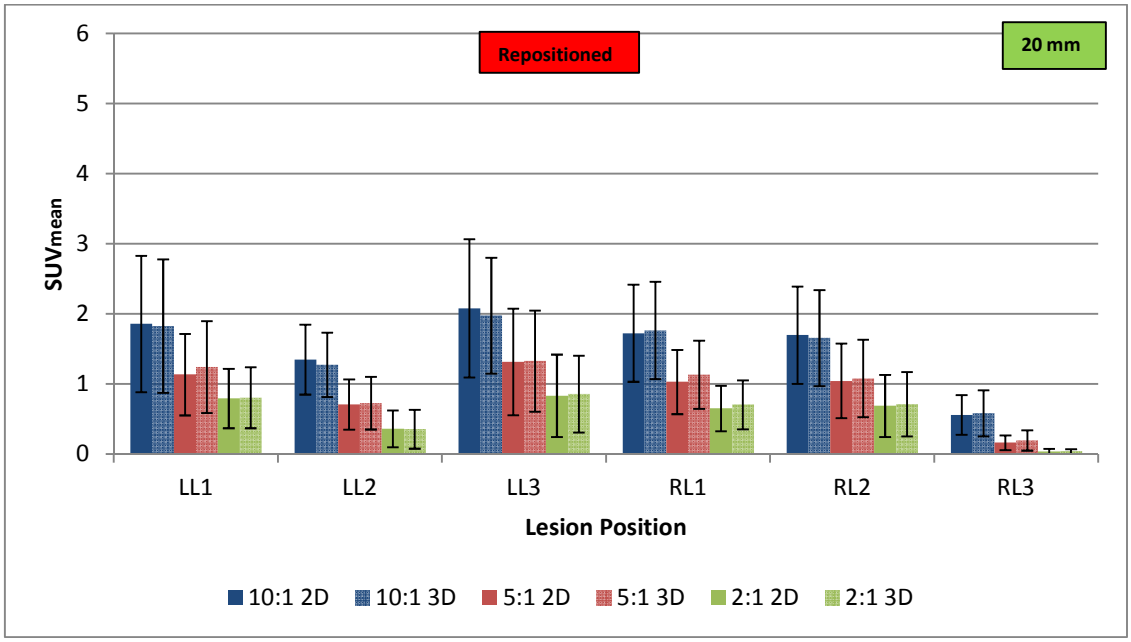

Figure 4-25: SUV_{mean} determined using <u>true coincidences</u> for 20 mm lesions in 2D and 3D-imaging for the left lung lesions (LL1 - LL3) and right lung lesions (RL1 - RL3) using 10:1, 5:1 and 2:1 contrast and by repositioning the phantom partly outside the FoV to determine the effect of lesion-to-lung contrast ratio and activity outside the FoV on SUV_{mean}. SUV_{mean} is shown for averaged breathing images.

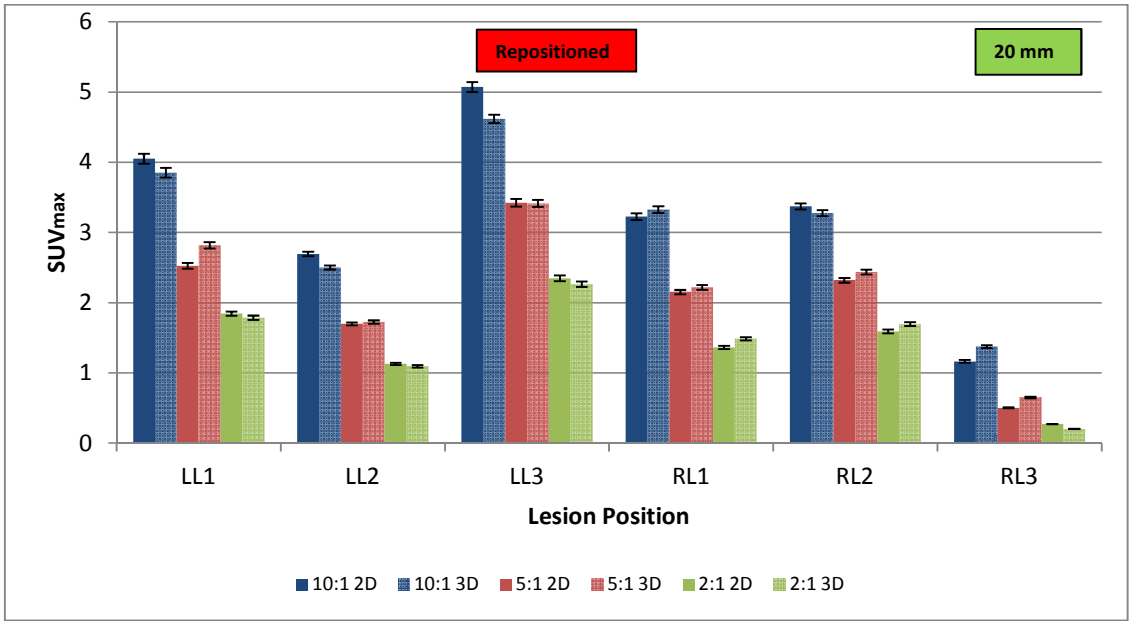

Figure 4-26: SUV_{max} determined using <u>true coincidences</u> for 20 mm lesions in 2D and 3D-imaging for the left lung lesions (LL1 - LL3) and right lung lesions (RL1 - RL3) using 10:1, 5:1 and 2:1 contrast and by repositioning the phantom partly outside the FoV to determine the effect of lesion-to-lung contrast ratio and activity outside the FoV on SUV_{max}. SUV_{max} is shown for averaged breathing images.

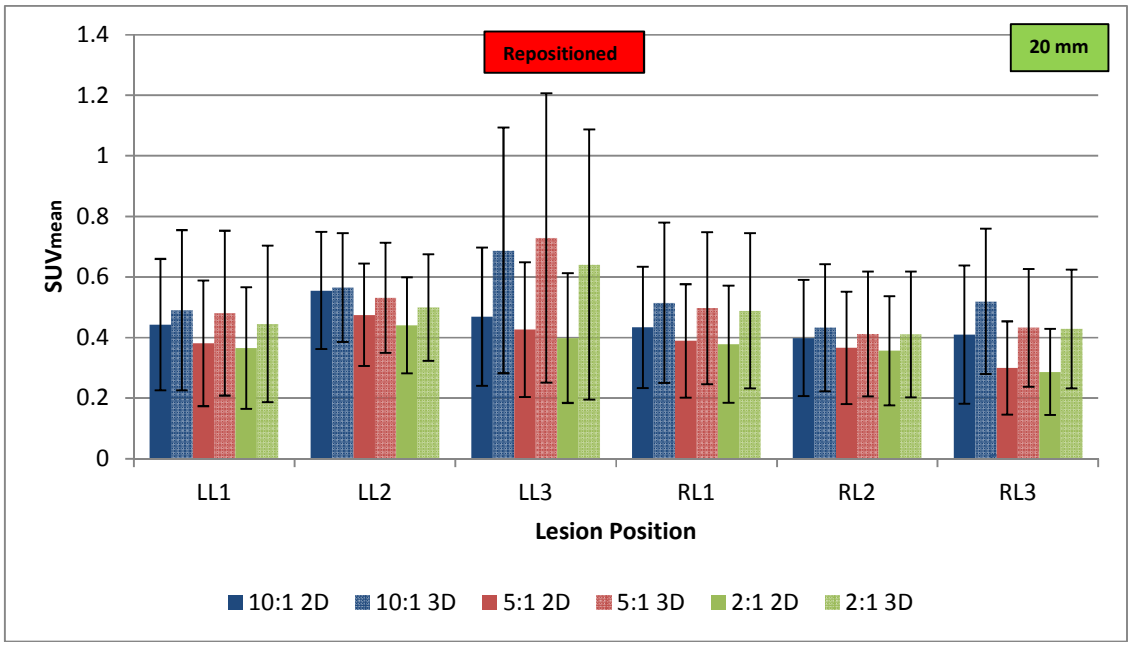

Figure 4-27: SUV_{mean} determined using <u>scattered coincidences</u> for 20 mm lesions in 2D and 3D-imaging for the left lung lesions (LL1 - LL3) and right lung lesions (RL1 - RL3) using 10:1, 5:1 and 2:1 contrast and by repositioning the phantom partly outside the FoV to determine the effect of lesion-to-lung contrast ratio and activity outside the FoV on SUV_{mean}. SUV_{mean} is shown for averaged breathing images.

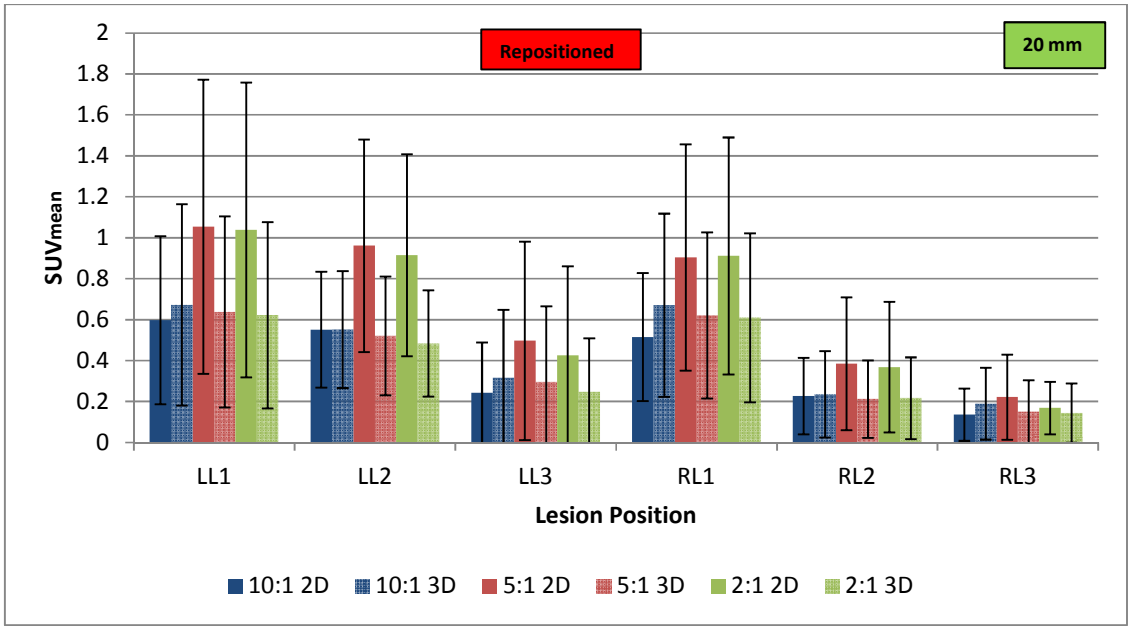

Figure 4-28: SUV_{mean} determined using random coincidences for 20 mm lesions in 2D and 3D-imaging for the left lung lesions (LL1 - LL3) and right lung lesions (RL1 - RL3) using 10:1, 5:1 and 2:1 contrast and by repositioning the phantom partly outside the FoV to determine the effect of lesion-to-lung contrast ratio and activity outside the FoV on SUV_{mean}. SUV_{mean} is shown for averaged breathing images.

A comparison of the percentage true-to-total coincidences, scattered-to-total coincidences and random-to-total coincidences can be seen in Figure 4-29, Figure 4-30 and Figure 4-31 respectively. It is noted that the scattered coincidences have a more significant contribution when the contrast is less, when the lesion is closer to the diaphragm and that the contribution in 3D mode is more when compared to 2D mode as was observed before the phantom was repositioned. When it is compared to Figure 4-17, which displayed the comparison of %scattered-to-total coincidences for the various lesion sizes and contrast ratios, it is also noted that for lesion RL3, the one closest to the liver which is outside the FoV, that the scatter-to-total fraction is significantly more than for the other lesions. The random coincidences are increased more in the apical region than in the other lung regions in particular when the contrast is less. Overall the percentage random-to-total coincidences seem to be more during 2D acquisition when compared to the 3D acquisition and it follows a similar pattern that was seen in Figure 4-18 although the percentage randoms-to-scatter for the repositioned scenario is less than when the phantom was in full FoV.

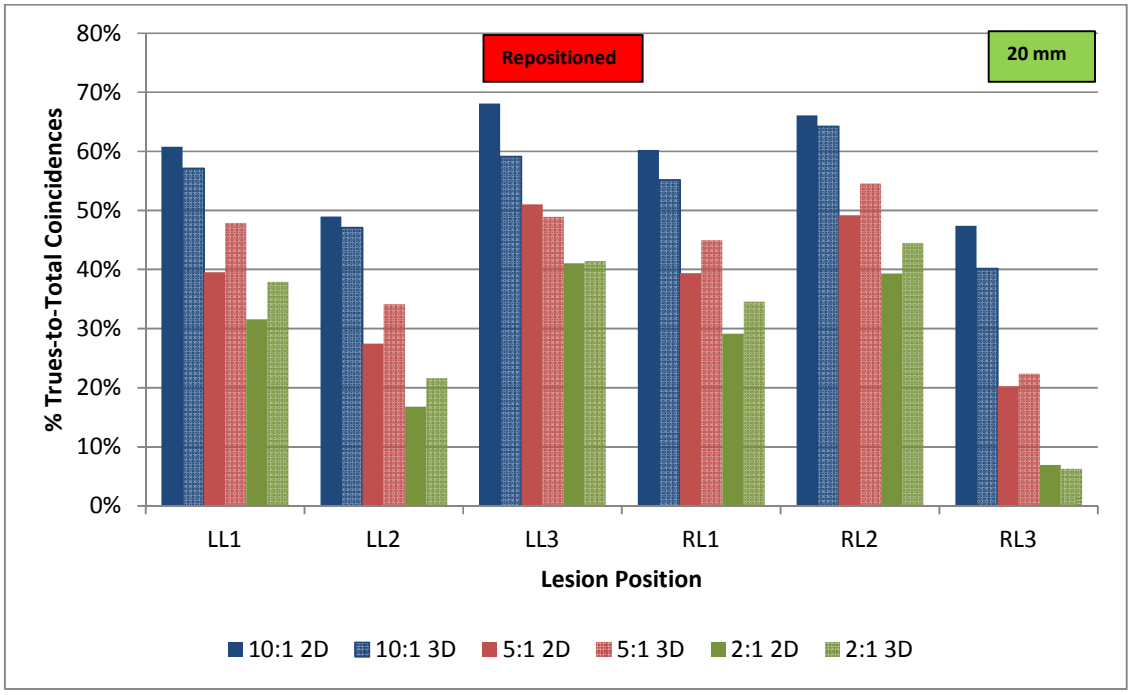

Figure 4-29: Comparison of %True-to-Total Coincidences for lesions with a diameter of 20 mm in the left lung (LL1 - LL3) and right lung (RL1 - RL3) of the XCAT phantom repositioned partly outside the FoV using 2:1, 5:1 and 10:1 contrast ratio in 2D- and 3D modes

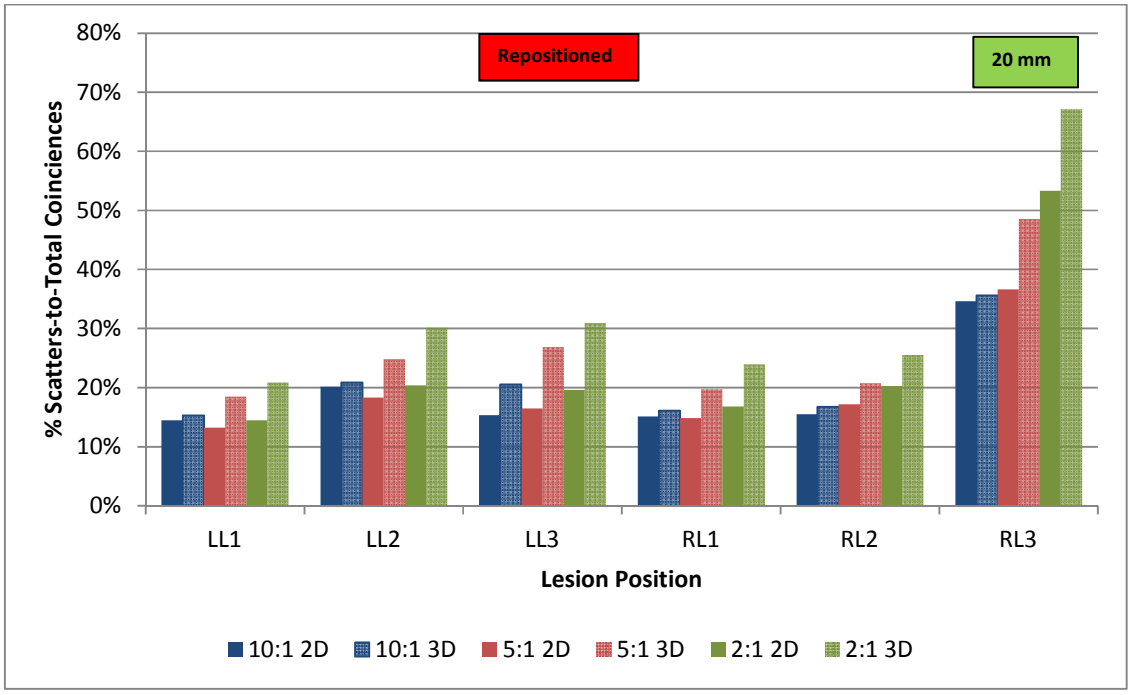

Figure 4-30: Comparison of %Scattered-to-Total Coincidences for lesions with a diameter of 20 mm in the left lung (LL1 - LL3) and right lung (RL1 - RL3) of the XCAT phantom repositioned partly outside the FoV using 2:1, 5:1 and 10:1 contrast ratio in 2D- and 3D modes

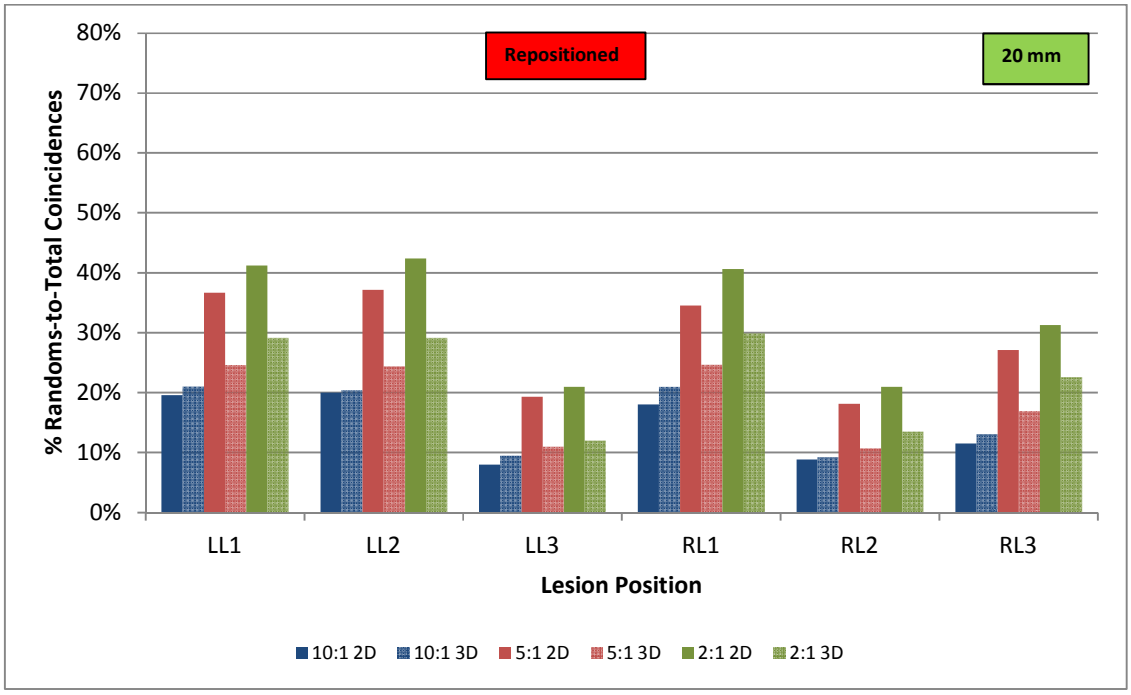

Figure 4-31: Comparison of %Random-to-Total Coincidences for lesions with a diameter of 20 mm in the left lung (LL1 - LL3) and right lung (RL1 - RL3) of the XCAT phantom repositioned partly outside the FoV using 2:1, 5:1 and 10:1 contrast ratio in 2D- and 3D modes

4.3.6 Determination of the influence of activity outside the FoV and the variation in lesion size on the SUV calculation

With the phantom that is repositioned partly outside the FoV, the influence of movement during breathing and the variation in the lesion size with a fixed lesion contrast on the calculation of the SUV is presented in this section.

Figure 4-32 displays the comparison of SUV_{mean} using all coincidences for different lesion sizes at a 10:1 lesion-to-lung contrast ratio for the XCAT phantom being repositioned partly outside the FoV. The effects of the different components of coincidences are discussed hereafter. Using only the true coincidences, the SUV_{mean} comparisons are shown in Figure 4-33 and the SUV_{max} can be seen in Figure 4-34. The differences in SUV_{mean} calculated for true coincidences for the various lesion sizes were statistically significant except the one that is shown in Table 4-18.

Table 4-18: Statistical analysis of differences between SUV_{mean} calculated for average breathing images, using various lesion sizes and by repositioning the phantom outside the FoV. A 10:1 contrast ratio was used. SUV_{mean} was calculated for true coincidences. Results are only given where the H_o ($p < 0.05$) could not be rejected.

Lesion	Lesion Size Comparison		F test: P(F<=f)	T-test P(T <=t)
LL3 (3D)	10 mm	30 mm	0.686	0.406

Including only the scattered coincidences, the comparison of SUV_{mean} is presented in Figure 4-35. As before, the SUV increases with an increase in the diameter of the lesions. The only difference in SUV_{mean} that was not significantly different is shown in Table 4-19. The rest of the differences were statistically significant.

Table 4-19: Statistical analysis of differences between SUV_{mean} calculated for average breathing images, using various lesion sizes and by repositioning the phantom outside the FoV. A 10:1 contrast ratio was used. SUV_{mean} was calculated for scattered coincidences. Results are only given where the H_o ($p < 0.05$) could not be rejected.

Lesion	Lesion Size Comparison		F test: P(F<=f)	T-test P(T <=t)
LL1 (3D)	10 mm	20 mm	0.006	0.925

Comparing the SUV_{mean} using the random coincidences, is shown in Figure 4-36. The differences in SUVs were statistically significant except for those lesions listed in Table 4-20. It is noted that the randoms are significantly increased for the 30 mm lesions, but that the trend is the same when it is compared to Figure 4-15, which displayed the SUV_{mean} using random coincidences for the lesions of different sizes and contrast ratios.

Table 4-20: Statistical analysis of differences between SUV_{mean} calculated for average breathing images, using various lesion sizes and by repositioning the phantom outside the FoV. A 10:1 contrast ratio was used. SUV_{mean} was calculated for random coincidences. Results are only given where the H_o ($p < 0.05$) could not be rejected.

Lesion	Lesion Size Comparison		F test: P(F<=f)	T-test P(T <=t)
LL1 (2D)	10 mm	20 mm	0.004	0.051
RL1 (2D)	10 mm	20 mm	0.005	0.183
RL1 (3D)	10 mm	20 mm	0.001	0.853

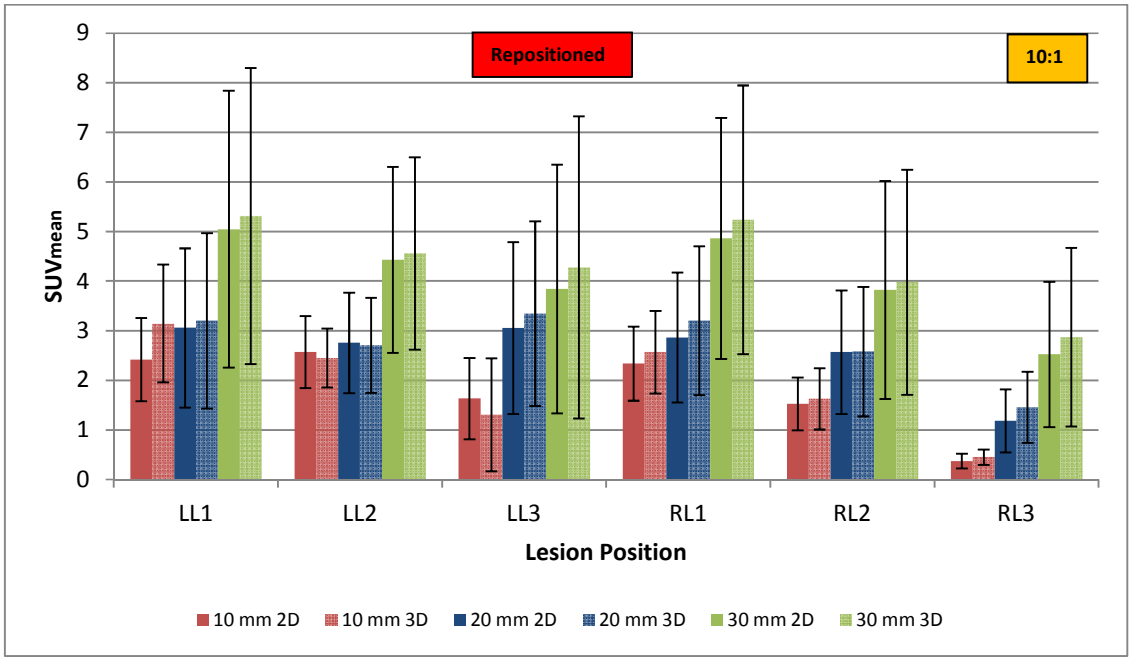

Figure 4-32: Comparison of SUV_{mean} determined using <u>all coincidences</u> for lesions with diameter of 10 mm, 20 mm and 30 mm in the left lung (LL1 - LL3) and right lung (RL1 - RL3) to determine the effect of different sizes of lesions and activity outside the FoV on SUV using a 10:1 contrast ratio in 2D mode by repositioning the phantom partly outside the FoV

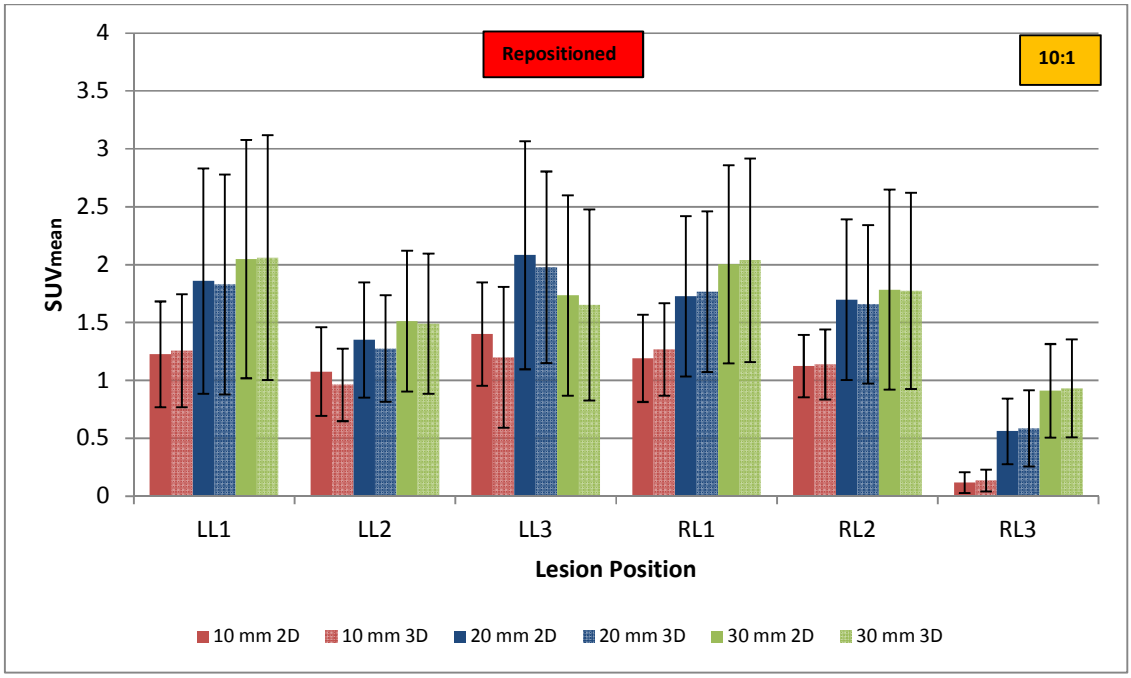

Figure 4-33: Comparison of SUV_{mean} determined using the <u>true coincidences</u> for lesions with diameter of 10 mm, 20 mm and 30 mm in the left lung (LL1 - LL3) and right lung (RL1 - RL3) to determine the effect of different sizes of lesions and activity outside the FoV on SUV using a 10:1 contrast ratio in 2D mode by repositioning the phantom partly outside the FoV

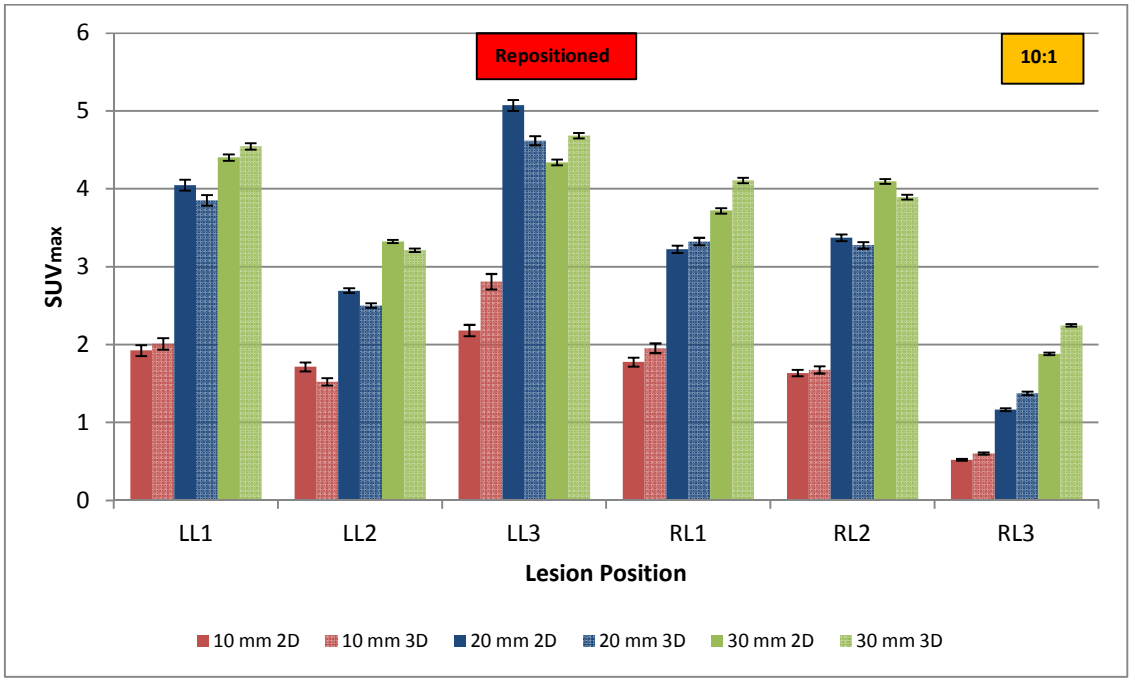

Figure 4-34: Comparison of SUV_{max} determined using the true coincidences for lesions with diameter of 10 mm, 20 mm and 30 mm in the left lung (LL1 - LL3) and right lung (RL1 - RL3) to determine the effect of different sizes of lesions and activity outside the FoV on SUV using a 10:1 contrast ratio in 2D mode by repositioning the phantom partly outside the FoV

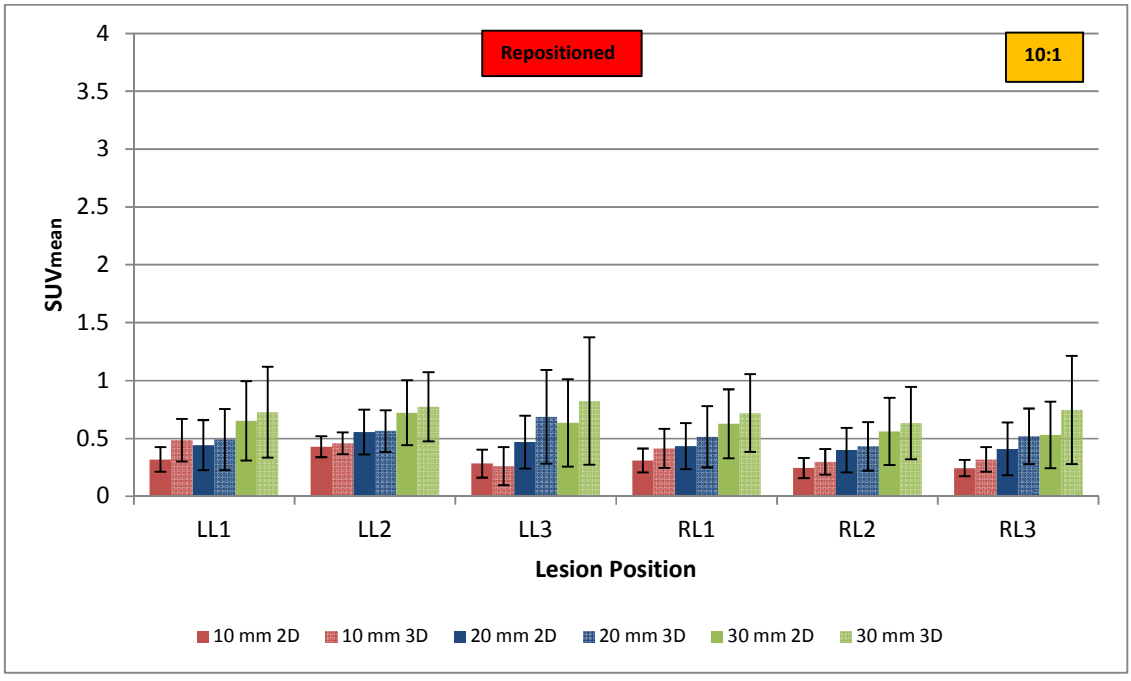

Figure 4-35: Comparison of SUV_{mean} determined using the scattered coincidences for lesions with diameter of 10 mm, 20 mm and 30 mm in the left lung (LL1 - LL3) and right lung (RL1 - RL3) to determine the effect of different sizes of lesions and activity outside the FoV on SUV using a 10:1 contrast ratio in 2D mode by repositioning the phantom partly outside the FoV

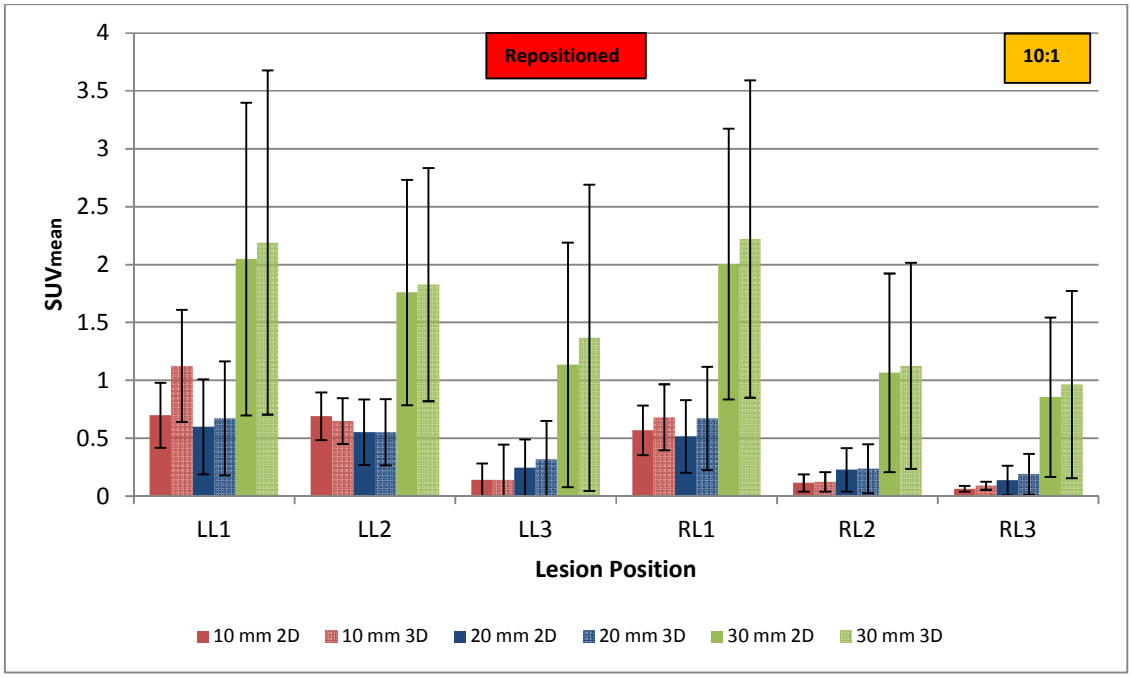

Figure 4-36: Comparison of SUV_{mean} determined using <u>random coincidences</u> for lesions with diameter of 10 mm, 20 mm and 30 mm in the left lung (LL1 - LL3) and right lung (RL1 - RL3) to determine the effect of different sizes of lesions and activity outside the FoV on SUV using a 10:1 contrast ratio in 2D mode by repositioning the phantom partly outside the FoV

The percentage true-to-total coincidences are presented in Figure 4-37, the percentage scattered-to-total coincidences in Figure 4-38 while the percentage of random-to-total coincidences is shown in Figure 4-39. The amount of trues-to-total is highest at the 10 mm lesions in the left basal area. It is noted that the percentage scatter-to-total is significantly greater at the right basal lesion closest to the liver with the liver being outside the FoV. The amount of scatter-to-total for the 10 mm lesion is 65.3% (2D) and 70.7% (3D), and 34.6% (2D) and 35.6% (3D) for the 20 mm lesion when the liver is positioned outside the FoV, compared to 29.4% (2D, 10 mm) and 37.6% (3D, 10 mm), 23.7% (2D, 20 mm) and 28.2% (3D, 20 mm) when the liver was inside the FoV. This is an indication that the smaller lesions are more affected by scatter from a source lying directly outside the FoV than other lesions that are further away from the source. The lesion in the left basal area experiences a larger influence from the heart being close by than from the repositioning of the liver outside of the FoV.

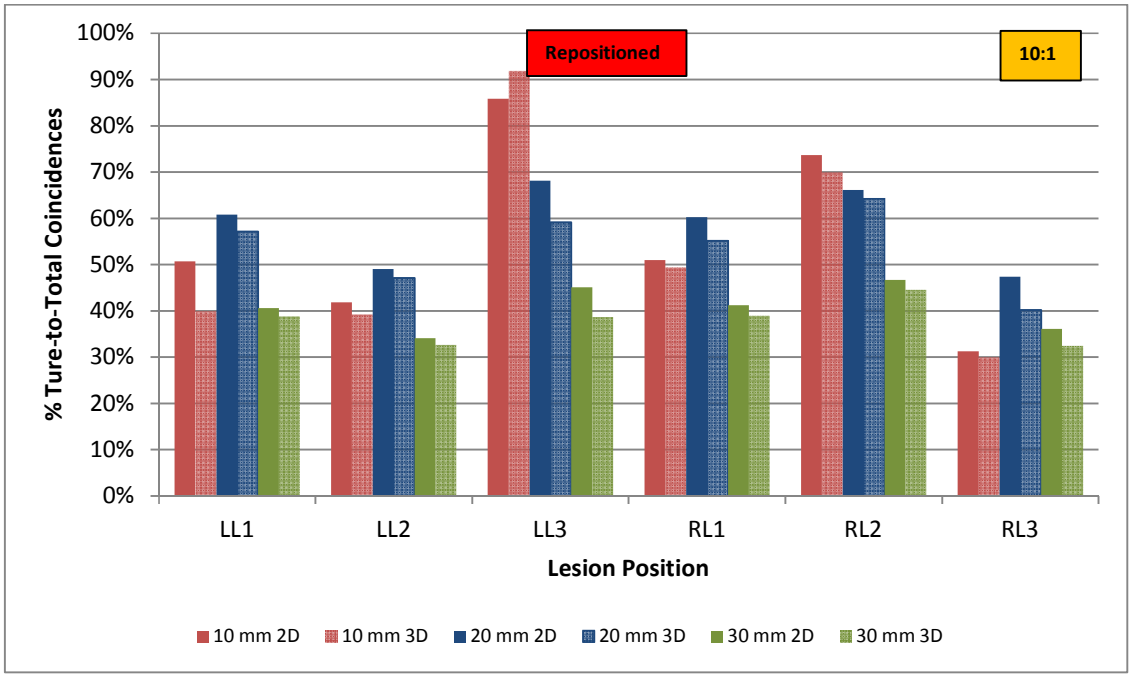

Figure 4-37: Comparison of %True-to-Total Coincidences for lesions with diameter of 10 mm, 20 mm and 30 mm in the left lung (LL1 - LL3) and right lung (RL1 - RL3) of the XCAT phantom repositioned partly outside the FoV using a 10:1 contrast ratio in 2D- and 3D modes

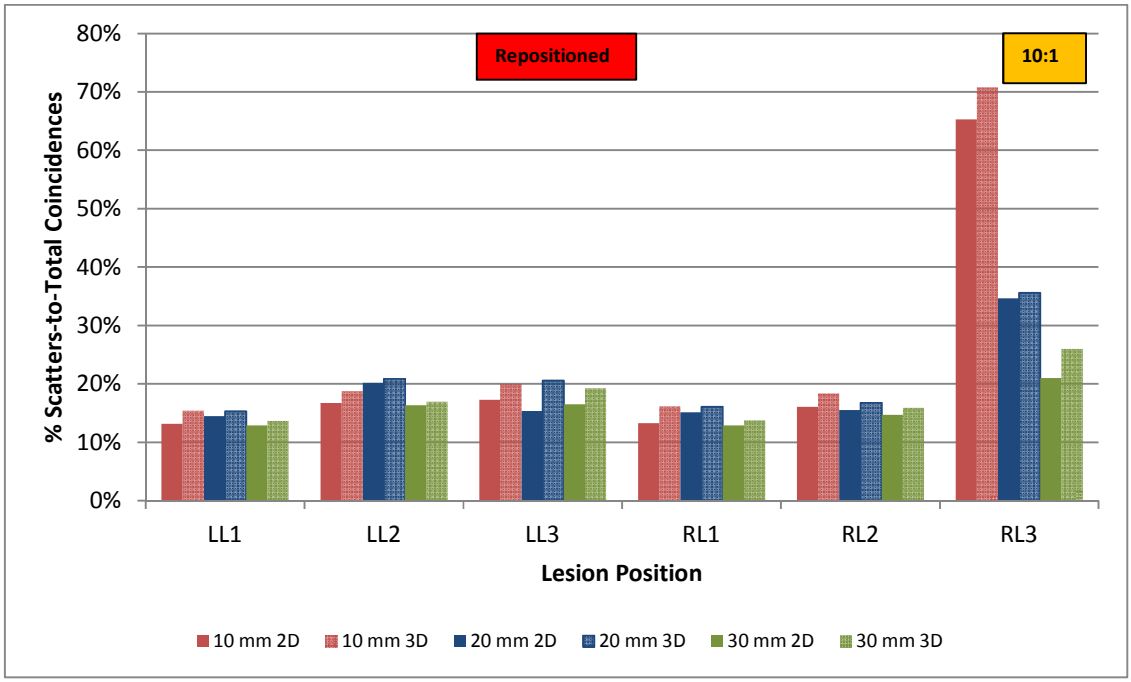

Figure 4-38: Comparison of %Scattered-to-Total Coincidences for lesions with diameter of 10 mm, 20 mm and 30 mm in the left lung (LL1 - LL3) and right lung (RL1 - RL3) of the XCAT phantom repositioned partly outside the FoV using a 10:1 contrast ratio in 2D- and 3D modes

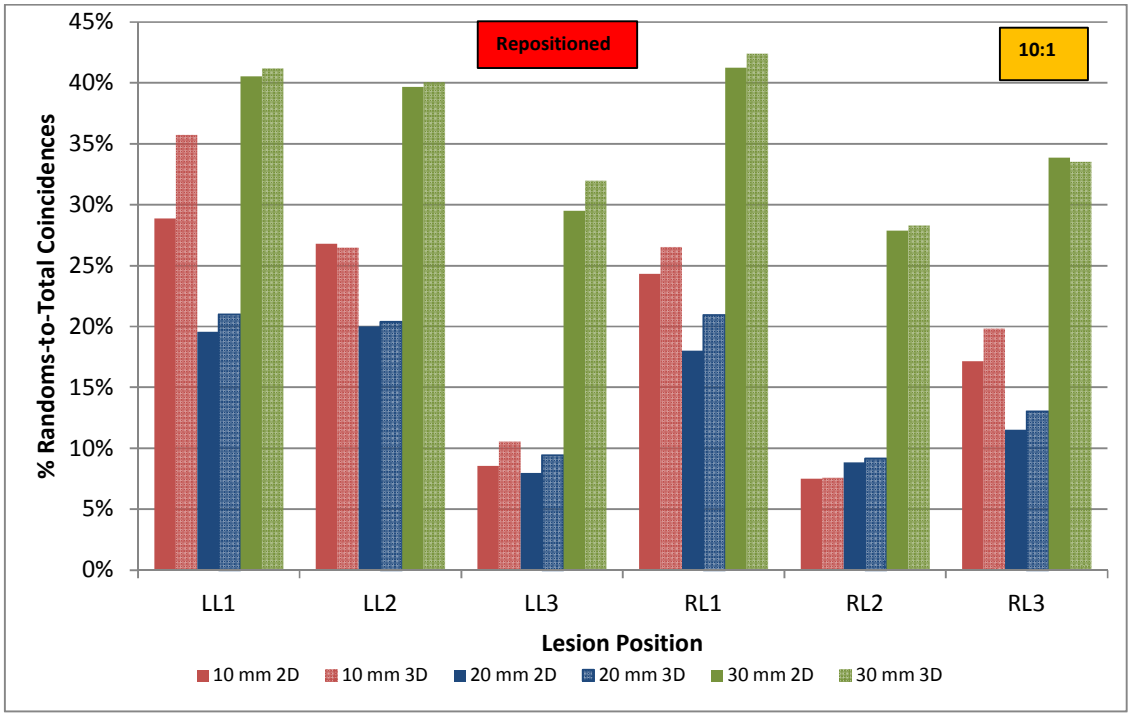

Figure 4-39: Comparison of %Random-to-Total Coincidences for lesions with diameter of 10 mm, 20 mm and 30 mm in the left lung (LL1 - LL3) and right lung (RL1 - RL3) of the XCAT phantom repositioned partly outside the FoV using a 10:1 contrast ratio in 2D- and 3D modes

4.4 Discussion

In this chapter, various parameters influencing the calculation of the SUV of pulmonary lesions were investigated. It was found that the location of the lesion made a difference in SUV when the same size lesions are compared to each other just based on where they are situated in the lungs. In this work, it was the intention to position the three lesions in each lung in the same axial position. It was however not possible to place the basal lesion in the left lung (LL3) directly under the other two because of the location of the heart, this lesion was thus positioned more posteriorly with respect to the others. The lesions were also placed near other structures viz. the middle and basal lesions in the left lung were located in the vicinity of the heart, the basal lesion in the right lung was close to the liver and the two middle lesions (LL2 and RL2) were near the bronchi. The two apical lesions were furthest from any other organs and during the breathing cycle, the apical lesions experienced the least amount of movement. It was expected that breathing and other organs or structures were to influence these lesions the least. It was reported by Miyauchi and Wahl (1996) who studied patients with known pulmonary lesions, that SUVs of lesions in the posterior part of the lungs were significantly higher than those of the anterior and mid portions and that the mean SUV of the lower lung field was significantly higher than the SUVs of the upper and middle lung fields. The investigation had found that the background activity was the most in the posterior aspect of the lungs as well as in the bottom parts. This was attributed to increased blood flow and FDG delivery to these areas as well as scatter from the heart and liver. In this work, a uniform background activity was allocated to the lungs. It is shown in section 4.3.1, that differences in SUV existed between the equivalent lesions in the left and right lungs, e.g. LL2 and RL2. This is probably due to RL2 that is positioned near or on top of a bronchial structure causing the SUV to be lower for RL2 than for LL2 as again be seen in Figure 4-2.

In Figure 4-7, it was noted that for the 10:1 contrast ratio, that the averaged SUV for the lesions under breathing circumstances was more than the SUVs of the same lesions under the static conditions of full inspiration and full expiration at the apical areas. It was fairly similar for the lesions in the central region and it was lower at the basal section. The

differences between the dynamic condition and the static conditions became more prominent when the contrast decreased. For the 10:1 contrast ratio, the largest difference in SUV_{mean} between full inspiration and full expiration was found to be 20.5% at RL3 considering all coincidences in 3D mode acquisition. The difference dropped to 15.3% for the same lesion when only true coincidences were taken into account. Erdi *et al.* (2004) reported an up to 24% variation in SUV_{max} between end expiration and end inspiration dependent on how the attenuation correction using CT was performed.

When comparing the SUVs of different contrast ratios in the six lesions it was found that the largest contrast ratio yielded the largest SUV when using the true coincidences. The percentage trues-to-total was highest at the 10 mm lesions and lowest at the 30 mm lesions. The SUVs comprising of the amount of scattered coincidences remained more or less the same for the different contrast ratios with most differences not being significant statistically. The scatter-to-true fraction was most at the basal lesions for 2:1 contrast which originate from the heart and liver. The amount of random coincidences in each lesion was increased at lower contrast levels in the 2D set-up, but this increase was less in 3D mode, indicating that randoms from other detector rings were detected as was also reported by Visvikis *et al.* (2004). The amount of randoms-to-total coincidences were more prominent in the apical lesions and overall the highest in the 30 mm lesions. This is also the area where the lesions were closest to the sternum, thoracic vertebrae, scapulae and clavicles each of which emitting radiation in different directions which could contribute to the amount of random coincidences that were detected in this area.

It was observed that with increasing lesion size for a fixed lesion contrast, the SUV increased when the true coincidences were included only as well as when the SUV was calculated to the scattered coincidences only or the random coincidences only. The percentage true-to-total coincidences however showed a decrease relatively with increase in lesion diameter. The percentage scatter-to-total coincidences increased relatively with a decrease in lesion size. Thus the scatter fraction has decreased as is evident from Figure 4-17. The fraction of random-to-total coincidences was highest for the apical

lesions and lowest for the basal lesions with the largest fraction recorded for the 30 mm diameter lesions.

Zaidi (2000) and Adam *et al.* (1999) reported that the scatter contribution from outside the field-of-view in 3D may be a challenge and should be investigated before scatter corrections can be applied. In this chapter, it was shown that moving the phantom partly outside the field-of-view had significant effects on the SUVs of objects that were still inside the FoV. In general an increase in the SUVs was observed when the true coincidences were used for the calculation. A decrease in true SUVs was found at the right basal lesion (RL3). The scatter-to-total coincidence percentage was increased in all cases that came about as a result of the liver that lay just outside the FoV.

From the abovementioned results, it can be therefore concluded that partial volume effects play a significant role when determining the SUV lesions in the lung when taking into account the size of the lesions and the amount of activity inside the lesion compared to the background activity. It could therefore be said that the lower the contrast, the more pronounced the PVE will be.

Since the relative standard deviations were found to be large for all coincidence types (between 27% and 64% for trues; between 25% and 62% for scatters; between 44% and 105% for randoms), the SUV_{mean} is influenced by many factors that determine what activity will be used in the calculation of the SUV, such as the choice of VoI, activity variation close to the lesion and the contrast of the lesion. The standard deviation increased also with an increase in the size of the lesion since more pixels were included containing a larger variety of pixel values.

It can also be concluded that the location of the lesions in the lung have an effect on SUV calculation during breathing based on the amount of movement of the lesions during the breathing cycle as well as a result of the surrounding tissue or organ structures but that the amount of scatter and random coincidences that are present at these locations must be taken into account. It can also be concluded that activity outside the field-of-view of the

PET/CT scanner contributed to a change in SUV determination as a result of scatter especially in 3D mode acquisition. By imaging in 2D mode the scatter from neighbouring rings can be effectively minimised.

4.5 References

Adam L-E, Karp JS, Brix G. 1999. Investigation of scattered radiation in 3D whole-body positron emission tomography using Monte Carlo simulations. *Phys Med Biol* 44: 2879-2895.

AMIDE: Amide's a Medical Imaging Data Examiner. Available from: http://amide.sourceforge.net/ (Accessed 12 February 2013).

Bailey DL, Townsend DW, Valk PE, Maisey MN (Eds). 2005. Positron Emission Tomography: Basic Sciences. 1st ed. *Springer, London*: 42-43.

Du Toit PD (dutoitpd@nuke.co.za). (20 May 2008 to 27 August 2008). Re: GATE: Discovery ST. Emails to and from Kirov A. (kirova@mskcc.org) and Schmidtlein CR (schmidtr@mskcc.org).

Erdi YE, Nehmeh SA, Pan T, Pevsner A, Rosenzweig KE, Mageras G, Yorke ED, Schöder H, Hsiao W, Squire OD, Vernon P, Ashman JB, Mostafavi H, Larson SM, Humm JL. 2004. The CT Motion Quantitation of Lung Lesions and Its Impact on PET-Measured SUVs. *J Nucl Med* 45:1287-1292.

GATE: Simulations of Preclinical and Clinical Scans in Emission Tomography, Transmission Tomography and Radiation Therapy. Available from: http://www.opengatecollaboration.org/ (Accessed 01 December 2013).

Hallet WA. 2004. Quantitation in clinical fluorodeoxyglucose positron emission tomography. *Nucl Med Commun* 25:647-650.

Hickeson M, Yun M, Matthies, Zhuang H, Adam L-E, Lacorte L, Alavi A. 2002. Use of a corrected standardized uptake value based on the lesion size on CT permits accurate characterization of lung nodules on FDG-PET. *Eur J Nucl Med* 29:1639-1647.

Jan S, Santin G, Strul D, Staelens S, Assié K, Autret D, Avner S, Barbier R, Bardiès M, Bloomfield PM, Brasse D, Breton V, Bruyndonckx P, Buvat I, Chatziioannou AF,

Choi Y, Chung YH, Comtat C, Donnarieix D, Ferrer L, Glick SJ, Groiselle CJ, Guez D, Honore P-F, Kerhoas-Cavata S, Kirov AS, Kohli V, Koole M, Krieguer M, van der Laan DJ, Lamare F, Largeron G, Lartizien C, Lazaro D, Maas MC, Maigne L, Mayet F, Melot F, Merheb C, Pennacchio E, Perez J, Pietrzyk U, Rannou FR, Rey M, Schaart DR, Schmidtlein CR, Simon L, Song TY, Vieira J-M, Visvikis D, Van de Walle R, Wieërs E, Morel C. 2004. GATE: a simulation toolkit for PET and SPET. *Phys Med Biol* 49:4543-4561.

Loening AM and Gambhir SS. 2003. AMIDE: A Free Software Tool for Multimodality Medical Image Analysis. *Mol Imaging* 2:131-137.

Miyauchi T and Wahl RL. 1996. Regional 2-[18F]fluoro-2-deoxy-D-glucose uptake varies in the normal lung. *Eur J Nucl Med* 23:517-523.

Nuzzo R. 2014. Statistical Errors. *Nature* 506:150-152.

Reader AJ, Stijn A, Bakatselos F, Manavaki R, Walledge RJ, Jeavons AP, Julyan PJ, Zhao S, Hastings DL, Zweit J. 2002. One-Pass List-Mode EM Algorithm for High-Resolution 3-D PET Image Reconstruction Into Large Arrays. *IEEE Trans Nucl Sci* 49:693-699.

ROOT: Data Analysis Framework. Available from: http://root.cern.ch/ (Accessed 17 September 2014).

Schmidtlein C, Turner A, Nehmeh S, Mawlawi O, Erdi Y, Humm J, Amols H, Kirov A. 2006. SU-FF-I-54: A Monte Carlo Model of the Discovery ST PET Scanner. *Med Phys 33:2009.*

Segars WP, Mahesh M, Beck TJ, Frey EC, Tsui BMW. 2008. Realistic CT simulation using the 4D XCAT phantom. *Med Phys* 35:3800-3808.

Segars WP, Sturgeon G, Mendonca S, Grimes J, Tsui BMW. 2010. 4D XCAT phantom for multimodality imaging research. *Med Phys* 37:4902-4915.

US Army Aeromedical Research Laboratory (USAARL). 1988. Anthropometry and mass distribution for human analogues, volume I: Military aviators (Report No 88-5), Fort Rucker AL, USA.

Visvikis D, Turzo A, Bizais Y, Cheze-Le Rest C. 2004c. Technology related parameters affecting quantification in positron emission tomography imaging. *Nucl Med Commun* 25:637-641.

XCAT phantom V1. Available from http://deckard.duhs.duke.edu/~wsegars/xcat/XCAT_V1_PC.zip (Accessed and downloaded 21 October 2011).

Zaidi H. 2000. Addendum to "Relevance of accurate Monte Carlo modeling in nuclear medicine imaging". *Med Phys* 27:816-817.

4.6 Appendices

4.6.1 Set-up of the XCAT phantom

```
*** DYNAMIC XCAT PHANTOM, version 1.0 in C***
-------------------------------------------
-----------------------------------------------
 PARAMETERS: (dynamic XCAT version 2.0 in C)
-----------------------------------------------
act_phan_each = 1  (activity phantom each frame saved)
act_phan_ave = 1 (time-average activity phantom saved)
atten_phan_each = 1  (atten. coeff. phantom each frame saved)
atten_phan_ave = 1 (time-average atten. coeff. phantom saved)
Respiration motion included only
 Total Output Period = time_per_frame*output_frames
time_per_frame =       0.2500 secs
Total Output Frames = 20
==>Total Output Period =       5.0000 secs

beating heart period =       1.0000 secs
Heart Start Phase Index =  0.0000
Respiratory period =       5.0000 secs
Resp. Start Phase Index =  0.0000
maximum diaphragm motion =       2.0000
heart scale =       1.0000
hrt_lv_length =       9.4300
hrt_lv_radius =       2.9700
body long axis =      34.5000
body short axis =      27.5000
body height =     192.0000
rib long axis =      30.0000
rib short axis =      22.7000
air_flag = 4
breast_type = 1    (prone position model)
which_breast = 0   (no breasts, male)
breast_long_axis =      18.2000
breast_short_axis =       7.0000
breast_height =      14.0000
rdiaph_liv_position =       3.4000
ldiaph_position =       1.9000
 intv (cm) =  1.0000
 pixel width =  0.3125 (cm/pixel)
 slice width =  0.3125 (cm/pixel)
 voxel volume (pixel width^2)(slice_width) =  0.030518 ml
 array_size = 128
 subvoxel_index = 2 => 8 subvoxels per voxel
 starting slice number    = 455
 ending slice number      = 514
apical_thin = 1.000000

Main orientation of heart:
```

```
    zy_rotation (beta)=  -90.00 (deg)
    xz_rotation ( phi)=  -20.00 (deg)
    yx_rotation ( psi)=  -50.00 (deg)

Translation of heart:
    X translation     =    0.00  (cm)
    Y translation     =    0.00  (cm)
    Z translation     =   20.00  (cm)

valve thickness <= 0 (no valves )
av_step =  0.3000 (smoothing between atria & ventr.)
total_rotation = 0 (no heart rotation during contraction )
activity_unit = 0 (no scaling of activity values)

radionuclide energy (keV)=     511.0000

------------------------------------------------
done checking,  general parameters O.K.
------------------------------------------------
------------------------------------------------------
Density of Tissues (g/cm^3):
   Body (water)  : 1.000000
   Muscle        : 1.050000
   Adipose (fat) : 0.920000
   Lung          : 0.300000
   Spine Bone    : 1.420000
   Rib Bone      : 1.920000
   Blood         : 1.060000
   Heart         : 1.050000
   Kidney        : 1.050000
   Liver         : 1.060000
   Lymph         : 1.030000
   Pancreas      : 1.040000
   Spleen        : 1.060000
   Intestine     : 1.030000
   Skull         : 1.610000
   Cartilage     : 1.100000
   Brain         : 1.040000

Linear Attenuation Coefficients (1/cm):
   Body (water)   =       0.0927
   Muscle         =       0.0968
   Adipose (fat)  =       0.0868
   Lung           =       0.0267
   Spine Bone     =       0.1101
   Rib Bone       =       0.1305
   Blood          =       0.0976
   Heart          =       0.0969
   Kidney         =       0.0968
   Liver          =       0.0977
   Lymph          =       0.0952
   Pancreas       =       0.0962
```

```
   Spleen          =       0.0977
   Intestine       =       0.0952
   Skull           =       0.1430
   Cartilage       =       0.1008
   Brain           =       0.0963

Linear Attenuation Coefficients (1/pixel):
   Body (water)    =       0.0290
   Muscle          =       0.0302
   Adipose (fat)   =       0.0271
   Lung            =       0.0084
   Spine Bone      =       0.0344
   Rib Bone        =       0.0408
   Blood           =       0.0305
   Heart           =       0.0303
   Kidney          =       0.0303
   Liver           =       0.0305
   Lymph           =       0.0298
   Pancreas        =       0.0301
   Spleen          =       0.0305
   Intestine       =       0.0297
   Skull           =       0.0447
   Cartilage       =       0.0315
   Brain           =       0.0301

--------------------------------------------------

--------------------------------------------------
--------------------------------------------------
CREATING FRAME #1 ...

Time =   0.000 seconds
Activity Ratios
--------------------------------------------------
  Body                    =       2.0000
  Liver                   =      40.0000
  Gall Bladder            =      60.0000
  Lung                    =       4.0000
  Stomach Wall            =       2.0000
  Stomach Contents        =       2.0000
  Kidney                  =      75.0000
  Spleen                  =      30.0000
  Vertebral Bone(head)    =       6.0000
  Vertebral Bone(process)=       6.0000
  Pelvis Bone             =       2.0000
  Wet Rib Bone            =       5.0000
  Bone Cartilage          =       2.0000
  Abdom. Artery           =       2.0000
  Abdom. Vein             =       2.0000
  Bladder                 =       2.0000
  Prostate                =      30.0000
  Asc. large int.         =       2.0000
```

```
  Asc. large int.(air)   =       2.0000
  Trans. large int.      =       2.0000
  Trans. large int.(air) =       2.0000
  Desc. large int.       =       2.0000
  Desc. large int.(air)  =       2.0000
  Rectum                 =       2.0000
  Rectum(air)            =       2.0000
  Seminal Vessicles      =       2.0000
  Vas deferens           =       2.0000
  Testes                 =       2.0000
  Ureter                 =       2.0000
  Urethra                =       2.0000
  Lymph (normal)         =       2.0000
  Lymph (abnormal)       =       2.0000

  LV Myocardium    =      75.0000
  LA Myocardium    =      75.0000
  RV Myocardium    =      75.0000
  RA Myocardium    =      75.0000

  LV Blood pool    =       2.0000
  LA Blood pool    =       2.0000
  RV Blood pool    =       2.0000
  RA Blood pool    =       2.0000
-------------------------------------------------

Current heart phase index =   0.000 (LV fully relaxed, i.e. end-
diastole)
Current resp phase index  =   0.000 (full exhalation)
RESPIRATION PARAMETERS -------------------------
diaphragm motion    =    0.00 mm
delta AP diameter =    0.00 mm


STATIC ORGAN VOLUMES (same for all frames):
Volume of Liver         =     80.154419 ml
Volume of Gall Bladder  =      0.000000 ml
Volume of Stomach       =      0.000000 ml
Volume of Kidneys(both) =      0.000000 ml
Volume of Spleen        =      0.000000 ml
Volume of Torso         =  14896.916992 ml
----------------------------------------
----------------------------------------

Volume of Right Lung    =   1532.401367 ml
Volume of Left Lung     =   1312.741089 ml
Volume of LV myocardium =   147.899628 ml
Volume of RV myocardium =    25.447845 ml
Volume of LA myocardium =    39.733887 ml
Volume of RA myocardium =    28.903961 ml
Volume of LV chamber    =   110.958099 ml
Volume of RV chamber    =   113.796234 ml
```

```
Volume of LA chamber    =    77.484131 ml
Volume of RA chamber    =    96.988678 ml
----------------------------------------
Volume of TOTAL HEART   =   640.178833 ml

Center of mass for the whole heart (pixels):
       X =   74.616111
       Y =   52.977993
       Z =    9.881012

Left Ventricle Center of Mass (pixels):
      X =   80.800702
      Y =   50.599056
      Z =    8.305512

Maximum activity per voxel =      75.000000
Total activity = 15952256.000000

Saving activity phantom in file : phantom20.bin_act_1
Saving attenuation coefficient phantom in file :
phantom20.bin_atn_1
-------------------------------------------------
-------------------------------------------------
-------------------------------------------------
.
.
.
.
.
.
.
.
CREATING FRAME #10 ...

Time =   2.250 seconds
Activity Ratios
-------------------------------------------------
  Body                    =       2.0000
  Liver                   =      40.0000
  Gall Bladder            =      60.0000
  Lung                    =       4.0000
  Stomach Wall            =       2.0000
  Stomach Contents        =       2.0000
  Kidney                  =      75.0000
  Spleen                  =      30.0000
  Vertebral Bone(head)    =       6.0000
  Vertebral Bone(process)=       6.0000
  Pelvis Bone             =       2.0000
  Wet Rib Bone            =       5.0000
  Bone Cartilage          =       2.0000
  Abdom. Artery           =       2.0000
  Abdom. Vein             =       2.0000
```

```
  Bladder                =       2.0000
  Prostate               =      30.0000
  Asc. large int.        =       2.0000
  Asc. large int.(air)   =       2.0000
  Trans. large int.      =       2.0000
  Trans. large int.(air) =       2.0000
  Desc. large int.       =       2.0000
  Desc. large int.(air)  =       2.0000
  Rectum                 =       2.0000
  Rectum(air)            =       2.0000
  Seminal Vessicles      =       2.0000
  Vas deferens           =       2.0000
  Testes                 =       2.0000
  Ureter                 =       2.0000
  Urethra                =       2.0000
  Lymph (normal)         =       2.0000
  Lymph (abnormal)       =       2.0000

  LV Myocardium    =      75.0000
  LA Myocardium    =      75.0000
  RV Myocardium    =      75.0000
  RA Myocardium    =      75.0000

  LV Blood pool    =       2.0000
  LA Blood pool    =       2.0000
  RV Blood pool    =       2.0000
  RA Blood pool    =       2.0000
-----------------------------------------------------

Current heart phase index =   0.000 (LV fully relaxed, i.e. end-
diastole)
Current resp phase index  =   0.450 (exhaling:   8% exhaled)
RESPIRATION PARAMETERS ------------------------
diaphragm motion    =  -19.55 mm
delta AP diameter =   11.73 mm


----------------------------------------
----------------------------------------

Volume of Right Lung    =   1716.070312 ml
Volume of Left Lung     =   1551.579590 ml
Volume of LV myocardium =    91.033936 ml
Volume of RV myocardium =    18.798828 ml
Volume of LA myocardium =    29.262543 ml
Volume of RA myocardium =    22.411346 ml
Volume of LV chamber    =    68.912506 ml
Volume of RV chamber    =    69.515228 ml
Volume of LA chamber    =    67.604065 ml
Volume of RA chamber    =    79.013824 ml
----------------------------------------
Volume of TOTAL HEART   =   446.552277 ml
```

```
Center of mass for the whole heart (pixels):
       X =   73.977373
       Y =   49.518872
       Z =    7.309698

Left Ventricle Center of Mass (pixels):
      X =   80.889164
      Y =   46.920927
      Z =    5.707761

Maximum activity per voxel =      75.000000
Total activity = 14145760.000000

Saving activity phantom in file : phantom20.bin_act_10
Saving attenuation coefficient phantom in file :
phantom20.bin_atn_10
--------------------------------------------------
--------------------------------------------------
.
.
.
.
CREATING FRAME #20 ...

Time =   4.750 seconds
Activity Ratios
--------------------------------------------------
  Body                    =       2.0000
  Liver                   =      40.0000
  Gall Bladder            =      60.0000
  Lung                    =       4.0000
  Stomach Wall            =       2.0000
  Stomach Contents        =       2.0000
  Kidney                  =      75.0000
  Spleen                  =      30.0000
  Vertebral Bone(head)    =       6.0000
  Vertebral Bone(process)=       6.0000
  Pelvis Bone             =       2.0000
  Wet Rib Bone            =       5.0000
  Bone Cartilage          =       2.0000
  Abdom. Artery           =       2.0000
  Abdom. Vein             =       2.0000
  Bladder                 =       2.0000
  Prostate                =      30.0000
  Asc. large int.         =       2.0000
  Asc. large int.(air)    =       2.0000
  Trans. large int.       =       2.0000
  Trans. large int.(air) =       2.0000
  Desc. large int.        =       2.0000
  Desc. large int.(air)   =       2.0000
  Rectum                  =       2.0000
```

```
  Rectum(air)            =       2.0000
  Seminal Vessicles      =       2.0000
  Vas deferens           =       2.0000
  Testes                 =       2.0000
  Ureter                 =       2.0000
  Urethra                =       2.0000
  Lymph (normal)         =       2.0000
  Lymph (abnormal)       =       2.0000

  LV Myocardium    =      75.0000
  LA Myocardium    =      75.0000
  RV Myocardium    =      75.0000
  RA Myocardium    =      75.0000

  LV Blood pool    =       2.0000
  LA Blood pool    =       2.0000
  RV Blood pool    =       2.0000
  RA Blood pool    =       2.0000
-------------------------------------------------

Current heart phase index =   0.000 (LV fully relaxed, i.e. end-
diastole)
Current resp phase index  =   0.950 (exhaling:  92% exhaled)
RESPIRATION PARAMETERS ------------------------
diaphragm motion    =   -0.73 mm
delta AP diameter =    0.44 mm

---------------------------------------
---------------------------------------

Volume of Right Lung    =   1535.530884 ml
Volume of Left Lung     =   1314.879150 ml
Volume of LV myocardium =   145.545959 ml
Volume of RV myocardium =    25.009155 ml
Volume of LA myocardium =    39.695740 ml
Volume of RA myocardium =    28.491974 ml
Volume of LV chamber    =   110.401154 ml
Volume of RV chamber    =   112.098694 ml
Volume of LA chamber    =    77.522278 ml
Volume of RA chamber    =    96.885681 ml
---------------------------------------
Volume of TOTAL HEART   =   634.661499 ml

Center of mass for the whole heart (pixels):
       X =   74.613422
       Y =   52.865767
       Z =    9.776911

Left Ventricle Center of Mass (pixels):
      X =   80.812077
      Y =   50.445720
      Z =    8.208340
```

```
Maximum activity per voxel =      75.000000
Total activity = 15848819.000000

Saving activity phantom in file : phantom20.bin_act_20
Saving attenuation coefficient phantom in file :
phantom20.bin_atn_20
-------------------------------------------------
Saving time-avg. atten. coeff. phantom in file :
phantom20.bin_atn_av
-------------------------------------------------
Saving time-avg activity phantom in file : phantom20.bin_act_av
-------------------------------------------------
```

4.6.2 Example of GATE Simulation macro used for XCAT Phantom

In this macro, the various components are colour-coded as follows:

- scanner definition – See Chapter 3
- description of the structure of the phantom
- description of the source or spread of activity inside the phantom
- physical processes involved – See Chapter 3
- detection processes and digitized – See Chapter 3
- random number generator model
- the output of the simulation

.
.
.

```
# V O X E L I Z E D  M A T R I X  X C A T  P H A N T O M
/gate/world/daughters/name XCAT
/gate/world/daughters/insert compressedMatrix
/gate/XCAT/geometry/insertReader interfile
/gate/XCAT/verbose 0

/gate/XCAT/interfileReader/insertTranslator range
/gate/XCAT/interfileReader/rangeTranslator/readTable
/auto/home/mount/dutoitpd/XCAT_10_48_2D/range.dat
/auto/home/mount/dutoitpd/XCAT_10_48_2D/phantomlesion
/gate/XCAT/interfileReader/rangeTranslator/describe 1
/gate/XCAT/interfileReader/readFile
/auto/home/mount/dutoitpd/XCAT_10_48_2D/phantomlesion.h33
/gate/XCAT/placement/setTranslation  0. 0. 0. mm
/gate/XCAT/placement/setRotationAxis 1 0 0
/gate/XCAT/placement/setRotationAngle 0 deg
/gate/XCAT/attachPhantomSD
/gate/XCAT/interfileReader/describe 1
#/gate/XCAT/addOutput doseOutput
#/gate/output/doseOutput/saveUncertainty true
#/gate/output/doseOutput/setFileName XCAT_paraDose.bin
```

```
.
.
.

# V O X E L   S O U R C E   B A S E D   O N   T H E   X C A T   P H A
N T O M

/gate/source/addSource voxel voxel
#/gate/source/verbose 0
/gate/source/voxel/reader/insert interfile
/gate/source/voxel/interfileReader/translator/insert range
/gate/source/voxel/interfileReader/rangeTranslator/readTable
/auto/home/mount/dutoitpd/XCAT_10_48_2D/activityRange.dat
/gate/source/voxel/interfileReader/rangeTranslator/describe 1
/gate/source/voxel/interfileReader/readFile
/auto/home/mount/dutoitpd/XCAT_10_48_2D/phantomlesion.h33
/gate/source/voxel/gps/particle e+
/gate/source/voxel/setForcedUnstableFlag true
/gate/source/voxel/gps/energytype Fluor18
/gate/source/voxel/setForcedHalfLife 6586.2 s
/gate/source/voxel/setPosition   -350. -350. -78.5  mm
/gate/source/voxel/gps/confine NULL
/gate/source/voxel/gps/angtype iso
/gate/source/voxel/dump 1
#/gate/source/voxel/verbose 0

/gate/source/list

.
.
.

#     O U T P U T

/gate/output/verbose 1

/gate/output/root/enable
/gate/output/root/setFileName XCAT2Dav
/gate/output/root/setRootHitFlag 0
/gate/output/root/setRootSinglesFlag 1
/gate/output/root/setRootCoincidencesFlag 1
/gate/output/root/setRootdelayFlag 1
/gate/output/root/setRootNtupleFlag 0
/gate/random/setEngineName JamesRandom
/gate/random/setEngineSeed auto
/gate/random/verbose 1

#     S T A R T
/gate/application/setTimeSlice  1 s
/gate/application/setTimeStart  0 s
/gate/application/setTimeStop   420 s

/gate/application/startDAQ
```

4.6.3 Example of *range.dat*

```
8
0   0    Air
1   2    Body
3   4    Lung
5   5    RibBone
6   6    SpineBone
7   24    Breast
25  40    Liver
41  75    Heart
```

4.6.4 Example of *activityRange.dat* for use in a 10:1 lesion-to-background ratio scenario

```
8
0 0 0
1 2 177
3 4 163
5 5 288
6 6 331
7 24 1630
25 35 530
36 75 1986
```

4.6.5 Total activity (MBq) in the XCAT phantom (thoracic area) with change in lesion size and contrast ratio based upon the activity concentrations listed in Table 4-3

Contrast	Lesion size		
Ratio	10 mm	20 mm	30 mm
2:1	80.07	80.00	80.45
5:1	84.60	85.15	86.85
10:1	92.30	93.74	97.51

4.6.6 Tables of Results

The SUV data for the XCAT phantom are listed in the following tables:

Table A 1: SUVs of 10 mm lesions, acquired during breathing using a 10:1 lesion-to-lung contrast

All

2D

		Diameter (mm)	Volume (ml)	min	max	mean	std dev	variance	std error
Lesions	LL1	10	0.524	0.4959	3.0700	1.9996	0.7506	0.5634	0.1132
	LL2	10	0.524	0.8697	3.4060	2.2268	0.6995	0.4893	0.1010
	LL3	10	0.524	0.2327	2.2632	1.2414	0.5635	0.3175	0.0760
	RL1	10	0.524	0.5794	3.8447	2.5328	0.7580	0.5745	0.1184
	RL2	10	0.524	0.3188	2.3915	1.4074	0.5135	0.2637	0.0726
	RL3	10	0.524	0.1979	1.9332	1.0587	0.3567	0.1273	0.0481

3D

		Diameter (mm)	Volume (ml)	min	max	mean	std dev	variance	std error
Lesions	LL1	10	0.524	0.6973	5.1958	3.1871	1.2595	1.5864	0.1899
	LL2	10	0.524	0.8910	3.0166	2.1035	0.5736	0.3291	0.0828
	LL3	10	0.524	0.2281	2.5526	1.4502	0.5850	0.3423	0.0789
	RL1	10	0.524	0.5993	3.7975	2.5029	0.7906	0.6250	0.1235
	RL2	10	0.524	0.3424	2.6403	1.5367	0.5973	0.3567	0.0845
	RL3	10	0.524	0.3344	1.3251	0.9215	0.2139	0.0458	0.0288

Trues

2D

		Diameter (mm)	Volume (ml)	min	max	mean	std dev	variance	std error
Lesions	LL1	10	0.524	0.3258	1.3704	0.9485	0.2824	0.0798	0.0426
	LL2	10	0.524	0.3585	1.4554	0.9677	0.2921	0.0853	0.0422
	LL3	10	0.524	0.2354	1.2435	0.8936	0.2677	0.0717	0.0361
	RL1	10	0.524	0.3127	1.5587	1.0508	0.2747	0.0755	0.0429
	RL2	10	0.524	0.3249	1.4078	0.9471	0.2541	0.0645	0.0359
	RL3	10	0.524	0.1277	1.3020	0.7626	0.2468	0.0609	0.0333

3D

		Diameter (mm)	Volume (ml)	min	max	mean	std dev	variance	std error
Lesions	LL1	10	0.524	0.3551	1.6616	1.1550	0.3568	0.1273	0.0538
	LL2	10	0.524	0.3689	1.3202	0.9297	0.2449	0.0600	0.0353
	LL3	10	0.524	0.1733	1.4161	0.9260	0.2911	0.0847	0.0392
	RL1	10	0.524	0.3563	1.6465	1.1192	0.3042	0.0926	0.0475
	RL2	10	0.524	0.3189	1.3877	0.9494	0.2659	0.0707	0.0376
	RL3	10	0.524	0.1938	1.1229	0.7652	0.1887	0.0356	0.0254

Scatters

2D

		Diameter (mm)	Volume (ml)	min	max	mean	std dev	variance	std error
Lesions	LL1	10	0.524	0.0687	0.3661	0.2489	0.0836	0.0070	0.0126
	LL2	10	0.524	0.1890	0.5706	0.3997	0.0975	0.0095	0.0141
	LL3	10	0.524	0.0794	0.4342	0.2683	0.1039	0.0108	0.0140
	RL1	10	0.524	0.0863	0.5333	0.3475	0.1009	0.0102	0.0158
	RL2	10	0.524	0.0990	0.4933	0.3027	0.0933	0.0087	0.0132
	RL3	10	0.524	0.1179	0.5200	0.3113	0.0866	0.0075	0.0117

3D

		Diameter (mm)	Volume (ml)	min	max	mean	std dev	variance	std error
Lesions	LL1	10	0.524	0.1188	0.7325	0.4697	0.1721	0.0296	0.0259
	LL2	10	0.524	0.2327	0.5511	0.4180	0.0764	0.0058	0.0110
	LL3	10	0.524	0.1070	0.4702	0.3379	0.0940	0.0088	0.0127
	RL1	10	0.524	0.1165	0.5334	0.3538	0.1086	0.0118	0.0170
	RL2	10	0.524	0.1166	0.5459	0.3317	0.1056	0.0111	0.0149
	RL3	10	0.524	0.1540	0.4663	0.3468	0.0719	0.0052	0.0097

Randoms

2D

		Diameter (mm)	Volume (ml)	min	max	mean	std dev	variance	std error
Lesions	LL1	10	0.524	0.1226	0.9132	0.5636	0.2395	0.0573	0.0361
	LL2	10	0.524	0.1405	0.7250	0.4488	0.1658	0.0275	0.0239
	LL3	10	0.524	0.0128	0.2234	0.1016	0.0617	0.0038	0.0083
	RL1	10	0.524	0.1337	1.0548	0.6662	0.2122	0.0450	0.0331
	RL2	10	0.524	0.0138	0.1528	0.0840	0.0357	0.0013	0.0050
	RL3	10	0.524	0.0192	0.1803	0.0991	0.0348	0.0012	0.0047

3D

		Diameter (mm)	Volume (ml)	min	max	mean	std dev	variance	std error
Lesions	LL1	10	0.524	0.2366	2.0108	1.1731	0.5233	0.2739	0.0789
	LL2	10	0.524	0.1210	0.5370	0.3551	0.1182	0.0140	0.0171
	LL3	10	0.524	0.0181	0.2822	0.1428	0.0712	0.0051	0.0096
	RL1	10	0.524	0.1301	0.9523	0.6106	0.2028	0.0411	0.0317
	RL2	10	0.524	0.0151	0.1870	0.0985	0.0491	0.0024	0.0069
	RL3	10	0.524	0.0276	0.1245	0.0837	0.0240	0.0006	0.0032

Table A 2: SUVs of 10 mm lesions, acquired during breathing using a 5:1 lesion-to-lung contrast

All

2D		Diameter (mm)	Volume (ml)	min	max	mean	std dev	variance	std error
Lesions	LL1	10	0.524	0.3370	2.4448	1.5606	0.5811	0.3377	0.0876
	LL2	10	0.524	0.7079	2.6714	1.7201	0.5498	0.3023	0.0794
	LL3	10	0.524	0.1790	1.7112	0.9061	0.4319	0.1866	0.0582
	RL1	10	0.524	0.4477	3.1001	1.9912	0.6037	0.3644	0.0943
	RL2	10	0.524	0.2053	1.6440	0.9427	0.3528	0.1245	0.0499
	RL3	10	0.524	0.1709	1.3194	0.7358	0.2463	0.0607	0.0332

3D		Diameter (mm)	Volume (ml)	min	max	mean	std dev	variance	std error
Lesions	LL1	10	0.524	0.5865	4.2488	2.5415	1.0345	1.0702	0.1560
	LL2	10	0.524	0.7675	2.2784	1.6069	0.4218	0.1779	0.0609
	LL3	10	0.524	0.2111	1.9690	1.1872	0.4627	0.2141	0.0624
	RL1	10	0.524	0.5422	2.9939	1.9674	0.6186	0.3827	0.0966
	RL2	10	0.524	0.2117	1.6999	0.9627	0.3933	0.1547	0.0556
	RL3	10	0.524	0.2296	1.0165	0.6766	0.1728	0.0299	0.0233

Trues

2D		Diameter (mm)	Volume (ml)	min	max	mean	std dev	variance	std error
Lesions	LL1	10	0.524	0.1596	0.6739	0.4814	0.1354	0.0183	0.0204
	LL2	10	0.524	0.2083	0.7682	0.5020	0.1462	0.0214	0.0211
	LL3	10	0.524	0.1266	0.6478	0.4498	0.1464	0.0214	0.0197
	RL1	10	0.524	0.1646	0.8782	0.5902	0.1601	0.0256	0.0250
	RL2	10	0.524	0.1468	0.7449	0.4841	0.1410	0.0199	0.0199
	RL3	10	0.524	0.1105	0.6476	0.3818	0.1163	0.0135	0.0157

3D		Diameter (mm)	Volume (ml)	min	max	mean	std dev	variance	std error
Lesions	LL1	10	0.524	0.2083	0.9931	0.6431	0.2044	0.0418	0.0308
	LL2	10	0.524	0.2215	0.6452	0.4617	0.1109	0.0123	0.0160
	LL3	10	0.524	0.1087	0.7211	0.5102	0.1462	0.0214	0.0197
	RL1	10	0.524	0.2178	0.9267	0.6221	0.1729	0.0299	0.0270
	RL2	10	0.524	0.1601	0.7647	0.4958	0.1514	0.0229	0.0214
	RL3	10	0.524	0.1650	0.5058	0.3447	0.0765	0.0059	0.0103

Scatters

2D		Diameter (mm)	Volume (ml)	min	max	mean	std dev	variance	std error
Lesions	LL1	10	0.524	0.0480	0.3716	0.2393	0.0810	0.0066	0.0122
	LL2	10	0.524	0.1846	0.5700	0.3874	0.1020	0.0104	0.0147
	LL3	10	0.524	0.0830	0.4065	0.2587	0.0934	0.0087	0.0126
	RL1	10	0.524	0.0865	0.5269	0.3406	0.0972	0.0095	0.0152
	RL2	10	0.524	0.0913	0.4660	0.2795	0.0877	0.0077	0.0124
	RL3	10	0.524	0.0986	0.4560	0.2879	0.0741	0.0055	0.0100

3D		Diameter (mm)	Volume (ml)	min	max	mean	std dev	variance	std error
Lesions	LL1	10	0.524	0.1190	0.6640	0.4200	0.1531	0.0234	0.0231
	LL2	10	0.524	0.2172	0.5147	0.3833	0.0860	0.0074	0.0124
	LL3	10	0.524	0.1113	0.5776	0.3866	0.1233	0.0152	0.0166
	RL1	10	0.524	0.0845	0.4995	0.3216	0.0961	0.0092	0.0150
	RL2	10	0.524	0.1310	0.5137	0.3246	0.0941	0.0089	0.0133
	RL3	10	0.524	0.1304	0.4548	0.3149	0.0761	0.0058	0.0103

Randoms

2D		Diameter (mm)	Volume (ml)	min	max	mean	std dev	variance	std error
Lesions	LL1	10	0.524	0.1003	0.8637	0.5285	0.2281	0.0520	0.0344
	LL2	10	0.524	0.1245	0.6296	0.3824	0.1444	0.0209	0.0208
	LL3	10	0.524	0.0121	0.1786	0.0850	0.0494	0.0024	0.0067
	RL1	10	0.524	0.1182	1.0349	0.6322	0.2090	0.0437	0.0326
	RL2	10	0.524	0.0130	0.1294	0.0727	0.0288	0.0008	0.0041
	RL3	10	0.524	0.0163	0.1729	0.0940	0.0326	0.0011	0.0044

3D		Diameter (mm)	Volume (ml)	min	max	mean	std dev	variance	std error
Lesions	LL1	10	0.524	0.1798	2.0249	1.1364	0.5445	0.2965	0.0821
	LL2	10	0.524	0.1185	0.4640	0.3103	0.1033	0.0107	0.0149
	LL3	10	0.524	0.0167	0.2448	0.1291	0.0621	0.0039	0.0084
	RL1	10	0.524	0.1489	0.9944	0.6336	0.2102	0.0442	0.0328
	RL2	10	0.524	0.0095	0.1353	0.0690	0.0369	0.0014	0.0052
	RL3	10	0.524	0.0208	0.1466	0.0897	0.0312	0.0010	0.0042

Table A 3: SUVs of 10 mm lesions, acquired during breathing using a 2:1 lesion-to-lung contrast

All

2D		Diameter (mm)	Volume (ml)	min	max	mean	std dev	variance	std error
Lesions	LL1	10	0.524	0.2903	1.9692	1.2431	0.4696	0.2205	0.0708
	LL2	10	0.524	0.5978	2.2852	1.4604	0.4636	0.2149	0.0669
	LL3	10	0.524	0.1426	1.4710	0.7408	0.3888	0.1512	0.0524
	RL1	10	0.524	0.3649	2.2123	1.4747	0.4291	0.1842	0.0670
	RL2	10	0.524	0.1455	1.2625	0.7179	0.2714	0.0736	0.0384
	RL3	10	0.524	0.1710	0.9568	0.5594	0.1701	0.0289	0.0229

3D		Diameter (mm)	Volume (ml)	min	max	mean	std dev	variance	std error
Lesions	LL1	10	0.524	0.4775	3.7134	2.1852	0.9199	0.8462	0.1387
	LL2	10	0.524	0.6667	1.8591	1.3307	0.3335	0.1112	0.0481
	LL3	10	0.524	0.1809	1.5449	0.9316	0.3706	0.1374	0.0500
	RL1	10	0.524	0.4883	2.5140	1.6335	0.5048	0.2548	0.0788
	RL2	10	0.524	0.1587	1.2760	0.7213	0.3021	0.0913	0.0427
	RL3	10	0.524	0.1745	0.7551	0.5090	0.1386	0.0192	0.0187

Trues

2D		Diameter (mm)	Volume (ml)	min	max	mean	std dev	variance	std error
Lesions	LL1	10	0.524	0.0760	0.4090	0.2572	0.0840	0.0071	0.0127
	LL2	10	0.524	0.1362	0.3780	0.2567	0.0639	0.0041	0.0092
	LL3	10	0.524	0.0803	0.3534	0.2133	0.0790	0.0062	0.0106
	RL1	10	0.524	0.1002	0.3305	0.2440	0.0580	0.0034	0.0091
	RL2	10	0.524	0.0717	0.3833	0.2502	0.0734	0.0054	0.0104
	RL3	10	0.524	0.0956	0.2931	0.1950	0.0462	0.0021	0.0062

3D		Diameter (mm)	Volume (ml)	min	max	mean	std dev	variance	std error
Lesions	LL1	10	0.524	0.2013	1.1991	0.7009	0.2684	0.0721	0.0405
	LL2	10	0.524	0.3624	0.9436	0.6826	0.1632	0.0266	0.0236
	LL3	10	0.524	0.0809	0.8061	0.4651	0.1964	0.0386	0.0265
	RL1	10	0.524	0.2707	1.0346	0.6986	0.2083	0.0434	0.0325
	RL2	10	0.524	0.0369	0.6334	0.3321	0.1663	0.0277	0.0235
	RL3	10	0.524	0.0365	0.2211	0.1542	0.0404	0.0016	0.0055

Scatters

2D		Diameter (mm)	Volume (ml)	min	max	mean	std dev	variance	std error
Lesions	LL1	10	0.524	0.0622	0.3547	0.2316	0.0810	0.0066	0.0122
	LL2	10	0.524	0.1811	0.5470	0.3792	0.1005	0.0101	0.0145
	LL3	10	0.524	0.0968	0.4841	0.3046	0.1127	0.0127	0.0152
	RL1	10	0.524	0.0724	0.5306	0.3422	0.1002	0.0100	0.0156
	RL2	10	0.524	0.0975	0.4796	0.2890	0.0911	0.0083	0.0129
	RL3	10	0.524	0.1129	0.3493	0.2347	0.0529	0.0028	0.0071

3D		Diameter (mm)	Volume (ml)	min	max	mean	std dev	variance	std error
Lesions	LL1	10	0.524	0.0928	0.7368	0.4537	0.1745	0.0304	0.0263
	LL2	10	0.524	0.2028	0.4973	0.3631	0.0762	0.0058	0.0110
	LL3	10	0.524	0.0851	0.5119	0.3496	0.1162	0.0135	0.0157
	RL1	10	0.524	0.0906	0.5310	0.3458	0.1002	0.0100	0.0157
	RL2	10	0.524	0.1119	0.5146	0.3217	0.1017	0.0103	0.0144
	RL3	10	0.524	0.1202	0.4146	0.2868	0.0731	0.0053	0.0099

Randoms

2D		Diameter (mm)	Volume (ml)	min	max	mean	std dev	variance	std error
Lesions	LL1	10	0.524	0.0921	0.8244	0.5104	0.2143	0.0459	0.0323
	LL2	10	0.524	0.1091	0.6394	0.3807	0.1471	0.0216	0.0212
	LL3	10	0.524	0.0098	0.1991	0.0866	0.0547	0.0030	0.0074
	RL1	10	0.524	0.1118	0.8524	0.5457	0.1733	0.0300	0.0271
	RL2	10	0.524	0.0095	0.1220	0.0661	0.0289	0.0008	0.0041
	RL3	10	0.524	0.0132	0.1483	0.0830	0.0269	0.0007	0.0036

3D		Diameter (mm)	Volume (ml)	min	max	mean	std dev	variance	std error
Lesions	LL1	10	0.524	0.1834	1.7775	1.0306	0.4770	0.2275	0.0719
	LL2	10	0.524	0.1015	0.4182	0.2851	0.0940	0.0088	0.0136
	LL3	10	0.524	0.0149	0.2269	0.1169	0.0580	0.0034	0.0078
	RL1	10	0.524	0.1269	0.9484	0.5891	0.1963	0.0385	0.0307
	RL2	10	0.524	0.0099	0.1280	0.0675	0.0341	0.0012	0.0048
	RL3	10	0.524	0.0178	0.1194	0.0681	0.0251	0.0006	0.0034

Table A 4: SUVs of 20 mm lesions, acquired during breathing using a 10:1 lesion-to-lung contrast

All

2D		Diameter (mm)	Volume (ml)	min	max	mean	std dev	variance	std error
Lesions	LL1	20	4.189	0.1652	5.2536	2.3390	1.1754	1.3815	0.0819
	LL2	20	4.189	0.7862	4.9092	2.8161	0.8541	0.7295	0.0532
	LL3	20	4.189	0.0882	4.3408	1.7204	1.0195	1.0393	0.0587
	RL1	20	4.189	0.2540	5.1173	2.6079	1.2110	1.4666	0.0830
	RL2	20	4.189	0.2078	4.2673	2.0397	0.9582	0.9182	0.0592
	RL3	20	4.189	0.1308	4.1425	1.6336	0.8503	0.7230	0.0488
3D		Diameter (mm)	Volume (ml)	min	max	mean	std dev	variance	std error
Lesions	LL1	20	4.189	0.1817	6.0073	2.6158	1.4282	2.0398	0.0995
	LL2	20	4.189	0.6494	4.9068	2.8878	0.8538	0.7289	0.0532
	LL3	20	4.189	0.0661	4.8402	1.7833	1.0824	1.1717	0.0623
	RL1	20	4.189	0.3445	5.3997	2.7287	1.1937	1.4249	0.0818
	RL2	20	4.189	0.2326	4.4010	2.0586	0.9827	0.9657	0.0607
	RL3	20	4.189	0.1185	3.7386	1.7562	0.8348	0.6968	0.0480

Trues

2D		Diameter (mm)	Volume (ml)	min	max	mean	std dev	variance	std error
Lesions	LL1	20	4.189	0.1266	2.2638	1.2806	0.4532	0.2054	0.0316
	LL2	20	4.189	0.4394	2.1648	1.3645	0.3768	0.1420	0.0235
	LL3	20	4.189	0.1363	2.2959	1.0775	0.4795	0.2300	0.0276
	RL1	20	4.189	0.2587	2.4241	1.3704	0.4958	0.2458	0.0340
	RL2	20	4.189	0.2191	2.1484	1.1905	0.4375	0.1914	0.0270
	RL3	20	4.189	0.1774	2.1511	1.0444	0.4154	0.1726	0.0239
3D		Diameter (mm)	Volume (ml)	min	max	mean	std dev	variance	std error
Lesions	LL1	20	4.189	0.1466	2.3126	1.3126	0.4896	0.2397	0.0341
	LL2	20	4.189	0.3840	2.1107	1.3194	0.3591	0.1289	0.0224
	LL3	20	4.189	0.1419	2.1792	1.0223	0.4496	0.2022	0.0259
	RL1	20	4.189	0.3225	2.2846	1.3072	0.4465	0.1993	0.0306
	RL2	20	4.189	0.2526	2.1007	1.1695	0.4364	0.1905	0.0270
	RL3	20	4.189	0.1547	2.0090	1.0519	0.4219	0.1780	0.0242

Scatters

2D		Diameter (mm)	Volume (ml)	min	max	mean	std dev	variance	std error
Lesions	LL1	20	4.189	0.0260	0.8983	0.3847	0.2093	0.0438	0.0146
	LL2	20	4.189	0.2275	1.0298	0.5904	0.1692	0.0286	0.0105
	LL3	20	4.189	0.0321	0.9435	0.3603	0.2006	0.0403	0.0115
	RL1	20	4.189	0.0442	0.8183	0.4086	0.1908	0.0364	0.0131
	RL2	20	4.189	0.0592	0.8627	0.4111	0.1842	0.0339	0.0114
	RL3	20	4.189	0.0493	0.9258	0.3873	0.1817	0.0330	0.0104
3D		Diameter (mm)	Volume (ml)	min	max	mean	std dev	variance	std error
Lesions	LL1	20	4.189	0.0398	1.1969	0.4740	0.2871	0.0825	0.0200
	LL2	20	4.189	0.2030	1.0270	0.6367	0.1642	0.0270	0.0102
	LL3	20	4.189	0.0252	0.9730	0.4287	0.2227	0.0496	0.0128
	RL1	20	4.189	0.0641	1.0044	0.4757	0.2202	0.0485	0.0151
	RL2	20	4.189	0.0700	0.9021	0.4367	0.1913	0.0366	0.0118
	RL3	20	4.189	0.0620	0.8971	0.4953	0.1966	0.0386	0.0113

Randoms

2D		Diameter (mm)	Volume (ml)	min	max	mean	std dev	variance	std error
Lesions	LL1	20	4.189	0.0145	1.5385	0.5100	0.3762	0.1416	0.0262
	LL2	20	4.189	0.0666	1.1034	0.4929	0.2239	0.0501	0.0139
	LL3	20	4.189	0.0008	0.5401	0.1442	0.1327	0.0176	0.0076
	RL1	20	4.189	0.0226	1.3322	0.5783	0.3484	0.1214	0.0239
	RL2	20	4.189	0.0028	0.6533	0.1891	0.1548	0.0240	0.0096
	RL3	20	4.189	0.0050	0.5973	0.1504	0.1254	0.0157	0.0072
3D		Diameter (mm)	Volume (ml)	min	max	mean	std dev	variance	std error
Lesions	LL1	20	4.189	0.0174	2.0667	0.6805	0.5288	0.2797	0.0368
	LL2	20	4.189	0.0522	1.1241	0.5197	0.2292	0.0525	0.0143
	LL3	20	4.189	0.0010	0.9133	0.1899	0.1990	0.0396	0.0114
	RL1	20	4.189	0.0317	1.4956	0.6071	0.3370	0.1136	0.0231
	RL2	20	4.189	0.0031	0.7183	0.1974	0.1689	0.0285	0.0104
	RL3	20	4.189	0.0046	0.4612	0.1424	0.1024	0.0105	0.0059

Table A 5: SUVs of 20 mm lesions, acquired during breathing using a 5:1 lesion-to-lung contrast

All

2D		Diameter (mm)	Volume (ml)	min	max	mean	std dev	variance	std error
Lesions	LL1	20	4.189	0.1126	5.3702	2.0561	1.2630	1.5953	0.0880
	LL2	20	4.189	0.6589	4.9142	2.5993	0.8978	0.8061	0.0559
	LL3	20	4.189	0.0328	3.8862	1.3036	0.9276	0.8604	0.0534
	RL1	20	4.189	0.0975	4.8788	2.3112	1.2552	1.5755	0.0860
	RL2	20	4.189	0.0890	3.8405	1.5038	0.8773	0.7697	0.0542
	RL3	20	4.189	0.0530	3.6350	1.1264	0.7530	0.5671	0.0433
3D		Diameter (mm)	Volume (ml)	min	max	mean	std dev	variance	std error
Lesions	LL1	20	4.189	0.1182	4.7003	1.9687	1.1875	1.4100	0.0827
	LL2	20	4.189	0.5027	3.8844	2.1907	0.6894	0.4753	0.0429
	LL3	20	4.189	0.0409	3.7112	1.2984	0.8781	0.7710	0.0505
	RL1	20	4.189	0.2268	4.2291	1.9726	0.9106	0.8292	0.0624
	RL2	20	4.189	0.1453	3.3202	1.4168	0.7503	0.5629	0.0464
	RL3	20	4.189	0.0702	2.4718	1.1408	0.5719	0.3271	0.0329

Trues

2D		Diameter (mm)	Volume (ml)	min	max	mean	std dev	variance	std error
Lesions	LL1	20	4.189	0.0568	1.1341	0.5276	0.2303	0.0530	0.0160
	LL2	20	4.189	0.2137	1.1715	0.6499	0.2201	0.0484	0.0137
	LL3	20	4.189	0.0663	1.0555	0.4568	0.2270	0.0515	0.0131
	RL1	20	4.189	0.0659	1.0976	0.6004	0.2544	0.0647	0.0174
	RL2	20	4.189	0.1027	1.0521	0.5465	0.2251	0.0507	0.0139
	RL3	20	4.189	0.0487	1.1790	0.4314	0.2381	0.0567	0.0137
3D		Diameter (mm)	Volume (ml)	min	max	mean	std dev	variance	std error
Lesions	LL1	20	4.189	0.0785	1.4366	0.6631	0.3227	0.1042	0.0225
	LL2	20	4.189	0.2324	1.1317	0.6843	0.2043	0.0417	0.0127
	LL3	20	4.189	0.0492	1.0855	0.4658	0.2399	0.0575	0.0138
	RL1	20	4.189	0.1095	1.2579	0.6328	0.2564	0.0658	0.0176
	RL2	20	4.189	0.1124	1.2329	0.6026	0.2727	0.0744	0.0168
	RL3	20	4.189	0.0744	1.7345	0.5649	0.2787	0.0777	0.0160

Scatters

2D		Diameter (mm)	Volume (ml)	min	max	mean	std dev	variance	std error
Lesions	LL1	20	4.189	0.0238	0.8236	0.3237	0.1892	0.0358	0.0132
	LL2	20	4.189	0.2001	0.8573	0.5219	0.1399	0.0196	0.0087
	LL3	20	4.189	0.0208	0.8423	0.3315	0.1830	0.0335	0.0105
	RL1	20	4.189	0.0287	0.8667	0.3975	0.2107	0.0444	0.0144
	RL2	20	4.189	0.0525	0.7738	0.3726	0.1655	0.0274	0.0102
	RL3	20	4.189	0.0451	0.7310	0.3137	0.1381	0.0191	0.0079
3D		Diameter (mm)	Volume (ml)	min	max	mean	std dev	variance	std error
Lesions	LL1	20	4.189	0.0257	1.0735	0.4595	0.2762	0.0763	0.0192
	LL2	20	4.189	0.1667	1.0340	0.6062	0.1688	0.0285	0.0105
	LL3	20	4.189	0.0205	1.0580	0.4120	0.2384	0.0568	0.0137
	RL1	20	4.189	0.0700	0.9929	0.4732	0.2153	0.0464	0.0148
	RL2	20	4.189	0.0646	0.9568	0.4265	0.1985	0.0394	0.0123
	RL3	20	4.189	0.0417	0.7803	0.4218	0.1713	0.0293	0.0098

Randoms

2D		Diameter (mm)	Volume (ml)	min	max	mean	std dev	variance	std error
Lesions	LL1	20	4.189	0.0300	2.8991	0.9252	0.7023	0.4932	0.0489
	LL2	20	4.189	0.1037	2.0160	0.8897	0.4143	0.1717	0.0258
	LL3	20	4.189	0.0016	1.1527	0.2774	0.2699	0.0728	0.0155
	RL1	20	4.189	0.0218	2.3717	0.9846	0.6187	0.3828	0.0424
	RL2	20	4.189	0.0044	1.2104	0.3200	0.2766	0.0765	0.0171
	RL3	20	4.189	0.0063	1.0864	0.2490	0.2261	0.0511	0.0130
3D		Diameter (mm)	Volume (ml)	min	max	mean	std dev	variance	std error
Lesions	LL1	20	4.189	0.0145	1.7749	0.6270	0.4771	0.2276	0.0332
	LL2	20	4.189	0.0381	1.0541	0.4789	0.2165	0.0469	0.0135
	LL3	20	4.189	0.0008	0.7513	0.1721	0.1807	0.0326	0.0104
	RL1	20	4.189	0.0297	1.3500	0.5610	0.3153	0.0994	0.0216
	RL2	20	4.189	0.0023	0.6613	0.1745	0.1546	0.0239	0.0096
	RL3	20	4.189	0.0041	0.3800	0.1265	0.0883	0.0078	0.0051

Table A 6: SUVs of 20 mm lesions, acquired during breathing using a 2:1 lesion-to-lung contrast

All

2D		Diameter (mm)	Volume (ml)	min	max	mean	std dev	variance	std error
Lesions	LL1	20	4.189	0.0838	4.3112	1.6029	1.0304	1.0617	0.0718
	LL2	20	4.189	0.5704	4.2379	2.0958	0.7906	0.6251	0.0492
	LL3	20	4.189	0.0229	3.1147	0.9788	0.7342	0.5391	0.0423
	RL1	20	4.189	0.0731	4.0776	1.8681	1.0346	1.0704	0.0709
	RL2	20	4.189	0.0617	2.8977	1.0853	0.6789	0.4609	0.0419
	RL3	20	4.189	0.0432	2.7539	0.8140	0.5793	0.3355	0.0333
3D		Diameter (mm)	Volume (ml)	min	max	mean	std dev	variance	std error
Lesions	LL1	20	4.189	0.0927	4.0810	1.5824	1.0439	1.0897	0.0727
	LL2	20	4.189	0.4222	3.2058	1.6994	0.5847	0.3418	0.0364
	LL3	20	4.189	0.0278	2.9072	0.9573	0.6767	0.4579	0.0389
	RL1	20	4.189	0.1519	3.2569	1.4818	0.7112	0.5058	0.0487
	RL2	20	4.189	0.0966	2.4593	0.9907	0.5666	0.3211	0.0350
	RL3	20	4.189	0.0479	1.9275	0.7845	0.4424	0.1957	0.0254

Trues

2D		Diameter (mm)	Volume (ml)	min	max	mean	std dev	variance	std error
Lesions	LL1	20	4.189	0.0196	0.5534	0.2001	0.1129	0.0128	0.0079
	LL2	20	4.189	0.0633	0.6103	0.2790	0.1224	0.0150	0.0076
	LL3	20	4.189	0.0209	0.4457	0.1719	0.0979	0.0096	0.0056
	RL1	20	4.189	0.0188	0.4189	0.2051	0.0915	0.0084	0.0063
	RL2	20	4.189	0.0413	0.4423	0.1979	0.0915	0.0084	0.0057
	RL3	20	4.189	0.0017	0.4466	0.1624	0.1078	0.0116	0.0062
3D		Diameter (mm)	Volume (ml)	min	max	mean	std dev	variance	std error
Lesions	LL1	20	4.189	0.0333	0.6570	0.2663	0.1556	0.0242	0.0108
	LL2	20	4.189	0.0785	0.5341	0.2763	0.1104	0.0122	0.0069
	LL3	20	4.189	0.0218	0.5071	0.2029	0.1294	0.0167	0.0074
	RL1	20	4.189	0.0398	0.3913	0.2079	0.0815	0.0066	0.0056
	RL2	20	4.189	0.0475	0.4586	0.2097	0.0980	0.0096	0.0061
	RL3	20	4.189	0.0046	0.3832	0.1709	0.0964	0.0093	0.0055

Scatters

2D		Diameter (mm)	Volume (ml)	min	max	mean	std dev	variance	std error
Lesions	LL1	20	4.189	0.0209	0.7349	0.3050	0.1718	0.0295	0.0120
	LL2	20	4.189	0.1674	0.8284	0.4804	0.1371	0.0188	0.0085
	LL3	20	4.189	0.0191	0.7938	0.3013	0.1758	0.0309	0.0101
	RL1	20	4.189	0.0237	0.8789	0.3956	0.2147	0.0461	0.0147
	RL2	20	4.189	0.0484	0.7827	0.3530	0.1664	0.0277	0.0103
	RL3	20	4.189	0.0317	0.7241	0.2950	0.1396	0.0195	0.0080
3D		Diameter (mm)	Volume (ml)	min	max	mean	std dev	variance	std error
Lesions	LL1	20	4.189	0.0269	1.1019	0.4411	0.2734	0.0748	0.0191
	LL2	20	4.189	0.1378	0.9982	0.5637	0.1696	0.0288	0.0106
	LL3	20	4.189	0.0157	0.9998	0.3779	0.2231	0.0498	0.0128
	RL1	20	4.189	0.0564	0.8432	0.4314	0.1884	0.0355	0.0129
	RL2	20	4.189	0.0566	0.8668	0.4041	0.1858	0.0345	0.0115
	RL3	20	4.189	0.0365	0.8033	0.3926	0.1643	0.0270	0.0094

Randoms

2D		Diameter (mm)	Volume (ml)	min	max	mean	std dev	variance	std error
Lesions	LL1	20	4.189	0.0251	2.7628	0.8890	0.6745	0.4550	0.0470
	LL2	20	4.189	0.0911	2.0020	0.8397	0.4093	0.1675	0.0255
	LL3	20	4.189	0.0014	1.0894	0.2583	0.2604	0.0678	0.0150
	RL1	20	4.189	0.0246	2.4709	1.0097	0.6390	0.4083	0.0438
	RL2	20	4.189	0.0035	1.0871	0.3048	0.2569	0.0660	0.0159
	RL3	20	4.189	0.0062	1.0370	0.2393	0.2147	0.0461	0.0123
3D		Diameter (mm)	Volume (ml)	min	max	mean	std dev	variance	std error
Lesions	LL1	20	4.189	0.0141	1.9270	0.6646	0.5223	0.2728	0.0364
	LL2	20	4.189	0.0417	1.0080	0.4540	0.2063	0.0426	0.0128
	LL3	20	4.189	0.0008	0.6363	0.1573	0.1568	0.0246	0.0090
	RL1	20	4.189	0.0330	1.4742	0.5629	0.3381	0.1143	0.0232
	RL2	20	4.189	0.0018	0.5775	0.1606	0.1407	0.0198	0.0087
	RL3	20	4.189	0.0033	0.3786	0.1245	0.0917	0.0084	0.0053

Table A 7: SUVs of 30 mm lesions, acquired during breathing using a 10:1 lesion-to-lung contrast

All

2D		Diameter (mm)	Volume (ml)	min	max	mean	std dev	variance	std error
Lesions	LL1	30	14.137	0.1374	10.3524	4.3422	2.3671	5.6030	0.0947
	LL2	30	14.137	0.6850	9.6781	4.5931	1.8257	3.3331	0.0666
	LL3	30	14.137	0.0152	8.7584	2.5891	2.0686	4.2789	0.0687
	RL1	30	14.137	0.3000	9.5710	4.3717	2.2274	4.9614	0.0895
	RL2	30	14.137	0.0497	7.6650	3.0243	1.9111	3.6525	0.0700
	RL3	30	14.137	0.1604	7.6157	2.8474	1.7205	2.9602	0.0576

3D		Diameter (mm)	Volume (ml)	min	max	mean	std dev	variance	std error
Lesions	LL1	30	14.137	0.1551	12.3197	4.7953	2.7937	7.8045	0.1117
	LL2	30	14.137	0.7109	9.0016	4.7109	1.7569	3.0866	0.0641
	LL3	30	14.137	0.0115	9.5052	2.8438	2.2953	5.2682	0.0763
	RL1	30	14.137	0.2395	8.8608	4.9587	2.2580	5.0986	0.0907
	RL2	30	14.137	0.0626	7.7088	3.1149	1.9661	3.8654	0.0720
	RL3	30	14.137	0.1259	8.3426	3.0404	1.8664	3.4834	0.0625

Trues

2D		Diameter (mm)	Volume (ml)	min	max	mean	std dev	variance	std error
Lesions	LL1	30	14.137	0.1406	2.7742	1.4804	0.5761	0.3319	0.0230
	LL2	30	14.137	0.2349	2.7745	1.5551	0.5281	0.2789	0.0193
	LL3	30	14.137	0.0098	2.7633	1.1137	0.6356	0.4040	0.0211
	RL1	30	14.137	0.1632	2.7746	1.5004	0.5799	0.3363	0.0233
	RL2	30	14.137	0.0850	2.6382	1.2689	0.6107	0.3730	0.0224
	RL3	30	14.137	0.0896	2.6716	1.1988	0.5937	0.3525	0.0199

3D		Diameter (mm)	Volume (ml)	min	max	mean	std dev	variance	std error
Lesions	LL1	30	14.137	0.1769	3.0333	1.5244	0.6364	0.4050	0.0255
	LL2	30	14.137	0.2387	2.5425	1.5431	0.4934	0.2434	0.0180
	LL3	30	14.137	0.0229	2.7655	1.1294	0.6381	0.4072	0.0212
	RL1	30	14.137	0.2479	2.5062	1.5458	0.5477	0.3000	0.0220
	RL2	30	14.137	0.0927	2.4686	1.2619	0.5966	0.3559	0.0218
	RL3	30	14.137	0.0715	2.6015	1.1938	0.5836	0.3405	0.0195

Scatters

2D		Diameter (mm)	Volume (ml)	min	max	mean	std dev	variance	std error
Lesions	LL1	30	14.137	0.0290	1.4279	0.6085	0.3323	0.1104	0.0133
	LL2	30	14.137	0.1623	1.5884	0.7819	0.2892	0.0836	0.0105
	LL3	30	14.137	0.0123	1.3837	0.4787	0.3299	0.1088	0.0110
	RL1	30	14.137	0.0532	1.3078	0.5939	0.2917	0.0851	0.0117
	RL2	30	14.137	0.0337	1.2889	0.5313	0.2990	0.0894	0.0109
	RL3	30	14.137	0.0435	1.3912	0.5754	0.2969	0.0881	0.0099

3D		Diameter (mm)	Volume (ml)	min	max	mean	std dev	variance	std error
Lesions	LL1	30	14.137	0.0309	1.7506	0.7243	0.4126	0.1703	0.0165
	LL2	30	14.137	0.1756	1.5988	0.8329	0.2803	0.0786	0.0102
	LL3	30	14.137	0.0095	1.6770	0.5793	0.3950	0.1560	0.0131
	RL1	30	14.137	0.0356	1.3012	0.7193	0.3164	0.1001	0.0127
	RL2	30	14.137	0.0474	1.3752	0.5746	0.3164	0.1001	0.0116
	RL3	30	14.137	0.0388	1.5620	0.6659	0.3425	0.1173	0.0115

Randoms

2D		Diameter (mm)	Volume (ml)	min	max	mean	std dev	variance	std error
Lesions	LL1	30	14.137	0.0331	5.6696	1.9790	1.3613	1.8532	0.0545
	LL2	30	14.137	0.1353	4.6376	1.7462	0.9230	0.8519	0.0337
	LL3	30	14.137	0.0007	3.9823	0.7607	0.8596	0.7390	0.0286
	RL1	30	14.137	0.0588	5.0051	1.9860	1.2338	1.5223	0.0496
	RL2	30	14.137	0.0024	3.1712	0.9150	0.8033	0.6452	0.0294
	RL3	30	14.137	0.0134	2.9221	0.8060	0.6636	0.4403	0.0222

3D		Diameter (mm)	Volume (ml)	min	max	mean	std dev	variance	std error
Lesions	LL1	30	14.137	0.0401	7.1176	2.2728	1.6264	2.6452	0.0651
	LL2	30	14.137	0.1291	4.3082	1.7856	0.8953	0.8016	0.0326
	LL3	30	14.137	0.0004	4.3441	0.8739	0.9954	0.9908	0.0331
	RL1	30	14.137	0.0538	4.8278	2.3775	1.2602	1.5880	0.0506
	RL2	30	14.137	0.0031	3.2220	0.9436	0.8322	0.6926	0.0305
	RL3	30	14.137	0.0184	3.4376	0.8998	0.7421	0.5506	0.0248

Table A 8: SUVs of 30 mm lesions, acquired during breathing using a 5:1 lesion-to-lung contrast

All

2D		Diameter (mm)	Volume (ml)	min	max	mean	std dev	variance	std error
Lesions	LL1	30	14.137	0.0809	9.3243	3.6246	2.1378	4.5700	0.0855
	LL2	30	14.137	0.5437	8.3377	3.8158	1.6192	2.6219	0.0590
	LL3	30	14.137	0.0131	7.7274	2.0825	1.8348	3.3664	0.0610
	RL1	30	14.137	0.2107	8.0170	3.5495	1.8948	3.5903	0.0761
	RL2	30	14.137	0.0391	6.4169	2.3697	1.6328	2.6661	0.0598
	RL3	30	14.137	0.1041	6.4560	2.1828	1.4609	2.1343	0.0489
3D		Diameter (mm)	Volume (ml)	min	max	mean	std dev	variance	std error
Lesions	LL1	30	14.137	0.1341	11.1507	4.1042	2.5077	6.2886	0.1003
	LL2	30	14.137	0.5862	7.8261	3.9119	1.5624	2.4411	0.0570
	LL3	30	14.137	0.0077	8.7672	2.2871	2.0073	4.0292	0.0667
	RL1	30	14.137	0.1796	7.8301	4.2407	2.0198	4.0797	0.0811
	RL2	30	14.137	0.0504	6.4558	2.4662	1.6696	2.7875	0.0611
	RL3	30	14.137	0.0941	6.8351	2.3796	1.5746	2.4795	0.0527

Trues

2D		Diameter (mm)	Volume (ml)	min	max	mean	std dev	variance	std error
Lesions	LL1	30	14.137	0.0493	1.7651	0.8227	0.3985	0.1588	0.0159
	LL2	30	14.137	0.1235	1.7002	0.8815	0.3435	0.1180	0.0125
	LL3	30	14.137	0.0189	1.8865	0.5641	0.4070	0.1657	0.0135
	RL1	30	14.137	0.0939	1.5537	0.7870	0.3333	0.1111	0.0134
	RL2	30	14.137	0.0494	1.5771	0.6820	0.3784	0.1432	0.0139
	RL3	30	14.137	0.0174	1.6012	0.5974	0.3771	0.1422	0.0126
3D		Diameter (mm)	Volume (ml)	min	max	mean	std dev	variance	std error
Lesions	LL1	30	14.137	0.0578	1.8327	0.8419	0.4203	0.1766	0.0168
	LL2	30	14.137	0.1292	1.5648	0.8799	0.3237	0.1048	0.0118
	LL3	30	14.137	0.0095	1.8947	0.5875	0.4134	0.1709	0.0137
	RL1	30	14.137	0.0828	1.5380	0.8385	0.3430	0.1177	0.0138
	RL2	30	14.137	0.0565	1.5262	0.6860	0.3762	0.1415	0.0138
	RL3	30	14.137	0.0062	1.6108	0.6237	0.3767	0.1419	0.0126

Scatters

2D		Diameter (mm)	Volume (ml)	min	max	mean	std dev	variance	std error
Lesions	LL1	30	14.137	0.0157	1.3839	0.5667	0.3102	0.0962	0.0124
	LL2	30	14.137	0.1427	1.4883	0.7197	0.2709	0.0734	0.0099
	LL3	30	14.137	0.0085	1.3844	0.4421	0.3182	0.1012	0.0106
	RL1	30	14.137	0.0510	1.2080	0.5725	0.2710	0.0734	0.0109
	RL2	30	14.137	0.0265	1.2863	0.5080	0.3002	0.0901	0.0110
	RL3	30	14.137	0.0555	1.2436	0.5176	0.2769	0.0767	0.0093
3D		Diameter (mm)	Volume (ml)	min	max	mean	std dev	variance	std error
Lesions	LL1	30	14.137	0.0373	1.7221	0.6680	0.3866	0.1495	0.0155
	LL2	30	14.137	0.1691	1.4339	0.7640	0.2629	0.0691	0.0096
	LL3	30	14.137	0.0057	1.5797	0.5066	0.3624	0.1313	0.0120
	RL1	30	14.137	0.0323	1.4166	0.6858	0.3182	0.1013	0.0128
	RL2	30	14.137	0.0342	1.2868	0.5532	0.3144	0.0988	0.0115
	RL3	30	14.137	0.0525	1.4361	0.5912	0.3170	0.1005	0.0106

Randoms

2D		Diameter (mm)	Volume (ml)	min	max	mean	std dev	variance	std error
Lesions	LL1	30	14.137	0.0290	5.7593	1.9377	1.3417	1.8002	0.0537
	LL2	30	14.137	0.1091	4.3850	1.6594	0.9024	0.8143	0.0329
	LL3	30	14.137	0.0006	3.9228	0.7607	0.8791	0.7728	0.0292
	RL1	30	14.137	0.0491	5.0065	1.8827	1.1943	1.4264	0.0480
	RL2	30	14.137	0.0021	3.0538	0.8552	0.7706	0.5938	0.0282
	RL3	30	14.137	0.0100	3.0220	0.7701	0.6494	0.4217	0.0217
3D		Diameter (mm)	Volume (ml)	min	max	mean	std dev	variance	std error
Lesions	LL1	30	14.137	0.0446	7.1655	2.2764	1.6220	2.6307	0.0649
	LL2	30	14.137	0.1246	4.0585	1.6913	0.8709	0.7584	0.0318
	LL3	30	14.137	0.0003	4.4672	0.8584	0.9968	0.9936	0.0331
	RL1	30	14.137	0.0609	4.7585	2.3686	1.2779	1.6329	0.0513
	RL2	30	14.137	0.0028	3.1015	0.8980	0.8013	0.6421	0.0293
	RL3	30	14.137	0.0144	3.2942	0.8662	0.7230	0.5227	0.0242

Table A 9: SUVs of 30 mm lesions, acquired during breathing using a 2:1 lesion-to-lung contrast

All

2D				min	max	mean	std dev	variance	std error
		Diameter (mm)	Volume (ml)						
Lesions	LL1	30	14.137	0.0686	8.4794	3.0664	1.9645	3.8591	0.0786
	LL2	30	14.137	0.4221	7.6092	3.2391	1.4610	2.1346	0.0533
	LL3	30	14.137	0.0096	6.9393	1.6769	1.5786	2.4920	0.0524
	RL1	30	14.137	0.1311	7.1589	3.0491	1.7327	3.0022	0.0696
	RL2	30	14.137	0.0306	5.4311	1.8795	1.3811	1.9074	0.0506
	RL3	30	14.137	0.0583	5.5117	1.7401	1.2831	1.6463	0.0430
3D				min	max	mean	std dev	variance	std error
		Diameter (mm)	Volume (ml)						
Lesions	LL1	30	14.137	0.0910	10.4304	3.5425	2.3457	5.5022	0.0938
	LL2	30	14.137	0.4745	7.1458	3.3698	1.4375	2.0664	0.0524
	LL3	30	14.137	0.0059	7.9767	1.9243	1.7909	3.2074	0.0595
	RL1	30	14.137	0.1277	6.7521	3.6013	1.7560	3.0836	0.0705
	RL2	30	14.137	0.0381	5.7144	1.9694	1.4402	2.0741	0.0527
	RL3	30	14.137	0.0667	6.0365	1.8987	1.3761	1.8937	0.0461

Trues

2D				min	max	mean	std dev	variance	std error
		Diameter (mm)	Volume (ml)						
Lesions	LL1	30	14.137	0.0076	1.3619	0.3811	0.2676	0.0716	0.0107
	LL2	30	14.137	0.0701	0.9901	0.4359	0.2176	0.0473	0.0079
	LL3	30	14.137	0.0051	0.9909	0.2362	0.2138	0.0457	0.0071
	RL1	30	14.137	0.0201	0.8431	0.3329	0.1890	0.0357	0.0076
	RL2	30	14.137	0.0332	0.8212	0.2947	0.2001	0.0401	0.0073
	RL3	30	14.137	0.0017	0.8745	0.2601	0.2198	0.0483	0.0074
3D				min	max	mean	std dev	variance	std error
		Diameter (mm)	Volume (ml)						
Lesions	LL1	30	14.137	0.0117	1.1817	0.3937	0.2670	0.0713	0.0107
	LL2	30	14.137	0.0597	1.1911	0.4423	0.2142	0.0459	0.0078
	LL3	30	14.137	0.0051	1.0173	0.2445	0.2205	0.0486	0.0073
	RL1	30	14.137	-0.8414	0.8802	0.3031	0.2317	0.0537	0.0093
	RL2	30	14.137	0.0320	0.7726	0.2856	0.1845	0.0340	0.0068
	RL3	30	14.137	0.0003	0.8345	0.2596	0.2151	0.0463	0.0072

Scatters

2D				min	max	mean	std dev	variance	std error
		Diameter (mm)	Volume (ml)						
Lesions	LL1	30	14.137	0.0133	1.3559	0.5215	0.3095	0.0958	0.0124
	LL2	30	14.137	0.1237	1.4228	0.6731	0.2649	0.0702	0.0097
	LL3	30	14.137	0.0058	1.4337	0.4134	0.3093	0.0957	0.0103
	RL1	30	14.137	0.0313	1.1582	0.5359	0.2719	0.0739	0.0109
	RL2	30	14.137	0.0212	1.2339	0.4857	0.2907	0.0845	0.0106
	RL3	30	14.137	0.0313	1.2206	0.4802	0.2665	0.0710	0.0089
3D				min	max	mean	std dev	variance	std error
		Diameter (mm)	Volume (ml)						
Lesions	LL1	30	14.137	0.0181	1.7353	0.6482	0.4012	0.1610	0.0160
	LL2	30	14.137	0.1331	1.4071	0.7200	0.2575	0.0663	0.0094
	LL3	30	14.137	0.0039	1.7062	0.4861	0.3638	0.1323	0.0121
	RL1	30	14.137	0.0369	1.3001	0.6532	0.2972	0.0883	0.0119
	RL2	30	14.137	0.0331	1.2959	0.5129	0.3009	0.0905	0.0110
	RL3	30	14.137	0.0205	1.3697	0.5557	0.3110	0.0967	0.0104

Randoms

2D				min	max	mean	std dev	variance	std error
		Diameter (mm)	Volume (ml)						
Lesions	LL1	30	14.137	0.0278	5.6818	1.8892	1.3139	1.7263	0.0526
	LL2	30	14.137	0.0942	4.3049	1.5967	0.8715	0.7596	0.0318
	LL3	30	14.137	0.0005	3.8502	0.7289	0.8522	0.7262	0.0283
	RL1	30	14.137	0.0508	4.7640	1.8836	1.2007	1.4417	0.0482
	RL2	30	14.137	0.0015	2.8992	0.8212	0.7412	0.5494	0.0271
	RL3	30	14.137	0.0097	2.7967	0.7458	0.6294	0.3961	0.0211
3D				min	max	mean	std dev	variance	std error
		Diameter (mm)	Volume (ml)						
Lesions	LL1	30	14.137	0.0446	7.1072	2.2082	1.6048	2.5753	0.0642
	LL2	30	14.137	0.1059	3.9691	1.6558	0.8689	0.7550	0.0317
	LL3	30	14.137	0.0003	4.6066	0.8507	0.9930	0.9860	0.0330
	RL1	30	14.137	0.0534	4.5846	2.2774	1.2182	1.4841	0.0489
	RL2	30	14.137	0.0020	3.0549	0.8624	0.7866	0.6188	0.0288
	RL3	30	14.137	0.0130	3.3725	0.8244	0.7051	0.4972	0.0236

Table A 10: SUVs of 20 mm lesions, acquired during expiration using a 10:1 lesion-to-lung contrast

All

2D		Diameter (mm)	Volume (ml)	min	max	mean	std dev	variance	std error
Lesions	LL1	20	4.189	0.0776	5.5030	2.2388	1.3533	1.8315	0.0929
	LL2	20	4.189	0.6654	6.8911	3.8133	1.4443	2.0861	0.0999
	LL3	20	4.189	0.0962	6.4924	2.5159	1.4928	2.2283	0.1045
	RL1	20	4.189	0.2805	5.0342	2.5592	1.2686	1.6093	0.0882
	RL2	20	4.189	0.2236	4.7612	2.4870	1.0973	1.2040	0.0757
	RL3	20	4.189	0.1631	5.7695	2.4571	1.3286	1.7651	0.0919
3D		Diameter (mm)	Volume (ml)	min	max	mean	std dev	variance	std error
Lesions	LL1	20	4.189	0.0700	5.7794	2.2157	1.4017	1.9648	0.0963
	LL2	20	4.189	0.7486	6.0559	3.3819	1.1590	1.3433	0.0802
	LL3	20	4.189	0.0942	5.4907	2.4621	1.3656	1.8649	0.0956
	RL1	20	4.189	0.2994	5.0563	2.5315	1.1498	1.3220	0.0799
	RL2	20	4.189	0.2662	4.5887	2.3715	0.9917	0.9834	0.0684
	RL3	20	4.189	0.1953	4.8091	2.2842	1.0985	1.2068	0.0760

Trues

2D		Diameter (mm)	Volume (ml)	min	max	mean	std dev	variance	std error
Lesions	LL1	20	4.189	0.0990	1.8078	0.9938	0.3964	0.1571	0.0272
	LL2	20	4.189	0.3615	2.2321	1.4185	0.4260	0.1814	0.0295
	LL3	20	4.189	0.1226	2.3609	1.2300	0.4958	0.2458	0.0347
	RL1	20	4.189	0.2375	1.7287	1.0339	0.3538	0.1251	0.0246
	RL2	20	4.189	0.2526	1.9255	1.1741	0.3780	0.1428	0.0261
	RL3	20	4.189	0.2142	2.3377	1.2012	0.4810	0.2314	0.0333
3D		Diameter (mm)	Volume (ml)	min	max	mean	std dev	variance	std error
Lesions	LL1	20	4.189	0.1098	1.9589	1.1002	0.4416	0.1950	0.0303
	LL2	20	4.189	0.3652	2.4122	1.4794	0.4380	0.1919	0.0303
	LL3	20	4.189	0.1436	2.3978	1.3111	0.5307	0.2816	0.0372
	RL1	20	4.189	0.3202	1.9745	1.1759	0.3954	0.1563	0.0275
	RL2	20	4.189	0.2567	2.0888	1.2487	0.4184	0.1750	0.0289
	RL3	20	4.189	0.2197	2.2804	1.2341	0.4797	0.2301	0.0332

Scatters

2D		Diameter (mm)	Volume (ml)	min	max	mean	std dev	variance	std error
Lesions	LL1	20	4.189	0.0142	0.6596	0.2922	0.1643	0.0270	0.0113
	LL2	20	4.189	0.1573	1.1013	0.6040	0.2144	0.0460	0.0148
	LL3	20	4.189	0.0298	1.0015	0.4330	0.2205	0.0486	0.0154
	RL1	20	4.189	0.0550	0.7011	0.3541	0.1640	0.0269	0.0114
	RL2	20	4.189	0.0628	0.7397	0.4244	0.1615	0.0261	0.0111
	RL3	20	4.189	0.0538	1.0223	0.4777	0.2165	0.0469	0.0150
3D		Diameter (mm)	Volume (ml)	min	max	mean	std dev	variance	std error
Lesions	LL1	20	4.189	0.0190	1.0978	0.3953	0.2633	0.0693	0.0181
	LL2	20	4.189	0.1971	1.3476	0.7303	0.2471	0.0611	0.0171
	LL3	20	4.189	0.0330	1.1060	0.5068	0.2641	0.0698	0.0185
	RL1	20	4.189	0.0462	1.0036	0.4786	0.2192	0.0480	0.0152
	RL2	20	4.189	0.0706	0.9276	0.4941	0.1951	0.0381	0.0135
	RL3	20	4.189	0.0581	1.1695	0.5790	0.2499	0.0625	0.0173

Randoms

2D		Diameter (mm)	Volume (ml)	min	max	mean	std dev	variance	std error
Lesions	LL1	20	4.189	0.0148	2.6195	0.8215	0.6359	0.4043	0.0437
	LL2	20	4.189	0.0802	2.8034	1.2049	0.6543	0.4281	0.0453
	LL3	20	4.189	0.0078	1.9674	0.5894	0.4802	0.2306	0.0336
	RL1	20	4.189	0.0583	2.2104	0.9687	0.5756	0.3313	0.0400
	RL2	20	4.189	0.0145	1.2932	0.5072	0.3231	0.1044	0.0223
	RL3	20	4.189	0.0107	1.6355	0.5370	0.3832	0.1468	0.0265
3D		Diameter (mm)	Volume (ml)	min	max	mean	std dev	variance	std error
Lesions	LL1	20	4.189	0.0083	2.1916	0.5976	0.5392	0.2908	0.0370
	LL2	20	4.189	0.0524	1.6455	0.6897	0.3748	0.1405	0.0259
	LL3	20	4.189	0.0026	1.1041	0.3557	0.2909	0.0846	0.0204
	RL1	20	4.189	0.0454	1.6317	0.6602	0.3913	0.1531	0.0272
	RL2	20	4.189	0.0083	0.8007	0.2899	0.1907	0.0364	0.0132
	RL3	20	4.189	0.0093	0.8185	0.2813	0.1925	0.0371	0.0133

Table A 11: SUVs of 20 mm lesions, acquired during expiration using a 5:1 lesion-to-lung contrast

All

2D

		Diameter (mm)	Volume (ml)	min	max	mean	std dev	variance	std error
Lesions	LL1	20	4.189	0.0523	4.4766	1.7401	1.1169	1.2475	0.0767
	LL2	20	4.189	0.5284	5.7373	3.0831	1.2250	1.5006	0.0847
	LL3	20	4.189	0.0752	5.3247	1.9273	1.2116	1.4680	0.0848
	RL1	20	4.189	0.1980	4.2403	2.0500	1.0769	1.1597	0.0749
	RL2	20	4.189	0.1364	3.6772	1.8369	0.8545	0.7301	0.0590
	RL3	20	4.189	0.0918	4.6619	1.9136	1.0786	1.1633	0.0746

3D

		Diameter (mm)	Volume (ml)	min	max	mean	std dev	variance	std error
Lesions	LL1	20	4.189	0.0536	4.3774	1.6428	1.1009	1.2120	0.0756
	LL2	20	4.189	0.6252	4.6916	2.6204	0.9232	0.8523	0.0639
	LL3	20	4.189	0.0613	4.4043	1.8209	1.0723	1.1498	0.0751
	RL1	20	4.189	0.2080	3.6674	1.8268	0.8455	0.7148	0.0588
	RL2	20	4.189	0.1630	3.5011	1.7064	0.7728	0.5972	0.0533
	RL3	20	4.189	0.1079	3.5657	1.6177	0.8151	0.6644	0.0564

Trues

2D

		Diameter (mm)	Volume (ml)	min	max	mean	std dev	variance	std error
Lesions	LL1	20	4.189	0.0402	0.8929	0.4796	0.2086	0.0435	0.0143
	LL2	20	4.189	0.2218	1.2982	0.7995	0.2484	0.0617	0.0172
	LL3	20	4.189	0.0694	1.3761	0.6733	0.2907	0.0845	0.0204
	RL1	20	4.189	0.0881	0.9569	0.5330	0.2114	0.0447	0.0147
	RL2	20	4.189	0.1245	1.0479	0.6267	0.2097	0.0440	0.0145
	RL3	20	4.189	0.0980	1.3410	0.6631	0.2844	0.0809	0.0197

3D

		Diameter (mm)	Volume (ml)	min	max	mean	std dev	variance	std error
Lesions	LL1	20	4.189	0.0329	1.3660	0.6790	0.2444	0.0597	0.0168
	LL2	20	4.189	0.4034	1.8682	1.2760	0.2762	0.0763	0.0191
	LL3	20	4.189	0.0303	2.1269	0.9599	0.4503	0.2028	0.0315
	RL1	20	4.189	0.1108	1.2272	0.7588	0.2057	0.0423	0.0143
	RL2	20	4.189	0.0892	1.7943	0.9494	0.2798	0.0783	0.0193
	RL3	20	4.189	0.0535	1.7699	0.8144	0.5051	0.2551	0.0349

Scatters

2D

		Diameter (mm)	Volume (ml)	min	max	mean	std dev	variance	std error
Lesions	LL1	20	4.189	0.0104	0.6653	0.2893	0.1701	0.0289	0.0117
	LL2	20	4.189	0.1487	1.0159	0.5791	0.1997	0.0399	0.0138
	LL3	20	4.189	0.0287	0.9562	0.4087	0.2143	0.0459	0.0150
	RL1	20	4.189	0.0476	0.6970	0.3389	0.1597	0.0255	0.0111
	RL2	20	4.189	0.0522	0.7409	0.4067	0.1533	0.0235	0.0106
	RL3	20	4.189	0.0469	1.0572	0.4967	0.2275	0.0517	0.0157

3D

		Diameter (mm)	Volume (ml)	min	max	mean	std dev	variance	std error
Lesions	LL1	20	4.189	0.0129	1.0728	0.3805	0.2575	0.0663	0.0177
	LL2	20	4.189	0.1731	1.2528	0.6807	0.2360	0.0557	0.0163
	LL3	20	4.189	0.0284	1.2046	0.5223	0.2790	0.0779	0.0195
	RL1	20	4.189	0.0548	0.9279	0.4478	0.1975	0.0390	0.0137
	RL2	20	4.189	0.0679	0.9184	0.4834	0.1967	0.0387	0.0136
	RL3	20	4.189	0.0494	1.0661	0.5484	0.2297	0.0527	0.0159

Randoms

2D

		Diameter (mm)	Volume (ml)	min	max	mean	std dev	variance	std error
Lesions	LL1	20	4.189	0.0153	2.5470	0.8200	0.6217	0.3865	0.0427
	LL2	20	4.189	0.0810	2.7389	1.1700	0.6347	0.4029	0.0439
	LL3	20	4.189	0.0058	1.9957	0.5845	0.4775	0.2280	0.0334
	RL1	20	4.189	0.0524	2.3387	0.9899	0.5945	0.3534	0.0413
	RL2	20	4.189	0.0123	1.2244	0.4889	0.3102	0.0962	0.0214
	RL3	20	4.189	0.0112	1.6662	0.5495	0.3852	0.1484	0.0266

3D

		Diameter (mm)	Volume (ml)	min	max	mean	std dev	variance	std error
Lesions	LL1	20	4.189	0.0078	1.9386	0.5833	0.5037	0.2537	0.0346
	LL2	20	4.189	0.0488	1.5706	0.6637	0.3520	0.1239	0.0243
	LL3	20	4.189	0.0026	1.0728	0.3386	0.2779	0.0772	0.0195
	RL1	20	4.189	0.0424	1.5122	0.6202	0.3652	0.1334	0.0254
	RL2	20	4.189	0.0059	0.7884	0.2736	0.1884	0.0355	0.0130
	RL3	20	4.189	0.0050	0.7297	0.2549	0.1749	0.0306	0.0121

Table A 12: SUVs of 20 mm lesions, acquired during expiration using a 2:1 lesion-to-lung contrast

All

2D				min	max	mean	std dev	variance	std error
		Diameter (mm)	Volume (ml)						
Lesions	LL1	20	4.189	0.0342	4.2363	1.4302	0.9983	0.9965	0.0686
	LL2	20	4.189	0.4737	5.1634	2.6708	1.0964	1.2021	0.0758
	LL3	20	4.189	0.0519	4.5853	1.5951	1.0372	1.0758	0.0726
	RL1	20	4.189	0.1491	3.3178	1.6219	0.8455	0.7148	0.0588
	RL2	20	4.189	0.0968	2.9095	1.4431	0.6983	0.4877	0.0482
	RL3	20	4.189	0.0645	3.7442	1.4500	0.8476	0.7185	0.0586
3D				min	max	mean	std dev	variance	std error
		Diameter (mm)	Volume (ml)						
Lesions	LL1	20	4.189	0.0338	3.8380	1.3061	0.9547	0.9115	0.0656
	LL2	20	4.189	0.5004	4.1672	2.1721	0.8068	0.6510	0.0558
	LL3	20	4.189	0.0456	3.4275	1.4242	0.8647	0.7477	0.0605
	RL1	20	4.189	0.1156	3.0973	1.4395	0.6920	0.4789	0.0481
	RL2	20	4.189	0.1033	2.7105	1.2766	0.5943	0.3532	0.0410
	RL3	20	4.189	0.0646	2.6530	1.1894	0.6176	0.3815	0.0427

Trues

2D				min	max	mean	std dev	variance	std error
		Diameter (mm)	Volume (ml)						
Lesions	LL1	20	4.189	0.0138	0.4175	0.1862	0.0918	0.0084	0.0063
	LL2	20	4.189	0.1588	0.7438	0.4377	0.1398	0.0195	0.0097
	LL3	20	4.189	0.0502	0.7736	0.3668	0.1686	0.0284	0.0118
	RL1	20	4.189	0.0366	0.3841	0.2241	0.0896	0.0080	0.0062
	RL2	20	4.189	0.0527	0.5049	0.2971	0.1026	0.0105	0.0071
	RL3	20	4.189	0.0542	0.6148	0.2955	0.1274	0.0162	0.0088
3D				min	max	mean	std dev	variance	std error
		Diameter (mm)	Volume (ml)						
Lesions	LL1	20	4.189	0.0158	0.5588	0.2273	0.1234	0.0152	0.0085
	LL2	20	4.189	0.1608	0.7533	0.4597	0.1381	0.0191	0.0096
	LL3	20	4.189	0.0556	0.7082	0.3780	0.1605	0.0258	0.0112
	RL1	20	4.189	0.0322	0.4679	0.2648	0.0945	0.0089	0.0066
	RL2	20	4.189	0.0617	0.5595	0.3073	0.1138	0.0130	0.0079
	RL3	20	4.189	0.0395	0.6229	0.2867	0.1337	0.0179	0.0092

Scatters

2D				min	max	mean	std dev	variance	std error
		Diameter (mm)	Volume (ml)						
Lesions	LL1	20	4.189	0.0118	0.6705	0.2516	0.1557	0.0242	0.0107
	LL2	20	4.189	0.1499	1.0480	0.5805	0.2050	0.0420	0.0142
	LL3	20	4.189	0.0253	0.9891	0.4070	0.2174	0.0472	0.0152
	RL1	20	4.189	0.0452	0.7303	0.3504	0.1664	0.0277	0.0116
	RL2	20	4.189	0.0525	0.7433	0.4078	0.1585	0.0251	0.0109
	RL3	20	4.189	0.0476	1.0100	0.4577	0.2138	0.0457	0.0148
3D				min	max	mean	std dev	variance	std error
		Diameter (mm)	Volume (ml)						
Lesions	LL1	20	4.189	0.0104	1.0885	0.3841	0.2649	0.0702	0.0182
	LL2	20	4.189	0.1695	1.1713	0.6585	0.2204	0.0486	0.0152
	LL3	20	4.189	0.0266	1.1498	0.4878	0.2565	0.0658	0.0180
	RL1	20	4.189	0.0376	0.9206	0.4273	0.2101	0.0441	0.0146
	RL2	20	4.189	0.0524	0.8828	0.4581	0.1845	0.0340	0.0127
	RL3	20	4.189	0.0534	0.9894	0.5008	0.2139	0.0458	0.0148

Randoms

2D				min	max	mean	std dev	variance	std error
		Diameter (mm)	Volume (ml)						
Lesions	LL1	20	4.189	0.0127	2.9098	0.8676	0.7022	0.4931	0.0482
	LL2	20	4.189	0.0825	2.7319	1.1685	0.6330	0.4007	0.0438
	LL3	20	4.189	0.0069	2.1267	0.5988	0.4932	0.2432	0.0345
	RL1	20	4.189	0.0455	2.1215	0.9331	0.5493	0.3017	0.0382
	RL2	20	4.189	0.0122	1.1702	0.4802	0.3011	0.0907	0.0208
	RL3	20	4.189	0.0100	1.6093	0.5270	0.3766	0.1418	0.0260
3D				min	max	mean	std dev	variance	std error
		Diameter (mm)	Volume (ml)						
Lesions	LL1	20	4.189	0.0070	2.0347	0.5827	0.5141	0.2643	0.0353
	LL2	20	4.189	0.0481	1.5854	0.6441	0.3569	0.1274	0.0247
	LL3	20	4.189	0.0028	1.0779	0.3304	0.2780	0.0773	0.0195
	RL1	20	4.189	0.0331	1.5958	0.6224	0.3742	0.1400	0.0260
	RL2	20	4.189	0.0067	0.6978	0.2646	0.1748	0.0306	0.0121
	RL3	20	4.189	0.0066	0.7188	0.2458	0.1689	0.0285	0.0117

Table A 13: SUVs of 20 mm lesions, acquired during inspiration using a 10:1 lesion-to-lung contrast

All

2D

		Diameter (mm)	Volume (ml)	min	max	mean	std dev	variance	std error
Lesions	LL1	20	4.189	0.0991	7.0017	2.7889	1.5984	2.5550	0.1095
	LL2	20	4.189	0.6706	7.2199	4.0201	1.5000	2.2500	0.1025
	LL3	20	4.189	0.0718	7.7701	3.1005	1.8514	3.4277	0.1263
	RL1	20	4.189	0.0388	6.1161	2.4380	1.6075	2.5840	0.1096
	RL2	20	4.189	0.1179	5.4813	2.6510	1.2296	1.5120	0.0839
	RL3	20	4.189	0.2837	6.4432	3.0428	1.4552	2.1176	0.1007

3D

		Diameter (mm)	Volume (ml)	min	max	mean	std dev	variance	std error
Lesions	LL1	20	4.189	0.1007	6.2388	2.6292	1.4449	2.0877	0.0990
	LL2	20	4.189	0.6253	5.6012	3.3880	1.1926	1.4224	0.0815
	LL3	20	4.189	0.1421	5.6505	2.8654	1.4129	1.9963	0.0964
	RL1	20	4.189	0.0614	4.9964	2.2185	1.2590	1.5852	0.0859
	RL2	20	4.189	0.1993	4.7312	2.4211	1.0444	1.0908	0.0712
	RL3	20	4.189	0.3050	6.3376	2.8727	1.3846	1.9171	0.0958

Trues

2D

		Diameter (mm)	Volume (ml)	min	max	mean	std dev	variance	std error
Lesions	LL1	20	4.189	0.1467	1.8128	1.0187	0.3764	0.1417	0.0258
	LL2	20	4.189	0.3029	2.2871	1.4049	0.4398	0.1934	0.0301
	LL3	20	4.189	0.1197	2.7057	1.3627	0.5911	0.3494	0.0403
	RL1	20	4.189	0.0731	1.8693	0.9824	0.4515	0.2038	0.0308
	RL2	20	4.189	0.1678	2.0592	1.1634	0.4189	0.1754	0.0286
	RL3	20	4.189	0.2999	2.4830	1.3970	0.5129	0.2631	0.0355

3D

		Diameter (mm)	Volume (ml)	min	max	mean	std dev	variance	std error
Lesions	LL1	20	4.189	0.1583	2.1129	1.1258	0.4428	0.1961	0.0303
	LL2	20	4.189	0.3426	2.5310	1.5458	0.4729	0.2236	0.0323
	LL3	20	4.189	0.1454	2.4323	1.3666	0.5431	0.2949	0.0370
	RL1	20	4.189	0.0869	2.0075	1.0751	0.4524	0.2046	0.0309
	RL2	20	4.189	0.1757	2.1083	1.2056	0.4295	0.1845	0.0293
	RL3	20	4.189	0.3634	2.8773	1.4574	0.5734	0.3288	0.0397

Scatters

2D

		Diameter (mm)	Volume (ml)	min	max	mean	std dev	variance	std error
Lesions	LL1	20	4.189	0.0097	0.9880	0.3988	0.2292	0.0525	0.0157
	LL2	20	4.189	0.1575	1.1341	0.6374	0.2195	0.0482	0.0150
	LL3	20	4.189	0.0324	1.1571	0.5249	0.2646	0.0700	0.0180
	RL1	20	4.189	0.0118	0.8557	0.3401	0.2135	0.0456	0.0146
	RL2	20	4.189	0.0542	0.8366	0.4599	0.1724	0.0297	0.0118
	RL3	20	4.189	0.0840	1.1216	0.5759	0.2408	0.0580	0.0167

3D

		Diameter (mm)	Volume (ml)	min	max	mean	std dev	variance	std error
Lesions	LL1	20	4.189	0.0175	1.3544	0.5328	0.3153	0.0994	0.0216
	LL2	20	4.189	0.1751	1.2487	0.7358	0.2570	0.0661	0.0176
	LL3	20	4.189	0.0667	1.2821	0.6744	0.2971	0.0882	0.0203
	RL1	20	4.189	0.0216	1.1030	0.4401	0.2698	0.0728	0.0184
	RL2	20	4.189	0.0706	0.9838	0.5340	0.2079	0.0432	0.0142
	RL3	20	4.189	0.1099	1.5191	0.7125	0.3074	0.0945	0.0213

Randoms

2D

		Diameter (mm)	Volume (ml)	min	max	mean	std dev	variance	std error
Lesions	LL1	20	4.189	0.0208	3.7496	1.1536	0.8464	0.7165	0.0580
	LL2	20	4.189	0.1432	3.1581	1.3878	0.7160	0.5127	0.0489
	LL3	20	4.189	0.0037	2.9218	0.8453	0.7130	0.5084	0.0486
	RL1	20	4.189	0.0056	2.5617	0.8881	0.6698	0.4486	0.0457
	RL2	20	4.189	0.0063	1.5685	0.5811	0.3820	0.1460	0.0261
	RL3	20	4.189	0.0159	2.0378	0.7463	0.4728	0.2235	0.0327

3D

		Diameter (mm)	Volume (ml)	min	max	mean	std dev	variance	std error
Lesions	LL1	20	4.189	0.0085	2.3542	0.7883	0.5804	0.3368	0.0398
	LL2	20	4.189	0.0731	1.6766	0.7673	0.3889	0.1512	0.0266
	LL3	20	4.189	0.0036	1.3310	0.4751	0.3481	0.1212	0.0237
	RL1	20	4.189	0.0061	1.3505	0.5140	0.3594	0.1292	0.0245
	RL2	20	4.189	0.0033	0.8583	0.3144	0.2171	0.0471	0.0148
	RL3	20	4.189	0.0080	1.4179	0.4653	0.3329	0.1108	0.0230

Table A 14: SUVs of 20 mm lesions, acquired during inspiration using a 5:1 lesion-to-lung contrast

All

2D

		Diameter (mm)	Volume (ml)	min	max	mean	std dev	variance	std error
Lesions	LL1	20	4.189	0.0826	5.9730	2.2209	1.3757	1.8926	0.0943
	LL2	20	4.189	0.5789	6.2020	3.3250	1.3046	1.7019	0.0892
	LL3	20	4.189	0.0451	6.7268	2.5080	1.6013	2.5643	0.1092
	RL1	20	4.189	0.0293	5.3017	2.0230	1.4073	1.9805	0.0960
	RL2	20	4.189	0.0797	4.1919	1.9996	0.9578	0.9173	0.0653
	RL3	20	4.189	0.1697	5.3210	2.3549	1.2057	1.4538	0.0834

3D

		Diameter (mm)	Volume (ml)	min	max	mean	std dev	variance	std error
Lesions	LL1	20	4.189	0.0732	5.1389	2.0826	1.2276	1.5071	0.0841
	LL2	20	4.189	0.4922	4.7417	2.6941	1.0150	1.0302	0.0694
	LL3	20	4.189	0.0869	4.1973	2.1973	1.1172	1.2481	0.0762
	RL1	20	4.189	0.0580	3.8393	1.6314	0.9918	0.9837	0.0676
	RL2	20	4.189	0.1326	3.7695	1.8333	0.8363	0.6993	0.0570
	RL3	20	4.189	0.1939	5.3750	2.3306	1.1981	1.4354	0.0829

Trues

2D

		Diameter (mm)	Volume (ml)	min	max	mean	std dev	variance	std error
Lesions	LL1	20	4.189	0.0697	0.9928	0.4896	0.1971	0.0388	0.0135
	LL2	20	4.189	0.1854	1.3324	0.7464	0.2542	0.0646	0.0174
	LL3	20	4.189	0.0934	1.6387	0.7615	0.3555	0.1264	0.0242
	RL1	20	4.189	0.0664	1.0734	0.4691	0.2492	0.0621	0.0170
	RL2	20	4.189	0.0825	1.0673	0.6078	0.2197	0.0483	0.0150
	RL3	20	4.189	0.1047	1.5482	0.7350	0.3228	0.1042	0.0223

3D

		Diameter (mm)	Volume (ml)	min	max	mean	std dev	variance	std error
Lesions	LL1	20	4.189	0.0935	1.1808	0.5704	0.2527	0.0638	0.0173
	LL2	20	4.189	0.1575	1.3124	0.7837	0.2746	0.0754	0.0188
	LL3	20	4.189	0.0805	1.3567	0.7886	0.3195	0.1021	0.0218
	RL1	20	4.189	0.0493	1.0168	0.5318	0.2342	0.0549	0.0160
	RL2	20	4.189	0.0918	1.1756	0.6456	0.2441	0.0596	0.0166
	RL3	20	4.189	0.1802	1.7335	0.8284	0.3598	0.1295	0.0249

Scatters

2D

		Diameter (mm)	Volume (ml)	min	max	mean	std dev	variance	std error
Lesions	LL1	20	4.189	0.0155	0.8361	0.3793	0.1993	0.0397	0.0137
	LL2	20	4.189	0.1630	1.1018	0.6227	0.2121	0.0450	0.0145
	LL3	20	4.189	0.0208	1.2145	0.5283	0.2976	0.0886	0.0203
	RL1	20	4.189	0.0121	0.8712	0.3485	0.2268	0.0514	0.0155
	RL2	20	4.189	0.0497	0.8267	0.4552	0.1752	0.0307	0.0119
	RL3	20	4.189	0.0767	1.1228	0.5558	0.2365	0.0560	0.0164

3D

		Diameter (mm)	Volume (ml)	min	max	mean	std dev	variance	std error
Lesions	LL1	20	4.189	0.0248	1.2502	0.5212	0.2881	0.0830	0.0197
	LL2	20	4.189	0.1745	1.2102	0.7162	0.2494	0.0622	0.0170
	LL3	20	4.189	0.0478	1.2201	0.6518	0.3040	0.0924	0.0207
	RL1	20	4.189	0.0255	0.9467	0.4112	0.2417	0.0584	0.0165
	RL2	20	4.189	0.0716	1.0192	0.5262	0.2103	0.0442	0.0143
	RL3	20	4.189	0.1215	1.4091	0.7174	0.3012	0.0907	0.0208

Randoms

2D

		Diameter (mm)	Volume (ml)	min	max	mean	std dev	variance	std error
Lesions	LL1	20	4.189	0.0203	3.6354	1.1535	0.8588	0.7376	0.0588
	LL2	20	4.189	0.1402	3.1175	1.3936	0.7119	0.5067	0.0487
	LL3	20	4.189	0.0029	2.8989	0.8405	0.6985	0.4878	0.0476
	RL1	20	4.189	0.0055	2.7675	0.9644	0.7350	0.5402	0.0501
	RL2	20	4.189	0.0057	1.5561	0.5714	0.3785	0.1433	0.0258
	RL3	20	4.189	0.0152	1.9615	0.7691	0.4724	0.2232	0.0327

3D

		Diameter (mm)	Volume (ml)	min	max	mean	std dev	variance	std error
Lesions	LL1	20	4.189	0.0090	2.3609	0.7790	0.5840	0.3410	0.0400
	LL2	20	4.189	0.0629	1.6193	0.7473	0.3900	0.1521	0.0267
	LL3	20	4.189	0.0027	1.1988	0.4348	0.3099	0.0960	0.0211
	RL1	20	4.189	0.0048	1.4735	0.5194	0.3804	0.1447	0.0259
	RL2	20	4.189	0.0036	0.8703	0.3175	0.2227	0.0496	0.0152
	RL3	20	4.189	0.0106	1.6679	0.5160	0.3773	0.1423	0.0261

Table A 15: SUVs of 20 mm lesions, acquired during inspiration using a 2:1 lesion-to-lung contrast

All

2D

		Diameter (mm)	Volume (ml)	min	max	mean	std dev	variance	std error
Lesions	LL1	20	4.189	0.0653	5.4222	1.9695	1.2407	1.5394	0.0850
	LL2	20	4.189	0.5374	5.4408	2.8524	1.1494	1.3211	0.0786
	LL3	20	4.189	0.0366	5.7218	2.1040	1.3993	1.9580	0.0954
	RL1	20	4.189	0.0280	4.4889	1.6851	1.1749	1.3805	0.0801
	RL2	20	4.189	0.0687	3.5601	1.6425	0.8140	0.6626	0.0555
	RL3	20	4.189	0.1235	4.4606	1.9145	1.0038	1.0077	0.0694

3D

		Diameter (mm)	Volume (ml)	min	max	mean	std dev	variance	std error
Lesions	LL1	20	4.189	0.0519	4.4633	1.6918	1.0700	1.1449	0.0733
	LL2	20	4.189	0.4353	3.9683	2.2219	0.8705	0.7578	0.0595
	LL3	20	4.189	0.0776	3.6494	1.8144	0.9708	0.9424	0.0662
	RL1	20	4.189	0.0415	2.8909	1.2686	0.7759	0.6020	0.0529
	RL2	20	4.189	0.1035	2.9983	1.4036	0.6601	0.4357	0.0450
	RL3	20	4.189	0.1197	4.2315	1.7778	0.9596	0.9207	0.0664

Trues

2D

		Diameter (mm)	Volume (ml)	min	max	mean	std dev	variance	std error
Lesions	LL1	20	4.189	0.0363	0.5135	0.2373	0.1063	0.0113	0.0073
	LL2	20	4.189	0.1190	0.6567	0.3767	0.1268	0.0161	0.0087
	LL3	20	4.189	0.0477	0.9462	0.3999	0.2210	0.0488	0.0151
	RL1	20	4.189	0.0297	0.5063	0.2273	0.1188	0.0141	0.0081
	RL2	20	4.189	0.0486	0.5117	0.2911	0.1002	0.0100	0.0068
	RL3	20	4.189	0.0538	0.7913	0.3591	0.1695	0.0287	0.0117

3D

		Diameter (mm)	Volume (ml)	min	max	mean	std dev	variance	std error
Lesions	LL1	20	4.189	0.0415	0.6543	0.2686	0.1413	0.0200	0.0097
	LL2	20	4.189	0.0973	0.6675	0.3843	0.1391	0.0194	0.0095
	LL3	20	4.189	0.0643	0.7409	0.4060	0.1828	0.0334	0.0125
	RL1	20	4.189	0.0530	0.4899	0.2364	0.1100	0.0121	0.0075
	RL2	20	4.189	0.0527	0.5265	0.3002	0.1102	0.0121	0.0075
	RL3	20	4.189	0.0545	0.9087	0.3923	0.1959	0.0384	0.0136

Scatters

2D

		Diameter (mm)	Volume (ml)	min	max	mean	std dev	variance	std error
Lesions	LL1	20	4.189	0.0175	0.8926	0.3706	0.2045	0.0418	0.0140
	LL2	20	4.189	0.1660	1.0750	0.5967	0.2117	0.0448	0.0145
	LL3	20	4.189	0.0219	1.1436	0.5155	0.2728	0.0744	0.0186
	RL1	20	4.189	0.0092	0.7924	0.3226	0.2053	0.0421	0.0140
	RL2	20	4.189	0.0517	0.7654	0.4352	0.1643	0.0270	0.0112
	RL3	20	4.189	0.0693	1.1153	0.5406	0.2288	0.0523	0.0158

3D

		Diameter (mm)	Volume (ml)	min	max	mean	std dev	variance	std error
Lesions	LL1	20	4.189	0.0165	1.1830	0.4913	0.2918	0.0851	0.0200
	LL2	20	4.189	0.1434	0.9851	0.5869	0.1875	0.0352	0.0128
	LL3	20	4.189	0.0466	1.0316	0.5428	0.2439	0.0595	0.0166
	RL1	20	4.189	0.0128	0.7435	0.3670	0.2026	0.0410	0.0138
	RL2	20	4.189	0.0964	0.7090	0.3153	0.1951	0.0381	0.0133
	RL3	20	4.189	0.0813	1.4922	0.6898	0.3054	0.0933	0.0211

Randoms

2D

		Diameter (mm)	Volume (ml)	min	max	mean	std dev	variance	std error
Lesions	LL1	20	4.189	0.0224	3.5608	1.1702	0.8317	0.6917	0.0570
	LL2	20	4.189	0.1260	3.1184	1.3950	0.7164	0.5132	0.0490
	LL3	20	4.189	0.0028	2.8898	0.8455	0.7081	0.5014	0.0483
	RL1	20	4.189	0.0068	2.8007	0.9613	0.7240	0.5241	0.0494
	RL2	20	4.189	0.0058	1.6240	0.5825	0.3946	0.1557	0.0269
	RL3	20	4.189	0.0148	2.0777	0.7606	0.4953	0.2454	0.0343

3D

		Diameter (mm)	Volume (ml)	min	max	mean	std dev	variance	std error
Lesions	LL1	20	4.189	0.0095	2.3947	0.7711	0.5807	0.3373	0.0398
	LL2	20	4.189	0.0711	1.5985	0.7370	0.3841	0.1476	0.0263
	LL3	20	4.189	0.0027	1.1366	0.4372	0.3075	0.0946	0.0210
	RL1	20	4.189	0.0051	1.3893	0.5118	0.3657	0.1337	0.0249
	RL2	20	4.189	0.0036	0.8947	0.3201	0.2203	0.0485	0.0150
	RL3	20	4.189	0.0105	1.3076	0.4596	0.3119	0.0973	0.0216

Table A 16: SUVs of 10 mm lesions, acquired during breathing using a 10:1 lesion-to-lung contrast, repositioned outside FoV.

All

2D		Diameter (mm)	Volume (ml)	min	max	mean	std dev	variance	std error
Lesions	LL1	10	0.524	0.7348	3.7380	2.4188	0.8405	0.7065	0.1282
	LL2	10	0.524	1.0163	3.6977	2.5728	0.7270	0.5285	0.1109
	LL3	10	0.524	0.2256	4.5300	1.6321	0.8202	0.6728	0.1348
	RL1	10	0.524	0.5377	3.7520	2.3383	0.7477	0.5590	0.1154
	RL2	10	0.524	0.1162	2.4682	1.5276	0.5317	0.2827	0.0802
	RL3	10	0.524	0.0466	0.7734	0.3737	0.1476	0.0218	0.0211
3D		Diameter (mm)	Volume (ml)	min	max	mean	std dev	variance	std error
Lesions	LL1	10	0.524	0.7041	5.2405	3.1482	1.1877	1.4106	0.1811
	LL2	10	0.524	0.9976	3.4423	2.4514	0.5953	0.3544	0.0908
	LL3	10	0.524	0.0718	6.0125	1.3065	1.1375	1.2939	0.1870
	RL1	10	0.524	0.6719	4.2039	2.5673	0.8327	0.6934	0.1285
	RL2	10	0.524	0.1426	2.6668	1.6283	0.6188	0.3829	0.0933
	RL3	10	0.524	0.0581	0.8075	0.4519	0.1541	0.0237	0.0220

Trues

2D		Diameter (mm)	Volume (ml)	min	max	mean	std dev	variance	std error
Lesions	LL1	10	0.524	0.2114	1.9237	1.2253	0.4571	0.2089	0.0697
	LL2	10	0.524	0.2602	1.7161	1.0770	0.3827	0.1465	0.0584
	LL3	10	0.524	0.2907	2.1824	1.4009	0.4458	0.1988	0.0733
	RL1	10	0.524	0.3411	1.7771	1.1911	0.3770	0.1421	0.0582
	RL2	10	0.524	0.2617	1.6377	1.1246	0.2694	0.0726	0.0406
	RL3	10	0.524	0.0041	0.5221	0.1168	0.0894	0.0080	0.0128
3D		Diameter (mm)	Volume (ml)	min	max	mean	std dev	variance	std error
Lesions	LL1	10	0.524	0.1827	2.0124	1.2558	0.4876	0.2378	0.0744
	LL2	10	0.524	0.2599	1.5244	0.9618	0.3134	0.0982	0.0478
	LL3	10	0.524	0.1752	2.8093	1.2000	0.6091	0.3710	0.1001
	RL1	10	0.524	0.4249	1.9556	1.2681	0.3996	0.1597	0.0617
	RL2	10	0.524	0.2941	1.6768	1.1384	0.3030	0.0918	0.0457
	RL3	10	0.524	0.0138	0.6042	0.1353	0.0932	0.0087	0.0133

Scatters

2D		Diameter (mm)	Volume (ml)	min	max	mean	std dev	variance	std error
Lesions	LL1	10	0.524	0.0994	0.4614	0.3192	0.1073	0.0115	0.0164
	LL2	10	0.524	0.2296	0.5549	0.4293	0.0903	0.0082	0.0138
	LL3	10	0.524	0.0640	0.7444	0.2826	0.1207	0.0146	0.0198
	RL1	10	0.524	0.0464	0.4849	0.3106	0.1030	0.0106	0.0159
	RL2	10	0.524	0.0314	0.4240	0.2455	0.0869	0.0075	0.0131
	RL3	10	0.524	0.0580	0.4024	0.2440	0.0705	0.0050	0.0101
3D		Diameter (mm)	Volume (ml)	min	max	mean	std dev	variance	std error
Lesions	LL1	10	0.524	0.1417	0.7910	0.4858	0.1840	0.0339	0.0281
	LL2	10	0.524	0.2165	0.6436	0.4595	0.0940	0.0088	0.0143
	LL3	10	0.524	0.0649	0.9832	0.2613	0.1637	0.0268	0.0269
	RL1	10	0.524	0.0675	0.6887	0.4157	0.1690	0.0286	0.0261
	RL2	10	0.524	0.0433	0.5096	0.2986	0.1104	0.0122	0.0166
	RL3	10	0.524	0.0569	0.5239	0.3196	0.1063	0.0113	0.0152

Randoms

2D		Diameter (mm)	Volume (ml)	min	max	mean	std dev	variance
Lesions	LL1	10	0.524	0.1809	1.0841	0.6987	0.2817	0.0794	0.0430
	LL2	10	0.524	0.2398	0.9788	0.6898	0.2067	0.0427	0.0315
	LL3	10	0.524	0.0082	0.8231	0.1397	0.1429	0.0204	0.0235
	RL1	10	0.524	0.0513	0.9776	0.5686	0.2134	0.0455	0.0329
	RL2	10	0.524	0.0028	0.3114	0.1146	0.0746	0.0056	0.0112
	RL3	10	0.524	0.0102	0.1490	0.0642	0.0247	0.0006	0.0035
3D		Diameter (mm)	Volume (ml)	min	max	mean	std dev	variance	std error
Lesions	LL1	10	0.524	0.2486	1.9228	1.1256	0.4829	0.2332	0.0736
	LL2	10	0.524	0.1886	0.9809	0.6491	0.1979	0.0392	0.0302
	LL3	10	0.524	0.0041	1.7750	0.1380	0.3069	0.0942	0.0504
	RL1	10	0.524	0.0742	1.1783	0.6810	0.2859	0.0818	0.0441
	RL2	10	0.524	0.0032	0.3058	0.1236	0.0841	0.0071	0.0127
	RL3	10	0.524	0.0049	0.1550	0.0895	0.0351	0.0012	0.0050

Table A 17: SUVs of 20 mm lesions, acquired during breathing using a 10:1 lesion-to-lung contrast, repositioned outside FoV

All

2D				min	max	mean	std dev	variance	std error
		Diameter (mm)	Volume (ml)						
Lesions	LL1	20	4.189	0.1320	6.9283	3.0578	1.6051	2.5765	0.1147
	LL2	20	4.189	0.5159	5.4344	2.7558	1.0135	1.0272	0.0632
	LL3	20	4.189	0.2823	8.1491	3.0558	1.7324	3.0011	0.1228
	RL1	20	4.189	0.3284	5.8674	2.8652	1.3128	1.7235	0.0900
	RL2	20	4.189	0.2300	5.6193	2.5686	1.2467	1.5543	0.0775
	RL3	20	4.189	0.1556	3.4535	1.1830	0.6370	0.4058	0.0417
3D				min	max	mean	std dev	variance	std error
		Diameter (mm)	Volume (ml)						
Lesions	LL1	20	4.189	0.1373	7.3269	3.2017	1.7687	3.1285	0.1263
	LL2	20	4.189	0.7539	5.3154	2.7089	0.9587	0.9190	0.0598
	LL3	20	4.189	0.2594	9.4066	3.3466	1.8605	3.4614	0.1319
	RL1	20	4.189	0.3516	6.9405	3.2038	1.5021	2.2563	0.1029
	RL2	20	4.189	0.1820	5.8293	2.5798	1.3053	1.7037	0.0811
	RL3	20	4.189	0.1222	3.6158	1.4594	0.7167	0.5137	0.0470

Trues

2D				min	max	mean	std dev	variance	std error
		Diameter (mm)	Volume (ml)						
Lesions	LL1	20	4.189	0.0624	4.0512	1.8581	0.9732	0.9472	0.0695
	LL2	20	4.189	0.0706	2.6951	1.3497	0.4976	0.2476	0.0310
	LL3	20	4.189	0.2106	5.0735	2.0816	0.9853	0.9709	0.0698
	RL1	20	4.189	0.1287	3.2261	1.7266	0.6920	0.4788	0.0474
	RL2	20	4.189	0.3188	3.3728	1.6982	0.6939	0.4815	0.0431
	RL3	20	4.189	0.0345	1.1657	0.5605	0.2828	0.0800	0.0185
3D				min	max	mean	std dev	variance	std error
		Diameter (mm)	Volume (ml)						
Lesions	LL1	20	4.189	0.0476	3.8537	1.8287	0.9507	0.9038	0.0679
	LL2	20	4.189	0.1129	2.5031	1.2758	0.4595	0.2111	0.0287
	LL3	20	4.189	0.3309	4.6202	1.9780	0.8269	0.6837	0.0586
	RL1	20	4.189	0.1867	3.3261	1.7661	0.6938	0.4814	0.0475
	RL2	20	4.189	0.3041	3.2764	1.6573	0.6845	0.4686	0.0425
	RL3	20	4.189	0.0166	1.3756	0.5861	0.3295	0.1085	0.0216

Scatters

2D				min	max	mean	std dev	variance	std error
		Diameter (mm)	Volume (ml)						
Lesions	LL1	20	4.189	0.0407	0.9223	0.4431	0.2168	0.0470	0.0155
	LL2	20	4.189	0.1475	1.0820	0.5555	0.1933	0.0374	0.0121
	LL3	20	4.189	0.0688	1.1127	0.4690	0.2281	0.0520	0.0162
	RL1	20	4.189	0.0496	0.8330	0.4339	0.1999	0.0399	0.0137
	RL2	20	4.189	0.0360	0.8616	0.3990	0.1919	0.0368	0.0119
	RL3	20	4.189	0.0707	1.4016	0.4098	0.2280	0.0520	0.0149
3D				min	max	mean	std dev	variance	std error
		Diameter (mm)	Volume (ml)						
Lesions	LL1	20	4.189	0.0531	1.1073	0.4903	0.2646	0.0700	0.0189
	LL2	20	4.189	0.1546	0.9960	0.5654	0.1795	0.0322	0.0112
	LL3	20	4.189	0.0723	2.1347	0.6881	0.4054	0.1644	0.0287
	RL1	20	4.189	0.0411	1.1431	0.5151	0.2647	0.0700	0.0181
	RL2	20	4.189	0.0436	0.9420	0.4328	0.2100	0.0441	0.0130
	RL3	20	4.189	0.1366	1.3245	0.5197	0.2398	0.0575	0.0157

Randoms

2D				min	max	mean	std dev	variance	std error
		Diameter (mm)	Volume (ml)						
Lesions	LL1	20	4.189	0.0190	1.7041	0.5983	0.4104	0.1684	0.0293
	LL2	20	4.189	0.0389	1.2881	0.5514	0.2831	0.0801	0.0177
	LL3	20	4.189	0.0036	0.9729	0.2439	0.2450	0.0600	0.0174
	RL1	20	4.189	0.0198	1.3001	0.5158	0.3131	0.0981	0.0215
	RL2	20	4.189	0.0012	0.7353	0.2271	0.1874	0.0351	0.0116
	RL3	20	4.189	0.0070	0.6823	0.1363	0.1280	0.0164	0.0084
3D				min	max	mean	std dev	variance	std error
		Diameter (mm)	Volume (ml)						
Lesions	LL1	20	4.189	0.0165	1.9062	0.6723	0.4915	0.2416	0.0351
	LL2	20	4.189	0.0474	1.3273	0.5523	0.2860	0.0818	0.0178
	LL3	20	4.189	0.0026	1.6452	0.3157	0.3334	0.1111	0.0236
	RL1	20	4.189	0.0220	1.7753	0.6709	0.4473	0.2001	0.0307
	RL2	20	4.189	0.0006	0.8149	0.2363	0.2109	0.0445	0.0131
	RL3	20	4.189	0.0086	1.0069	0.1900	0.1754	0.0308	0.0115

Table A 18: SUVs of 20 mm lesions, acquired during breathing using a 5:1 lesion-to-lung contrast, repositioned outside FoV

All

2D				min	max	mean	std dev	variance	std error
		Diameter (mm)	Volume (ml)						
Lesions	LL1	20	4.189	0.1397	7.0795	2.8751	1.6341	2.6701	0.1167
	LL2	20	4.189	0.4234	5.5779	2.5871	1.1152	1.2436	0.0696
	LL3	20	4.189	0.1274	7.6040	2.5809	1.7818	3.1749	0.1263
	RL1	20	4.189	0.1874	5.8207	2.6175	1.3575	1.8429	0.0930
	RL2	20	4.189	0.0650	5.3358	2.1286	1.2910	1.6666	0.0802
	RL3	20	4.189	0.0762	4.0437	0.8179	0.6460	0.4174	0.0423
3D				min	max	mean	std dev	variance	std error
		Diameter (mm)	Volume (ml)						
Lesions	LL1	20	4.189	0.1463	6.3195	2.5976	1.4893	2.2180	0.1064
	LL2	20	4.189	0.5022	4.6368	2.1386	0.9043	0.8177	0.0564
	LL3	20	4.189	0.1721	9.4646	2.7139	1.8368	3.3737	0.1302
	RL1	20	4.189	0.1578	5.5800	2.5220	1.2574	1.5811	0.0862
	RL2	20	4.189	0.0893	4.9080	1.9835	1.1484	1.3188	0.0714
	RL3	20	4.189	0.0468	2.9404	0.8908	0.5629	0.3169	0.0369

Trues

2D				min	max	mean	std dev	variance	std error
		Diameter (mm)	Volume (ml)						
Lesions	LL1	20	4.189	0.0497	2.5255	1.1371	0.5814	0.3381	0.0415
	LL2	20	4.189	0.0482	1.6990	0.7103	0.3569	0.1274	0.0223
	LL3	20	4.189	0.0796	3.4244	1.3178	0.7609	0.5789	0.0539
	RL1	20	4.189	0.1347	2.1512	1.0308	0.4569	0.2088	0.0313
	RL2	20	4.189	0.0771	2.3204	1.0467	0.5318	0.2828	0.0330
	RL3	20	4.189	0.0009	0.5044	0.1655	0.1067	0.0114	0.0070
3D				min	max	mean	std dev	variance	std error
		Diameter (mm)	Volume (ml)						
Lesions	LL1	20	4.189	0.0452	2.8189	1.2438	0.6535	0.4271	0.0467
	LL2	20	4.189	0.0519	1.7261	0.7296	0.3748	0.1404	0.0234
	LL3	20	4.189	0.1260	3.4157	1.3285	0.7222	0.5216	0.0512
	RL1	20	4.189	0.1276	2.2180	1.1348	0.4857	0.2359	0.0333
	RL2	20	4.189	0.0711	2.4363	1.0822	0.5536	0.3064	0.0344
	RL3	20	4.189	0.0022	0.6510	0.1991	0.1457	0.0212	0.0095

Scatters

2D				min	max	mean	std dev	variance	std error
		Diameter (mm)	Volume (ml)						
Lesions	LL1	20	4.189	0.0337	0.8841	0.3813	0.2074	0.0430	0.0148
	LL2	20	4.189	0.1018	0.9150	0.4753	0.1693	0.0287	0.0106
	LL3	20	4.189	0.0600	1.0897	0.4265	0.2223	0.0494	0.0158
	RL1	20	4.189	0.0391	0.8020	0.3891	0.1873	0.0351	0.0128
	RL2	20	4.189	0.0291	0.8096	0.3665	0.1856	0.0344	0.0115
	RL3	20	4.189	0.0629	0.8517	0.2997	0.1542	0.0238	0.0101
3D				min	max	mean	std dev	variance	std error
		Diameter (mm)	Volume (ml)						
Lesions	LL1	20	4.189	0.0427	1.1591	0.4808	0.2721	0.0740	0.0194
	LL2	20	4.189	0.1509	0.9817	0.5313	0.1814	0.0329	0.0113
	LL3	20	4.189	0.0635	2.5702	0.7294	0.4777	0.2282	0.0339
	RL1	20	4.189	0.0424	1.0819	0.4972	0.2512	0.0631	0.0172
	RL2	20	4.189	0.0417	0.9249	0.4123	0.2058	0.0423	0.0128
	RL3	20	4.189	0.0894	1.1026	0.4323	0.1947	0.0379	0.0128

Randoms

2D				min	max	mean	std dev	variance	std error
		Diameter (mm)	Volume (ml)						
Lesions	LL1	20	4.189	0.0332	2.9126	1.0543	0.7182	0.5158	0.0513
	LL2	20	4.189	0.0585	2.3354	0.9614	0.5193	0.2697	0.0324
	LL3	20	4.189	0.0067	1.8322	0.4968	0.4841	0.2344	0.0343
	RL1	20	4.189	0.0366	2.2816	0.9038	0.5529	0.3057	0.0379
	RL2	20	4.189	0.0016	1.3195	0.3853	0.3240	0.1049	0.0201
	RL3	20	4.189	0.0108	1.1312	0.2217	0.2081	0.0433	0.0136
3D				min	max	mean	std dev	variance	std error
		Diameter (mm)	Volume (ml)						
Lesions	LL1	20	4.189	0.0176	1.8365	0.6382	0.4670	0.2181	0.0334
	LL2	20	4.189	0.0373	1.3392	0.5210	0.2900	0.0841	0.0181
	LL3	20	4.189	0.0029	2.0121	0.2973	0.3690	0.1361	0.0262
	RL1	20	4.189	0.0199	1.6330	0.6208	0.4057	0.1646	0.0278
	RL2	20	4.189	0.0005	0.7468	0.2125	0.1894	0.0359	0.0118
	RL3	20	4.189	0.0063	0.8496	0.1505	0.1539	0.0237	0.0101

Table A 19: SUVs of 20 mm lesions, acquired during breathing using a 2:1 lesion-to-lung contrast, repositioned outside FoV

All

2D				min	max	mean	std dev	variance	std error
		Diameter (mm)	Volume (ml)						
Lesions	LL1	20	4.189	0.1568	6.3310	2.5218	1.4889	2.2167	0.1063
	LL2	20	4.189	0.2944	4.8395	2.1608	1.0004	1.0007	0.0624
	LL3	20	4.189	0.0811	6.1573	2.0309	1.5161	2.2984	0.1075
	RL1	20	4.189	0.0918	5.0649	2.2457	1.2314	1.5164	0.0844
	RL2	20	4.189	0.0278	4.7125	1.7593	1.1893	1.4145	0.0739
	RL3	20	4.189	0.0409	2.4449	0.5379	0.3992	0.1593	0.0261
3D				min	max	mean	std dev	variance	std error
		Diameter (mm)	Volume (ml)						
Lesions	LL1	20	4.189	0.1466	4.9872	2.1300	1.2326	1.5194	0.0880
	LL2	20	4.189	0.3158	3.5180	1.6588	0.7423	0.5510	0.0463
	LL3	20	4.189	0.0895	7.1193	2.0704	1.4791	2.1878	0.1049
	RL1	20	4.189	0.0734	4.5991	2.0409	1.1174	1.2487	0.0766
	RL2	20	4.189	0.0387	4.0695	1.6074	1.0334	1.0678	0.0642
	RL3	20	4.189	0.0296	1.7940	0.6383	0.3746	0.1403	0.0245

Trues

2D				min	max	mean	std dev	variance	std error
		Diameter (mm)	Volume (ml)						
Lesions	LL1	20	4.189	0.0567	1.8448	0.7964	0.4233	0.1792	0.0302
	LL2	20	4.189	0.0143	1.1277	0.3633	0.2619	0.0686	0.0163
	LL3	20	4.189	0.0127	2.3499	0.8344	0.5880	0.3457	0.0417
	RL1	20	4.189	0.0187	1.3642	0.6546	0.3246	0.1053	0.0222
	RL2	20	4.189	0.0063	1.5904	0.6917	0.4426	0.1959	0.0275
	RL3	20	4.189	0.0001	0.2706	0.0375	0.0413	0.0017	0.0027
3D				min	max	mean	std dev	variance	std error
		Diameter (mm)	Volume (ml)						
Lesions	LL1	20	4.189	0.0515	1.7869	0.8076	0.4347	0.1889	0.0310
	LL2	20	4.189	0.0085	1.0959	0.3586	0.2778	0.0772	0.0173
	LL3	20	4.189	0.0234	2.2658	0.8581	0.5478	0.3000	0.0388
	RL1	20	4.189	0.0175	1.4882	0.7065	0.3484	0.1214	0.0239
	RL2	20	4.189	0.0051	1.6963	0.7156	0.4583	0.2100	0.0285
	RL3	20	4.189	0.0003	0.2022	0.0402	0.0337	0.0011	0.0022

Scatters

2D				min	max	mean	std dev	variance	std error
		Diameter (mm)	Volume (ml)						
Lesions	LL1	20	4.189	0.0319	0.8626	0.3660	0.2008	0.0403	0.0143
	LL2	20	4.189	0.0959	0.8550	0.4406	0.1586	0.0251	0.0099
	LL3	20	4.189	0.0591	1.0686	0.3987	0.2143	0.0459	0.0152
	RL1	20	4.189	0.0320	0.8437	0.3784	0.1930	0.0372	0.0132
	RL2	20	4.189	0.0250	0.7899	0.3565	0.1804	0.0325	0.0112
	RL3	20	4.189	0.0433	0.8216	0.2867	0.1420	0.0202	0.0093
3D				min	max	mean	std dev	variance	std error
		Diameter (mm)	Volume (ml)						
Lesions	LL1	20	4.189	0.0424	1.0594	0.4454	0.2587	0.0669	0.0185
	LL2	20	4.189	0.1263	0.9310	0.4993	0.1762	0.0311	0.0110
	LL3	20	4.189	0.0377	2.4446	0.6412	0.4456	0.1986	0.0316
	RL1	20	4.189	0.0378	1.0868	0.4887	0.2563	0.0657	0.0176
	RL2	20	4.189	0.0310	0.8826	0.4107	0.2075	0.0430	0.0129
	RL3	20	4.189	0.0355	1.0597	0.4285	0.1958	0.0383	0.0128

Randoms

2D				min	max	mean	std dev	variance	std error
		Diameter (mm)	Volume (ml)						
Lesions	LL1	20	4.189	0.0339	2.9773	1.0391	0.7201	0.5185	0.0514
	LL2	20	4.189	0.0586	2.2527	0.9152	0.4937	0.2437	0.0308
	LL3	20	4.189	0.0046	1.9723	0.4255	0.4360	0.1901	0.0309
	RL1	20	4.189	0.0342	2.3729	0.9116	0.5788	0.3350	0.0397
	RL2	20	4.189	0.0011	1.3117	0.3687	0.3193	0.1019	0.0198
	RL3	20	4.189	0.0105	0.6018	0.1684	0.1282	0.0164	0.0084
3D				min	max	mean	std dev	variance	std error
		Diameter (mm)	Volume (ml)						
Lesions	LL1	20	4.189	0.0169	1.7932	0.6215	0.4549	0.2070	0.0325
	LL2	20	4.189	0.0368	1.1427	0.4839	0.2595	0.0673	0.0162
	LL3	20	4.189	0.0024	1.3366	0.2486	0.2614	0.0683	0.0185
	RL1	20	4.189	0.0152	1.6892	0.6094	0.4131	0.1707	0.0283
	RL2	20	4.189	0.0005	0.7787	0.2170	0.1994	0.0398	0.0124
	RL3	20	4.189	0.0027	0.7295	0.1440	0.1444	0.0209	0.0095

Table A 20: SUVs of 30 mm lesions, acquired during breathing using a 10:1 lesion-to-lung contrast, repositioned outside FoV

All

2D

		Diameter (mm)	Volume (ml)	min	max	mean	std dev	variance	std error
Lesions	LL1	30	14.137	0.2000	12.5025	5.0482	2.7917	7.7934	0.1114
	LL2	30	14.137	0.4728	9.5166	4.4322	1.8742	3.5126	0.0683
	LL3	30	14.137	0.1104	11.4190	3.8442	2.5093	6.2964	0.1075
	RL1	30	14.137	0.2143	9.7430	4.8614	2.4315	5.9121	0.0982
	RL2	30	14.137	0.0916	9.4027	3.8240	2.1995	4.8378	0.0802
	RL3	30	14.137	0.0434	6.7182	2.5239	1.4663	2.1501	0.0574

3D

		Diameter (mm)	Volume (ml)	min	max	mean	std dev	variance	std error
Lesions	LL1	30	14.137	0.1962	12.6843	5.3156	2.9833	8.9002	0.1190
	LL2	30	14.137	0.5025	9.5010	4.5600	1.9408	3.7666	0.0708
	LL3	30	14.137	0.1114	13.2263	4.2777	3.0458	9.2769	0.1305
	RL1	30	14.137	0.1500	11.2243	5.2385	2.7099	7.3433	0.1095
	RL2	30	14.137	0.0959	9.5033	3.9805	2.2699	5.1524	0.0827
	RL3	30	14.137	0.0465	9.1453	2.8722	1.8022	3.2479	0.0706

Trues

2D

		Diameter (mm)	Volume (ml)	min	max	mean	std dev	variance	std error
Lesions	LL1	30	14.137	0.0440	4.4040	2.0478	1.0290	1.0589	0.0411
	LL2	30	14.137	0.0765	3.3267	1.5123	0.6076	0.3691	0.0222
	LL3	30	14.137	0.1506	4.3403	1.7341	0.8661	0.7502	0.0371
	RL1	30	14.137	0.1809	3.7196	2.0036	0.8565	0.7335	0.0346
	RL2	30	14.137	0.1951	4.0964	1.7842	0.8644	0.7472	0.0315
	RL3	30	14.137	0.0380	1.8829	0.9106	0.4040	0.1632	0.0158

3D

		Diameter (mm)	Volume (ml)	min	max	mean	std dev	variance	std error
Lesions	LL1	30	14.137	0.0480	4.5479	2.0604	1.0574	1.1180	0.0422
	LL2	30	14.137	0.1042	3.2145	1.4896	0.6054	0.3665	0.0221
	LL3	30	14.137	0.1414	4.6861	1.6524	0.8256	0.6816	0.0354
	RL1	30	14.137	0.1914	4.1098	2.0387	0.8790	0.7727	0.0355
	RL2	30	14.137	0.1964	3.8963	1.7726	0.8473	0.7179	0.0309
	RL3	30	14.137	0.0382	2.2509	0.9310	0.4225	0.1785	0.0165

Scatters

2D

		Diameter (mm)	Volume (ml)	min	max	mean	std dev	variance	std error
Lesions	LL1	30	14.137	0.0367	1.5377	0.6531	0.3438	0.1182	0.0137
	LL2	30	14.137	0.1009	1.5119	0.7235	0.2819	0.0794	0.0103
	LL3	30	14.137	0.0243	1.8450	0.6347	0.3771	0.1422	0.0162
	RL1	30	14.137	0.0333	1.2448	0.6272	0.2982	0.0889	0.0120
	RL2	30	14.137	0.0423	1.3147	0.5613	0.2897	0.0839	0.0106
	RL3	30	14.137	0.0265	1.3880	0.5311	0.2887	0.0834	0.0113

3D

		Diameter (mm)	Volume (ml)	min	max	mean	std dev	variance	std error
Lesions	LL1	30	14.137	0.0646	1.7794	0.7273	0.3922	0.1538	0.0156
	LL2	30	14.137	0.1110	1.4395	0.7742	0.2990	0.0894	0.0109
	LL3	30	14.137	0.0369	2.9703	0.8243	0.5509	0.3035	0.0236
	RL1	30	14.137	0.0294	1.5171	0.7201	0.3355	0.1126	0.0136
	RL2	30	14.137	0.0493	1.4170	0.6337	0.3127	0.0978	0.0114
	RL3	30	14.137	0.0460	2.4853	0.7461	0.4676	0.2186	0.0183

Randoms

2D

		Diameter (mm)	Volume (ml)	min	max	mean	std dev	variance	std error
Lesions	LL1	30	14.137	0.0437	5.9119	2.0472	1.3505	1.8239	0.0539
	LL2	30	14.137	0.0433	4.4665	1.7587	0.9735	0.9477	0.0355
	LL3	30	14.137	0.0047	5.0265	1.1341	1.0550	1.1130	0.0452
	RL1	30	14.137	0.0315	4.6201	2.0054	1.1691	1.3667	0.0472
	RL2	30	14.137	0.0019	3.4454	1.0660	0.8574	0.7352	0.0312
	RL3	30	14.137	0.0059	3.2515	0.8546	0.6876	0.4728	0.0269

3D

		Diameter (mm)	Volume (ml)	min	max	mean	std dev	variance	std error
Lesions	LL1	30	14.137	0.0521	6.1641	2.1911	1.4870	2.2110	0.0593
	LL2	30	14.137	0.0432	4.4639	1.8269	1.0067	1.0134	0.0367
	LL3	30	14.137	0.0051	5.7625	1.3678	1.3230	1.7502	0.0567
	RL1	30	14.137	0.0273	5.7729	2.2214	1.3708	1.8790	0.0554
	RL2	30	14.137	0.0016	3.4834	1.1257	0.8904	0.7928	0.0324
	RL3	30	14.137	0.0047	3.7142	0.9630	0.8089	0.6544	0.0317

Chapter V

Conclusion

Table of Contents

5.1 Introduction

The goal of this study was to assess the relative importance of the physical factors that affect the accuracy of a single SUV measurement using Monte Carlo Simulations. The objectives that were set to reach this goal were to investigate the importance of partial volume effects on SUV accuracy, to investigate the contribution of breathing motion and to investigate the activity from outside the field-of-view on the calculation of the SUV. In addition, the relative contribution of true-, scattered- and random coincidences in the images were assessed. Monte Carlo simulations using GATE were utilised to obtain the objectives.

The literature survey indicated the importance of using the SUV in the clinical environment for diagnosis and prognosis, therapy planning and for assessing the outcome of therapy. The literature also pointed out that there are many factors that influence the SUV which had to be considered. The factors were technical, biological and physical in nature. In this project, the physical factors that were considered were the partial volume effect as a result of the size of lesions, imaging matrix size as well as the presence of scattered and random coincidences in addition to the true coincidences and activity outside the FoV during PET acquisition. The biological factors that were taken into account were the movement of pulmonary lesions during breathing and the location of these lesions on the calculation of SUV. The technical factors, such as scanner instrumentation, image acquisition protocols and processing methods, were regarded as invariable during this research.

The first phase of the assessment, which comprised of the Monte Carlo simulations, was performed using a static phantom. Primarily, the GATE software was benchmarked against the provided standard for use on the computer cluster. Secondly, as part of the first phase of the study, the Monte Carlo simulations were verified against phantom studies that were performed using a General Electric Discovery ST PET/CT scanner. The IEC Body Phantom^{TM} was used throughout this section. It was necessary to develop a mathematical equivalent of the phantom, as it had not existed before and was created to use as input for the Monte Carlo simulations. The partial volume effect was studied by

using different sphere sizes in combination with various sphere-to-background contrast ratios. An investigation was also done to assess the influence of sampling size on the determination of SUVs by varying the image matrix sizes. For each of the above investigations the contribution of the true-, scattered- and random coincidences were determined. Finally, the influence of VoI size was explored and its effect on the determination of SUV_{mean}.

The second phase of the project consisted of the quantification of the influences of various parameters on the SUV calculation of lesions in a human phantom. The XCAT phantom was used during this phase for the Monte Carlo Simulations. Lesions were placed at various locations in the lungs. The partial volume effect was studied by using different sphere sizes in combination with the lesion-to-background ratios as in the previous phase under breathing and non-breathing conditions. The contributions of the different types of coincidences were studied as well as the influence of activity that lay outside the FoV of the scanner on the lesions inside the FoV.

5.2 Objectives Achieved

To evaluate the success of the project, the achievement of the objectives as set out initially are summarised here.

Creation of the Voxelised IEC Body Phantom

A mathematical version of the NEMA IEC Body Phantom™ was created successfully by obtaining CT-images of the physical phantom using a contrast medium inside the spheres and water surrounding the spheres. This ensured that a difference in CT number existed between the material inside and outside the spheres. Distinct allocation of radioactive activity could therefore be made to the volumes inside and outside the spheres respectively. The phantom could then be imported into the GATE simulation software as a voxelised phantom.

Validation of GATE against an international benchmark

The software was successfully benchmarked (section 3.3.2) for application on the UFS computer cluster for simulation using one processor as well as for when 400 processors were used which was the case for the simulations in this project.

5.2.1 Partial Volume Effects

5.2.1.1 Comparison of SUV_{max} and SUV_{mean} for different sizes of spheres in the IEC Body Phantom™

It was found that the partial volume effect was present when evaluating the SUVs of the activity in the spheres of the Body Phantom when scanned on a PET/CT scanner as well as performing GATE simulations using the previously created voxelised version of the phantom. Statistically there were no significant differences between the two scanning modes and it was therefore concluded that the simulations would deliver similar results as would have been the case using a physical PET scan. The SUVs followed a logarithmic trend when compared to sphere size, a phenomenon that was also observed by Pandey *et al.*(2012) when they determined recovery coefficients. Partial volume effects have been known to influence the determination of the SUV (Thie, 2004; Soret *et al.*, 2007), and it was evident in this work as well as was shown by the logarithmic trends. It was found that the SUV_{mean} (true coincidences) between the largest sphere and the smallest sphere vary up to 54.2% (10:1 contrast ratio, 3D mode). The difference became smaller when the contrast ratio was less viz. 50.5% (5:1 contrast, 3D mode) and 32.9% when using a 2:1 contrast ratio and 3D acquisition mode.

5.2.1.2 Comparison of different matrix sizes to assess sampling size using the Body Phantom

Boellaard *et al.* (2004) stated that the image matrix (and consequently the pixel size) affects image resolution which they tested with a simulation study using a 128×128 matrix and a 256×256 matrix. Similar research was performed by Westerterp *et al.* (2007) who performed their investigations using phantom and patient scans. In the current work, the effects of matrix size on image resolution were investigated by noting the change in SUV_{mean}. Matrix sizes included in this study were: 64×64, 128×128,

256×256 and 512×512. It was found that SUV_{mean} increased as the voxel sizes became smaller as a result of better fitting to the true edges of the VoIs used for the analysis. Statistically no significant difference could be found between the 256×256 matrix results and those obtained from the 512×512 matrix and also not between the SUVs obtained using the 128×128 matrix and the 256×256 matrix. The 64×64 matrix produced images that were visually poor as a result of pixelation and delivered SUVs that were statistically significantly different when compared to those obtained when using other matrix sizes. The choice of matrix also influenced the amount of partial volume effect that was experienced. When the SUV_{mean} between the largest and smallest spheres was assessed, a maximum difference of 70.5% was found for the 64×64 matrix and 36.5% when using a 512×512 matrix during acquisition. It is recommended that the highest possible matrix size is used that is appropriate for the type of scanner and examination to minimise the PVE.

5.2.1.3 Assessment of the contribution of true-, scattered- and random coincidences in the Body Phantom

The relative contributions of true-, scatter- and random coincidences demonstrated that the true coincidences were the major contributor when assessing the data from this phantom. With a decrease in sphere volume it was observed that the SUVs decreased as was mentioned in previous sections. The relative contribution of the true coincidences to the total coincidences decreased similarly and the scattered- and random coincidence relative contributions increased.

It was also observed that when the contrast ratio decreased, the relative amount of true coincidences decreased with a resulting increase in the relative scatter- and random coincidence contributions. For the 37 mm diameter sphere imaged in 3D mode, where PVE was minimal, the trues-to-total ratio was 95.6% at 10:1 contrast ratio and it decreased to 79.9% at the 2:1 contrast ratio. The respective scatters-to-total ratio was 4.1% (10:1) and 16.2% (2:1), with the respective randoms-to-total ratio being 0.3% (10:1) and 2.5% (2:1).

For diminishing object sizes the relative contribution of true coincidences became smaller when the voxel size increased. This confirms the fact that an appropriate matrix size for the scanner should be selected.

The contributions of scatters and randoms were increased during the 3D mode acquisitions compared to 2D mode as was expected since the presence of the septa during 2D mode absorbed much of the scattered and random coincidences that had arisen from neighbouring detector rings. It is therefore recommended rather to use 2D acquisition mode when low contrast structures are studied.

5.2.1.4 Assessment of the influence of VoI size on SUV calculation in the Body Phantom

Literature showed that many methods exist to determine relevant RoIs or VoIs especially when applied to the selection of GTV. In this work, VoIs were based on the lesion size as seen on the CT images. Krak *et al.* (2005) found that fixed dimension and threshold-based methods to define RoIs are the best methods. The effects of small changes in diameter of VoI were investigated by varying the diameter from 90% of the diameter of the VoI as seen on the CT to 110% of the same in increments of 5%. It was found that the contribution of the true coincidences to the total coincidences decreased with an increase in VoI size and consequently it resulted in a decrease in the SUV_{mean}. The largest difference in SUV_{mean} of 2.5% was found when assessing the 37 mm diameter sphere that was acquired in 3D mode at a 5:1 contrast ratio using a $90\%VoI_{CT}$ and a $110\%VoI_{CT}$. At the same time, the scattered- and random coincidence contributions increased as the VoI increased. Boellaard *et al.* (2004) experienced similar results when measuring residual uptake in various types of RoIs, but their RoI variations had been much more in size. At the completion of this phase, it was decided to use a specific VoI size, viz. the 100%VoI, to be consistent when selecting a VoI describing a lesion. In the clinical situation, with the CT acquisition being performed along with the PET acquisition, it is recommended to use the $100\%VoI_{CT}$ for lesion selection and for comparative purposes.

5.2.2 Effects of Breathing Motion

5.2.2.1 Determination of the influence of breathing on the SUV calculation using the XCAT phantom

Motion results in image blurring and contrast reduction that deteriorates the qualitative accuracy of PET. Motion also causes distortion of the lesion shape and volume and this can potentially be negative for radiotherapy planning when the lesion cannot be properly delineated if the lesion size is overestimated on the PET image (Nehmeh et al., 2002; Liu *et al.*, 2009). Although many methods for correction for respiratory motion exist (Nehmeh and Erdi, 2008; Reyes *et al.*, 2007; Lamare *et al.*, 2007; Hatt *et al.*, 2012), it remains important to know how breathing affects the lesions before corrections can be applied or devised.

In this work, it was found that the location of the lesion made a difference in SUV when the same size lesions are compared to each other based on where they are situated in the lungs. The lesions near the apex in the lungs experienced the least amount of motion during breathing, they were distorted less and as a result, had the least amount of variation in SUV_{mean}. Similar results were found by Liu *et al.* (2009) who reported on the effects of breathing on SUV_{max}. From the analyses of the influence of breathing, the effect of breathing on SUV_{mean} is more pronounced at low contrast situations for the lesions in different locations in the lung.

The sensitivity during 3D acquisition was more than in 2D mode and therefore the SUVs measured in 3D mode were higher than in 2D, as was expected.

SUV_{mean} for lesions under breathing circumstances was mostly less than the SUV of the same lesions during the static conditions of full inspiration and full expiration. The effect was enhanced at the lower contrast ratios where more statistically significant differences between the dynamic condition and the static conditions were found. It is recommended therefore that where possible gated breathing be used or corrections that are specific to the amount of movement in the lungs, be applied to compensate for breathing

5.2.2.2 Determination of the influence of breathing and the variation in lesion-to-lung contrast on the SUV calculation using the XCAT phantom

When comparing the SUVs of different contrast ratios in the six lesions it was found that the largest contrast ratio yielded the largest SUV when using the true coincidences. The percentage trues-to-total was highest at the 10 mm diameter lesions and lowest at the 30 mm diameter lesions. The amount of scattered coincidences remained more or less the same for the different contrast ratios with most differences not being statistically significant. The scatter-to-total fraction was maximal at the basal lesions for a 2:1 contrast level. The scattered events originated from the heart and liver. The amount of random coincidences in each lesion was increased at lower contrast levels in the 2D set-up, but differences were noted in 3D mode indicating that randoms from other detector rings were detected as was also reported by Visvikis *et al.* (2004). The amount of random-to-total coincidences was more prominent in the apical 10 mm diameter lesions than the others with a maximum of 47.2% compared to a minimum of 6.0%. Overall the randoms ratio was the highest at the 30 mm diameter lesions for all lesions with a minimum of 28.3% and maximum of 63.2%.

5.2.2.3 Determination of the influence of breathing and the variation in lesion size on the SUV calculation using the XCAT phantom

It was observed that with increasing lesion size for a fixed lesion contrast, the SUV increased when the true coincidences were included only because of the partial volume effects. The same results were noted as well when the SUV was calculated from the scattered coincidences only or the randoms only. However, the percentage true-to-total coincidences showed a relative decrease with increase in lesion diameter. The percentage scatter-to-total coincidences remained relatively constant with change in lesion size. The fraction of random-to-total coincidences was highest for the apical lesions and lowest for the basal lesions with the largest fraction recorded for the 30 mm diameter lesions. Since the true coincidences contributed most to the total image, it can be concluded that the partial volume effect was a significant factor in the amount of true coincidences being misrepresented in the images exacerbated by the inclusion of breathing motion.

5.2.3 Effects of Activity outside the Field-of-View

Zaidi (2000) and Adam *et al.* (1999) reported that the scatter contribution from outside the field-of-view in 3D may be a challenge and should be investigated before scatter corrections can be applied. In this chapter, it was shown that moving the phantom partly outside the field-of-view had significant effects on the SUVs of objects that were still inside the FoV. In general an increase in the SUVs was observed when the true coincidences were used for the calculation. A decrease in true SUVs was found at the right basal lesion (RL3) with the largest difference being 95.3% that was found between LL3 and RL3 at a 2:1 contrast ratio in 2D acquisition mode. The scatter-to-total coincidence percentage was increased in all cases that came about as a result of the liver that lay just outside the FoV. The scatter-to-total for all other lesions was between 13.3% and 31.0%, whereas the ratios for RL3 lay between 34.6% and 67.1% for a 20 mm diameter lesion.

5.3 Recommendation for further work

It was found that there are many different fractions of scatter and randoms present during PET scanning when observing different size objects with different uptake and that to apply a uniform randoms correction or scatter correction may not deliver the optimal results. This is an opportunity for further investigation.

5.4 Conclusion

Simulations of a clinical PET scanner were performed successfully using a novel mathematical equivalent phantom created from a commercially available phantom. It was therefore possible to compare the outcomes obtained with a clinical GE Discovery ST PET/CT scanner to data obtained from a simulated version of the scanner. These were the first simulations of its kind for the Discovery ST. Similar simulations were employed using an anthropomorphic phantom to assess the effect of breathing on pulmonary lesions and the determination of the SUVs of these lesions.

It can be therefore concluded that partial volume effects play a significant role when determining the SUV of spheres in a phantom, and of lesions in the lung when taking into account the size of the objects and the amount of activity inside the objects compared to the background activity.

It is possible to conclude that the location of the lesions in the lung have an effect on SUV calculation during breathing based on the amount of movement of the lesions during the breathing cycle as well as a result of the surrounding tissue or organ structures. Activity outside the field-of-view of the PET/CT scanner contributed to a change in SUV determination in particular to the lower regions of the lung as a result of scatter especially during 3D mode acquisition.

In this research, it was therefore possible to assess successfully some of the physical factors that affect the accuracy of a single SUV measurement.

In the clinical situation it is important to note that when no correction is made for breathing, the influence of breathing motion on the accuracy of SUVs will be more in the basal parts of the lungs compared to the lesions in the apical region. In addition, there is a dependence on the size of the lesions, the activity inside and surrounding the lesions and the amount of random- and scattered coincidences that arise from these different parameters. Since there are so many variables that play a role, it is therefore not possible to provide an accurate assessment of the relative contributions of these factors and their relative importance on the determination of an SUV measurement. Applying various correction factors based on the factors that were investigated in this research may aid in improving the accuracy of the SUVs and thus the assessment of tumours and tumour response to therapy in patients.

5.5 References

Adam L-E, Karp JS, Brix G. 1999. Investigation of scattered radiation in 3D whole-body positron emission tomography using Monte Carlo simulations. *Phys Med Biol* 44: 2879-2895.

Boellaard R, Krak NC Hoekstra OS, Lammertsma AA. 2004. Effects of Noise, Image Resolution, and ROI Definition on the Accuracy of Standard Uptake Values: A Simulation Study. *J Nucl Med* 45:1519-1527.

Hatt M, Le Maitre A, Wallach D, Fayad H, Visvikis D. 2012. Comparison of different methods of incorporating respiratory motion for lung cancer tumor volume delineation on PET images: a simulation study. *Phys Med Biol* 57:7409-7430.

Krak NC, Boellaard R, Hoekstra OS, Twisk JWR, Hoekstra CJ, Lammertsma AA. 2005. Effects of ROI definition and reconstruction method on quantitative outcome and applicability in a response monitoring trial. *Eur J Nucl Med Mol Imaging* 32:294-301.

Lamare F, Ledesma Carbayo MJ, Cresson T, Kontaxakis G, Santos A, Cheze-le Rest C, Reader AJ, Visvikis D. 2007. List-mode-based reconstruction for respiratory motion correction in PET using non-rigid body transformations. *Phys Med Biol* 52:5187-5204.

Liu C, Pierce LA, Alessio AM, Kinahan PE. 2009. The impact of respiratory motion on tumor quantification and delineation in static PET/CT imaging. *Phys Med Biol* 54:7345-7362.

Nehmeh SA, Erdi YE. 2008. Respiratory Motion in Positron Emission Tomography/Computed Tomography: A Review. *Semin Nucl Med* 38:167-179.

Nehmeh SA, Erdi YE, Ling CC, Rosenzweig KE, Squire OD, Braban LE, Ford E, Sidhu K, Mageras GS, Larson SM, Humm JL. 2002. Effect of respiratory gating on reducing lung motion artifacts in PET imaging of lung cancer. *Med Phys* 29:366-371.

Pandey AK, Sharma P, Pandey M, Aswathi K K, Malhotra A, Kumar R. 2012. Spreadsheet program for estimating recovery coefficient to get partial volume corrected standardized uptake value in clinical positron emission tomography-computed tomography studies. *Indian J Nucl Med* 27:89-94.

Reyes M, Malandain G, Koulibaly P, González-Ballester MA, Darcourt J. 2007. Model-based respiratory motion compensation for emission tomography image reconstruction. *Phys Med Biol* 52:3579-3600.

Soret M. Bacharach SL, Buvat I. 2007. Partial-Volume Effect in PET Tumor Imaging. *J Nucl Med* 48:932-945.

Thie JA. 2004. Understanding the Standardized Uptake Value, Its Methods, and Implications for Usage. *J Nucl Med* 45:1431-1434.

Westerterp M, Pruim J, Oyen W, Hoekstra O, Paans A, Visser E, van Lanschot J, Sloof G, Boellaard R. 2007. Quantification of FDG PET studies using standardised uptake values in multi-centre trials: effects of image reconstruction, resolution and ROI definition parameters. *Eur J Nucl Med Mol Imaging* 34:392-404.

Zaidi H. 2000. Addendum to "Relevance of accurate Monte Carlo modeling in nuclear medicine imaging". *Med Phys* 27:816-817.

Abstract

Positron emission tomography (PET) is an imaging method that uses tracers labelled with positron emitting isotopes for the monitoring and evaluation of *in vivo* molecular processes. Semi-quantitative determination of tracer uptake in a lesion is accomplished by calculating the standardised uptake value (SUV), an index that represents the amount of uptake in a given volume-of-interest (VoI) in relation to the average uptake throughout the body. The SUV is influenced by biological and physical factors that determine the uptake or detectability of the tracers which may result in false results. Changes in SUV of small lesions or lesions with low activity uptake cannot be determined with enough certainty and precision to be used for decision-making and it is therefore necessary to investigate the factors affecting the SUV.

The aim of this study was to assess the relative importance of the physical factors that affect the accuracy of a single SUV measurement using Monte Carlo modelling.

Phantom studies were performed to determine the influence of the partial volume effect due to spatial resolution using a PET scanner. Comparative Monte Carlo simulations were performed on a computer cluster using a voxelised version of the same phantom. The XCAT anthropomorphic phantom was used to assess the influences on SUV in a human-like configuration and was set-up to simulate movement in the thorax during breathing. SUVs were calculated using simulations of the phantom in 2D and 3D modes to assess the influence of the partial volume effect by variation of the size of the lesions, by variation of the contrast ratios and by placing the lesions in different areas in the lungs during. Influence of activity from outside the field-of-view (FoV) was also assessed as well as the impact the various coincidence types have. Statistical methods were used to compare the difference in data for statistical significance.

It was found that the partial volume effect was present when evaluating the SUVs of the activity in the spheres of the phantom when scanned on a PET/CT scanner as well as when performing Monte Carlo simulations. Statistically there were no significant

differences between the two scanning modes. The mean SUV increased as the voxel sizes became smaller. The choice of matrix influenced the amount of partial volume effect.

The relative contributions of true-, scatter- and random coincidences demonstrated that the true coincidences were the major contributor when assessing the data from this phantom. The relative contribution of the trues-to-total coincidences decreased with a decrease in lesion size and contrast ratio whereas the relative contributions of the scattered- and random coincidences increased. The contributions of scatters and randoms increased during the 3D acquisition mode compared to 2D mode. The contribution of the trues-to-total coincidences decreased with an increase in VoI size and consequently caused a decrease in the mean SUV.

The location of the lesion made a difference in SUV when the same size lesions are compared to each other. Apical lesions experienced the least amount of motion during breathing, were distorted less and had the least amount of variation in SUV. By moving the phantom partly outside the FoV, significant effects on the SUVs of objects still inside the FoV were found. An increase in the SUVs was observed when the true coincidences were used for the calculation. A decrease in true SUVs was found at the right basal lesion.

In conclusion, partial volume effects play a significant role when determining the SUV of objects based on their size and contrast ratio; the location of pulmonary lesions affects SUV calculation during breathing; and activity outside the field-of-view of the scanner contributed to a change in SUV in particular to the central and basal regions of the lung.

Keywords: positron emission tomography, PET, standardised uptake value, SUV, true coincidences, scattered coincidence, random coincidence, partial volume effect, breathing, lesion size, contrast ratio

Opsomming

Positron-emissietomografie (PET) is ’n beeldingsmetode wat gebruik maak van spoorders gemerk aan positron-uitstralende isotope vir die monitering en evaluering van *in vivo* molekulêre prosesse. Semi-kwantitatiewe bepaling van spoorderopname in ’n letsel word bereik deur die gestandaardiseerde opnamewaarde (GOW) te bereken, ’n indeks wat die hoeveelheid opname in ’n bepaalde volume-van-belang (VvB) verteenwoordig, in verhouding met die gemiddelde opname in die res van die liggaam. Die GOW word beïnvloed deur biologiese en fisiese faktore wat die opname of waarneembaarheid van die spoorders bepaal en wat kan veroorsaak dat onjuiste resultate ontstaan. Veranderinge in GOW van klein letsels of letsels met ’n lae opname, kan nie met genoegsame sekerheid of presisie bepaal word nie en daarom is dit nodig om die faktore wat die GOW beïnvloed, te ondersoek.

Die doel van die studie was om die relatiewe belangrikheid van die fisiese faktore wat die akkuraatheid van ’n enkele GOW-meting beïnvloed, te bepaal met behulp van Monte Carlo modellering.

Fantoomstudies is gedoen om die invloed te bepaal van die parsiële volume-effek wat bestaan weens ruimtelike oplosvermoë, deur gebruik te maak van ’n PET-skandeerder. Vergelykende Monte Carlo simulasies is uitgevoer by ’n rekenaarbondel met ’n digitale weergawe van dieselfde fantoom. Die XCAT antropomorfiese fantoom is opgestel om beweging in die borskas te simuleer tydens asemhaling en is gebruik om die invloed op GOW in ’n mens-konfigurasie te ondersoek. GOWs is bereken na simulasies van die fantoom in 2D- en 3D opname modusse gedoen is om die invloed van die parsiële volume-effek te bepaal deur verandering in letselgrootte, in kontrasverhouding en deur die letsels in verskillende gebiede in die longe te plaas. Invloed van aktiwiteit wat buite die gesigsveld voorkom is ook ondersoek asook die impak wat die verskillende koïnsidensie-tipes uitoefen. Statistiese metodes is gebruik om die verskille in data vir statistieke beduidendheid te toets.

Daar is gevind dat die parsiële volume-effek teenwoordig is met die evaluering van die GOWs van die aktiwiteit in die sfere van die fantoom wat op die PET/RT skandeerder gebeeld is asook wanneer die simulasies uitgevoer is. Die gemiddelde GOW het verhoog as die voxelgroottes kleiner geword het. Die matriks-keuse beïnvloed die grootte van die parsiële volume-effek.

Met die analise van die relatiewe bydrae van die egte-, verstrooide en ewekansige koïnsidensies uit data van hierdie fantoom, is gevind dat die egte koïnsidensies die hoofbydraende gebeurtenis was in die beeldvorming. Die relatiewe bydrae van die egte-tot-totale koïnsidensies het afgeneem met ’n verkleining van letselgrootte en kontrasverhouding terwyl die relatiewe bydraes van die verstrooide en ewekansige koïnsidensies toegeneem het. Die bydraes van verstrooide en ewekansige koïnsidensies het verhoog tydens 3D opname vergeleke met 2D opname. Die bydrae van die egtes-tot-totale koïnsidensies het afgeneem met ’n vergroting in VvB en gevolglik ’n verlaging in GOW veroorsaak.

Die ligging van die letsels het ’n verskil gemaak in GOW wanneer dieselfde grootte letsels met mekaar vergelyk is. Apikale letsels het die minste beweging ondervind gedurende asemhaling, is die minste vervorm en het die kleinste variasie in GOW getoon. Deur die fantoom gedeeltelik buite die gesigsveld te plaas, is beduidende effekte in die GOW van die voorwerpe wat steeds binne die gesigsveld geleë was, ondervind. ’n Verhoging in GOW is bespeur as die egte koïnsidensies gebruik is in die berekening. ’n Verlaging in egte GOWs is gevind by die regter basale letsel.

Gevolglik speel parsiële volume-effekte’n beduidende rol by die bepaling van GOW van voorwerpe, gebaseer op die groottes en kontrasverhoudings; die ligging van die pulmonêre letsels affekteer die GOW tydens asemhaling; en die aktiwiteit buite die gesigsveld dra by tot ’n verandering in GOW, veral by die sentrale en basale gedeeltes van die long.

Sleutelwoorde: positron-emissietomografie, PET, gestandaardiseerde opnamewaarde, egte koïnsidensies, verstrooide koïnsidensies, ewekansige koïnsidensies, parsiële volume-effek, asemhaling, letselgrootte, kontrasverhouding.